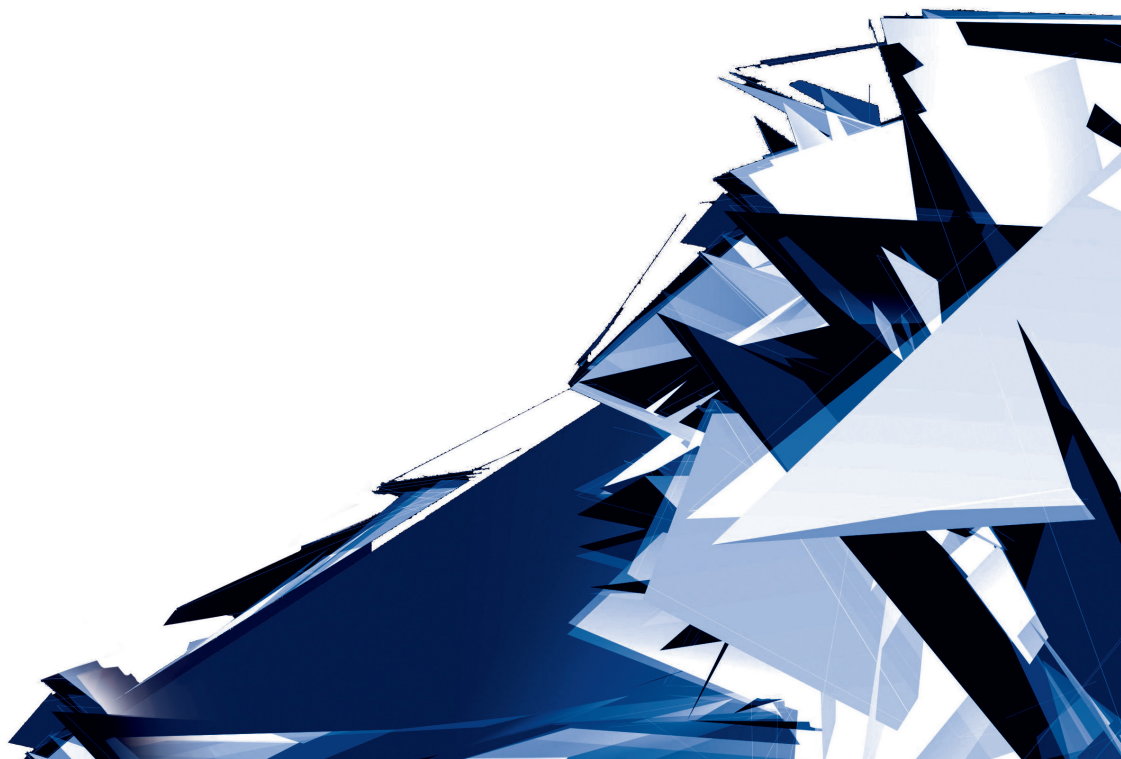


Technical Transactions

Czasopismo Techniczne

Volume 3

Year 2017 (114)



Chairman of the Cracow University of Technology Press Editorial Board
Przewodniczący Kolegium Redakcyjnego Wydawnictwa Politechniki Krakowskiej

Tadeusz Tatara

Editor-in-chief
Redaktor naczelny

Józef Gawlik
(jgawlik@mech.pk.edu.pl)

Scientific Council
Rada Naukowa

Jan Błachut – University of Liverpool (UK)
Wojciech Bonenberg – Poznan University of Technology (Poland)
Tadeusz Burczyński – Silesian University of Technology (Poland)
Massimo Corcione – Sapienza University of Rome (Italy)
Leszek Demkowicz – The University of Texas at Austin (USA)
Joseph El Hayek – University of Applied Sciences (Switzerland)
Ameen Farooq – Technical University of Atlanta (USA)
Zbigniew Florjańczyk – Warsaw University of Technology (Poland)
Marian Giżejowski – Warsaw University of Technology (Poland)
Sławomir Gzell – Warsaw University of Technology (Poland)
Allan N. Hayhurst – University of Cambridge (UK)
Maria Kušnierova – Slovak Academy of Sciences (Slovakia)
Krzysztof Magnucki – Poznan University of Technology (Poland)
Herbert Mang – Vienna University of Technology (Austria)
Arthur E. McGarity – Swarthmore College (USA)
Antonio Monestiroli – Polytechnic of Milan (Italy)
Ivor Samuels – University of Birmingham (UK)
Miroslaw J. Skibniewski – University of Maryland (USA)
Günter Wozny – Technical University in Berlin (Germany)
Roman Zarzycki – Lodz University of Technology (Poland)

Native Speakers

Weryfikacja językowa

Tim Churcher
Robin Gill
Justin Nnorom

Section Editor
Sekretarz Sekcji

Dorota Sapek
(dsapek@wydawnictwo.pk.edu.pl)

Editorial Compilation
Opracowanie redakcyjne

Dorota Sapek
(dsapek@wydawnictwo.pk.edu.pl)

Typesetting
Skład i łamanie

Anna Basista

Design
Projekt graficzny

Michał Graffstein

Series Editors
Redaktorzy Serii

ARCHITECTURE AND URBAN PLANNING:

Mateusz Gyurkovich
(mgyurkovich@pk.edu.pl)

CHEMISTRY:

Radomir Jasiński
(radomir@chemia.pk.edu.pl)

CIVIL ENGINEERING:

Marek Piekarczyk
(mpiekar@pk.edu.pl)

ELECTRICAL ENGINEERING:

Piotr Drozdowski
(pdrozdow@usk.pk.edu.pl)

ENVIRONMENTAL ENGINEERING:

Michał Zielina
(mziel@vistula.wis.pk.edu.pl)

**PHYSICS, MATHEMATICS
AND COMPUTER SCIENCES:**

Włodzimierz Wójcik
(puwojcik@cyf-kr.edu.pl)

MECHANICS:

Andrzej Sobczyk
(andrzej.sobczyk@mech.pk.edu.pl)

www.ejournals.eu/Czasopismo-Techniczne
www.technicaltransactions.com
www.czasopismotechniczne.pl

Contents

ARCHITECTURE AND URBAN PLANNING:

Patrycja Haupt

In the land of the elements. Nature in the recreational spaces of the cities of Finland.....5

CHEMISTRY:

Monika Gwadera, Krzysztof Kupiec

Diffusion with chemical reaction – assessment of the accuracy of an approximate kinetic model for spherical pellets..... 19

Elżbieta Hędrzak, Piotr Michorczyk

The application of 3D printing in the designing of channel structures in monolithic catalysts dedicated to the oxidative coupling of methane..... 31

Adam Kozak, Aleksander Kozak, Beata Fryźlewicz-Kozak

An unified formula for deriving the molecular composition of hydrocarbons..... 41

Arkadiusz Matwijczuk, Alicja Matwijczuk, Dariusz Karcz, Sławomir Wybraniec,

Dariusz Kluczyk, Mariusz Gagoś, Andrzej Niewiadomy
Spectroscopic studies of dual fluorescence effects in a selected 1,3,4-thiadiazole derivative in organic solvents and aqueous solutions..... 47

Jakub Szyman, Bolesław Tabiś

The implementation of a mathematical model of variously structured bioreactors cascades.. 63

CIVIL ENGINEERING:

Łukasz Bednarski, Rafał Sieńko, Tomasz Howiacki, Mariusz Poślajko

The monitoring of a substrate strengthened with concrete columns 73

Tadeusz Majcherczyk, Zbigniew Niedbalski

The influence of underground coal mining on an overhead high-voltage power line..... 87

Grzegorz Świt, Anna Adamczak

Stress corrosion of epoxy-glass composites monitored using acoustic emission 101

Andrzej Więckowski

Influence, of time randomness execution of work, on lenght of the construction cycle..... 115

ENVIRONMENTAL ENGINEERING:

Paweł Falaciński

Influence of fly ash from the thermal treatment of municipal sewage sludge on chosen properties of hardening slurries 125

Paweł Popielski, Apoloniusz Kodura, Błażej Smoliński

Analysis of the technical condition of the sewage collector with the use of numerical simulation..... 139

Małgorzata Kryłów, Piotr Rezka	
<i>Polybrominated flame retardants in sewage sludge and sediments (review)</i>	153
Sebastian Kujawiak, Małgorzata Makowska, Radosław Matz, Anna Gawrońska	
<i>The efficiency of the aeration process in airlift reactors with moving beds</i>	167

MECHANICS:

Krzysztof Kędzia	
<i>An algorithm for the determination of the control parameters of a multisource drive system</i>	173
Anna Korzeń, Dawid Taler	
<i>Mathematical modelling of the unsteady operation of a plate and fin heat exchanger for the time-varying mass flow rate of liquid and air velocity</i>	183
Paweł Ziółkowski, Janusz Badur	
<i>A thermodynamic and technical analysis of a zero-emission power plant in Pomerania</i>	197

Patrycja Haupt (phaupt@pk.edu.pl)

Chair of Housing Environment, Institute of Urban Design, Faculty of Architecture,
Cracow University of Technology

IN THE LAND OF THE ELEMENTS. NATURE IN THE RECREATIONAL SPACES
OF THE CITIES OF FINLAND

W KRAINIE ŻYWIOŁÓW. ELEMENTY NATURY W PRZESTRZENIACH
REKREACYJNYCH MIAST FINLANDII

Abstract

Since the beginning of the twentieth century, Finland has been a ground for experiments in the field of the housing environment. A low population density, as well as the unique natural and landscape values of the country have led to a clear trend of respect for nature in its architectural tradition. The paper, based on the theory of the Modern Movement – represented by, among others, Alvar Aalto, as well as on the tenets of Finnish the garden city of Tapiola – provides a characteristic of the role of natural elements in the composition of urban recreational spaces. The paper also discusses the structure of modern building complexes on the basis of the latest residential districts of Helsinki – as well as other cities of southern Finland, focusing on the compositional and functional role played by elements of nature within recreational spaces of a place of residence.

Keywords: recreational spaces, architecture of Finland, housing environment, residential complexes

Streszczenie:

Finlandia od początku XX wieku była polem eksperymentów w zakresie środowiska mieszkaniowego. Niska gęstość zaludnienia oraz unikatowe walory przyrodnicze i krajobrazowe kraju sprawiły, że w tradycji architektonicznej wyraźny jest nurt poszanowania natury. W artykule, opierając się na teorii ruchu Modern Movement reprezentowanego przez m.in. Alvara Aalto, a także na założeniach fińskiego miasta-ogrodu Tapioli, scharakteryzowano rolę elementów przyrodniczych w kompozycji miejskich przestrzeni rekreacyjnych. Na podstawie najnowszych realizacji dzielnic mieszkaniowych Helsinek i innych miast południowej Finlandii omówiono strukturę współczesnych zespołów zabudowy, koncentrując się na kompozycyjnej i funkcjonalnej roli elementów natury na terenach wypoczynkowych w miejscu zamieszkania.

Słowa kluczowe: przestrzenie rekreacji, architektura Finlandii, środowisko mieszkaniowe, zespoły mieszkaniowe

„It is not only the environment that affects man, as man also affects his environment; nature shapes man and man shapes nature.”

J.W. Goethe

1. Introduction. The land of the elements

Finland can be described as one of the least urbanised countries of Europe. With a surface area of 338 424 km², which is only slightly smaller than that of Poland, it is a home to nearly 5,5 million people. This results in a population density of around 15 persons per km², one of the lowest on our continent. Most of Finland's population resides in the south, in the capital agglomeration, with a surface area of almost 400 km², which is comprised of the cities of Helsinki and Espoo. It has a population of around 1.2 million, which is over 1/6 of the inhabitants of the entire country. The remaining part of the country is dominated by smaller towns and nature, the surface of which has over 33 thousand km² of inland waterways. The basis of Finland's geological structure is almost entirely composed of the crystalline rock of the Baltic Shield, with up to 74% of its surface taken by forests. This is why it is called the land of forests, rocks and lakes.

Nature, which dominates the open landscape, is also visible in urban space. The perception of beauty as an effect of the synergy of nature and architecture has emerged around the turn of the XX century. According to John Ruskin, natural beauty is the harmony between buildings and the landscape [2, p. 136]. The surface of Helsinki, crisscrossed by natural bays, as well as artificial canals, which serve both active and former port facilities, can be considered an expression of this view. The city is being developed with respect to the distinct physiognomy of the coast, which influences the complexity of its urban structure. The distinct geological structure of the terrain is made evident within the area of the city in the form of its varied topography, as well as elements of greenery-covered moraine hills, which constitute the foundation of urban interiors. What is distinct of Finnish cities is the separation of urban tissue by fragments of forest, which serves as a space of recreation for the inhabitants – which is something that can be observed both in the capital, as well as in other cities: Tampere, Jyväskylä or Lahti. Elements of nature such as greenery or water are seen in them as an integral part of the composition of urban space.

2. Research problem and methodology

The presented research scope includes the role of elements of nature in shaping urban recreational space. The specified research problem covers the influence of natural elements specific to Finnish landscape on the composition of recreational areas and their location in the city structure, along with the impact on the quality of urban environment and the citizens' conditions of living. The research was led in two streams – public space in the scale of the city as well as the recreational areas in residential settlements appearing in the structure of the paper in the form of following chapters. The methodology used was based upon the characteristics of natural elements that occur within Finland and analysing urban areas in

the context of their appearance. The influence of natural environment on the placement of recreational areas in the structure of the city was studied. The analyses of the use of natural elements of composition such as greenery, water was conducted in order to discover their significance in the design of recreational areas within the residential settlements. There were statements of the theoreticians of the architecture and urban design quoted as the background of contemporary investments. Special attention was paid to contextual works of Alvar Aalto.

3. Recreation in public spaces

The integration of architectural tissue with nature also has an impact on the character of public spaces. On the one hand these are urban areas – streets, squares planned in accordance with the tenets of the various epochs during which they were built. It is also in such areas, in the historical centre of Helsinki, that we can find cities which are a testament to the distinct geological structure of Finland. We can find an example of this in the square outlined by the Tempelkatu and Lutherinkatu streets, which is the site of the Tempelisaari church in Helsinki (Fig. 1). The building, constructed in accordance with a design by Timo and Tuomo Suomalainen in 1969, has been carved in the rock which constitutes the base of the square. Its surface was partially left untouched, filling the interior created by the walls of the buildings with a space that has a natural character. Its base is made up of an outcropping of natural granite rock covered in low-lying greenery, with taller forms placed here and there, hidden between the walls of 8 story town houses from the turn of the century.

The second face of the recreational areas of Helsinki are expansive natural areas – large tracts of land with low greenery, water bodies or forest fragments that play the part of an urban park and serve the inhabitants for recreation. Within the scope of the strict city centre, in the western part of the city near the main train station, there is a meadow forming a green corridor that runs deep into the structure of the city, that starts at the areas near Stephen Holl's *Kiasma* museum of modern art building. It forms a compositional link between the congress and concert centre by Alvaro Aalto from 1975 – with its continuation from 2011 – and the newly-built office complex located at the opposite side. From the side of the city, recreational areas start with the foregrounds of the Helsinki Music Center (Fig. 3, 4). Architects from the LPR Architects design office have designed it on an artificial elevated surface formed by the green roof that covers the shape of the structure. Its surface has been shaped in the form of steps, allowing it to serve as seats oriented towards the Center, forming an observation point of the activity near the *Kiasma* museum, which is the main point of the crossing of the pedestrian routes used by inhabitants. This place has the form of a transit point, a border between a space that is representative – tied with one of the main streets of the city, Mannerheimintie, and an area devoted to the needs associated with recreation outside of the frontage of the buildings. It contains walkways, playgrounds which are located near a lake – around which are running and bicycle routes which are meant for the recreation of the inhabitants of the strict city centre. They have been linked with a network of coastal walking routes, crossing the barrier formed by railway tracks with the use of a foot and bicycle bridge.



Fig. 1. The square with Tempeliakio church



Fig. 2. The recreational spaces of the Tapiola, the garden city, Espoo (by the author)



Fig. 3. Recreational areas in front of the Helsinki Music Center (by the author)



Fig. 4. Recreational spaces in the centre of Helsinki (by the author)

The image of the recreational areas is an expression of respect towards nature and care for the quality of the urban environment, as well as for the comfort and health of inhabitants. The roots of this manner of arranging urban space can be traced to the work of Alvaro Aalto, who, as Mieczysław Piprek wrote, has proven that “...we can shape squares, on which the pedestrian is the privileged party, that we can inject the organic qualities of nature into the urban environment, as well as inscribe elements of urban culture into nature” [5, p. 27].

Such an approach has its roots in the works of Alvaro Aalto, about which Sigfried Giedion wrote that modern architecture was something more than a generally agreed upon manner of beautifying life. It was so much a product of our time, that it had to exhibit certain universal tendencies: on the other hand it dealt too much in the problems of real life to disregard local differences in requirements, custom, materials. Finland under the leadership of Alvar Aalto showed us how architecture could be enriched in a universal manner by using solutions adapted to distinct conditions of local environments [3, p. 674].

4. Recreational spaces of residential complexes

Juhani Pallasmaa wrote that the housing environment reflects, either consciously or unconsciously: the existence of harmony – or lack thereof – in everyday life; an organic belonging to one’s environment and community – or isolation; a continuity of tradition or its loss; respect for nature and the landscape or an indifference to them, as well as a spiritual or material perception of the world [4, p. 2]. When looking at the modern residential areas of Helsinki, we can see that respect for nature is engrained within Finnish building tradition. Aside from the composition of urban spaces – shaped as a result of the processes of the development of tissue with the simultaneous preservation of the character of nature – it manifests itself in the design of residential complexes. Since the beginning of the XX century they have been shaped in accordance with Alvar Aalto’s synthesis, where nature, residential culture and work harmoniously blend into an environment of living. The architect approached residential matters with particular responsibility. He was of the opinion that it was one of the great mysteries of human life and that without residential culture there could be no mention of establishing any culture at all [5, p. 12].

One of the most famous designs which express this manner of thinking was the design and construction of the Tapioli garden city within the city of Espoo (Fig. 2). The competition for this design was won by a team of Polish urban designers: J. Chmielewski, J. Kazubiński and K. Kuraś. The housing complex was built in the 1960’s and 1970’s, with Aulis Blomsted, Aarne Ervi, Viljo Revell and Heikki Siren participating in the development of its design. The area is composed of numerous small complexes of terrace houses which harmonised with the landscape, as well as multi-family buildings located around an expansive green recreational area. The layout of the complex was based on the concept of a garden city. The various forms of use were laid out in zones – residential buildings were located along the outer zone, in the vicinity of greenery, with public services placed in the inner zone, adjacent to the recreational areas. Commercial services were grouped near

a rapid transit railway station near a road leading to the centre of Helsinki. The district is still today thought of as a model area, although its revitalisation is being planned due to the use of technologies from over 50 years ago [8].

Seeking beauty in the harmony of architecture and its natural surroundings is also a distinct quality of modern residential complexes. In their latest projects, architects make references to all the natural elements that are specific to the landscape of Finland – greenery, rock and water, searching for a modern manner of paying homage to the local cultural and landscape identity in the connection between nature and architecture.

One such project is the residential complex in southern Lautasaari – its construction having been finished in 2015 – in Helsinki, designed by the Arkkitehdit NRT Oy design office (Fig. 5, 6). Its architecture was developed as an answer to the guidelines of a competition for the development of this part of the capital, which had been held in 2002. The idea of the endeavour was to provide a view of the sea from the highest possible number of apartments, as well as to expand the waterfront area. The guidelines were implemented by having the buildings that were located near the water to hang over it, standing on pillars. The recreational spaces of the courtyards stretch between the belts of the buildings, with a view of the sea. This has also allowed the introduction of water into the composition as a floor of the urban enclosure [9]. A different form of a layout featuring water was used in the Rainbow Housing Project in Helsinki (Fig. 7, 8). Architects from the ARK-House design office placed the buildings of the complex around the ending of an unused port canal running through the Vuosaari district. The site is located in a border zone between the landscape of Helsinki's



Fig. 5. Residential complex in Lautasaari, Arkkitehdit NRT Oy, Helsinki, 2012 (by the author)



Fig. 6. Residential complex in Lautasaari, Arkkitehdit NRT Oy, Helsinki, 2012 (by the author)

suburbs and a natural area, which was heretofore used for taking walks. The buildings – which were built in 2012 – feature apartments for rent. The composition of the facade facing towards the south from the side of the canal is open by the means of a series of balconies and loggias. The northern facade – on the contrary, constitutes a curved wall surface with singular colour accents in the form of bay windows, thus the name of the complex – Rainbow Housing [10].

Aside from water bodies, the landscape of Finland also features distinct moraine hills covered by forests, which can sometimes also be seen within the landscape of cities. An example of a complex which makes use of their qualities as recreational areas is the capital's Viikinmäki district (Fig. 9). Residential buildings were placed there, making use of the natural topography of the terrain, as well as its geological structure. The complex of multi-family houses, of varied form and character, is connected by a network of walkways that create a labyrinth of winding paths, which ascend and descend in accordance with the terrain. They constitute recreational areas for the inhabitants of this part of the capital, in the form of forested moraine hills. The point that links the walkway routes that were created in this manner is the Quarter House social centre building (Fig. 10). Built in 2015 in accordance with a design by the AFKS design office, this public building (the only one in the Viikinmäki district) houses a kindergarten and primary school, as well as common use areas [11]. The outer courtyard of the building is located near recreational spaces, forming their foreground.

Another example of the use of naturally forested areas for recreation accompanying residential buildings is the Ruotutorppa Social Housing complex, composed of multi-family



Fig. 7. The Rainbow Housing residential complex, ARK-house, Helsinki 2012. (by the author)



Fig. 8. The recreational areas of the Vuosaari residential complex, Helsinki (by the author)





Fig. 9. Recreational areas of the residential complex of the Viikinmäki district, Helsinki (by the author)



Fig. 10. Viikinmäki Quarter House social centre, AFKS, Helsinki, 2015 (by the author)



Fig. 11. Ruotutorppa Social Housing, Arkkitehdit Hannunkari & Mäkipaja Architects, Helsinki, 2010
(by the author)



Fig. 12. Puukuokka Housing Block, OOEPA, Jyväskylä, 2015 (by the author)



buildings in the northern part of Helsinki (Fig. 11). The complex, composed of two residential buildings, was built in 2010 in accordance with a design by Arkkitehdit Hannunkari & Mäkipaja Architects [12]. The site, located in the suburban zone of the capital and constituting municipal property, is characterised by its proximity to a forest, which was used as a form of a recreational area for the residents of the complex, which features 62 apartments with 1 to 3 rooms (48–95 m²).

The Puukuokka multi-family building complex in the city of Jyväskylä (Fig. 2) was placed in a similar place. The priority of the architects from the OOEPEAA design office was the construction of energy efficient buildings with sustainable properties. The project has been under construction since the year 2015 and is being financed from the municipal residential construction fund. Apart from a non-standard payment system, it is set apart by its structure, as the 8 story building features a timber post and beam structure [13]. The project, which is to be comprised of 3 buildings, is accompanied by recreational areas – an untouched part of the site – a moraine hill – which used to be a fragment of a forest. It is connected with a forest area with a similar geological structure, which serves the residents as a place of active recreation, which at the same time constitutes the border of the city's built-up area.

5. Conclusion

The study allowed to formulate conclusions proving the possible creative use of natural elements as a material in the creation of both, the public spaces as the elements of the structure of the city, as well as in the design of recreational areas within residential settlements. The inclusion of elements of nature enriches the composition of urban space, affecting its diversity and attractiveness. It also provides the ability to create the network of connections through green infrastructure desirable from the point of view of the local ecosystem. It also creates the possibility of promoting a healthy lifestyle among the residents.

The respect for the natural qualities of an area, as well as for the landscape, that is evident in current construction projects has its basis in the Finnish tradition of building construction. Beauty that lies in the skillful combination of architecture and its surroundings has become one of the indicators of the qualities of the urban composition of city spaces, which is also viable today. At the same time, as one of the principles of *Green Architecture* formulated by Brenda and Robert Bale, it fits in with modern trends of sustainable design [7, p. 15]. This quality was also paid attention to by Alvar Aalto. In a monograph published in 1987, titled *Aalto Alvar, Idee di architettura – scritti scelti 1921–1968*, Marcello Fagiolo wrote about his views as such: “Architecture requires scholars – researchers, in order to understand the new requirements that are being placed before it, as well as to convert society into an effective system, in which everyone can live in proper biological conditions, represented by the sun, the air and light” [1]. This idea, formulated in a broader manner, is currently present in the field of studying the urban environment, and which invariably indicate the possibility of man's contact with nature as a basic factor, one which is indispensable in the creation of high quality residential areas.

References

- [1] Aalto A., Fagiolo M., *Idee di architettura: scritti scelti 1921–1968*; Zanichelli, Bologna 1987 [after:] F. Fascia, Alvar Aalto and the Bio-Architecture, [https://pl.scribd.com/doc/24680394/ Architecture-eBook-Alvar-Aalto-Alvar-Aalto-and-the-Bio-Architecture](https://pl.scribd.com/doc/24680394/Architecture-eBook-Alvar-Aalto-Alvar-Aalto-and-the-Bio-Architecture), accessed on: 21.11.2016.
- [2] Eco U. (ed.), *Historia piękna*, Rebis, Poznań 2006.
- [3] Giedion S., *Przestrzeń, czas i architektura*, Warsaw 1968.
- [4] *Kształtowanie Środowiska Mieszkaniowego w Finlandii*, (katalog wystawy), Wydawnictwo Centralnego Biura Wystaw Artystycznych, Warsaw 1979.
- [5] Piprek M., *Alvar Aalto*, Arkady, Warsaw 1987.
- [6] Schildt G., *Alvar Aalto. Masterworks*, Thames & Hudson, London 1998.
- [7] Vale R., Vale B., *Ökologische Architektur: Entwürfe für eine bewohnbare Zukunft*, Campus, 1991.

Internet sources

- [1] The T3 Plan – A Facelift For Finland’s Epicenter Of Modernist City Planning, <https://urbanfinland.com/2012/02/26/the-t3-plan-a-facelift-for-finlands-epicenter-of-modernist-city-planning/>, accessed on: 21.11.2016 r.
- [2] Housing in East Lauttasaari / Arkkitehdit NRT Oy, <http://www.archdaily.com/773186/merenkulkijanranta-arkkitehdit-nrt-oy>, accessed on: 21.11.2016 r.
- [3] Rainbow Housing Project / ARK-house Architects, <http://www.archdaily.com/338024/rainbow-housing-project-ark-house-architects>, accessed on: 21.11.2016 r.
- [4] Viikinmäki Quarter House, <http://www.archdaily.com/771425/viikinmaki-quarter-house-afks>, accessed on: 21.11.2016 r.
- [5] Ruutorppa Social Housing, <http://www.archdaily.com/113043/ruutorppa-social-housing-arkkitehdit-hannunkari-makipaja-architects>, accessed on: 21.11.2016 r.
- [6] Puukuokka Housing Block, <http://www.archdaily.com/614915/puukuokka-housing-block-oopeaa>, accessed on: 21.11.2016 r.

All photographs have been made by the author.

Monika Gwadera (mgwadera@indy.chemia.pk.edu.pl)

Krzysztof Kupiec

Chair of Chemical and Process Engineering, Faculty of Chemical Engineering and
Technology, Cracow University of Technology

DIFFUSION WITH CHEMICAL REACTION – ASSESSMENT OF THE
ACCURACY OF AN APPROXIMATE KINETIC MODEL FOR SPHERICAL
PELLETS

DYFUZJA Z REAKCJĄ CHEMICZNĄ – OCENA DOKŁADNOŚCI
PRZYBLIŻONEGO MODELU KINETYCZNEGO
DLA ZIAREN KULISTYCH

Abstract

Diffusion with a first-order chemical reaction in a spherical pellet of a catalyst with third-type boundary conditions was considered; such a process can be described by a kinetic model based on the continued fraction approximation. Results of calculations obtained from an approximate kinetic model were compared with the exact solution. It was found that the application of this approximate model provides a good level of accuracy and requires short calculation times.

Keywords: diffusion, chemical reaction, approximate kinetic model

Streszczenie

Rozważono dyfuzję z reakcją chemiczną I rzędu w kulistym ziarnie katalizatora z warunkami brzegowymi III rodzaju. Taki proces można opisać modelem kinetycznym opartym na aproksymacji ułamkami łańcuchowymi. Wyniki obliczeń uzyskane z przybliżonego modelu kinetycznego porównano z rozwiązaniem ścisłym. Stwierdzono, że stosowanie przybliżonego modelu zapewnia dobrą dokładność wyników oraz krótkie czasy obliczeń.

Słowa kluczowe: dyfuzja, reakcja chemiczna, przybliżony model kinetyczny

Nomenclature

Bi	– Biot number
c	– component concentration, mol/m ³
D_e	– effective diffusion coefficient, m ² /s
k_1	– reaction rate constant, 1/s
k_c	– mass transfer coefficient, m/s
n	– approximation order
r	– spatial coordinate, m
R_p	– radius of pellet, m
t	– time, s
Y	– dimensionless component concentration

Greek symbols

β_n	– eigenvalues
ξ	– dimensionless spatial coordinate
η	– effectiveness factor
η_G	– global effectiveness factor
τ	– dimensionless time
Φ	– Thiele modulus

Subscripts and superscripts

app	– approximate
b	– bulk
ex	– exact
–	– average value

1. Introduction

Mathematical models of catalytic reactors and adsorbers are systems of partial differential equations; the equation that refers to mass balance in a fluid flowing through the reactor/adsorber is an example of one of these. The other example refers to the kinetics of mass transport inside the catalyst/adsorbent. Solving such systems of equations is difficult. The problem of time-consuming calculations is especially significant in cases where a complex procedure is required in order to perform them. This is why it is favourable to use a simplification in the mathematical description of diffusion in porous pellets which results in the elimination of the spatial coordinate in a pellet. After the elimination of the spatial coordinate, the considered system is described by a system of ordinary differential equations.

The description of diffusive transport kinetics with approximate equations has been known for a long time. Historically, the LDF equation proposed by Glueckauf [1] was the first such equation. Due to substantial inaccuracies with this equation, a number of other

approximate kinetic equations were proposed. They referred both to the process of diffusion with adsorption [2–5] and diffusion with chemical reaction [6–16].

In the work by Lee & Kim [17], a new approach to the problem of approximate equations of diffusive mass transport kinetics is presented. This model is based on: the application of the Laplace transform for the diffusion equation; the transformation of the solution to the form of a continued fraction; the truncation of the resulting expression for the number of terms which are needed to ensure the required level of accuracy. The first-order approximation corresponds to the LDF equation. The authors proposed their model for different pellet shapes (slab, cylinder, sphere) wherein they assumed that the mass transfer resistance in a fluid surrounding the catalyst/adsorbent pellet (external resistance) can be neglected. Moreover, it was assumed in the model that the concentration of the component in the fluid is time-invariant.

In work [18], the discussed model was extended for the case when transfer resistances are in both solid and fluid phases; therefore, a parameter characterising the relationship between the external and the internal resistance to mass transfer was introduced into the model – this is the Biot number (for a spherical pellet):

$$Bi = \frac{k_c R}{D_e} \quad (1)$$

In work [19], the changes of the component concentration in the bulk of a fluid surrounding a pellet was taken into account in the approximate model. It was shown [18, 19] that models using the continued fraction approximation give results consistent with exact solutions (analytical or numerical). This numerical verification, however, referred to systems without chemical reactions. Hence, processes of alternate adsorption-desorption in a pellet and moreover, adsorption in a perfect-mixing tank were considered.

When a chemical reaction occurs in a system, the diffusion equation describing the rate of transfer of a component in a porous pellet must be complemented with the source term which results from the elimination or formation of the component. For diffusion with a chemical reaction, the kinetic relationships contain (except from the Biot number) the Thiele modulus (internal diffusion modulus), which for a spherical pellet and a first-order reaction is defined as follows [20]:

$$\Phi = R \sqrt{\frac{k_1}{D_e}} \quad (2)$$

In this work, the results of kinetic calculations for diffusion with a first-order chemical reaction occurring in a spherical pellet of a catalyst are presented. Calculations were conducted on the basis of the approximate kinetic model based on the approximation of the continued fraction and the obtained results were compared with the analytical solution. Calculations were conducted for different values of the Biot number, different values of the Thiele modulus and different orders of approximation. The aim of this work is to determine the effect of the approximation order on accuracy and calculation time.



2. The diffusion and chemical reaction equation

The equation of diffusion and chemical reaction in a spherical pellet of a catalyst has the form:

$$\frac{\partial c}{\partial t} = D_e \left(\frac{\partial^2 c}{\partial r^2} + \frac{2}{r} \frac{\partial c}{\partial r} \right) + R \quad (3)$$

while the first-order reaction rate is:

$$R = -k_1 c \quad (4)$$

The following initial condition was assumed:

$$t = 0 \quad c = 0 \quad (5)$$

The boundary condition for the centre of a spherical pellet has the form:

$$r = 0 \quad \frac{\partial c}{\partial r} = 0 \quad (6)$$

The external mass transfer resistance was taken into account in the condition for the pellet surface:

$$r = R \quad -D_e \frac{\partial c}{\partial r} = k_c (c - c_b) \quad (7)$$

The equations were transformed to the dimensionless form. The following dimensionless variables were introduced:

$$Y = \frac{c}{c_b} \quad \xi = \frac{r}{R} \quad \tau = \frac{D_e t}{R^2} \quad (8)$$

these relate to component concentration, position variable and time, respectively.

The dimensionless equation of diffusion with a chemical reaction has the form:

$$\frac{\partial Y}{\partial \tau} = \frac{\partial^2 Y}{\partial \xi^2} + \frac{2}{\xi} \frac{\partial Y}{\partial \xi} - \Phi^2 Y \quad (9)$$

with the initial condition:

$$\tau = 0 \quad Y = 0 \quad (10)$$

and boundary conditions:

$$\eta = 0 \quad \frac{\partial Y}{\partial \eta} = 0 \quad (11)$$

$$\xi = 1 \quad \frac{\partial Y}{\partial \xi} = Bi(1 - Y) \quad (12)$$

The average concentration of a component in a pellet results from the following relationship:

$$\bar{Y} = 3 \int_0^1 \xi^2 Y \cdot d\xi \quad (13)$$

3. The approximate kinetic model

As a result of the applied approximation, a partial differential equation is replaced by a system of n ordinary differential equations where n is the approximation order. If the external mass transfer resistances are significant and have to be taken into account, this system of differential equations in the matrix form is as follows [18]:

$$\dot{\mathbf{x}} = \mathbf{d}^{-1} \mathbf{a} \mathbf{x} + \mathbf{d}^{-1} \mathbf{b} \quad (14)$$

where vectors $\dot{\mathbf{x}}$, \mathbf{x} and \mathbf{b} are defined in the following way:

$$\dot{\mathbf{x}} = [\dot{x}_1 \quad \dot{x}_2 \quad \dots \quad \dot{x}_n]^T \quad (15)$$

$$\mathbf{x} = [x_1 \quad x_2 \quad \dots \quad x_n]^T \quad (16)$$

$$\mathbf{b} = [3 \quad 3 \quad \dots \quad 3]^T \quad (17)$$

Matrix \mathbf{d} has the form:

$$\mathbf{d} = \mathbf{I} + \frac{1}{3Bi} \cdot \mathbf{b} \mathbf{q} \quad (18)$$

while matrix \mathbf{a} :

$$\mathbf{a} = \begin{bmatrix} -p_1 q_1 & -p_1 q_2 & -p_1 q_3 & \dots & -p_1 q_{n-1} & -p_1 q_n \\ -p_1 q_1 & -p_2 q_2 & -p_2 q_3 & \dots & -p_2 q_{n-1} & -p_1 q_n \\ -p_1 q_1 & -p_2 q_2 & -p_3 q_3 & \dots & \dots & -p_1 q_n \\ \dots & \dots & -p_3 q_3 & \dots & \dots & \dots \\ \dots & -p_2 q_2 & \dots & \dots & -p_{n-1} q_{n-1} & -p_{n-1} q_n \\ -p_1 q_1 & -p_2 q_2 & -p_3 q_3 & \dots & -p_{n-1} q_{n-1} & -p_n q_n \end{bmatrix} - \Phi^2 \mathbf{I} \quad (19)$$

where the values of p_i and q_i are:

$$p_i = 2i^2 + i \quad (20)$$

$$q_i = 4i + 1 \quad (21)$$

In the above formulas, $i = 1, 2, \dots, n$, while \mathbf{I} is the identity matrix. The system of equations (14) should be solved with the initial condition:

$$\tau = 0; \quad \mathbf{x} = [0 \ 0 \ \dots \ 0]^T \quad (22)$$

As a result of solving the system of differential equations (14), one gets the vector function $\mathbf{x}(\tau)$, on the basis of which the scalar function $\bar{Y}(\tau)$ can be determined:

$$\bar{Y} = \mathbf{q}\mathbf{x} \quad (23)$$

The calculation problem is as follows: for the given values of the Thiele modulus Φ and the Biot number Bi , the average dimensionless concentration of a component in a catalyst pellet \bar{Y} after time τ should be determined. For calculation purposes, the approximation order n should be assumed – the accuracy of calculations depends on it.

The calculation algorithm is presented below. Elements of vectors \mathbf{p} and \mathbf{q} are determined according to (20) & (21), elements of matrices \mathbf{d} and \mathbf{a} are then found according to formulas (18) & (19), respectively. In the next step, one should find the inverse of matrix \mathbf{d} and determine products $\mathbf{d}^{-1}\mathbf{a}$ and $\mathbf{d}^{-1}\mathbf{b}$. As the result of solving the system of differential equations (14), values of function \mathbf{x} are found, which after substitution into relationship (23), provide the solution.

4. Analytical solution

The analytical solution of equation (9) with conditions (10–12) for spherical pellets has the form [9]:

$$\bar{Y} = \eta_G + \frac{6Bi}{\Phi^3} \sum_{i=1}^{\infty} \frac{-\Phi\sqrt{\beta_i} \cdot \cos(\Phi\sqrt{\beta_i}) + \sin(\Phi\sqrt{\beta_i})}{(\beta_i + 1)\sqrt{\beta_i} [Bi \cdot \cos(\Phi\sqrt{\beta_i}) - \Phi\sqrt{\beta_i} \cdot \sin(\Phi\sqrt{\beta_i})]} \cdot \exp[-(\beta_i + 1)\Phi^2\tau] \quad (24)$$

where the global effectiveness factor η_G is given by the relationship:

$$\eta_G = \frac{\eta}{1 + \frac{\Phi^2\eta}{3Bi}} \quad (25)$$

The effectiveness factor η depends only on the Thiele modulus according to the following formula for spherical pellets:

$$\eta = \frac{3}{\Phi} \left[\frac{1}{\tanh(\Phi)} - \frac{1}{\Phi} \right] \quad (26)$$

If there are no external mass transfer resistances ($Bi \rightarrow \infty$), then $\eta_G = \eta$. Values β_j ($j = 1, 2, \dots$) are subsequent roots of the algebraic equation:

$$\Phi\sqrt{\beta} \cdot \cos(\Phi\sqrt{\beta}) + (Bi-1) \cdot \sin(\Phi\sqrt{\beta}) = 0 \quad (27)$$

The interpretation of roots of this equation is presented in Fig. 1. Substituting into (27):

$$x = \Phi\sqrt{\beta} \quad (28)$$

one obtains:

$$\cot(x) = \frac{1-Bi}{x} \quad (29)$$

In Fig. 1, the graphs of functions $y_1(x)$ and $y_2(x)$ are presented; these functions are given as follows:

$$y_1 = \cot(x) \quad y_2 = \frac{1-Bi}{x} \quad (30 \text{ a, b})$$

The abscissas of the intersection points of these functions are the solutions to equation (29). The graph of function y_1 does not depend on Bi , while the graph of function y_2 depends on this parameter. In Table 1, the first three roots of equation (29) for different values of Bi are presented.

Table 1. The zeros of equation (29) for different values of Bi

Bi	0.1	0.2	0.5	1	2	5	10	20	50	100
x_1	0.5423	0.7593	1.1656	1.5708	2.0288	2.5704	2.8363	2.9857	3.0788	3.1102
x_2	4.5157	4.5379	4.6042	4.7124	4.9132	5.3540	5.7173	5.9783	6.1582	6.2204
x_3	7.7382	7.7511	7.7899	7.8540	7.9787	8.3029	8.6587	8.9831	9.2384	9.3308

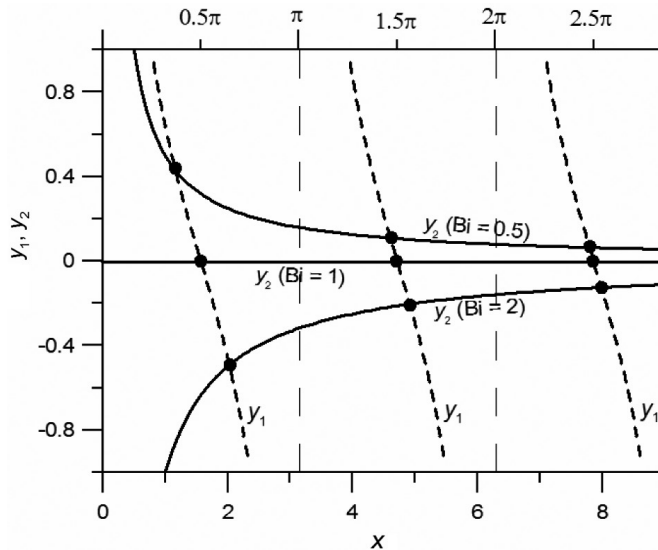


Fig. 1. The zeros of equation (29) for $Bi = 0.5$, $Bi = 1$ and $Bi = 2$

5. Results of calculations

The exact values of \bar{Y}_{ex} were determined according to the analytical solution (24–27). The approximate values of \bar{Y}_{app} were determined on the basis of the algorithm presented in Section 3 for the approximation order $n = 5$. The obtained results are presented in charts.

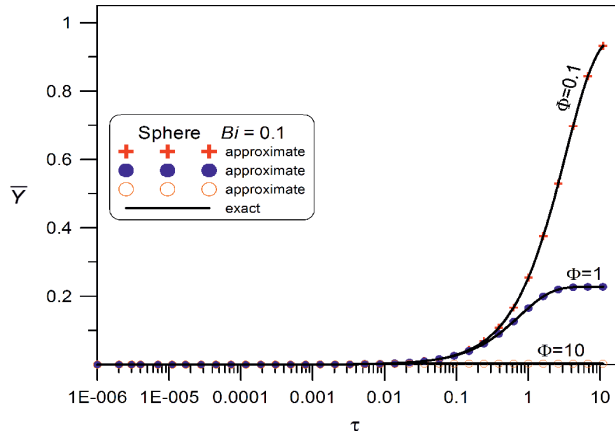


Fig. 2a. Comparison between the results of approximate and exact calculations for spherical pellets and different values of the Thiele modulus. The results refer to $Bi = 0.1$ and $n = 5$

In Figs. 2a, b, c & d, the relationships between the average dimensionless concentration of a component in a pellet and the dimensionless time of the process of diffusion with chemical reaction in a spherical pellet of a catalyst are presented. The charts determined on the basis of the approximate model and the charts resulting from the exact solution for different combinations of the values of the Biot number and Thiele modulus are presented. The consistency between the approximate and exact charts is very high.

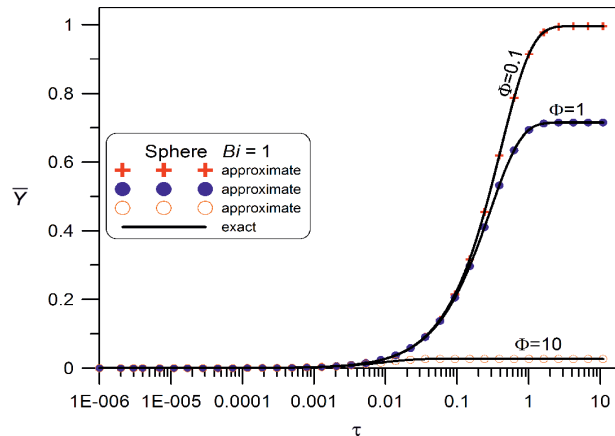


Fig. 2b. Comparison between the results of approximate and exact calculations for spherical pellets and different values of the Thiele modulus. The results refer to $Bi = 1$ and $n = 5$

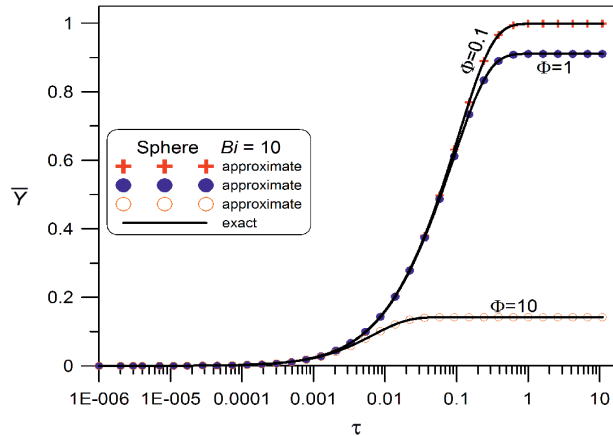


Fig. 2c. Comparison between the results of the approximate and exact calculations for spherical pellets and different values of the Thiele modulus. The results refer to $Bi = 10$ and $n = 5$

Concentration of the component increases over time; moderately at first, then the concentration increase is greater. For long durations, the average dimensionless concentration in pellets stabilises at the value of the global effectiveness factor. For small values of the Thiele modulus (which correspond to a small rate reaction), the limit concentrations in pellets have high values. For large values of Φ , which correspond to the high-rate reactions, concentrations in pellets have smaller values because of the reaction of the component.

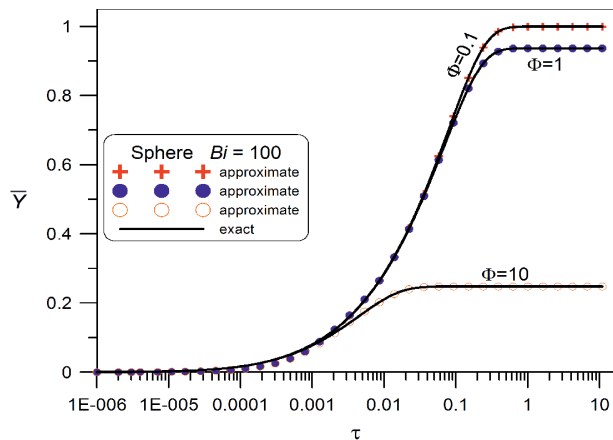


Fig. 2d. Comparison between the results of approximate and exact calculations for spherical pellets and different values of the Thiele modulus. The results refer to $Bi = 100$ and $n = 5$

In Fig. 3, temporal variations of the dimensionless concentrations of a component for a constant value of $\Phi = 1$ and different values of the Biot number are presented. The greater the Biot number, the greater the concentration values – this results from the fact that the mass transfer resistance gets smaller.

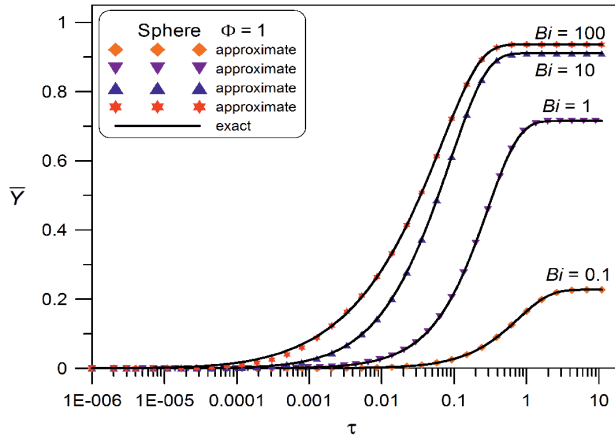


Fig. 3. Comparison between the results of approximate and exact calculations for spherical pellets and different values of the Biot number. The results refer to $\Phi = 1$ and $n = 5$

6. The effect of the approximation order on the accuracy of results and calculation time

In Fig. 4, the effect of the approximation order on the accuracy of results obtained from the approximate model is presented. The ratio between the approximate \bar{Y}_{app} and exact \bar{Y}_{ex} values, which characterises the accuracy of approximation, is presented on the vertical axis. It can be seen from this figure that the accuracy considerably depends on the approximation order and process time; the shorter this time is, the less accurate is the approximation that is obtained. For short durations, it is useful to apply high approximation orders. For $n = 10$, the approximation model is accurate across the whole time range.

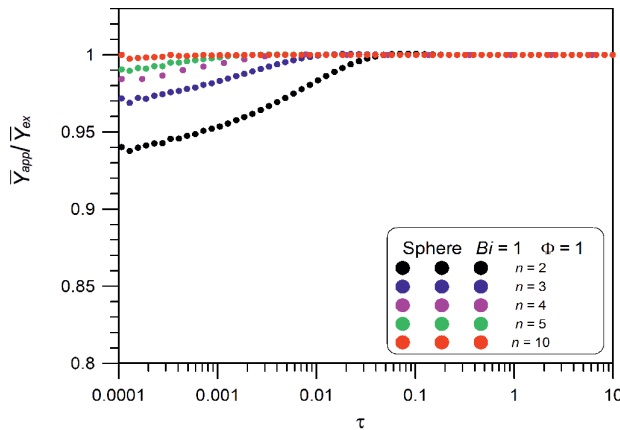


Fig. 4. Comparison of the results of approximate and exact calculations for spherical pellets and different orders of approximation. Calculations refer to $Bi = 1$ and $\Phi = 1$

The times of calculations were also analysed. The results are presented in Fig. 5. The calculation time for the approximate model significantly depends upon the approximation order – this is obvious in view of the sizes of matrices which are used for algebraic calculations. For comparative reasons, the time of numerical calculations for the finite difference method is presented. For the considered process parameters ($Bi = 10$, $\Phi = 1$), the time of calculations according to the approximate model presented in this work is shorter than the time of numerical calculations when the approximation order $n < 7$.

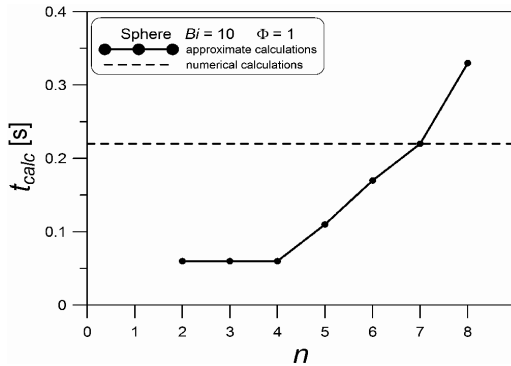


Fig. 5. Comparison of approximate and numerical calculation times

7. Conclusions

- ▶ The process of diffusion with a first-order chemical reaction with third-type boundary conditions can be described properly with the approximate kinetic model based on the approximation of continued fractions.
- ▶ The approximate model gives results consistent with the analytical solution.
- ▶ The accuracy of results obtained from the approximate model significantly depends upon the approximation order and process time. The longer the process lasts, the smaller is the order of approximation that is needed to ensure the required level of accuracy.
- ▶ Calculation times according to the approximate model are usually shorter than times required for conducting numerical calculations. It is only for high approximation orders that the times of approximate calculations do not fulfil this relationship.
- ▶ The model presented in this work is a calculation alternative for the classical numerical methods.

References

- [1] Glueckauf E., *Theory of chromatography. Part 10. Formulae for diffusion into spheres and their application to chromatography*, Transactions of the Faraday Society, Vol. 51, 1955, 1540–1551.
- [2] Cruz P., Mendes A., Magalhaes F.D., *High-order approximations for intra-particle mass transfer*, Chemical Engineering Science, Vol. 59, 2004, 4393–4399.

- [3] Georgiou A., Kupiec K., *Nonlinear driving force approximations for intraparticle mass transfer in adsorption processes. Nonlinear isotherm systems with macropore diffusion control*, Chemical Engineering Journal, Vol. 92, 2003, 185–191.
- [4] Georgiou A., *Asymptotically exact driving force approximation for intraparticle mass transfer rate in diffusion and adsorption processes: nonlinear isotherm systems with macropore diffusion control*, Chemical Engineering Science, Vol. 59, 2004, 3591–3600.
- [5] Yao C., *A new intraparticle mass transfer rate model for cyclic adsorption and desorption in a slab, cylinder or sphere*, Adsorption, Vol. 19, 2013, 77–81.
- [6] Szukiewicz M., Petrus R., *Approximate model for diffusion and reaction in a porous pellet and an effectiveness factor*, Chemical Engineering Science, Vol. 59, 2004, 479–483.
- [7] Georgiou A., Tabiś B., *Metoda aproksymacyjna badania niustalonego procesu dyfuzji i reakcji chemicznej w ziarnie katalizatora*, Inżynieria Chemiczna i Procesowa, Vol. 16, 1995, 379–391.
- [8] Goto M., Hirose T., *Approximate rate equation for intraparticle diffusion with or without reaction*, Chemical Engineering Science, Vol. 48, 1993, 1912–1915.
- [9] Goto M., Smith J.M., McCoy B.J., *Parabolic profile approximate (linear driving force model) for chemical reaction*, Chemical Engineering Science, Vol. 45, 1990, 445–448.
- [10] Lee J., Kim D.H., *Global approximations of unsteady-state adsorption, diffusion, and reaction in a porous catalyst*, AIChE Journal, Vol. 59, Issue 7, 2013, 2540–2548.
- [11] Szukiewicz M.K., *New approximate model for diffusion and reaction in a porous catalyst*, AIChE Journal, Vol. 46, Issue 3, 2000, 661–665.
- [12] Szukiewicz M.K., *Approximate model for diffusion and reaction in a porous catalyst with mass-transfer resistances*, AIChE Journal, Vol. 47, Issue 9, 2001, 2131–2135.
- [13] Szukiewicz M.K., *An approximate model for diffusion and reaction in a porous pellet*, Chemical Engineering Science, Vol. 57, 2002, 1451–1457.
- [14] Peralta Reyes E., Regalado Méndez A., Vidriales Escobar G., González Rugerio C.A., *Approximate solution to the diffusion-reaction problem with nonlinear kinetics in transient systems*, Innovations and Advanced Techniques in Computer and Information Sciences and Engineering, 2007, 133–138.
- [15] Burghardt A., Berezowski M., *Stability analysis of steady-state solutions for porous catalytic pellets: influence of the shape of the pellet*, Chemical Engineering Science, Vol. 50, 1995, 661–671.
- [16] Burghardt A., Berezowski M., *Analysis of the bifurcation of oscillatory solutions in a porous catalytic pellets: influence of the order of reaction*, Chemical Engineering Science, Vol. 51, 1996, 3307–3316.
- [17] Lee J., Kim D.H., *Simple high-order approximations for unsteady-state diffusion, adsorption and reaction in a catalyst: A unified method by a continued fraction for slab, cylinder and sphere geometries*, Chemical Engineering Journal, Vol. 173, 2011, 644–650.
- [18] Kupiec K., Gwadera M., *Approximations for unsteady state diffusion and adsorption with mass transfer resistance in both phases*, Chemical Engineering and Processing: Process Intensification, Vol. 65, 2013, 76–82.
- [19] Gwadera M., Kupiec K. *Batch adsorption in a finite volume reservoir – application of an approximate kinetic model*, Technical Transaction, Vol. 1-Ch, 2014, 3–13.
- [20] Burghardt A., Bartelmus G., *Inżynieria reaktorów chemicznych, tom II. Reaktory dla układów heterogenicznych*, PWN, Warszawa 2001.

Elżbieta Hędrzak (ehedrzak@indy.chemia.pk.edu.pl)

Piotr Michorczyk

Institute of Organic Chemistry and Technology, Faculty of Chemical Engineering and Technology, Cracow University of Technology

THE APPLICATION OF 3D PRINTING IN THE DESIGNING OF CHANNEL
STRUCTURES IN MONOLITHIC CATALYSTS DEDICATED TO THE OXIDATIVE
COUPLING OF METHANE

ZASTOSOWANIE DRUKOWANIA 3D DO MODELOWANIA STRUKTURY
KANALÓW W MONOLITYCZNYCH KATALIZATORACH DEDYKOWANYCH
DLA PROCESU UTLENIAJĄCEGO SPRZĘGANIA METANU

Abstract

In this work, a new preparation method is proposed to obtain high temperature monolithic structures for catalytic applications. A commercial 3D printer was used to synthesise polymeric templates that were utilised in the designing of channel structures in monolithic catalysts. New materials with manganese and sodium tungstate supported on corundum with macropores of well-defined shapes and sizes were prepared; their catalytic performance was investigated in the process of the oxidative coupling of methane.

Keywords: monolithic catalysts, 3D printing, oxidative coupling of methane

Streszczenie

W niniejszym artykule zaproponowano nową metodę otrzymywania wysokotemperaturowych struktur monolitycznych do zastosowań katalitycznych. Wykorzystano komercyjną drukarkę 3D, aby zsyntezować polimerowe templaty, których użyto do modelowania struktury kanałów w monolitycznych katalizatorach. Przygotowano nowe materiały zawierające mangan i wolframan sodowy na nośniku korundowym, posiadające makropory o dobrze zdefiniowanym kształcie i rozmiarze. Ich właściwości katalityczne zostały zbadane w procesie utleniającego sprzęgania metanu.

Słowa kluczowe: katalizatory monolityczne, drukowanie 3D, utleniające sprzęganie metanu

1. Introduction

Currently, natural gas is under-utilised as there are no feasible ways to convert large amounts of methane, the main component of natural gas, into products that are of any value. The oxidative coupling of methane (OCM) is a promising route for the production of ethane or ethene. Ethylene is a vital building block in the chemical industry which has seen, as expected, an increasingly high demand over the last few years. Feedstock such as naphtha or ethane, from which ethylene is produced using the cracking process, is beginning to run out; therefore, the OCM process is worthy of investigation. Thus far, no economically viable process has been put into practice despite many attempts to do so; the reason for this is the lack of active, selective and, in particular, stable catalysts [1, 2].

A large number of catalyst systems have been studied extensively. Sodium-tungsten-manganese-supported-silica catalyst (with commonly used composition of 2wt.% of Mn and 5wt.% of Na_2WO_4) is one of the most active catalysts that shows good performance and stability over a long period on stream in the OCM process with up to 30% methane conversion and 80% selectivity to ethane and ethene. However, the obtained yield and stability still need to be improved for industrial applications [1–6].

Apart from conventional particle catalysts, some monolithic catalysts were tested in the OCM process, e.g. Na_2WO_4 -Mn/SiC (foam) [7], Mn- Na_2WO_4 /SiO₂/Al₂O₃/FeCrAl (alloy foil) [8], Na₃PO₄-Mn/SiO₂/cordierite (two-stage catalyst bed reactor with Na_2WO_4 -Mn/SiO₂ particle catalyst) [9], Ce- Na_2WO_4 -Mn/SBA-15/Al₂O₃/FeCrAl (dual-bed reactor with Na_2WO_4 -Mn/SiO₂ particle catalyst) [10] – all of these exhibited a strong level of performance [7–10]. Recently, Mn- and Na_2WO_4 -containing ceramic monoliths, which were obtained on the basis of 3D printed polymeric templates, were tested by our research group. These catalysts exhibited excellent performance in the OCM process [11].

In this work, monolithic catalysts with manganese and sodium tungstate supported on corundum with macropores (channels) with well-defined shapes and sizes were prepared. In order to obtain high temperature monoliths, a novel preparation method was proposed. This method involved the use of a commercial 3D printer to synthesise polymeric templates for catalysts. Five catalysts were prepared – these differed from each other in the way in which their active components were added or in the type of macropores. Their catalytic performance was investigated in the process of oxidative coupling of methane.

2. Experimental

2.1. Catalysts preparation

Two digital models of matrixes were designed using the SketchUp software program and printer software – these models are presented in Fig. 1. Subsequently, the models were converted into STL files and mathematically sliced into 25 µm layers by the printer software. The matrixes were then printed using a digital light processing method with a resolution

of 30 μm and acrylic resin. After printing, they were washed with acetone and cured under UV lamp for six hours. Full details of the 3D printing procedures and a description of the currently applied techniques have been previously described by the authors in mini-reviews [12, 13]. The hardened polymeric matrixes were used as hard templates for the preparation of monolithic catalysts.

Reagents used for the synthesis were: corundum (alumina oxide powder, Microgrit WCA, size 15 μm); commercial solution of sodium water glass (sodium silicate, CAZET Kampinos); sodium tungstate dihydrate (pure p.a., >99%, Polish Chemical Reagents, size 100 μm); manganese (II) nitrate tetrahydrate (pure p.a., Chempur); ethyl alcohol (96% pure, POCH).

Five monolithic catalysts with manganese and sodium tungstate supported on corundum were prepared. The concentrations of solutions and mixtures were selected in order to obtain the catalysts containing 2wt.% of Mn and 5wt.% of Na_2WO_4 relative to the weight of $\alpha\text{-Al}_2\text{O}_3$. The catalysts differed in the type of the template used and/or the way in which the active components were added. The steps involved in the preparation of the catalysts are described in Table 1 and presented in Figs. 2 and 3. The synthesis of the catalysts consisted of 4–7 steps. These steps were: pre-impregnation with heating; filling template with mixture of support or catalyst precursor; drying; calcination; impregnations followed by calcinations. The monolithic structures were obtained in the process of the calcination in air, during which the templates were burnt.

2.2. Catalytic performance

The catalytic tests were carried out in a continuous flow quartz reactor. The reactor was 16 mm in external diameter, 300 mm in length and had a wall thickness of 1 mm. The weight of the catalyst sample was 4.5 g each time. Before the process, the catalyst placed in the reactor was heated in helium (99.99% purity, Linde) for 30 minutes at 780°C. During the process, the reactor was fed with a mixture of methane (99.95% purity, Linde), oxygen (99.5% purity, Linde) and helium. After 20 minutes on stream, the first data point (i.e. the instantaneous composition of the reaction gas) was measured. The reaction mixture was composed on-line with Bronkhorst volumetric flow regulators. The temperature that was measured with a thermocouple was the central temperature of the tube furnace in the middle of which the catalyst was placed. The influence of process parameters such as temperature, methane to oxygen molar ratio and complete substrate volumetric flow rate (or gas hourly space velocity) was studied for three catalysts – IMs, MMs and IIs. Additionally, the influence of temperature was examined for OMs and IIt catalysts.

The composition of the mixture after the process was analysed on-line using the Agilent 6890N gas chromatograph equipped with two columns (molecular sieve 5A for the analysis of CO and O_2 and Hayesep Q for the analysis of H_2 , CO_2 , H_2O and hydrocarbons) and thermal conductivity detectors. Conversion of methane (α_{CH_4}), selectivity to ethane and ethene (S_{C_2}), and selectivity to propane and propene (S_{C_3}) were calculated as described below. The carbon mass balance was always better than 90%.

Table 1. Steps of 2%Mn-5%Na₂WO₄/Al₂O₃ catalyst preparation. Designation: first letter – the way of introducing Mn; second letter – the way of introducing Na₂WO₄; third letter – the type of grid holes (0 – the lack of a component, M – in mass, I – impregnated, s – square, t – triangle)

Catalyst designation		Step 1	Step 2	Step 3	Step 4	Step 5	Step 6	Step 7	Step 8
0Ms			Filling template with mixture of support/catalyst precursor						
IMs		-	Al ₂ O ₃ + Na ₂ SiO ₄ sol. + Na ₂ WO ₄ · 2H ₂ O = 1:0.5: 0.056 (wt.)				850°C 2h (rate 2.7°C/min)		
MMs		Al ₂ O ₃ + ethanol sol. of Mn(NO ₃) ₂ ·4H ₂ O Al ₂ O ₃ :Mn = 1:0.02 (wt.) 250°C 100 min	Mn/Al ₂ O ₃ + Na ₂ SiO ₄ sol. + Na ₂ WO ₄ · 2H ₂ O = 1.032: 0.5:0.056 (wt.)	20°C 24 h and 120°C 4h (rate 2°C/min)	850°C 2h (rate 2.7°C/min)				
IIs		-	Al ₂ O ₃ + Na ₂ SiO ₄ sol. = 1:0.5 (wt.)			aqueous sol. of Na ₂ WO ₄ · 2H ₂ O Al ₂ O ₃ : Na ₂ WO ₄ = 1:0.05 (wt.)	850°C 2h (rate 2.7°C/min)	ethanol sol. of Mn(NO ₃) ₂ ·4H ₂ O Al ₂ O ₃ :Mn = 1:0.02 (wt.)	850°C 2h (rate 2.7°C/min)
IIt		-							

$$\alpha_{\text{CH}_4} = \frac{\sum a_i n_i}{\sum a_i n_i + \alpha_{\text{CH}_4} \cdot n_{\text{CH}_4}} \cdot 100\%$$

$$S_{\text{C}_2} = \frac{(a_{\text{C}_2\text{H}_6} \cdot n_{\text{C}_2\text{H}_6} + a_{\text{C}_2\text{H}_4} \cdot n_{\text{C}_2\text{H}_4})}{\sum a_i n_i} \cdot 100\%$$

$$S_{\text{C}_3} = \frac{(a_{\text{C}_3\text{H}_8} \cdot n_{\text{C}_3\text{H}_8} + a_{\text{C}_3\text{H}_6} \cdot n_{\text{C}_3\text{H}_6})}{\sum a_i n_i} \cdot 100\%$$

where:

n_i – the number of products moles in outlet;

a_i – the number of carbon atoms in ‘i’ product.

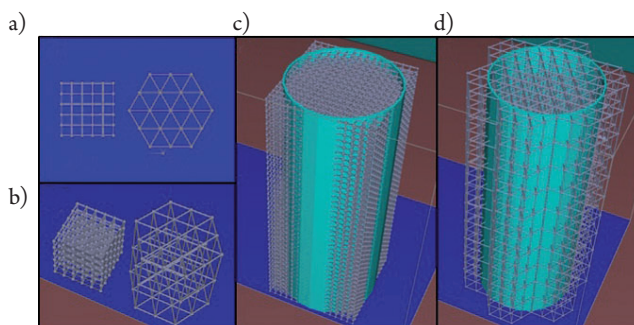


Fig. 1. Design of the templates (view from the printer software): building units (a–b); model giving square type grid holes (c); model giving triangular type grid holes (d)

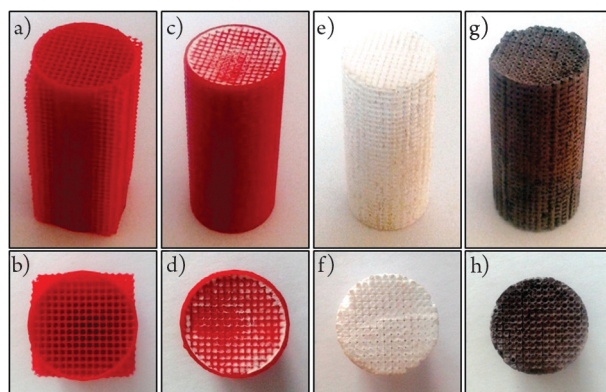


Fig. 2. Monolithic catalyst preparation: printed polymeric template with square type grid holes (a–b); template filled with support precursor (c–d); monolithic support after calcination (e–f); monolithic $\text{Mn-Na}_2\text{WO}_4/\text{Al}_2\text{O}_3$ catalyst after double impregnation (g–h). Dimensions: template – 40 mm in height; 16 mm in external and 15 mm in internal diameter; rods forming spatial structure of template – 0.27 mm thick; grid holes – 0.72 mm length of square side; catalyst (after tooling) – 32 mm in height; 15 mm in external diameter; catalyst pores – 0.25 mm in diameter

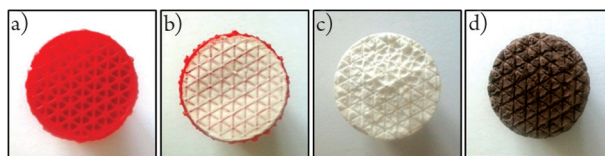


Fig. 3. Monolithic catalyst preparation: printed polymeric template with triangular type grid holes (a); template filled with support precursor (b); monolithic support after calcination (c); monolithic $\text{Mn-Na}_2\text{WO}_4/\text{Al}_2\text{O}_3$ catalyst after double impregnation (d). Dimensions: as objects in Fig. 2, except for grid holes – 1.20 mm height of triangle

3. Results and discussion

Table 2 as well as Figs. 4 and 5 summarise the catalytic results obtained over prepared catalysts in the process of the oxidative coupling of methane.

Table 2. Variation of methane conversion, selectivity to C_2 , selectivity to C_3 hydrocarbons, ethene to ethane molar ratio with GHSV and methane to oxygen molar ratio at 780°C

Catalyst	GHSV [$\text{cm}^3 \cdot \text{g}_{\text{cat}}^{-1} \cdot \text{h}^{-1}$]	Feed gas $\text{CH}_4:\text{O}_2:\text{He}$ [mol:mol:mol]	Conversion of CH_4 [%]	Selectivity to C_2 [%]	$\text{C}_2\text{H}_4:\text{C}_2\text{H}_6$ molar ratio	Selectivity to C_3 [%]
IMs	2067	2:1:2.1	29.9	43.2	2.3	1.6
		3.75:1:4.8	22.3	56.5	2.1	2.0
		7:1:9.85	12.8	70.8	1.3	1.7
	4133	2:1:2.1	18.6	54.0	1.4	1.3
		3.75:1:4.8	7.8	69.8	0.5	0.0
		7:1:9.85	5.1	77.0	0.4	0.0
6200	3.75:1:4.8	4.2	62.3	0.3	0.0	
MMs	2067	2:1:2.1	32.0	33.9	2.2	1.0
		3.75:1:4.8	21.6	60.0	2.0	1.7
		7:1:9.85	13.0	72.3	1.2	1.6
	4133	2:1:2.1	20.3	50.5	1.7	1.2
		3.75:1:4.8	8.6	71.7	0.7	0.0
		7:1:9.85	5.3	79.6	0.4	0.0
6200	3.75:1:4.8	4.2	74.5	0.3	0.0	
IIs	2067	2:1:2.1	35.0	36.6	2.3	1.2
		3.75:1:4.8	22.7	59.6	2.0	1.9
		7:1:9.85	13.6	71.2	1.3	1.5
	4133	2:1:2.1	22.7	50.3	1.8	1.3
		3.75:1:4.8	10.2	70.8	0.7	0.0
		7:1:9.85	5.8	76.4	0.4	0.0
6200	3.75:1:4.8	4.9	71.9	0.3	0.0	

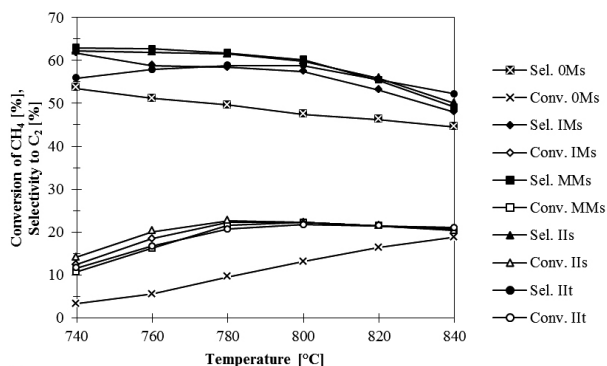


Fig. 4. Variation of methane conversion and selectivity to C_2 hydrocarbons versus temperature. Process conditions: molar ratio of $CH_4:O_2:He = 3.75:1:4.8$, $GHSV = 2067 \text{ cm}^3 \cdot \text{g}_{\text{cat}}^{-1} \cdot \text{h}^{-1}$

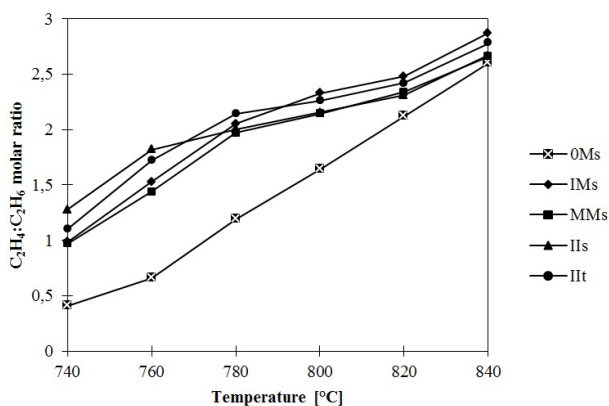


Fig. 5. Variation of ethene to ethane molar ratio versus temperature. Process conditions: molar ratio of $CH_4:O_2:He = 3.75:1:4.8$, $GHSV = 2067 \text{ cm}^3 \cdot \text{g}_{\text{cat}}^{-1} \cdot \text{h}^{-1}$

With increasing methane to oxygen molar ratio and GHSV (or total volumetric flow rate), methane conversion and ethene to ethane molar ratio decreased, and selectivity to C_2 hydrocarbons increased for three catalysts: IMs, MMs and IIs.

When temperature increased, methane conversion increased and remained almost constant between 780°C and 840°C for all the catalysts expect for 0Ms, for which the conversion increased across the entire studied temperature range. Selectivity to C_2 hydrocarbons decreased for catalysts 0Ms, IMs, MMs and IIs with increasing temperature. For the IIt catalyst, selectivity to C_2 hydrocarbons slightly increased to 780°C and then decreased. For all the catalysts, ethene to ethane molar ratio increased with increasing temperature. The results obtained when using the 0Ms catalyst were noticeably worse than those obtained when using all the others with the exception of results relating to very high temperatures. When the monolith of pure support was used, the results were the worst (4.5% methane conversion, 35.0% selectivity to C_2 and 0.7 ethene to ethane molar ratio at 780°C).

The stability of the $Mn-Na_2WO_4$ monolith with the same composition as the IIs catalyst, which was synthesised in a similar way, was investigated in the OCM process ($T = 820^\circ\text{C}$; $GHSV = 2200 \text{ cm}^3 \cdot \text{g}_{\text{cat}}^{-1} \cdot \text{h}^{-1}$; $CH_4:O_2:He = 3.8:1.5:4.2$). For a period of 20 hours on stream, the

conversion of methane, yield and selectivity to C_2 remained constant. Therefore, $Mn-Na_2WO_4$ catalysts which are described in this work would exhibit good catalytic stability [11].

Comparing the results obtained in the current study with the results obtained by other groups of scientists who investigated the thus far best known conventional $Mn-Na_2WO_4/SiO_2$ catalyst, it can be observed that the first are slightly inferior. Over the best IIs monolithic catalyst, 22.7% methane conversion and 59.6% selectivity to C_2 hydrocarbons were obtained ($T = 780^\circ C$; molar ratio of $CH_4:O_2:He = 3.75:1:4.8$; $GHSV = 2067 \text{ cm}^3 \cdot g_{\text{cat}}^{-1} \cdot h^{-1}$). Over the best particle catalysts supported on silica, 20–30% methane conversion and 70–80% selectivity to C_2 hydrocarbons were achieved [14]. General variations of methane conversion and selectivity to C_2 hydrocarbons obtained in this work are in accordance with literature, e.g. the increase of selectivity to C_2 is usually accompanied by the decrease of methane conversion [14–18]. The increase of CH_4 conversion is due to the fact that at higher temperatures, more methane molecules have sufficient energy to reduce the activation energy in the presence of the catalyst (reaching the maximum at about $800^\circ C$ in the case of $Mn-Na_2WO_4$ catalysts); at lower $CH_4:O_2$ molar ratios, more oxygen is available for the reaction and at lower helium dilution of the reaction gas (lower GHSV), the contact time with the catalyst is longer. The decrease of C_2 selectivity is a consequence of undesirable oxidation reactions – total oxidation of CH_4 and further oxidation of C_{2+} hydrocarbons; these reactions are favoured by high temperature, high oxygen content in the feed and long contact time with the catalyst. The increase of the $C_2H_4:C_2H_6$ ratio is caused by an increase in the importance of the consecutive oxidative and non-oxidative dehydrogenation reactions of ethane (both catalytic and thermal) at high temperature and high oxygen content, and for long contact times [14, 19–22]. It has also been confirmed that the addition of manganese to the catalysts is necessary to obtain better results [3].

It is very likely that the results can be improved by optimising the process conditions and the structural properties of the catalysts (e.g. size and shape of channels).

The method used to add the active components had little influence on methane conversion, selectivity to C_2 hydrocarbons and ethene to ethane molar ratio for $Mn-Na_2WO_4/Al_2O_3$ catalysts in the same process conditions. Slightly better C_2 yields were reached using the catalyst obtained by the double impregnation method compared to the other two catalysts. The differences in the results were probably connected with the concentration of the active components on the surface of the investigated catalysts. In the case of the samples prepared by the double impregnation method, the concentration of the active compounds was higher than in the case of the monoliths in which these components were incorporated into mass (bulk). Higher surface concentration may be responsible for slightly higher activity at the beginning of the process but can also result in the loss of catalyst activity later, e.g. due to loss of metal oxides after long-term exposure under OCM conditions. This is in line with the results obtained for the conventional catalysts – the catalyst activity values for different preparation methods were comparable but the catalyst prepared by mixture slurry method had better stability than those prepared by impregnation method [1, 18].

In this study, the type of catalyst macropores had very little influence on selectivity to C_2 hydrocarbons, methane conversion and ethene to ethane molar ratio in the same process

conditions. It was expected that the type of macropores would yield more differing results; however, due to the fact that reactions largely occurred not only in the internal pores but on the external walls of the monolith with a relatively large surface – it is difficult to determine whether type of catalyst channels will affect catalyst performance.

4. Conclusions

The monolithic catalysts obtained by using acrylic templates from 3D printing are fairly active and selective in the process of the oxidative coupling of methane to ethylene and ethane. The method of the incorporation of active components into the monoliths did not significantly affect the catalytic performance. Over the prepared Mn-Na₂WO₄/Al₂O₃ catalysts (in the conditions: $T = 780^{\circ}\text{C}$; molar ratio of CH₄:O₂:He = 3.75:1:4.8; GHSV = 2067 cm³·g_{cat}⁻¹·h⁻¹), selectivity to hydrocarbon products – ethane, ethene, propane and propene, and methane conversion varied in narrow ranges – 58–62% and 21–23%, respectively.

The obtained results suggest that monolithic catalysts can be a good alternative for the conventional catalysts in the OCM process. The new method of the preparation of monolithic catalysts with the use of a 3D printer will be very useful in carrying out more advanced studies in this field.

References

- [1] Chua Y.T., Mohamed A.R., Bhatia S., *Oxidative coupling of methane for the production of ethylene over sodium-tungsten-manganese-supported-silica catalyst (Na-W-Mn/SiO₂)*, Applied Catalysis A: General, vol. 343, 2008, 142–148.
- [2] Arndt S., Otremba T., Simon U., Yildiz M., Schubert H., Schomäcker R., *Mn-Na₂WO₄/SiO₂ as catalyst for the oxidative coupling of methane. What is really known?*, Applied Catalysis A: General, vol. 425–426, 2012, 53–61.
- [3] Elkins T.W., Hagelin-Weaver H.E., *Characterization of Mn-Na₂WO₄/SiO₂ and Mn-Na₂WO₄/MgO catalysts for the oxidative coupling of methane*, Applied Catalysis A: General, vol. 497, 2015, 96–106.
- [4] Michorczyk B., Suszyński K., Smoleń P., Hędrzak E., *Utleniające sprzężanie metanu zintegrowane w jednym reaktorze z odwodornieniem etanu do etenu*, Przemysł Chemiczny, vol. 95, 2016, 1936–1940.
- [5] Michorczyk B., Ogonowski J., Michorczyk P., Węgrzyniak A., *Katalizatory dla procesu utleniającego sprzężania metanu*, Przemysł Chemiczny, vol. 93, 2014, 1166–1173.
- [6] Michorczyk B., Hędrzak E., *Study of oxidative coupling of methane integrated with CO oxidation*, Technical Transactions, 2017 (article accepted for publication).
- [7] Liu H., Yang D., Gao R., Chen L., Zhang S., Wang X., *A novel Na₂WO₄-Mn/SiC monolithic foam catalyst with improved thermal properties for the oxidative coupling of methane*, Catalysis Communications, vol. 9, 2008, 1302–1306.



- [8] Greish A.A., Glukhov L.M., Finashina E.D., Kustov L.M., Sung J.S., Choo KY., Kim T.H., *Comparison of activities of bulk and monolith Mn-Na₂WO₄/SiO₂ catalysts in oxidative coupling of methane*, *Mendelev Communications*, vol. 19, 2009, 337–339.
- [9] Wang W., Ji S., Pan D., Li C., *A novel particle/monolithic two-stage catalyst bed reactor and their catalytic performance for oxidative coupling of methane*, *Fuel Processing Technology*, vol. 92, 2011, 541–546.
- [10] Wang W., Zhang Z., Ji S., *Particle/metal-based monolithic catalysts dual-bed reactor with beds-interspace supplementary oxygen: Construction and performance for oxidative coupling of methane*, *Journal of Natural Gas Chemistry*, vol. 21, 2012, 400–406.
- [11] Michorczyk P., Hędrzak E., Węgrzyniak A., *Preparation of monolithic catalysts using 3D printed templates for oxidative coupling of methane*, *Journal of Materials Chemistry A*, vol. 4, 2016, 18753–18756.
- [12] Hędrzak E., Michorczyk P., *Trójwymiarowe drukowanie: od projektu do gotowego produktu*, [in:] Leśny J., Panfil M., Nyckowiak J. (Eds.), *Badania i Rozwój Młodych Naukowców w Polsce. Nauki Techniczne i Inżynieryjne. Część V, Młodzi Naukowcy*, Poznań 2016, 65–71.
- [13] Hędrzak E., Michorczyk P., *Trójwymiarowe drukowanie: przegląd metod*, [in:] Leśny J., Panfil M., Nyckowiak J. (Eds.), *Badania i Rozwój Młodych Naukowców w Polsce. Nauki Techniczne i Inżynieryjne. Część V, Młodzi Naukowcy*, Poznań 2016, 72–78.
- [14] Godini H.R., Gili A., Görke O., Arndt S., Simon U., Thomas A., Schomäcker R., Wozny G., *Sol-gel method for synthesis of Mn-Na₂WO₄/SiO₂ catalyst for methane oxidative coupling*, *Catalysis Today*, vol. 236, 2014, 12–22.
- [15] Pak S., Qiu P., Lunsford J.H., *Elementary reactions in the oxidative coupling of methane over Mn/Na₂WO₄/SiO₂ and Mn/Na₂WO₄/MgO catalysts*, *Journal of Catalysis*, vol. 179, 1998, 222–230.
- [16] Liu H., Wang X., Yang D., Gao R., Wang Z., Yang J., *Scale up and stability test for oxidative coupling of methane over Na₂WO₄-Mn/SiO₂ catalyst in a 200 ml fixed-bed reactor*, *Journal of Natural Gas Chemistry*, vol. 17, 2008, 59–63.
- [17] Shahri S.M.K., Pour A.N., *Ce-promoted Mn/Na₂WO₄/SiO₂ catalyst for oxidative coupling of methane at atmospheric pressure*, *Journal of Natural Gas Chemistry*, vol. 19, 2010, 47–53.
- [18] Wang J., Chou L., Zhang B., Song H., Zhao J., Yang J., Li S., *Comparative study on oxidation of methane to ethane and ethylene over Na₂WO₄-Mn/SiO₂ catalysts prepared by different methods*, *Journal of Molecular Catalysis A: Chemical*, vol. 245, 2006, 272–277.
- [19] Tiemersma T.P., Tuinier M.J., Gallucci F., Kuipers J.A.M., van Sint Annaland M., *A kinetics study for the oxidative coupling of methane on a Mn/Na₂WO₄/SiO₂ catalyst*, *Applied Catalysis A: General*, vol. 433–434, 2012, 96–108.
- [20] Koirala R., Büchel R., Pratsinis S.E., Baiker A., *Oxidative coupling of methane on flame-made Mn-Na₂WO₄/SiO₂: Influence of catalyst composition and reaction conditions*, *Applied Catalysis A: General*, vol. 484, 2014, 97–107.
- [21] Daneshpayeh M., Khodadadi A., Mostoufi N., Mortazavi Y., Sotudeh-Gharebagh R., Talebizadeh A., *Kinetic modeling of oxidative coupling of methane over Mn/Na₂WO₄/SiO₂ catalyst*, *Fuel Processing Technology*, vol. 90, 2009, 403–410.
- [22] Shahri S.M.K., Alavi S.M., *Kinetic studies of the oxidative coupling of methane over the Mn/Na₂WO₄/SiO₂ catalyst*, *Journal of Natural Gas Chemistry*, vol. 18, 2009, 25–34.

Adam Kozak

Cracow College of Health Promotion

Aleksander Kozak (akozak@pk.edu.pl)

Institute of Building Materials and Structures, Faculty of Civil Engineering, Cracow University of Technology

Beata Fryźlewicz-Kozak

Chair of Chemical and Process Engineering, Faculty of Chemical Engineering and Technology, Cracow University of Technology

AN UNIFIED FORMULA FOR DERIVING THE MOLECULAR COMPOSITION OF HYDROCARBONS

NOWY SPOSÓB WYZNACZANIA WZORÓW CZĄSTECZKOWYCH DLA WSZYSTKICH WĘGLOWODORÓW

Abstract

An unified method of designing molecular formulae for all types hydrocarbons is proposed in this paper. The developed formula provides the molecular composition of hydrocarbons regardless of the number of chemical bonds and bond types or the number of rings they contain. Moreover, a small modification to that formula makes it suitable for deriving the molecular composition of hydrocarbons with oxygen atoms bound to carbon atoms with single and double bonds.

Keywords: molecular formulas of hydrocarbons, hydrocarbons

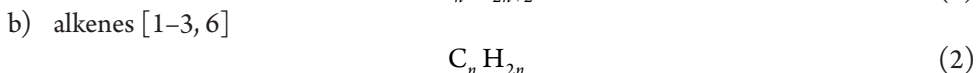
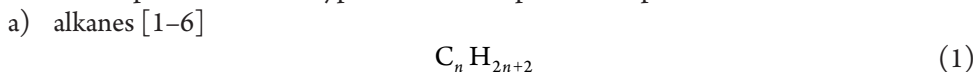
Streszczenie

W artykule przedstawiono ujednolicony sposób ustalania wzorów sumarycznych dla wszystkich węglowodorów. Zaproponowano stosowanie jednego ogólnego wzoru słusznego dla wszystkich węglowodorów w miejsce oddzielnie stosowanych obecnie wzorów właściwych tylko dla jednej grupy związków. Opracowany wzór pozwala podać wzory cząsteczkowe bez względu na ilość i typ wiązań chemicznych, jak również ilość pierścieni. Ponadto niewielka modyfikacja tego wzoru pozwala podać wzory cząsteczkowe węglowodorów zawierających zarówno wiązania pojedyncze, jak i podwójne pomiędzy atomami węgla i tlenu.

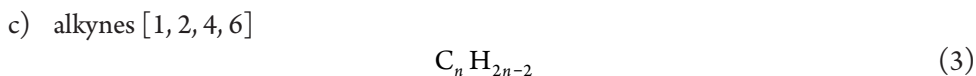
Słowa kluczowe: wzory cząsteczkowe węglowodorów, węglowodory

1. Introduction

Commonly, organic chemistry textbooks present a set of three formulae for deriving the molecular compositions of one type of bond in a specific compound:



and



The above formulae are characterized by significant limitations. In the case of non-saturated bonds, the formulae are correct only if there is one bond of a given type in a chain. If any non-saturated hydrocarbon contains more than one bond of a given kind or mixed bonds, then formulas (2) and (3) do not allow determining molecular formula. No mathematical relationships have been found in the latest literature that enable to calculate molecular formulas for such hydrocarbons containing multiple bonds as well as mixed ones.

For cyclic and aromatic hydrocarbons, no formulae are known which take into account the number of rings and bonds as well as the diversity of these bonds and side chains. Both types of hydrocarbons require separate formulae for determining their molecular composition. In the case of saturated cyclic hydrocarbons formula (4) is used and in the case of monocyclic aromatic hydrocarbons formula (5) is used, respectively [3, 5–7]:



2. Results and discussion

One general formula (6) which determines the molecular composition of different types and numbers of chemical bonds is now presented.



where:

- C, H – carbon and hydrogen atoms, respectively;
- n – the number of carbon atoms;
- D – the number of double bonds;
- T – the number of triple bonds;
- R – the number of rings.

This formula is also valid for alkyloaromatic hydrocarbons.

Since alkanes contain no multiple carbon – carbon bonds, hence D , T and $R = 0$, then formula (6) is reduced to well-known shape given below:

$$C_n H_{2(n+1-0-2x0-0)} = C_n H_{2n+2}$$

In alkenes with one double bond, $D = 1$, $T = 0$ and $R = 0$; therefore, formula (6) transforms as follows:

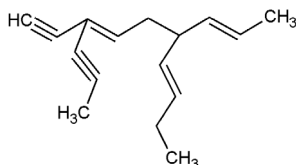
$$C_n H_{2(n+1-1-2x0-0)} = C_n H_{2n}$$

For alkynes bearing one triple bond ($D = 0$, $T = 1$ and $R = 0$) formula (6) takes the common form:

$$C_n H_{2(n+1-0-2x1-0)} = C_n H_{2n-2}$$

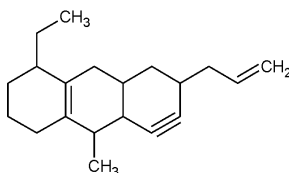
Some examples of calculations based on the proposed formula (6) are presented below.

For a structure containing sixteen carbon atoms, three double bonds and two triple ones ($D = 3$, $T = 2$, $R = 0$), the molecular formula of the below compound calculated according to the authors' formula (6) is as follows:



$$C_{16} H_{2(16+1-3-2x2-0)} = C_{16} H_{20}$$

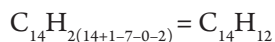
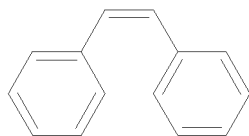
Another example shows that the proposed formula is also true for a hypothetical, complex and non-saturated cyclic hydrocarbon containing twenty carbon atoms, three rings, two double bonds, one triple bond as well as side chains. The structure of the compound is presented below:



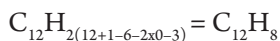
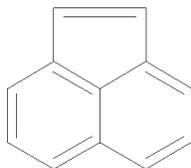
Using the formula (6), the molecular composition of the compound is derived below:

$$C_{20} H_{2(20+1-2-2x1-3)} = C_{20} H_{28}$$

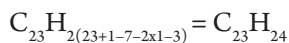
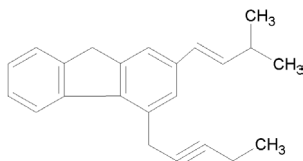
In order to show an application of the proposed formula for aromatic hydrocarbons, calculations to present the molecular formula of stilbene are provided. The compound contains fourteen carbon atoms, two rings and seven double bonds. A method of calculating the molecular formula of the compound according to formula (6) is presented below:



Formula (6) is also correct for compounds of a structure such as acenaphthylene with twelve carbon atoms and three rings:



Another calculation according to formula (6) has been done for a more complex, hypothetical hydrocarbon, which contains 23 carbon atoms and 24 hydrogen atoms:



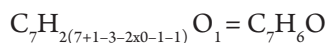
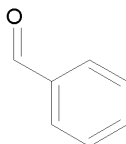
A small modification to formula (6) also enables it to provide molecular formulas of hydrocarbons containing oxygen in a side chain connected with carbon by means of double bonding. If we use the formula:



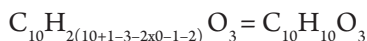
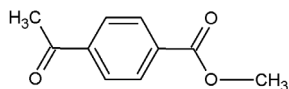
where:

X – the number of double bonds between carbon and oxygen,

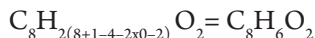
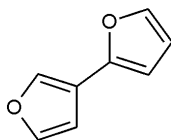
Y – the total number of oxygen atoms, we can calculate the molecular formula of benzaldehyde:



Formula (7) is also correct if a hydrocarbon contains both single and double bonds between carbon and oxygen atoms. For example:



If there are endocyclic oxygen atoms in the molecule, Eq. (7) is still applicable because the oxygen atoms are bound with single bonds as below:



3. Conclusions

A new, unified formula has been presented which allows the designing of molecular formulas of aliphatic and aromatic hydrocarbons. Thus far, separate relationships have been used for each homologous series and the equations have had a lot of limitations. Moreover, the formulae are not correct if the molecule contains more than one bond of a given hydrocarbon type or when there are simultaneously mixed, single, double and triple bonds. The proposed formula fits all types of hydrocarbons regardless of their structure, i.e. it takes into account the number of bonds, their diversity and in the case of cyclic and aromatic hydrocarbons, the number of rings. The formula is easy to memorise and based on it, one can readily establish the molecular formula of any hydrocarbons. Moreover, a small modification extends the approach to the molecular formulae of hydrocarbons with exocyclic oxygen atoms.

References

- [1] Chang R., *General Chemistry*, 1st Edition, 1986.
- [2] Hart H., Craine L., Hart D.J., Madad Ch.M., *Organic chemistry. A short course*, 12-th edition, Copyright 2007 by Houghton Mifflin Company, 2006.
- [3] Mc Murry J., *Organic chemistry*, 5th edition, 1999.
- [4] Morrison R.T., Boyd R.N., *Organic chemistry*, 1998.
- [5] Patrick G., *Instant notes in organic chemistry*, Bios Scientific Publishers Limited, 2000.
- [6] Russell J.B., *General Chemistry*, 2nd Edition, 1992.
- [7] http://www.sakshieducation.com/EAMCET/QR/Chemistry/Jr%20Chem/13.OC%20Aromatic%20hydrocarbons%20_Benzene_.pdf (date of access: 2016-03-22).

Arkadiusz Matwiczuk (arkadiusz.matwiczuk@up.lublin.pl)

Alicja Matwiczuk

Department of Biophysics, University of Life Sciences in Lublin

Dariusz Karcz, Sławomir Wybraniec

Department of Analytical Chemistry, Faculty of Chemical Engineering and Technology,
Cracow University of Technology

Dariusz Kluczyk, Mariusz Gagoś

Department of Cell Biology, Institute of Biology, Maria Curie-Skłodowska University

Andrzej Niewiadomy

Department of Chemistry, University of Life Sciences in Lublin

SPECTROSCOPIC STUDIES OF DUAL FLUORESCENCE EFFECTS IN
A SELECTED 1,3,4-THIADIAZOLE DERIVATIVE IN ORGANIC SOLVENTS
AND AQUEOUS SOLUTIONS

BADANIA SPEKTROSKOPOWE EFEKTÓW PODWÓJNEJ
FLUORESCENCJI W WYBRANYM ZWIĄZKU Z GRUPY 1,3,4-TIADIAZOLI
W ROZPUSZCZALNIKACH ORGANICZNYCH ORAZ ROZTWORACH WODNYCH

Abstract

Spectroscopic studies of the fluorescence emission of selected 1,3,4-thiadiazoles in organic solvents and an aqueous solution were carried out. An interesting effect of pH-induced dual fluorescence was observed in the aqueous solution. The use of organic solvents resulted either in a single fluorescence maximum, double fluorescence (two well-resolved emission bands), or the dual fluorescence effect. The results obtained suggest that the fluorescence emission effects in 1,3,4-thiadiazoles are associated with both the conformational isomerism and the chromophore aggregation phenomena.

Keywords: double fluorescence, dual fluorescence effect, molecular spectroscopy, chromophore aggregation, 1,3,4-thiadiazole, charge transfer (CT)

Streszczenie

W niniejszym artykule przedstawiono wyniki badań emisji fluorescencji wybranych związków z grupy 1,3,4-tiadiazoli w rozpuszczalnikach organicznych oraz roztworach wodnych. W środowisku wodnym dla badanych związków zaobserwowano interesujący efekt podwójnej fluorescencji indukowany między innymi zmianami pH. W rozpuszczalnikach innych niż woda obserwowano efekt albo pojedynczej fluorescencji lub dwóch rozdzielonych pasm emisji fluorescencji oraz efektu podwójnej fluorescencji. Na podstawie prezentowanych wyników badań zaproponowano, że na obserwowane efekty fluorescencyjne wpływ mogą mieć zarówno zmiany konformacyjne jak również procesy związane z agregacją chromoforową.

Słowa kluczowe: efekt podwójnej fluorescencji, spektroskopia molekularna, agregacja chromoforowa, 1,3,4-tiadiazole, transfer ładunku (CT)

1. Introduction

The development of successful therapeutic agents against cancer and neurodegenerative disorders such as Alzheimer's or Parkinson's diseases is one of the most challenging tasks in contemporary medicinal science. Furthermore, the increased resistance of microbes to conventional antibiotics has become a major obstacle in the successful treatment of various infections. Therefore, there is a constant need for the development of new biologically active substances with potency against cancers, neurodegenerative disorders, and various microbes.

In this context, thiadiazole derivatives are of particular interest. These heterocyclic compounds were first obtained in 1882 by Fisher, but their detailed structural characterisation was not made until 1890 [1]. Although various isomers are known, 1,3,4-thiadiazoles are the most extensively studied. According to the numerous reports, a broad array of biological activity exhibited by 1,3,4-thiadiazoles results from the presence of thioimine moiety, which constitutes the 5-membered core ring [2, 3]. Due to this unique structural feature, 1,3,4-thiadiazoles can act as potential antiproliferative, antifungal, antibacterial, anti-inflammatory, or antiviral agents, just to name a few [4–13].

The biological activity of 1,3,4-thiadiazoles is often accompanied by unusual physicochemical properties which makes them an interesting subject for in-depth spectroscopic studies. With this in mind, a series 1,3,4-thiadiazoles substituted with resorcinyly moiety is particularly worth emphasizing. For instance, these compounds exhibit various solvent polarizability-induced effects such as the keto-enol tautomerism [40, 43], polymorphism, and the solvatomorphism of crystals [14–17]. Furthermore, through interaction with lipids, they influence the molecular organisation and other structural properties of biomembranes [18]. Various excited state-related effects, including the nature of the fluorescence emission properties of 1,3,4-thiadiazoles, were extensively studied, pointing at the differences between the dual fluorescence and double fluorescence phenomena [19, 41–42]. The most recent reports refer to 1,3,4-thiadiazoles as ligands in the synthesis of transition metal complexes with an implication for the antineurodegenerative activity [20, 21].

The dual fluorescence effect relies on the appearance of two (or more) bands of fluorescence emission as a result of an excitation with a specific wavelength [22, 23]. In 1,3,4-thiadiazoles, such effects may be induced either by pH, solvent polarity, temperature or pressure. The difference between the dual fluorescence effect and the effect of two distinctly separated fluorescence emission bands should also be emphasised. In the former, two distinct joined bands can be observed after electron excitation, whereas the latter is characterised by two clearly separate fluorescence emission bands resulting from two separate excitations. *N,N*-dimethylaminobenzonitrile (DMABN) is a frequently given example of a molecule exhibiting this effect [24]. The dual fluorescence effect is commonly explained as being a result of intramolecular charge transfer (CT) accompanied with twisting deformation of the molecule, referred to as 'twisted intramolecular charge transfer' (TICT) [25–28]. The TICT model was introduced in the nineteen-seventies the 20th century by K. Rotkiewicz, K.H. Grellmann and Z.R. Grabowski and remains one of the most popular theoretical models used in a large number of molecular spectroscopy studies. It has been reported that a significant change in the dipole

moment of the excited molecule compared to that in the ground state is required for TICT to take place [29, 30]. Molecules exhibiting effects associated with TICT states are also highly sensitive to solvent effects. Moreover, the initial and final orbitals have to be spatially separated from each other so that its dipole moment can undergo changes resulting from electron transition (and absence of molecule symmetry). Importantly, the acceptor and donor fragments of the electron have to be located in close proximity to molecules exhibiting CT (or TICT). An excited-state intramolecular proton transfer (ESIPT) is another process that allows the explanation of dual fluorescence effects [31–33]. This model requires a close proximity between the potential proton acceptor and the proton donor group [34]. Furthermore, molecules in which (intra- or intermolecular) ESIPT is observed have similar fragments with the -OH group bound *via* a hydrogen linkage with an electron-negative atom, e.g. N. This molecule conformation facilitates proton transfer along the hydrogen bond and thus processes associated with ESIPT. Additionally, molecular aggregation, which results in the formation of excimers may contribute to the dual fluorescence effect.

The main aim of this work is the spectroscopic investigation of mechanisms of inter- and intramolecular interactions in chosen 1,3,4-thiadiazole derivatives in organic solvents as well as in aqueous solutions with varied pH values. A well known 2-(4-fluorophenylamino)-5-(2,4-dihydroxyphenyl)-1,3,4-thiadiazole (FABT) served as the model compound in these studies. Although this compound was previously studied [4], its more detailed spectroscopic characterisation is given herein. Moreover, an in-depth examination of the nature of interactions in this group of compounds may reflect on the design of a further series of derivatives with higher biological activity and their potential practical applications.

2. Materials and methods

2.1. Materials

The 2-(4-fluorophenylamino)-5-(2,4-dihydroxybenzeno)-1,3,4-thiadiazole (FABT) (see Scheme 1) was synthesized in the Department of Chemistry of the University of Life Sciences in Lublin using the previously reported protocol [2]. The structure of FABT is present in the Cambridge Crystallographic Data Centre with entries: CCDC 768785–768787.

All solvents were purchased from Sigma-Aldrich and were of highest purity available. The following solvent systems were used: 1 – 1-butanol (Bu-OH); 2 – methanol (Me-OH); 3 – Acetonitrile (ACN); 4 – ethanol (Et-OH); 5 – acetone; 6 – dimethyl sulfoxide (DMSO); 7 – propane-2-ol (Pr-OH).

2.2. Methods

The pH values of all aqueous solutions were measured with an Elmetron CP-502 pH meter at room temperature. For propan-2-ol solutions, FABT was first dissolved in selected solvents and then the pH was changed by the slow addition of 0.1M HCl to the glass flask. For

water-FABT and other compound solutions, 0.1M NaOH was first added to water to obtain pH 12. Afterwards, the powdered FABT or another compound was dissolved in water. To obtain a certain pH in the water-FABT solution, 0.1M HCl acid was slowly added. The pH was continuously controlled.

The electronic absorption spectra of FABT were recorded on a double-beam UV-Vis spectrophotometer Cary 300 Bio (Varian) equipped with a thermostat-equipped cuvette holder with a 6 × 6 multi-cell Peltier block. Temperature was controlled using a thermocouple probe (Cary Series II from Varian) placed directly inside the solutions of the samples. All UV-Vis absorption spectra were recorded at a temperature of 23°C.

Fluorescence excitation and emission spectra were recorded on a Cary Eclipse spectrofluorometer (Varian). Fluorescence spectra were recorded with a resolution of 0.5 nm and corrected for the lamp and photomultiplier spectral characteristics. The excitation and emission slits were set to 2 nm. Resonance light scattering (RLS) measurements were performed as in Pasternack and Collings [35, 36]. The excitation and emission monochromators of the spectrofluorimeter were synchronously scanned (0.0 nm interval between excitation and emission wavelengths); the slits were set to obtain a spectral resolution of 1.5 nm. All emission spectra, namely the fluorescence emission, fluorescence excitation and resonance light scattering excitation (RLS) were recorded at a temperature of $T = 23^{\circ}\text{C}$. The spectral analysis was performed with the use of Grams/AI 8.0 software (Thermo Electron Corporation).

3. Result and Discussion

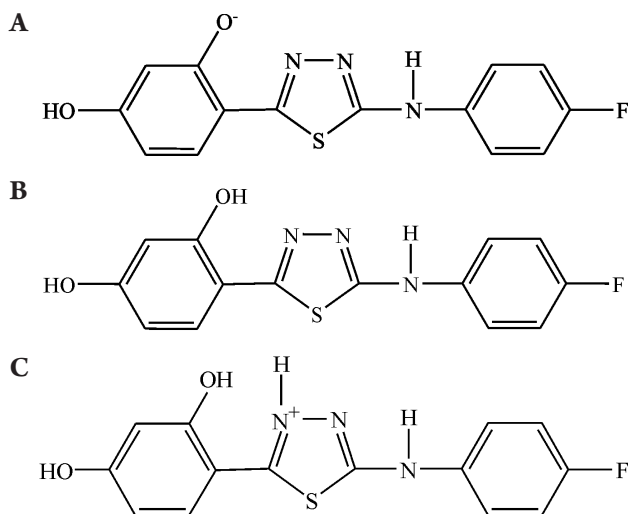


Fig. 1. Structures of FABT: A) – anionic form with deprotonated –OH group at the *ortho* position regarding the thiadiazole ring; B) – enolic form; C) – cationic form obtained by protonation of one of the thiadiazole nitrogen atoms

Fig. 1 illustrates the various forms of the FABT molecule which may occur depending on environment/solvent used. The structure 1A with deprotonated -OH group at the *ortho* position with respect to the thiadiazole ring is characteristic of basic pH (high pH values). The enolic form of FABT (Fig. 1B) is the most common form of this compound occurring within the pH range similar to that of physiological. Finally, Fig. 1C represents the cationic form of FABT, which according to crystallographic studies consists of the protonated thiadiazole ring, with the protonation occurring at the nitrogen atom (N3), which resides in close proximity to the resorcinylyl -OH group [17]. Although the rotation of resorcinylyl moiety is possible and may result in a conformation in which the -OH group resides near the thiadiazole sulphur atom, the crystallographic data suggests that the form 1C is more favourable [17, 19] and occurs in acidic solutions (low pH values). All forms of FABT presented in Scheme 1 are planar and do not occur in other conformations.

The UV-Vis spectroscopic studies carried out in the pH range of 1 to 12 reveal that the most notable shifts in the positioning of the absorption maxima occur in the pH range similar to that of physiological pH [19]. Also, a comparison of the absorption spectrum of FABT recorded at pH = 7, with those recorded at both acidic and basic conditions shows a respective hypsochromic and bathochromic shifts of the absorption maxima. Moreover, it has been reported that these changes are associated with the deprotonation of resorcinylyl *ortho* -OH (low pH) and protonation of the thiadiazole nitrogen (high pH) (Fig. 1A and 1C) [19]. These results are consistent with UV-Vis spectroscopic data obtained in this work.

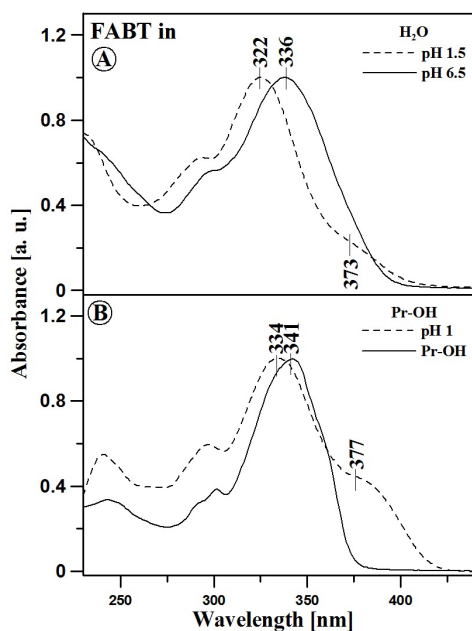


Fig. 2. UV-Vis absorption spectra of FABT: A) Spectra recorded in aqueous solutions at pH = 1.5 and 6.5; B) Spectra recorded in Pr-OH and acidified Pr-OH (so-called apparent pH = 1). The spectra are normalised to an a. u. value of 1 at their absorption maxima

The representative UV-Vis absorption spectra of FABT recorded in various conditions (pH and solvents) are given in Fig. 2. In aqueous solution at the pH of 6.5, FABT absorbs at 336 nm (29762 cm⁻¹), while at the pH of 1.5, its absorption maximum shifts to 322 nm (30960 cm⁻¹) and a new low intensity broad band appears at ~370 nm (26810 cm⁻¹). A similar trend is observed in Pr-OH solution, where the addition of 0.1M HCl (apparent pH= 1.5) results in shift of the main absorption maxima from 341 nm (29326 cm⁻¹) to 334 nm (29940 cm⁻¹), and appearance of a new absorption band at 377 nm (26525 cm⁻¹). The new, low energy absorption bands result most likely from aggregated FABT molecules [37]. Resonance light scattering (RLS) studies are in agreement with the UV-Vis absorption results, and confirm that the aggregation of FABT chromophores takes place (Fig. 6).

The formula (1) allows for the calculation of the distance between the neighbouring FABT chromophores based on the excitonic splitting theory and the UV-Vis studies [38].

$$R_{\beta} = 1.71 \sqrt[3]{\frac{\mu^2 \kappa}{n^2 \beta}} \quad (1)$$

Where μ represents the dipole moment of molecule transition (in the case of the analysed 1,3,4-thiadiazoles, its value is around 5D). The κ parameter is related to the orientation of molecules within the aggregate. The values of $\kappa = 1$ and $\kappa = -2$ correspond to 'card pack' and 'head-to-tail' orientations, respectively. N – is the refractive index, and β is the dipole-dipole interaction energy (in the classical approach). Formula (1) considers the aggregated structure formed as an effect of interactions between identical molecules. It assumes a model system, in which the transition dipole moments of neighbouring molecules are parallel. The transition dipole moment values calculated for the FABT monomer in selected solvents are given in Table 1. The calculated distance between FABT dimers in an aqueous solution equals 3.71 Å [19], in Pr-OH, it is 3.79 Å. The exciton splitting theory-based calculations are consistent with the crystallographic data. In particular, the distance between neighbouring molecules in crystals obtained from the aqueous solution equals 3.32 Å, while in crystal formed in Pr-OH, it is 3.39 Å [17].

The solutions of FABT were also examined by fluorescence emission spectroscopy and the representative set of spectra is given in Fig. 3, which illustrates the pH dependence of the fluorescence emission. It is noteworthy that the spectra recorded using an identical excitation wavelength (330 nm) differ significantly depending on the pH. At basic pH (10.5) only a single emission maximum is present at ~430 nm, while at acidic pH (starting from 6.5), this maximum shifts by approximately 15 nm to a higher energy region and an additional emission maximum of ~500 nm appears. These results are consistent with previously reported data [19] and correspond to the formation of FABT aggregates.

The comparison of emission spectra of FABT recorded in pure Pr-OH (panel A) with those in acidified Pr-OH solutions is given in Fig. 4. Regardless of the excitation wavelength used, only a single fluorescence maximum is present in spectra recorded in pure Pr-OH (Panel A). More notable changes are observed in acidified Pr-OH solutions (Panel B)

where the excitation wavelength-dependence of the emission maxima is clearly visible. The excitation wavelength of either 334 nm or 344 nm effects in only a single emission maximum. This is a characteristic feature of the FABT monomer and is only slightly broader than those recorded in pure Pr-OH. The excitation with use of the wavelength characteristic of the FABT aggregates (e.g. 377 nm) gives rise to an additional emission maximum at approximately 490 nm. It is worth emphasizing that this is not an effect of dual fluorescence regardless of the fact that two well resolved (only partly overlapping) emission bands are present. It is expected that the wavelength of 377 nm excites both the monomeric and aggregated form of FABT; therefore, two different absorption maxima are observed.

Excitation at 296 nm results in a similar pattern of two emission maxima; however, at short wavelengths, only the monomeric form absorbs; thus, the hypothesis that the observed emission maxima originate solely from the FABT monomer. This effect is called dual fluorescence. On the other hand, in both low pH aqueous solution and acidified Pr-OH, the emission maxima observed are of low intensity, which usually is attributed to aggregation. This in turn may suggest that the aggregation-related dual emission cannot be excluded.

In order to address that issue, a set of fluorescence excitation spectra was recorded (Fig. 5) at conditions similar to those, at which the fluorescence emission spectra were recorded. The excitation with 401 nm, and 410 nm (neutral and acidified Pr-OH solution, respectively) gave the spectra characteristic of the monomeric FABT and similar to those of the Uv-Vis absorption. The excitation at 484nm results in the appearance of a new band, with a maximum at 378 nm, with the characteristic broadening at the lower energy site, similar to that of the UV-Vis absorption spectra. Similar effects are observed in spectra recorded in water (not shown). In the case of the fluorescence excitation spectra recorded with use of long excitation wavelengths, additional bands (e.g. 357 nm) are present (see Fig. 5). This may serve as additional evidence for the formation of not only dimers but also more complex aggregates. Such structures may differ in size (see RLS results) and, depending on the excitation wavelength, can also give rise to variable fluorescence emission spectra.

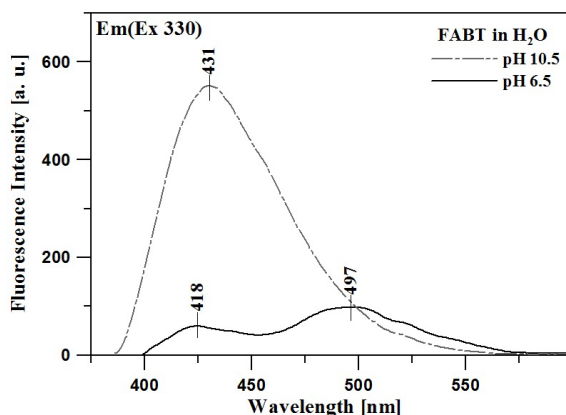


Fig. 3. Fluorescence emission spectra (Em) of FABT recorded in an aqueous solution at pH = 6.5 (black line) and 10.5 (dotted line) at an excitation wavelength of 330 nm

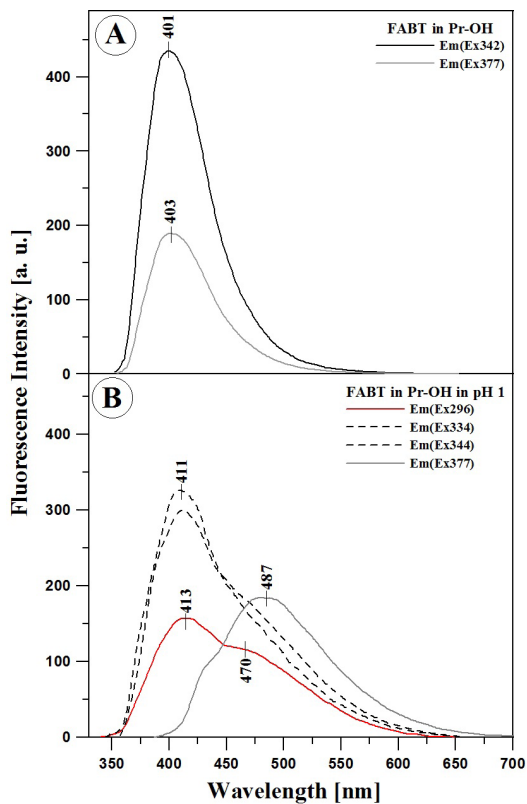


Fig. 4. Selected fluorescence emission spectra of FABT recorded in Pr-OH (Panel A) and in acidified Pr-OH (apparent pH = 1) (Panel B). Em(Ex), refers to the emission recorded for the respective excitation wavelength

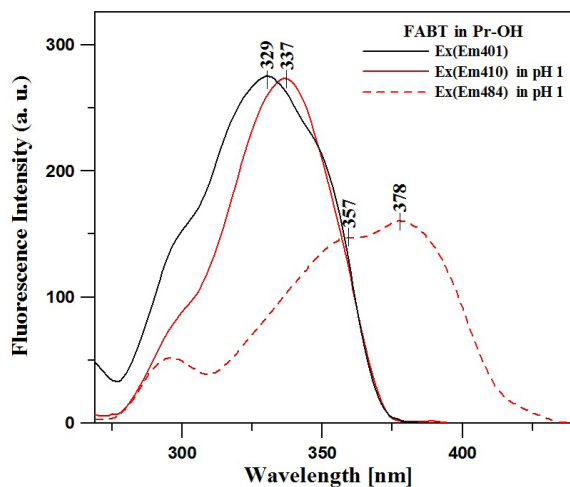


Fig. 5. Selected fluorescence excitation spectra (Ex) of FABT recorded in Pr-OH (black) and in acidified solution of Pr-OH (apparent pH = 1) (red, and red dotted). Em401, Em410, and Em484 refer to the respective excitation wavelengths

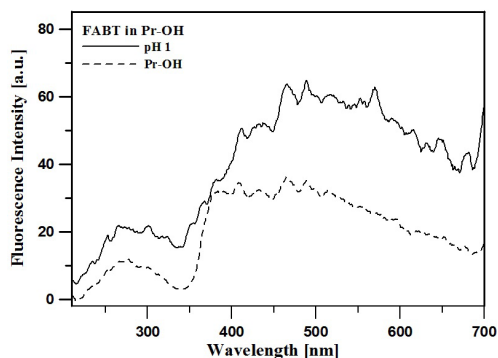


Fig. 6. RLS spectra of FABT recorded In Pr-OH (dotted line) and in an aqueous solution at pH 1 (black line)

The aggregation of FABT molecules is also supported by the resonance light scattering spectroscopy results (Fig. 6). The RLS spectra obtained are characteristic of highly intensive bands, which according to Parkash and Pasternack [35, 36], are associated with the presence of aggregates and are consistent with the results of Uv-Vis, fluorescence emission, and excitation spectroscopy. It is also worth emphasizing that the large number of RLS bands is most likely as a result of the formation of a large number of various aggregated structures. The highest intensity of RLS signals are observed in the spectra recorded at the pH range of 1–7, this is characteristic of the dual fluorescence of FABT. At the pH above 7 the intensity of RLS bands decreases significantly, and the disappearance of the long wavelength emission band in the fluorescence spectra is observed (the dual fluorescence emission phenomenon disappears).

The spectroscopic experiments carried out at various temperatures revealed a similar trend, specifically, that the highest intensity RLS signals were observed at low temperatures, while the temperature increase resulted in lowering the intensity of the RLS bands, as well as the disappearance of the dual fluorescence emission [19]. This in turn suggests a direct link between the aggregation and dual fluorescence emission, but it does not exclude other factors which may contribute to the spectroscopic effects observed in FABT.

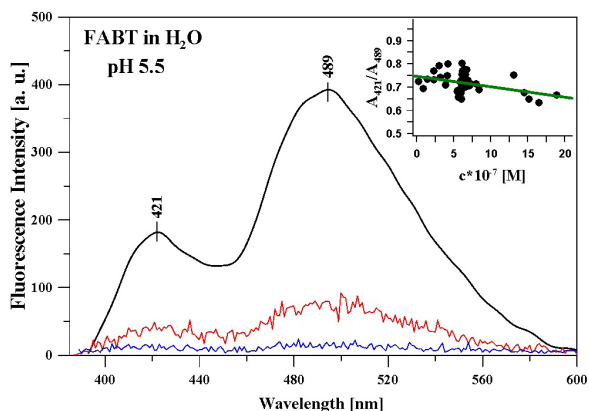


Fig. 7. Fluorescence emission spectra of FABT in aqueous solutions at pH = 5.5 recorded for three different concentrations. Insert: Ratio of the fluorescence maxima as a function of the FABT concentration

Another set of experiments carried out in this work was the examination of the concentration-dependence of dual fluorescence emission in FABT (Fig. 7). The spectra were recorded using the aqueous solution of FABT at pH = 5.5, which in these conditions, exists as a stable dual fluorescence emitting form. All spectra in this experiment set were recorded using the identical excitation wavelength (328 nm). The dual fluorescence effect was observed even at concentrations below 10^{-7} M and the intensities of emission bands were proportional to the FABT concentrations tested. The Figure 7 inset depicts the ratio of the fluorescence maxima as a function of the FABT concentration. It is clearly visible that the dual fluorescence emission effect depends on the concentration of the compound and is observed even at very low concentrations, which is consistent with previously reported data [20]. It is also clear that in aqueous solutions, the concentration increase effects in a variable ratio of fluorescence bands intensity. In particular, the higher the concentration, the more intensive the emission band at the lower energy side of the spectrum. This effect is clearly associated with the aggregation of the FABT chromophore, which occurs in an aqueous solution at increased levels of concentration [19].

It is not only the aggregation of the molecules that are known to contribute to the dual fluorescence effect but also conformational changes [19]. Usually, this effect is observed in conformation, where the resorcynyl -OH group resides in close proximity to one of the nitrogen atoms of the thiadiazole ring. The single fluorescence band or two resolved fluorescence maxima (but not originating from dual fluorescence effect) are characteristic of the opposite conformation, at which the resorcynyl -OH resides near the thiadiazole sulphur atom [19]. Secondly, the crystallographic studies on FABT report that the protonation site of thiadiazole ring which occurs at low pH also contributes to the fluorescence pattern [17, 39].

Comparison with other compounds which demonstrate dual fluorescence leads to the conclusion that this phenomenon in FABT is not related to TICT, PICT or ESPIT and cannot be fully explained based on these theories [25–34]. The results obtained suggest that the dual fluorescence effect in FABT and similar thiadiazole derivatives is more likely resultant of both chromophore aggregation and molecular conformation. The aggregation may induce changes in electron density, which may trigger a specific intramolecular charge transfer. This, in turn effects in the dual fluorescence emission. This explanation is further supported by calculations carried out based on the spectroscopic data, such as the dependence of the dipole moment (calculated from an integration of the absorption spectrum) on the Debay polarity (function dependent on the environment/solvent dielectrical constant) (Fig. 8).

The obtained results show that an increase in the Debay function is accompanied with a notable change in the dipole moment value of the examined molecules. According to the literature, such an effect is usually associated with inter- or intramolecular charge transfer, and supports the postulated intramolecular charge transfer origin of dual fluorescence emission in FABT.

The data from an integration of the absorption spectrum served as data for the calculation of the dielectric constant ϵ and the series of solvent polarity-related parameters (Tab. 1) – these results, together with charge transfer effects in FABT and other similar thiadiazole derivatives will be a subject of future studies.

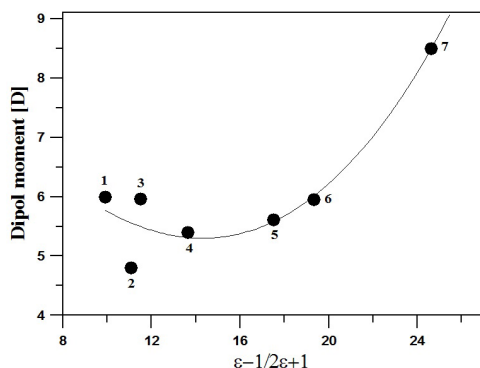


Fig. 8. Dependence of the dipole moment (calculated from an integration of the absorption spectrum) on the Debye polarity function (function dependent on environment/solvent dielectrical constant). A 2nd degree curve was fitted to data points 1–6 (details of assignment of the solvents to the respective numbers are provided in the Material and Methods section)

Table 1. Dielectric constant, dipole transition moment, and Debye polarity function values calculated for the selected solvents

FABT in	ϵ	$\epsilon - 1/2\epsilon + 1$	μ (D)
Pr-OH	20.18	11.09	4.81
DMSO	47.24	24.62	8.52
Me-OH	33.00	17.51	5.63
Et-OH	25.30	13.65	5.45
ACN	36.64	19.32	5.95
Acetone	21.00	11.51	5.96
Bu-OH	17.84	9.92	5.99

4. Conclusions

In conclusion, a series of spectroscopic experiments on 1,3,4-thiadiazole derivative FABT was carried out. Spectroscopic techniques such as UV-Vis absorption, steady state fluorescence, fluorescence excitation, and resonance light scattering revealed the highly complex nature of the dual fluorescence effect which is characteristic of this group of compounds. The results obtained confirmed that the dual fluorescence of FABT may occur in aqueous solutions at various pH levels – this is consistent with previously reported data. Additionally, a similar dual fluorescence effect is observed in organic solvents, both neutral and acidified with HCl. It is clear that both pH-dependent and solvent-dependent conformational changes in FABT notably influence its spectroscopic properties as well as the aggregation behaviour. In particular, the conformation in which the resorcynyl –OH group resides near the thiadiazole N atom is considered to be the main form responsible for the dual emission. Secondly, the

RLS and fluorescence excitation spectra together with a series of fluorescence emission measurements carried out on various concentrations suggest that the aggregation of FABT significantly contributes to the dual fluorescence effect. Moreover, the aggregation-related effects may take place both in organic and aqueous solutions.

An examination of the fluorescence excitation spectra allowed for the assignment of the fluorescence bands to the specific FABT conformations. These conformations, together with the aggregation are most likely responsible for the specific charge distribution around the FABT molecule, which in turn, introduces an intramolecular charge transfer (CT) and gives rise to the dual fluorescence effect. It is also worth emphasizing that the dual fluorescence effect can be observed upon excitation with high energy (short wavelength) at low pH values – this clearly indicates the involvement of CT processes. To sum up, it is worth stressing that the fluorescence effects observed in the analysed 1,3,4-thiadiazole compound are inherent traits of these compounds (as well as structurally similar molecules). This indicates that the several effects, which have not been analysed in other molecules in such systems, are involved in the observed fluorescence effects.

Acknowledgments

The research was supported by a grant from the University of Life Science in Lublin (TKF/MN/5 to AM).

References

- [1] Jain A.K., Sharma S., Vaidya A., Ravichandran V., Agrawal R.K., *1, 3, 4-Thiadiazole and its Derivatives: A Review on Recent Progress in Biological Activities*, Chemical Biology & Drug Design, 2013, 557–576.
- [2] Juszcak M., Matysiak J., Brzana W., Niewiadomy A., Rzeski W., *Evaluation of the antiproliferative activity of 2-(monohalogenophenylamino)-5-(2, 4-dihydroxyphenyl)-1, 3, 4-thiadiazoles*, *Arzneimittelforschung*, 2008, 353–357.
- [3] Juszcak M., Matysiak J., Szeliga M., Pożarowski P., Niewiadomy A., Albrecht J., Rzeski W., *2-Amino-1, 3, 4-thiadiazole derivative (FABT) inhibits the extracellular signal-regulated kinase pathway and induces cell cycle arrest in human non-small lung carcinoma cells*, *Bioorganic & medicinal chemistry letters*, 2012, 5466–5469.
- [4] Noolvi M.N., Patel H.M., Kamboj S., Cameotra S.S., *Synthesis and antimicrobial evaluation of novel 1, 3, 4-thiadiazole derivatives of 2-(4-formyl-2-methoxyphenoxy) acetic acid*, *Arabian Journal of Chemistry*, 2012.
- [5] Supurana C.T., *Complexes with biologically active ligands. Part 9 Metal complexes of 5-benzoylamino-and 5-(3-nitrobenzoyl-amino)-i, 3, 4-thiadiazole-2-sulfonamide as carbonic anhydrase inhibitors*, 1997.
- [6] Turan N., Topçu M.F., Ergin Z., Sandal S., Tuzcu M., Akpolat N., Yilmaz B., Sekerci M., Karatepe M., *Pro-oxidant and antiproliferative effects of the 1, 3, 4-thiadiazole-based Schiff base and its metal complexes*, *Drug and Chemical Toxicology*, 2011, 369–378.
- [7] Chabner B.A., Roberts T.G., *Chemotherapy and the war on cancer*, *Nature Reviews Cancer*, 2005, 65–72.

- [8] Rajak H., Deshmukh R., Aggarwal N., Kashaw S., Kharya M.D., Mishra P., *Synthesis of Novel 2, 5-Disubstituted 1, 3, 4-Thiadiazoles for Their Potential Anticonvulsant Activity: Pharmacophoric Model Studies*, *Archiv der Pharmazie*, 2009, 453–461.
- [9] Bhongade B.A., Talath S., Gadad R.A., Gadad A.K., *Biological activities of imidazo [2, 1-b][1, 3, 4] thiadiazole derivatives: A review*, *Journal of Saudi Chemical Society*, 2013.
- [10] Li Y., Geng J., Liu Y., Yu S., Zhao G., *Thiadiazole a Promising Structure in Medicinal Chemistry*, *ChemMedChem*, 2013, 27–41.
- [11] Matysiak J., Nasulewicz A., Pełczyńska M., Świtalska M., Jaroszewicz I., Opolski A., *Synthesis and antiproliferative activity of some 5-substituted 2-(2, 4-dihydroxyphenyl)-1, 3, 4-thiadiazoles*, *European Journal of Medicinal Chemistry*, 2006, 475–482.
- [12] Carstensen J., *Solid-state chemistry of drugs*. By Stephen R. Byrn, Academic Press, 111 Fifth Avenue, Pharmaceutical Sciences, New York 1984, 573–573.
- [13] Cressier D., Prouillac C., Hernandez P., Amourette C., Diserbo M., Lion C., Rima G., *Synthesis, antioxidant properties and radioprotective effects of new benzothiazoles and thiadiazoles*, *Bioorganic & Medicinal Chemistry*, 2009, 5275–5284.
- [14] Gagoś M., Matwijczuk A., Kamiński D., Niewiadomy A., Kowalski R., Karwasz G.P., *Spectroscopic studies of intramolecular proton transfer in 2-(4-fluorophenylamino)-5-(2, 4-dihydroxybenzeno)-1, 3, 4-thiadiazole*, *Journal of Fluorescence*, 2011, 1–10.
- [15] Matwijczuk A., Górecki A., Kamiński D., Myśliwa-Kurdziel B., Fiedor L., Niewiadomy A., Karwasz G.P., Gagoś M., *Influence of Solvent Polarizability on the Keto-Enol Equilibrium in 4-[5-(naphthalen-1-ylmethyl)-1, 3, 4-thiadiazol-2-yl] benzene-1, 3-diol*, *Journal of Fluorescence*, 2015, 1867–1874.
- [16] Hoser A.A., Kamiński D.M., Matwijczuk A., Niewiadomy A., Gagoś M., Woźniak K., *On polymorphism of 2-(4-fluorophenylamino)-5-(2, 4-dihydroxybenzeno)-1, 3, 4-thiadiazole (FABT) DMSO solvates*, *CrystEngComm*, 2013, 1978–1988.
- [17] Kamiński D.M., Hoser A.A., Gagoś M., Matwijczuk A., Arczewska M., Niewiadomy A., Woźniak K., *Solvatomorphism of 2-(4-Fluorophenylamino)-5-(2, 4-dihydroxybenzeno)-1, 3, 4-thiadiazole Chloride*, *Crystal Growth & Design*, 2010, 3480–3488.
- [18] Kamiński D.M., Matwijczuk A., Pocięcha D., Górecka E., Niewiadomy A., Dmowska M., Gagoś M., *Effect of 2-(4-fluorophenylamino)-5-(2, 4-dihydroxyphenyl)-1, 3, 4-thiadiazole on the molecular organisation and structural properties of the DPPC lipid multibilayers*, *Biochimica et Biophysica Acta (BBA)-Biomembranes*, 2012, 2850–2859.
- [19] Matwijczuk A., Kaminski D., Górecki A., Ludwiczuk A., Niewiadomy A., Mackowski S., Gagoś M., *Spectroscopic Studies of Dual Fluorescence in 2-((4-Fluorophenyl) amino)-5-(2, 4-dihydroxybenzeno)-1, 3, 4-thiadiazole*, *The Journal of Physical Chemistry A*, 2015, 10791–10805.
- [20] Karcz D., Matwijczuk A., Boroń B., Creaven B., Fiedor L., Niewiadomy A., Gagoś M., *Isolation and spectroscopic characterization of Zn(II), Cu(II), and Pd(II) complexes of 1,3,4-thiadiazole-derived ligand*, *Journal of Molecular Structure*, 2016.
- [21] Skrzypek A., Matysiak J., Niewiadomy A., Bajda M., Szymański P., *Synthesis and biological evaluation of 1,3,4-thiadiazole analogues as novel AChE and BuChE inhibitors*, *Eur J Med Chem*, 2013, 311–319.



- [22] Andersson P.O., Bachilo S.M., Chen R.-L., Gillbro T., *Solvent and temperature effects on dual fluorescence in a series of carotenes. Energy gap dependence of the internal conversion rate*, The Journal of Physical Chemistry, 99 1995, 16199–16209.
- [23] Prabhu A.A.M., Sankaranarayanan R., Venkatesh G., Rajendiran N., *Dual fluorescence of fast blue RR and fast violet B: effects of solvents and cyclodextrin complexation*, The Journal of Physical Chemistry B, 2012, 9061–9074.
- [24] Kobayashi T., Futakami M., Kajimoto O., *4-(N, N-Dimethylamino) benzonitrile solvated by a polar molecule: Structural demand for charge-transfer state formation*, Chemical Physics Letters, 1986, 63–66.
- [25] Rettig W., *Charge separation in excited states of decoupled systems—TICT compounds and implications regarding the development of new laser dyes and the primary process of vision and photosynthesis*, Angewandte Chemie International Edition in English, 1986, 971–988.
- [26] Grabowski Z.R., Rotkiewicz K., Siemiarczuk A., Cowley D., Baumann W., *Twisted intra-molecular charge-transfer states (TICT)-new class of excited-states with a full charge separation*, Nouveau Journal De Chimie-New Journal of Chemistry, 1979, 443–454.
- [27] Zachariasse K.A., *Comment on “Pseudo-Jahn–Teller and TICT-models: a photophysical comparison of meta-and para-DMABN derivatives” [Chem. Phys. Lett. 305 (1999) 8]: The PICT model for dual fluorescence of aminobenzonitriles*, 2000, 8–13.
- [28] Wei X., Yang X., Feng Y., Ning P., Yu H., Zhu M., Xi X., Guo Q., Meng X., *A TICT based two-photon fluorescent probe for cysteine and homocysteine in living cells*, Sensors and Actuators B: Chemical, 2016, 285–292.
- [29] Ravi M., Soujanya T., Samanta A., Radhakrishnan T., *Excited-state dipole moments of some Coumarin dyes from a solvatochromic method using the solvent polarity parameter, ENT*, J. Chem. Soc., Faraday Trans., 1995, 2739–2742.
- [30] Zhao G.-J., Han K.-L., *pH-Controlled twisted intramolecular charge transfer (TICT) excited state via changing the charge transfer direction*, Physical Chemistry Chemical Physics, 2010, 8914–8918.
- [31] Sytnik A., Kasha M., *Excited-state intramolecular proton transfer as a fluorescence probe for protein binding-site static polarity*, Proceedings of the National Academy of Sciences, 1994, 8627–8630.
- [32] Zhao J., Ji S., Chen Y., Guo H., Yang P., *Excited state intramolecular proton transfer (ESIPT): from principal photophysics to the development of new chromophores and applications in fluorescent molecular probes and luminescent materials*, Physical Chemistry Chemical Physics, 2012, 8803–8817.
- [33] Klymchenko A.S., Demchenko A.P., *Multiparametric probing of intermolecular interactions with fluorescent dye exhibiting excited state intramolecular proton transfer*, Physical Chemistry Chemical Physics, 2003, 461–468.
- [34] Demchenko A.P., Tang K.-C., Chou P.-T., *Excited-state proton coupled charge transfer modulated by molecular structure and media polarization*, Chemical Society Reviews, 2013, 1379–1408.
- [35] Pasternack R.F., Collings P.J., *Resonance light scattering: a new technique for studying chromophore aggregation*, Science, 1995, 935.

- [36] Parkash J., Robblee J.H., Agnew J., Gibbs E., Collings P., Pasternack R.F., de Paula J.C., *Depolarized resonance light scattering by porphyrin and chlorophyll a aggregates*, Biophysical journal, 1998, 2089–2099.
- [37] Binder H., Gutberlet T., Anikin A., Klose G., *Hydration of the dienic lipid dioctadecadienoylphosphatidylcholine in the lamellar phase—an infrared linear dichroism and x-ray study on headgroup orientation, water ordering, and bilayer dimensions*, Biophysical Journal, 1998, 1908–1923.
- [38] Kasha M., Rawls H., Ashraf El-Bayoumi M., *The exciton model in molecular spectroscopy*, Pure and Applied Chemistry, 1965, 371–392.
- [39] Kaminski D., Matwijczuk A., Hoser A.A., Niewiadomy A., Woźniak K., Gagoś M., *Characteristics of 2-methylamino-5-(2,4-dihydroxybenzene)-1,3,4-thiadiazole chloride*, in: *Science and Industry – Spectroscopic studies in practice new challenges and potentials*, UMCS – Maria Curie-Skłodowska University, Lublin 2011.
- [40] Matwijczuk A., Kluczyk D., Górecki A., Niewiadomy A., Gagoś M., *Solvent Effects on Molecular Aggregation in 4-(S-Heptyl-1,3,4-thiadiazol-2-yl)benzene-1,3-diol and 4-(S-Methyl-1,3,4-thiadiazol-2-yl)benzene-1,3-diol*, Journal of Physical Chemistry B, 2016, 7958–7969.
- [41] Kluczyk D., Matwijczuk A., Górecki A., Karpińska M.M., Szymanek M., Niewiadomy A., Gagoś M., *Molecular Organisation of Dipalmitoylphosphatidylcholine Bilayers Containing Bioactive Compounds 4-(S-heptyl-1,3,4-thiadiazol-2-yl) benzene-1,3-diol and 4-(S-methyl-1,3,4-thiadiazol-2-yl) benzene-1,3-diol*, Journal of Physical Chemistry B, 2016, 12047–12063.
- [42] Matwijczuk A., Karcz D., Walkowiak R., Matwijczuk A., Niewiadomy A., Wybraniec S., Karwasz G.P., Gagoś M., *Keto-enol tautomerism of 2-(4-fluorophenyl)-5-(2,4-dihydroxyphenyl)-1,3,4-thiadiazole. Spectroscopic studies Tautomeria keto-enolowa w 2-(4-fluorofenylo)-5-(2,4-dihydroksyfenylo)-1,3,4-tiadiazolu. Badania spektroskopowe*, Przemysł Chemiczny 1, 2016, 40–44.
- [43] Matwijczuk A.P., Karcz D., Walkowiak R. J., Furso J., Gładyszewska B., Wybraniec S., Niewiadomy A., Karwasz G.P. and Gagoś M., *Effect of Solvent Polarizability on the Keto/Enol Equilibrium of Selected Bioactive Molecules from the 1,3,4-Thiadiazole Group with a 2,4-Hydroxyphenyl Function*, 2017.

For further details, see the published papers available on www.technicaltransactions.com (click the appropriate series for previous issues).

Jakub Szyman (jszyman@chemia.pk.edu.pl)

Bolesław Tabiś

Department of Chemical and Process Engineering, Faculty of Chemical Engineering and Technology, Cracow University of Technology

THE IMPLEMENTATION OF A MATHEMATICAL MODEL OF VARIOUSLY STRUCTURED BIOREACTORS CASCADES

IMPLEMENTACJA MODELU MATEMATYCZNEGO KASKAD BIOREAKTORÓW O RÓŻNYCH STRUKTURACH

Abstract

This paper presents the results of the stationary characteristics of CSTR bioreactor cascades with a modifiable structure, obtained by the way of numerical experiments. As a technological example, the biodegradation of phenol was chosen.

Keywords: bioreactor, cascade, biodegradation, substrate inhibition

Streszczenie

W artykule przedstawiono charakterystykę stacjonarną kaskady bioreaktorów z idealnym wymieszaniem o modyfikowalnej strukturze, uzyskaną w wyniku eksperymentów numerycznych. Jako modelowy przypadek przyjęto biodegradację fenolu.

Słowa kluczowe: bioreaktor, kaskada, biodegradacja, inhibicja substratem

1. Introduction

Cascades of bioreactors are commonly applied in industry; for example, in biotechnology or wastewater treatment [1]. The model of the serial connection of bioreactors has already been obtained and well described [2]. A model of a cascade with an unlimited number of bioreactors may be attached in calculating a model of a tube plug-flow reactor [3]. A significant influence on cascade operation may also be the location of the inlet stream and the recirculation of the outlet stream. Productivity may be also increased by applying a cyclic reversed-flow [4]. For the mentioned case, chaotic solutions has been reported [5]. Work [6] proposes that if there is a cascade of two reactors which are operating under the same conditions, their composition of output streams are also the same.

The formulation and analysis of steady-state estimations are helpful in describing the operation regime. This work is inspired by the modified bioreactor cascades model, in which particular vessels can be connected in any way [7].

2. Experimental data

As a technological example, phenol biodegradation was chosen; the kinetics parameters are as follows: $m_{\max} = 0.569 \text{ h}^{-1}$; $K = 0.018539 \text{ kgm}^{-3}$; $K_i = 0.09937 \text{ kgm}^{-3}$; $w_{BA} = 0.628$ [8]. Fig. 1. presents the structure of the examined cascade with inlet and outlet streams.

The mathematical model may be defined by the mass balances of degraded substrate and biomass in each reactor. The balance of the degraded substrate is expressed by:

$$V_1 \frac{dc_{A1}}{dt} = F_{V1}c_{A0} - F_{V1}c_{A1} - V_1 \frac{1}{w_{BA}} \frac{\mu_{\max} c_{A1} c_{B1}}{K + c_{A1} + \frac{c_{A1}^2}{K_i}} \quad (1)$$

$$V_2 \frac{dc_{A2}}{dt} = F_{V2}c_{A1} - F_{V2}c_{A2} - V_2 \frac{1}{w_{BA}} \frac{\mu_{\max} c_{A2} c_{B2}}{K + c_{A2} + \frac{c_{A2}^2}{K_i}} \quad (2)$$

$$V_3 \frac{dc_{A3}}{dt} = F_{V3}c_{A1} - F_{V3}c_{A3} - V_3 \frac{1}{w_{BA}} \frac{\mu_{\max} c_{A3} c_{B3}}{K + c_{A3} + \frac{c_{A3}^2}{K_i}} \quad (3)$$

where:

- V_i – volume of i th reactor;
- c_{Ai} – concentration of substrate in i th reactor;
- t – time;
- F_{Vi} – volumetric flow rate through i th reactor;
- K – saturation constant;
- c_{Bi} – concentration of biomass in i th reactor;

- m_{\max} – maximal rate of biomass growth;
- K_i – inhibition constant;
- w_{BA} – yield of biomass production.

Similarly, biomass balance in each bioreactor may be purposed:

$$V_1 \frac{dc_{B1}}{dt} = F_{V1}c_{B0} - F_{V1}c_{B1} - V_1 \frac{\mu_{\max} c_{A1} c_{B1}}{K + c_{A1} + \frac{c_{A1}^2}{K_i}} \quad (4)$$

$$V_2 \frac{dc_{B2}}{dt} = F_{V2}c_{B1} - F_{V2}c_{B2} - V_2 \frac{\mu_{\max} c_{A2} c_{B2}}{K + c_{A2} + \frac{c_{A2}^2}{K_i}} \quad (5)$$

$$V_3 \frac{dc_{B3}}{dt} = F_{V3}c_{B1} - F_{V3}c_{B3} - V_3 \frac{\mu_{\max} c_{A3} c_{B3}}{K + c_{A3} + \frac{c_{A3}^2}{K_i}} \quad (6)$$

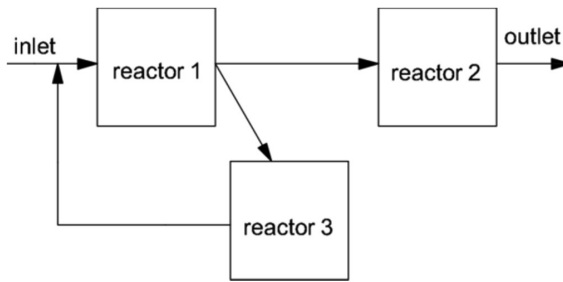


Fig. 1. Schematic drawing of investigated cascade

In the presented model, index i corresponds to the ordinal numbers of the reactors (as shown in Fig. 1). The concentration in the inlet stream is indicated by $i = 0$. In this work, it was assumed that all reactors have the same volume; thus:

$$V = V_1 = V_2 = V_3 \quad (7)$$

The total stream feeding the first reactor can be stated by the equation (8).

$$F_{V1} = F_{Vf} + F_{V3} \quad (8)$$

where:

F_{Vf} – volumetric flow rate of inlet stream.

Instead of no change to the total mass inside the cascade, it can be noted that volumetric flow rate of inlet and outlet stream are the same.

$$F_{Vf} = F_{V2} \quad (9)$$

Values c_{A0} , c_{B0} are expressed by the mass balance in the inlet of reactor 1:

$$F_{Vf}c_{Af} + F_{V3}c_{A3} = F_{V1}c_{A0} \quad (10)$$

$$F_{V3}c_{B3} = F_{V1}c_{B0} \quad (11)$$

Additionally, dimensionless variables will be introduced; degree of conversion the substrate in the i th bioreactor:

$$\alpha_{Ai} = \frac{c_{Af} - c_{Ai}}{c_{Af}} \quad (12)$$

dimensionless concentration of biomass in i th bioreactor:

$$\beta_i = \frac{c_{Bi}}{c_{Af}} \quad (13)$$

and average residence time in each bioreactor:

$$\tau_i = \frac{V}{F_{Vi}} \quad (14)$$

After substitution equations (7)–(11) to model (1)–(6), the dimensionless model of the investigated cascade is stated as:

$$\frac{d\alpha_{A1}}{dt} = \frac{\alpha_{A1}}{\tau_1} - \frac{\alpha_{A3}}{\tau_3} + \frac{1}{w_{BA}} \frac{\mu_{\max} c_{Af} (1 - \alpha_{A1}) \beta_1}{K + c_{Af} (1 - \alpha_{A1}) + \frac{c_{Af}^2 (1 - \alpha_{A1})^2}{K_i}} \quad (15)$$

$$\frac{d\alpha_{A2}}{dt} = \frac{\alpha_{A2}}{\tau_2} - \frac{\alpha_{A1}}{\tau_2} + \frac{1}{w_{BA}} \frac{\mu_{\max} c_{Af} (1 - \alpha_{A2}) \beta_2}{K + c_{Af} (1 - \alpha_{A2}) + \frac{c_{Af}^2 (1 - \alpha_{A2})^2}{K_i}} \quad (16)$$

$$\frac{d\alpha_{A3}}{dt} = \frac{\alpha_{A3}}{\tau_3} - \frac{\alpha_{A1}}{\tau_3} + \frac{1}{w_{BA}} \frac{\mu_{\max} c_{Af} (1 - \alpha_{A3}) \beta_3}{K + c_{Af} (1 - \alpha_{A3}) + \frac{c_{Af}^2 (1 - \alpha_{A3})^2}{K_i}} \quad (17)$$

$$\frac{d\beta_1}{dt} = \frac{\beta_1}{\tau_1} - \frac{\beta_3}{\tau_3} + \frac{\mu_{\max} c_{Af} (1 - \alpha_{A1}) \beta_1}{K + c_{Af} (1 - \alpha_{A1}) + \frac{c_{Af}^2 (1 - \alpha_{A1})^2}{K_i}} \quad (18)$$

$$\frac{d\beta_2}{dt} = \frac{\beta_2}{\tau_2} - \frac{\beta_1}{\tau_2} + \frac{\mu_{\max} c_{Af} (1 - \alpha_{A2}) \beta_2}{K + c_{Af} (1 - \alpha_{A2}) + \frac{c_{Af}^2 (1 - \alpha_{A2})^2}{K_i}} \quad (19)$$

$$\frac{d\beta_3}{dt} = \beta_3 - \frac{\beta_1}{\tau_3} + \frac{\mu_{\max} c_{Af} (1 - \alpha_{A3}) \beta_3}{K + c_{Af} (1 - \alpha_{A3}) + \frac{c_{Af}^2 (1 - \alpha_{A3})^2}{K_i}} \quad (20)$$

Additionally, the average residence time in the cascade may be introduced as:

$$\tau = \frac{3V}{F_{Vf}} \quad (21)$$

From equations (9), (14) and (21), relations (22) can be obtained:

$$\tau = 3\tau_2 \quad (22)$$

The division of stream F_{V1} may be characterised by parameter x :

$$x = \frac{F_{V3}}{F_{V2}} \quad (23)$$

Thanks to equations (8), (9), (22) and parameter x , the relations between residence times in each reactor and total residence time in the cascade could be obtained:

$$\tau_3 = \frac{\tau}{3x} \quad (24)$$

$$\tau_1 = \frac{\tau}{3(1+x)} \quad (25)$$

The final form of model in steady state is presented by equations (26)–(31):

$$0 = \frac{3}{\tau} (x\alpha_{A3} - (1+x)\alpha_{A1}) + \frac{1}{w_{BA}} \frac{\mu_{\max} c_{Af} (1 - \alpha_{A1}) \beta_1}{K + c_{Af} (1 - \alpha_{A1}) + \frac{c_{Af}^2 (1 - \alpha_{A1})^2}{K_i}} \quad (26)$$

$$0 = \frac{3}{\tau} (\alpha_{A1} - \alpha_{A2}) + \frac{1}{w_{BA}} \frac{\mu_{\max} c_{Af} (1 - \alpha_{A2}) \beta_2}{K + c_{Af} (1 - \alpha_{A2}) + \frac{c_{Af}^2 (1 - \alpha_{A2})^2}{K_i}} \quad (27)$$

$$\frac{3x}{\tau} (\alpha_{A1} - \alpha_{A3}) + \frac{1}{w_{BA}} \frac{\mu_{\max} c_{Af} (1 - \alpha_{A3}) \beta_3}{K + c_{Af} (1 - \alpha_{A3}) + \frac{c_{Af}^2 (1 - \alpha_{A3})^2}{K_i}} \quad (28)$$

$$0 = \frac{3}{\tau} (x\beta_3 - (1+x)\beta_1) + \frac{\mu_{\max} c_{Af} (1 - \alpha_{A1}) \beta_1}{K + c_{Af} (1 - \alpha_{A1}) + \frac{c_{Af}^2 (1 - \alpha_{A1})^2}{K_i}} \quad (29)$$

$$0 = \frac{3}{\tau}(\beta_1 - \beta_2) + \frac{\mu_{\max} c_{Af} (1 - \alpha_{A2}) \beta_2}{K + c_{Af} (1 - \alpha_{A2}) + \frac{c_{Af}^2 (1 - \alpha_{A2})^2}{K_i}} \quad (30)$$

$$0 = \frac{3x}{\tau}(\beta_1 - \beta_3) + \frac{\mu_{\max} c_{Af} (1 - \alpha_{A3}) \beta_3}{K + c_{Af} (1 - \alpha_{A3}) + \frac{c_{Af}^2 (1 - \alpha_{A3})^2}{K_i}} \quad (31)$$

It can be noted that the solution of the presented model may be continued by the three main process parameters: c_{Af} , x and τ . This has been achieved through the use of continuation and bifurcation tools. The continuation was realised for two concentrations of substrate in the feed: $c_{Af} = 0.5 \text{ kgm}^{-3}$ and $c_{Af} = 1 \text{ kgm}^{-3}$. After the initial backward continuation for $x = 0.4$, forward two-parametric continuation was realised in order to obtain the catastrophic graphs. Continuation was then realised for three representative values of x : 0.4, 0.8 and 1.2.

3. Results

3.1. Catastrophic plots

Obtained plots are presented in Fig. 2a and Fig. 2b.

In both cases, the washout area (region I) lies in the same place. Regions of the fivefold steady state (III and V) are wider, when c_{Af} is higher. The other regions are triple steady states.

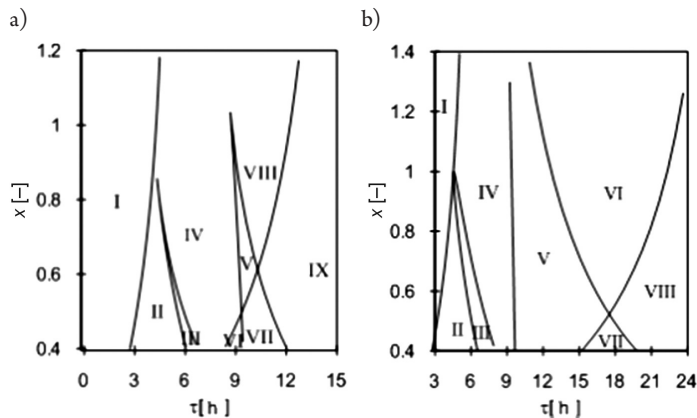


Fig. 2. Catastrophic plots of the investigated cascade (upper): a) for $c_{Af} = 0.5 \text{ kgm}^{-3}$ and (lower), b) for $c_{Af} = 1 \text{ kgm}^{-3}$. Catastrophic sections are numbered by I–IX

3.2. Branches of steady states

Figs. 3 & 4 present branches of steady states for the three selected values of x parameter: $x = 0.4$, $x = 0.8$ and $x = 1.2$.

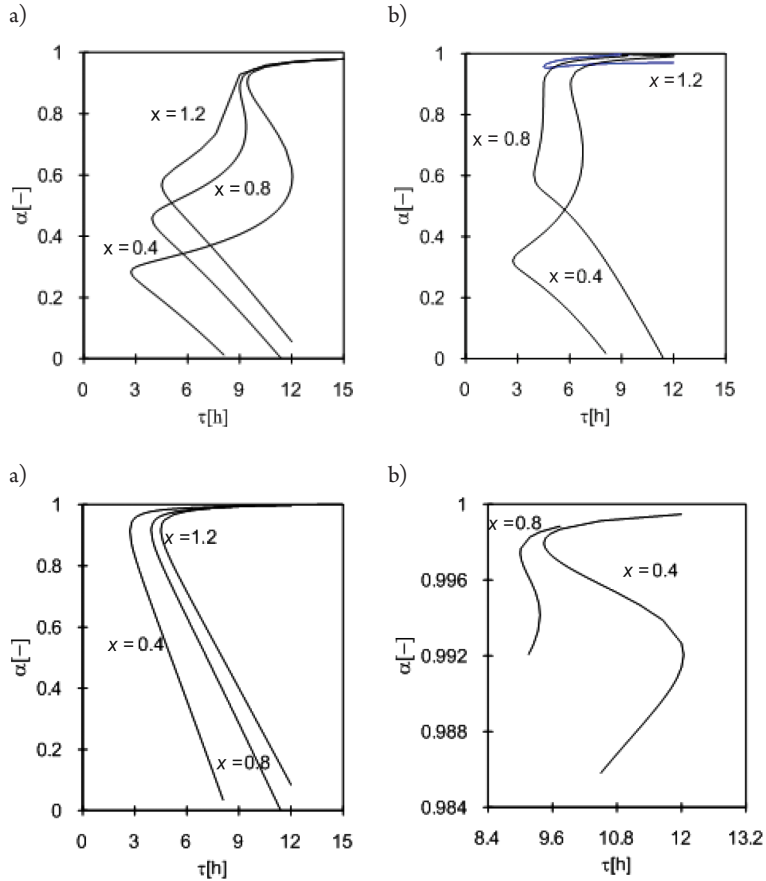


Fig. 3. Branches of steady states for $c_{Af} = 0.5 \text{ kgm}^{-3}$; a) (upper left) a_1 , b) (upper right) a_2 , c) (lower left) a_3 and d) (lower right) enlargement of upper states of a_3 branch

The obtained results suggest that forcing on cascade to operate in the upper states may be realised not only by increasing the total residence time, but also by changing parameter x (for example, by way of setting the tree-way valve), especially in the case of higher concentration of substrate in the feed. Additionally, the width of upper states (Fig. 4e; region V in Fig. 2b) may provide protection against falling down to middle states under various values of total residence time. This indicates the practical application of such devices when the stream of the feed is changing during the process. On the other hand, further increasing the x parameter may result in biomass washout in reactors 1 and 3, and consequently, in such conditions, only reactor 2 can work effectively.

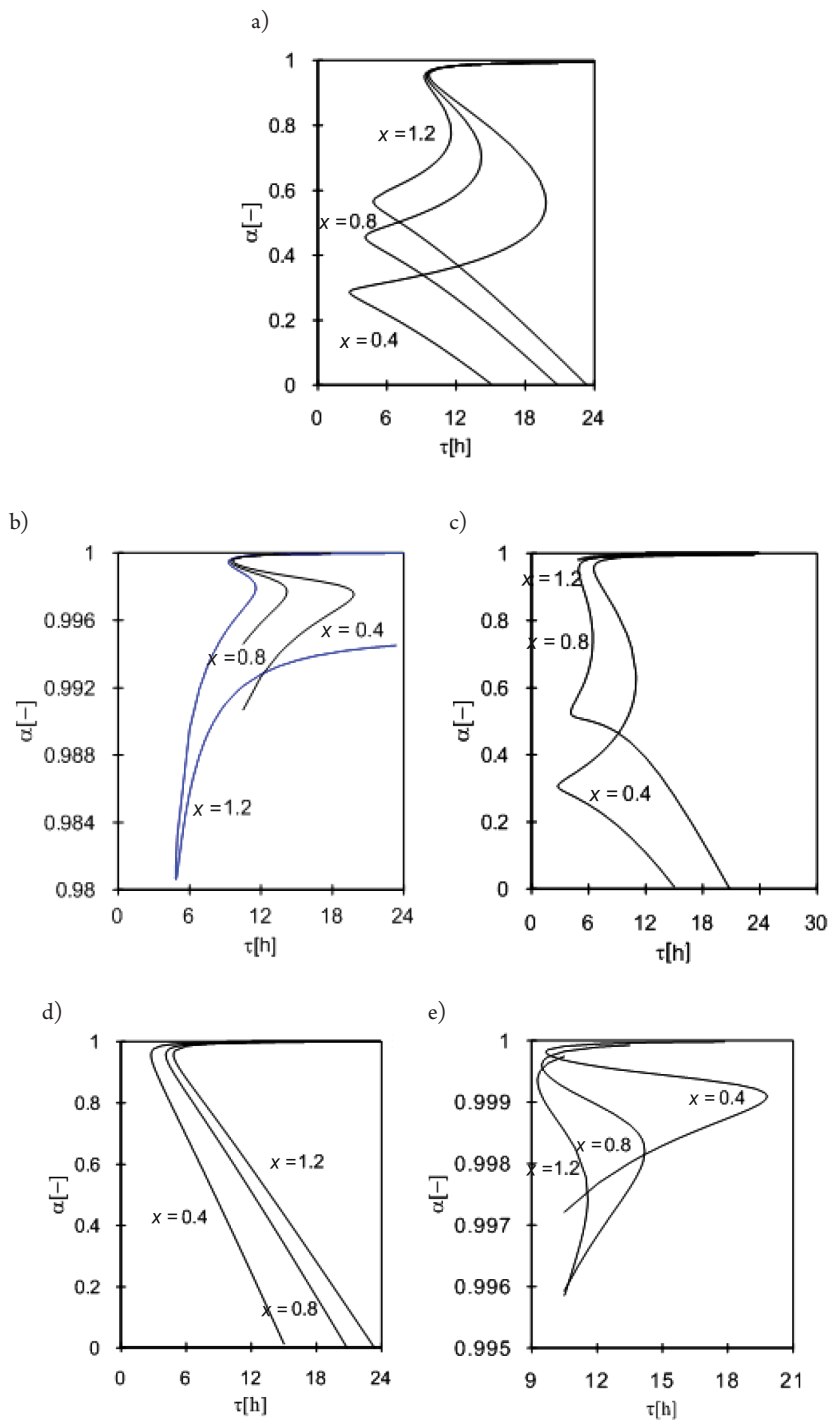


Fig. 4. Branches of steady states for $c_{Af} = 1 \text{ kgm}^{-3}$; a) a_1 (first row), b) a_2 (second row, left), d) (third row, left) a_3 and enlargements of upper states for c) (second row, right) a_2 ; e) (third row, right) a_3

References

- [1] Pasternak G., *Bioreaktory oraz ich zastosowanie w inżynierii i ochronie środowiska*, J. Ecol. Health, vol. 15(3), 2011, 121–125.
- [2] Siudzińska R., *Analiza wpływu warunków napowietrzania na właściwości stacjonarne kaskad biochemicznych w procesie degradacji aerobowej*, Ph.D. thesis, Politechnika Krakowska, Kraków 2005.
- [3] Elgeti K., *A new equation for correlating a pipe flow reactor with a cascade of mixed reactors*, Chem. Eng. Sci., vol. 51(23), 1996, 5077–5080.
- [4] Berezowski M., *Bifurcation analysis of the conversion degrees in systems based on the cascade of tank reactors*, Chem. Eng. Sci., 61, 2011, 5219–5223.
- [5] Berezowski M., Kulik B., *Periodicity of chaotic solutions of the model of thermally coupled cascades of chemical tank reactors with flow reversal*, Chaos Soliton Fract., 40(1), 2009, 331–336.
- [6] Hortsh R., *A Two-Stage CSTR Cascade for studying the effect of inhibitory and toxic substances in bioprocess*, [in:] C. Loser, T. Bley, Eng. Life Sci., 6, 2008, 650–657.
- [7] Szyman J., *Implementacja modelu matematycznego i analiza stanów stacjonarnych kaskady bioreaktorów zawieszinowych do oczyszczania ścieków fenolowych*, M.Sc. thesis, Politechnika Krakowska, Kraków, 2015.
- [8] Grzywacz R., *Airlift Bioreactor*, Wydawnictwo PK, Kraków 2013.

Lukasz Bednarski

AGH University of Science and Technology in Cracow

Rafał Sienko (rsienko@pk.edu.pl)

Tomasz Howiacki

Institute of Building Material and Structures, Faculty of Civil Engineering, Cracow
University of Technology

Mariusz Poślajko

Mariusz Poślajko, Keller Polska

THE MONITORING OF A SUBSTRATE STRENGTHENED WITH CONCRETE COLUMNS

MONITOROWANIE PODŁOŻA WZMOCNIONEGO KOLUMNAMI BETONOWYMI

Abstract

The process of interaction between the ground and screw displacement columns (SDC) in transferring loads has not yet been sufficiently investigated. This paper presents the results of pioneering tests in this field, carried out with the application of a long-term structural health monitoring system.

Keywords: SDC columns, force distribution, structural health monitoring systems

Streszczenie

Proces współpracy pomiędzy gruntem i kolumnami przemieszczeniowymi (SDC) w przeniesieniu obciążeń nie został dotychczas wystarczająco zbadany. W artykule przedstawiono wyniki pilotażowych badań w tym zakresie, przeprowadzonych z wykorzystaniem długoterminowego systemu monitorowania.

Słowa kluczowe: kolumny SDC, dystrybucja siły, systemy monitorowania konstrukcji

1. Introduction

In situations with unfavourable ground conditions, screw displacement columns (SDC) are increasingly used to strengthen the ground and to safely construct foundations. During the construction of foundations, soil is not extracted, but compressed laterally [1]. This has a positive effect on the state of soil compaction and improves the axial stiffness and load-bearing capacity of columns.

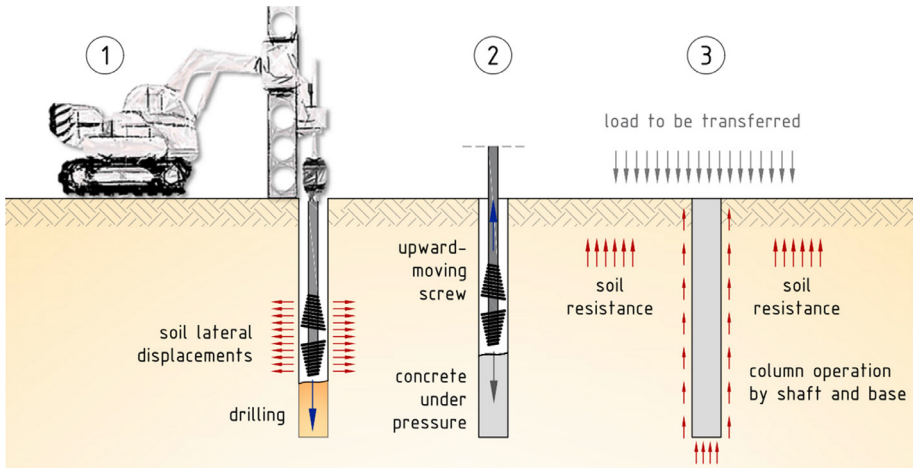


Fig. 1. Construction scheme of screw displacement columns

Other advantages of this technology include the fact that it is a process that does not produce shocks, it produces low noise levels, it has the possibility of being implemented alongside existing facilities without the risk of soil loosening, and it is fast and efficiently executed [2]. However, despite its theoretically simple technology, the design process of displacement columns still causes a lot of problems [3]. The phenomenon of force distribution between the column shaft and the base is insufficiently identified as well as its interaction with the surrounding soil. In [4, 5, 11, 12] some design solutions for displacement columns have been proposed; however, there has been an insufficient number of systematic pieces of in situ research, especially in Poland. In many countries, the standard procedure is to use measuring apparatus during load tests performed with static methods, which enable the measurement of force distribution along the pile or column shaft [6]. Such pieces of research have been conducted more and more frequently in Poland over recent years [7, 8].

This article presents an analysis of the operation of displacement columns on the basis of an automatic structural health monitoring system. The continuous measurement strategy provides the possibility to analyse the interaction between the concrete column and the surrounding soil in the context of load distribution transferred by the foundation slab through the transmission layer to the ground and columns over a long period of time.

2. Description of measuring problem

The analysed multi-family building is located within an area where the use of conventional, direct foundation by a shallow foundation slab was not an option due to the geological conditions. Under the building were layers of multigrain sands with thicknesses from 3.5 to 6.0 m and compaction degrees from $ID = 0.25$ to 0.75 ; below, there is a layer of sandy silt and humous clay. The thickness of the organic soil layer ranged from 1.5 to 4.0 m. Unfavourably within the foundations there is the water table – as presented in Fig. 2.

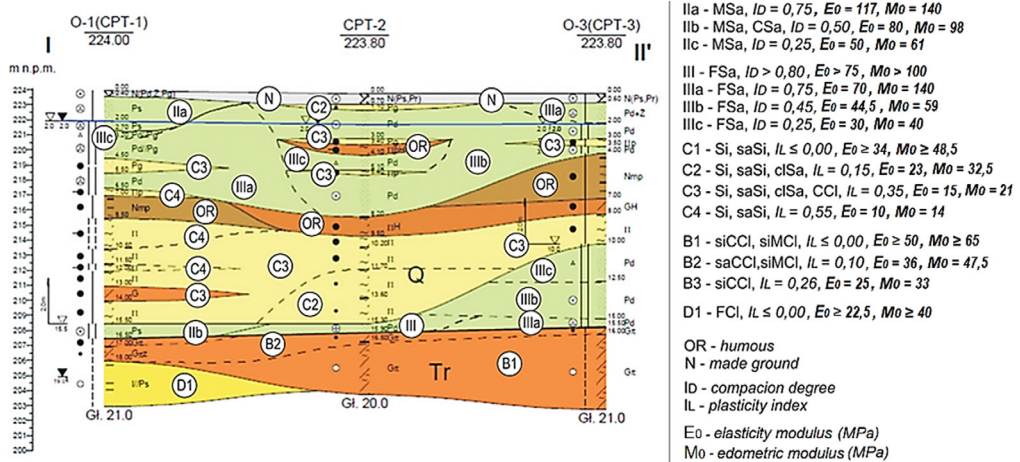


Fig. 2. Geotechnical cross section (author: Ł. Pietrusa, 2011)

Therefore, it was decided to strengthen the ground through the use of concrete columns made in SDC technology. The diameter of the column was 400 mm, the length was approximately 13 m, the spacing was approximately 1.6×1.6 m. The columns have been set in a layer of medium and thick sands with a compaction degree of $ID = 0.50$. At about 4.5 m below the contractual building level of ± 0.00 m, in a layer of clay and fine sand, a so-called transmission layer of 0.5m was constructed from aggregate. Its compaction index IS (ratio of current bulk density to its maximum value) was equal to 0.98 and the secondary elasticity modulus was $E_2 = 100$ MPa. Above transmission layer a 0.1 m thick layer of lean concrete was placed, a foundation slab with a thickness of 0.9 m was then concreted. The analysed building is a near elongated rectangle with dimensions of approximately 62.0×15.5 m – Fig. 3, the building height above ground level is around 35 m (11 storeys).

Foundations located on ground strengthened by columns assumes interaction between the ground and the columns with regard to carrying loads transferred by the foundation slab. The uniform transfer of load to the ground and columns is provided by a transmission layer. The aim of measurements taken with the structural health monitoring system was to determine: the value of force captured by one selected column; the stress (pressure) in the subsoil lying beneath the transmission layer. Automation of measurements allowed for the observation of this interaction over a long period of time.

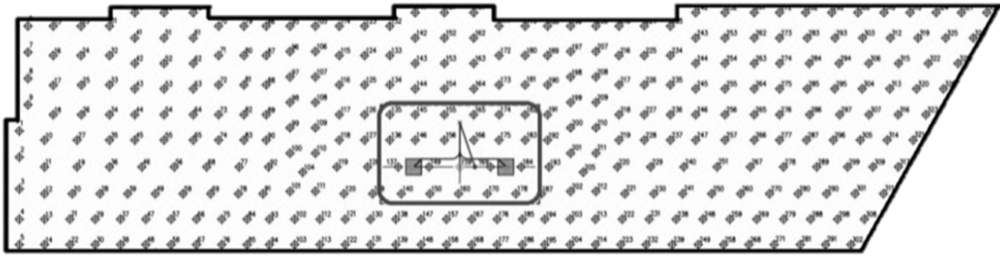


Fig. 3. Location of the analysed area on the plan showing the location of the columns (own elaboration)

3. Structural health monitoring system construction

To build a structural health monitoring system, sensors or measuring sets were applied on the basis of a vibrating wire sensing technique [9]. In addition to high measuring accuracy, vibrating wire sensors are characterised by their resistance to external conditions and their decades-long stability of measurements; therefore, they are widely used as elements of automatic, long-term structural health monitoring systems. All vibrating wire sensors include thermistors, which enable temperature measurements to be conducted simultaneously. These measurements are taken into account while correcting the obtained results. They are also used in the analysis of structural response to temperature loading. In the analysed example, the measuring system is equipped with additional temperature sensors (next to the VW-sensors) installed in the transmission layer and the foundation slab. As part of the SHM process, measurements of the following physical quantities are carried out:

- ▶ axial force in selected concrete column;
- ▶ stress (pressure) in the ground under the transmission layer in a vertical direction next to the analysed column;
- ▶ temperature in the ground, the transmission layer, the foundation slab and the air.

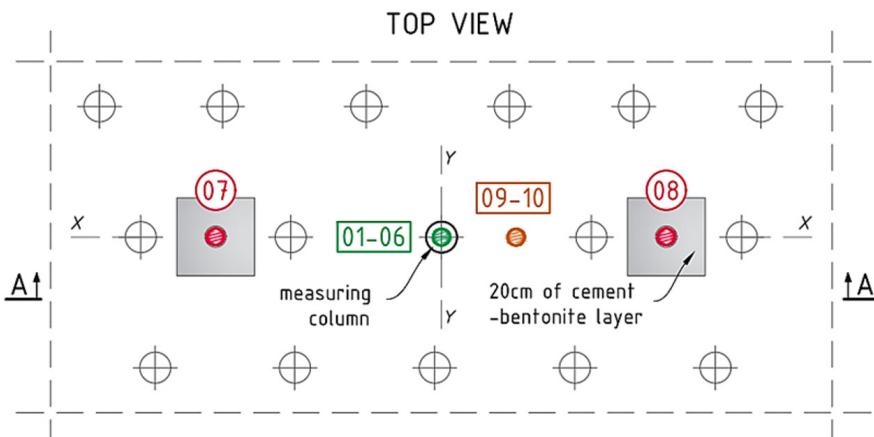


Fig. 4. SHM system scheme with locations of the measuring points: top view (own elaboration)

Measurement of the axial force in the concrete column is performed by a specially created force gauge. This element was made from a steel tube with an outer-diameter of 250 mm, a wall-thickness of 5 mm and a height of 200 mm. On the external surface of the tube, at half its height, six vibrating wire sensors were installed using spot welding. The full range of these sensors is $3,000 \cdot 10^{-6}$ ($3,000 \mu\epsilon$) and the measuring base is 50 mm (see Fig. 5 and 7).

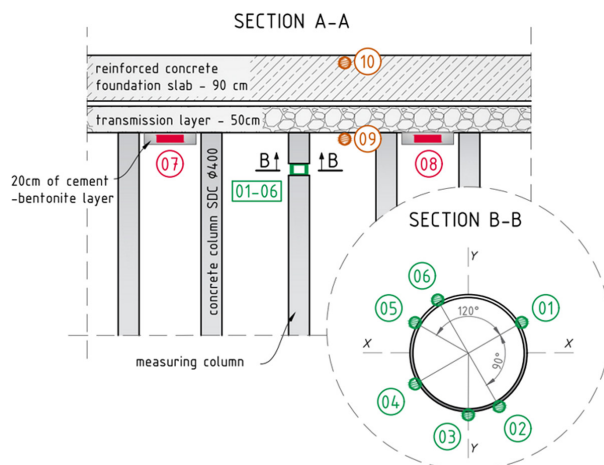


Fig. 5. SHM system scheme: side view and force gauge cross section (own elaboration)

Basic technical specifications of the applied vibrating wire sensors are as follows:

- ▶ measuring base – 50 mm;
- ▶ range of strains measurements – $3,000 \mu\epsilon$;
- ▶ resolution of strains measurements: $1 \mu\epsilon$;
- ▶ accuracy of strains measurements – $\pm 0.1\%$ of full-scale range;
- ▶ range of temperature measurements – -20 do $+80^\circ\text{C}$;
- ▶ resolution of temperature measurements – 0.1°C ;
- ▶ accuracy of temperature measurements – $\pm 0.2^\circ\text{C}$;
- ▶ signing: ‘+’ means strains resulting in compression.

To enable analysis of uniformity force transmission (its eccentricity), strain sensors were arranged around the tube circumference at 120° and at 90° (Fig. 5). On the basis of data obtained from system operation, it was found that loads are transferred to the force gauge in such a way as to cause its uniform (axial) compression (strain increases measured by each VW sensor create parallel lines – Fig. 6).

Calibration of the force gauge was performed on a testing machine with a measuring range of 1500 kN in a laboratory of the Institute of Building Materials and Structures at Cracow University of Technology. Force control was performed manually by visual reading on the manometer. During the entire test, all sensors were read at time intervals of 10 secs; the temperature was also recorded for all sensors. During the entire calibration process, it changed by no more than 0.3°C – this is less than thermistors accuracy. It has been concluded that the temperature effect on strain sensor readings was negligible and it has not been included in calculations.

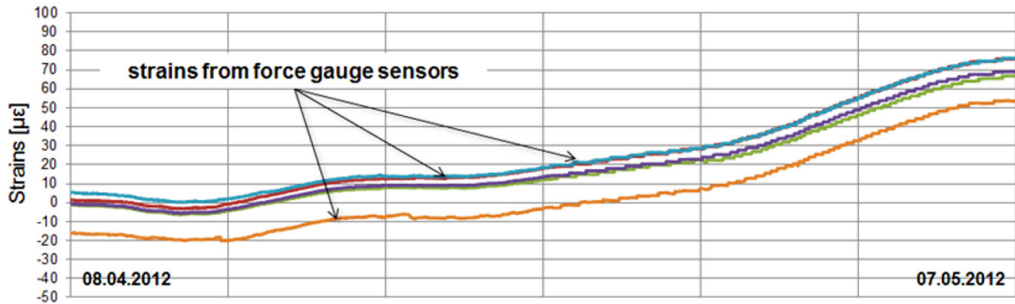


Fig. 6. Strains from vibrating wire sensors installed on force gauge

Strain value indicated by sensors is calculated with following equation:

$$\varepsilon = (R_1 - R_0) \cdot G \cdot B \quad (1)$$

where:

- ε – strain increment with respect to the initial value, [-];
- G, B – sensor calibration coefficients;
- R_0 – initial reading of string frequency, [Hz²/1000];
- R_1 – actual reading of string frequency, [Hz²/1000].

After calculating the average strains and minimising the error with the least squares method, the parameters of linear function were determined:

$$\varepsilon = a \cdot P + b \quad (2)$$

After converting the expression (2), we obtain the formula describing force value P as a function of measured strain:

$$P = (\varepsilon - b) \div a \quad (3)$$

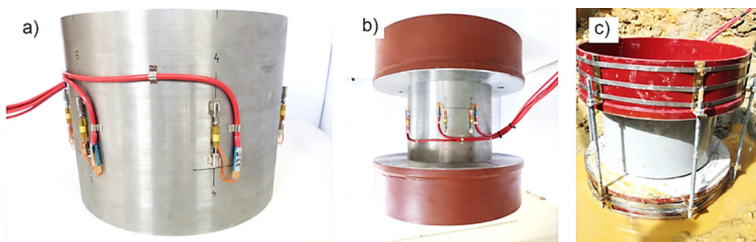


Fig. 7. Force gauge: a) during calibration test; b) with mounting heads; c) after installation in the lower part of the column (photo by Łukasz Bednarski)

After calibration, the force gauge was prepared for installation. Steel heads were specially designed for this purpose, the aim of which was to close interrupted parts of the concrete column in such a way that the geometrical axis of the column aligns with the gauge axis. The device was protected from the outside by a cover made from a section of PVC piping, the gap between the steel tube and the plastic pipe was filled with a permanently-elastic material.

Subsoil stress measurement is performed with two pressure sensors with a measuring range of 350 kPa located directly beneath the transmission layer near the analysed column. These sensors take measurements of vertical stress changes in the ground by measuring the change of hydraulic fluid pressure between two steel plates in the shape of a circle, joined at the periphery by welding. The fluid presses against the membrane which is connected to the vibrating wire. The sensors were factory-calibrated.

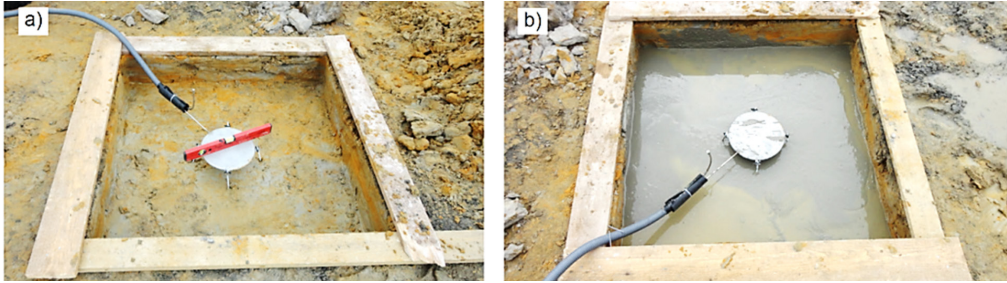


Fig. 8. Stress (pressure) sensor in the ground: a) before pouring with the cement-bentonite mixture; b) during pouring (photo by Łukasz Bednarski)

Basic technical specification of applied stress sensors are as follows:

- ▶ diameter – 230 mm;
- ▶ range of pressure (stress) measurements – 350 kPa;
- ▶ resolution of pressure measurements – 0.025% of full-scale range;
- ▶ accuracy of pressure measurements – $\pm 0.1\%$ of full-scale range (linear calibration);
- ▶ range of temperature measurements – -20 to $+80^{\circ}\text{C}$;
- ▶ resolution of temperature measurements – 0.1°C ;
- ▶ accuracy of temperature measurements – $\pm 0.2^{\circ}\text{C}$;
- ▶ signing: ‘+’ means increase in pressure (compressing stress) in the ground.

In order to eliminate local pressure on the sensor plate and to ensure the best compliance of ground medium operation within the direct vicinity of the sensor with the medium located outside sensor impact area, it was placed in a cube made of a mixture of bentonite and cement with dimensions of $1.0 \times 1.0 \times 0.2$ m. The sensors were equipped with sealed steel tubes, connected hydraulically with the sensor chamber in the interior. These tubes were permanently mechanically clamped after cement and bentonite mixture bonding. This clamp increases the pressure in the measuring chamber and the alignment of the sensor plates with the surrounding medium.

Additional temperature sensors were installed within the transmission layer and the foundation slab – these were located at a depth of approximately 0.05m below the top surface of the transmission layer and approximately 0.10 m below the top surface of the concrete slab. The applied temperature sensors (thermistors) have the following properties:

- ▶ measuring range – -20 to $+80^{\circ}\text{C}$;
- ▶ resolution of measurements – 0.1°C ;
- ▶ accuracy of measurements – $\pm 0.2^{\circ}\text{C}$.

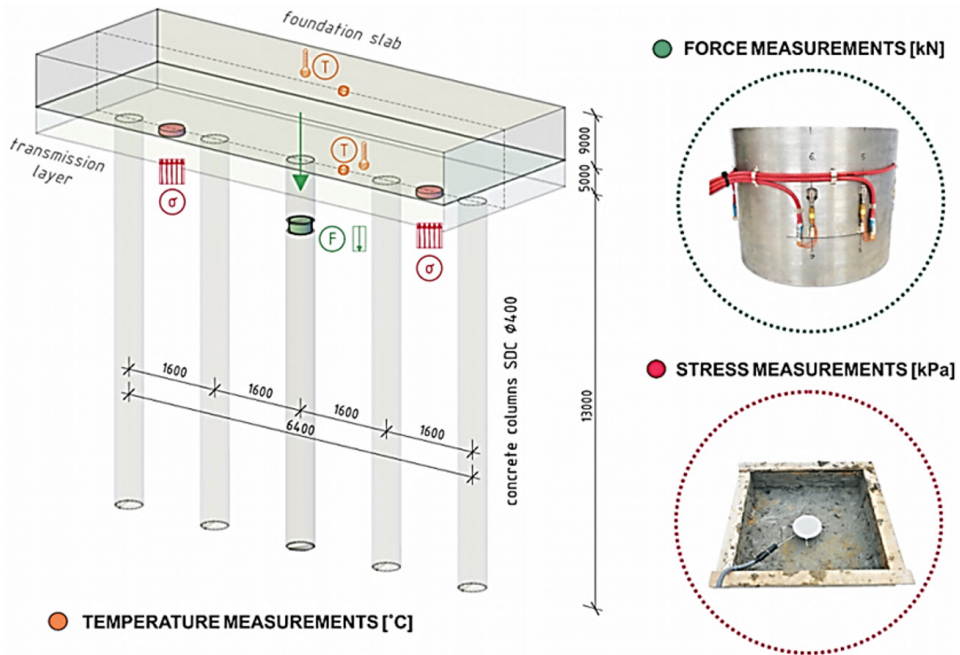


Fig. 9. Spatial visualisation of the structural health monitoring system (own elaboration)

4. Measuring data presentation

The measuring system was launched on 8th April 2012; the initial reading values were defined then and these are the reference for all the other measurements. Therefore, values of selected physical quantities presented in this article (except for temperature) should be treated as relative values (increments). During system operation, measurements were carried out with different time intervals from 10 minutes to 2 hours.

If a high level of accuracy of ground stress measurements is required, it is necessary to take into account the impact of atmospheric pressure fluctuations on the obtained results. Up until October 2012, the SHM system was equipped with a barometer; thus, stress results from the initial operation period were corrected for atmospheric pressure variations. In subsequent years, we have benefited from data provided by the Krakow Fiolkowa weather station, which is located a few hundred meters from the analysed building. Data analysis revealed, among other things, that in 2014, the maximum fluctuation of atmospheric pressure was around 4kPa with a standard deviation of 0.6 kPa.

Because the system covers only one concrete column, analysis and inference presented within this article is primarily qualitative rather than quantitative in nature; therefore, the omission of slight atmospheric pressure changes in the calculation does not affect the correctness of inference. The following plot presents the changes in atmospheric pressure in 2014 (for the initial reading, the first measurement carried out this year was defined).

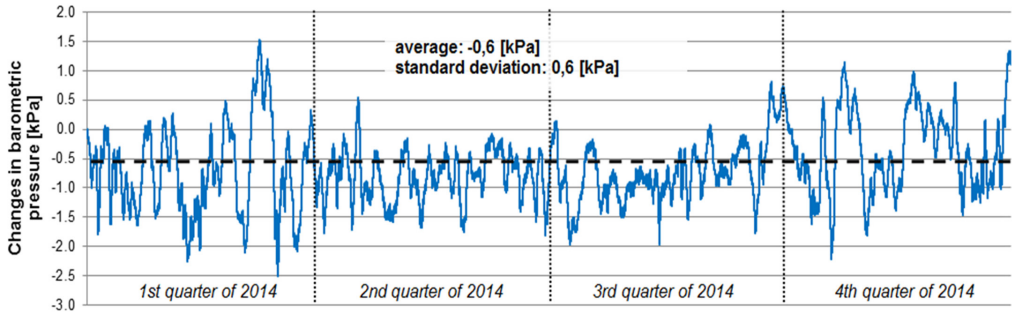


Fig. 10. Changes in atmospheric pressure in 2014 on the basis of measurements obtained from the Kraków Fiolkowa weather station

For the analysed plots, data is presented for three time periods: from 08.04.2012 to 04.12.2012; from 17.05.2013 to 20.08.2013; from 28.02.2015 to 27.05.2015. There are a few distinctive points in time (points 1-3 are marked on the plots):

1. 11.05.2012 – foundation slab concreting;
2. 19.06.2012 – concreting of slab above ground floor;
3. 31.07.2012 – concreting of slab above second floor;
4. 05.02.2013 – (building) shell;
5. the end of October 2013 – finished state.

Below, the increments of force in the concrete column and increments of ground stress registered by the pressure sensors are presented.

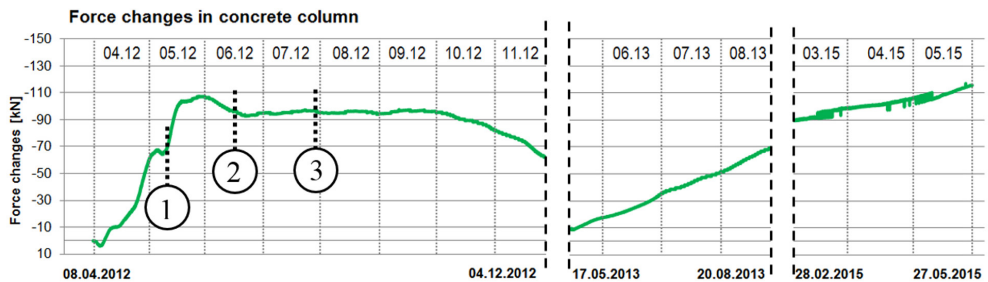


Fig. 11. Increments of force in concrete column over the considered periods of time

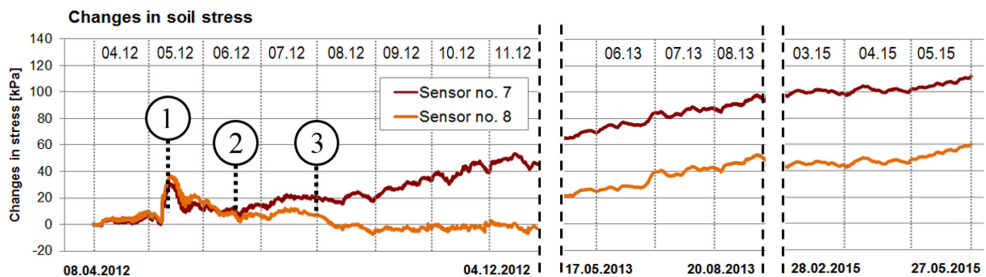


Fig. 12. Increments of stress in pressure sensors located on both sides of concrete column

To better illustrate load distribution between concrete column and the ground, these two charts can be presented within one, converting the stress values from pressure sensors (7 and 8) to the value of force. For this calculations reference area of ground around considered column as shown in Fig. 13 was assumed. In the analysis, the value of stress in the ground was assumed as an average value from data registered by sensors 7 and 8.

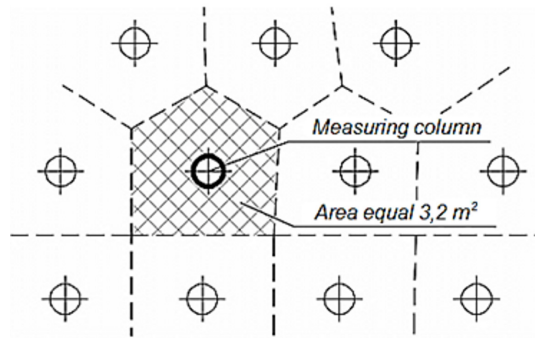


Fig. 13. Reference area for calculation of stress in the ground surrounding considered column

The following plot shows the percentage of force in the concrete column with regard to the total value of the load transferred to the strengthened substrate. In the initial period, the concrete column has taken about 70–80% of the total load; however, since September 2012, a gradual redistribution of stresses has been observed, this has resulted in a decrease in force carried by the column. After three years of operation of the structure, this value has been identified as approximately 30% of the load transferring to the analysed area – this corresponds to a value of force in concrete column of approximately 100 kN.

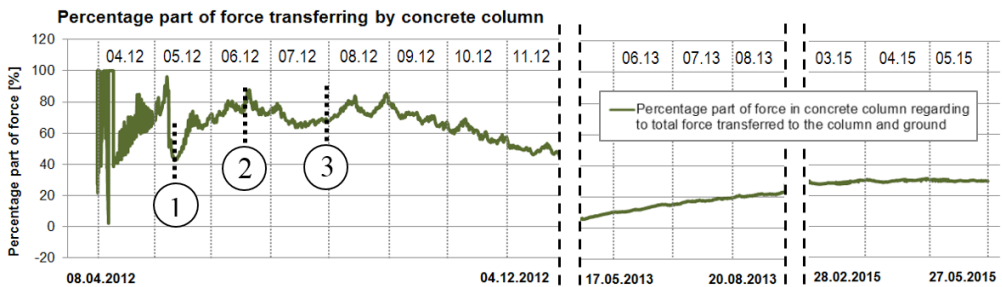


Fig. 14. Reference area for the calculation of stress in the ground surrounding the considered column

5. Temperature distribution

Within the structural health monitoring system, the values of temperature are recorded by strain sensors installed in the force gauge, stress sensors in the ground, in the transmission layer of the aggregate and in the concrete of the foundation slab. The plot below shows the

distribution of measured temperatures during the considered periods of time and more detailed close-ups in three selected periods.

Regardless of the temperature of the season, amplitudes in the concrete foundation slab are larger than in the other measuring points; sensors located below the slab indicate similar values of temperature.

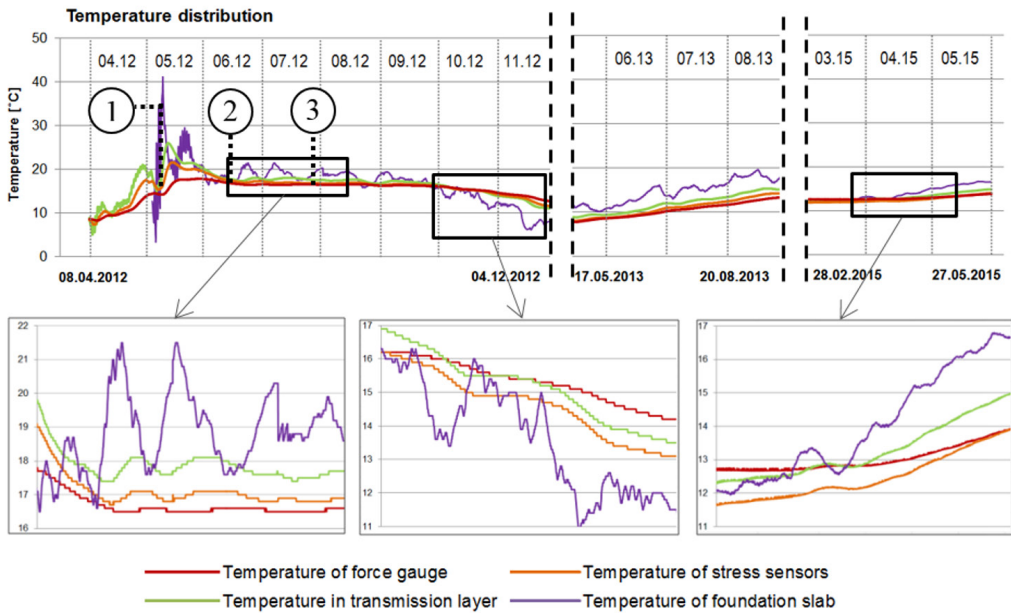


Fig. 15. Temperature distribution in each of the measuring points

6. Interpretation of results and conclusions

Described research was one of the first of its kind to be conducted in Poland. The aim was to identify the possibilities of determining the manner of load distribution transferred to a strengthened substrate through a foundation slab placed on a transmission layer. In the considered case, the reduction in the compressive force in the concrete column and the simultaneous increase in stress in the ground located between columns was observed after a few months of operation. Identification of the definite reasons for this phenomenon is not possible on such a small test field; however, measurements have shown that transferring loads through substrate-concrete columns system may be associated with the redistribution of stresses between the columns and the ground. Reaching the static equilibrium is a long-term process depending upon many factors associated with both the substrate and its strengthening.

It should also be noted that the measurements did not include the foundation slab itself, which, as a result of mechanical actions (external loads, the impact of columns and ground) and non-mechanical actions (temperature, concrete shrinkage), is deformed and causes changes in ground stress and forces in the concrete columns.

Analysis of the pressure measurements in the ground provides interesting findings. Extreme values in the vertical stress function correspond to the time of concreting, when the foundation slab does not yet have any bending stiffness. Then, the whole load resulting from the dead weight of the transmission layer and the slab is transferred evenly on the ground – the measured value corresponds to the calculated theoretical value. After concrete hardening, stiffening of the slab occurs – this causes the load value to be transferred to the selected area of the substrate and is dependent upon overall stiffness. This property of substrate strengthened by concrete columns means that over a certain period of time, we can observe ground relief. Longer observation indicates the redistribution of stress between the columns and the ground – this results in an increase in ground stress. Load captured by the ground is associated with pressing columns into the ground. The influence of a concrete creep effect is also possible. Increase in the load-bearing capacity of a substrate strengthened by the columns could also be justified by the partial restriction of ground horizontal displacements, what is caused by resistance of the columns.

Drawing general conclusions based on a small number of sensors installed in one building is impossible. In the future, similar studies should be planned in such a manner that includes the measurements of a minimum of three concrete columns and the surrounding ground. It would be advantageous to monitor at least two groups of columns (min. three columns in each of the group) located in different substrate conditions. The described test may be supplemented by: measurements of columns strains over their length; measurements of deformations (strains) of foundation slab; vertical ground displacements along the column length; pore water pressure in the ground under the slab. It would also be beneficial to measure changes in the vertical 'stress' in concrete columns to determine changes in the elastic modulus and creep of concrete over time. Of course, the research range should be determined in each case depending on local conditions and possibility of measurement result interpretations [10]. The aim of such a research is to provide structural health monitoring system data which enables the building of a correct model of interaction between the foundation and the substrate strengthened by screw displacement columns. Conducting such kind of research is also necessary in the context of developing Polish guidelines for designing and constructing concrete columns. This work will probably be modelled on the French guidelines [11, 12]. It would be advisable to include considerations derived from Polish experience covering the very broad issue of strengthening the ground through the use of concrete columns.

References

- [1] Krasieński A., *Badania terenowe przemieszczeniowych pali i kolumn wkręcanych typu SDP i SDC, Drogi i Mosty*, 1-2/2011, 21–58.
- [2] Gwizdała K., Krasieński A., *Zastosowanie przemieszczeniowych pali wkręcanych w podłożu uwarstwionym na przykładzie realizacji obiektu w warunkach gruntowych delty Wisły*, „Inżynieria i Budownictwo”, 3/2009, 133–136.

- [3] Gwizdała K., Krasiński A., Brzozowski T., *Experience gained at the application of Atlas piles in Poland*, Proceedings of 10th International Conference on Piling and Deep Foundations, Amsterdam, 31.05.–02. 06. 2006, 460–464.
- [4] Bustamante M., Gianceselli L., *Installation parameters and capacity of screwed piles*, Proceedings of International Geotechnical Seminar on Deep Foundations on Bored and Auger Piles, BAP III. Balkema, Rotterdam, 1998, 95–108.
- [5] Van Impe W. F., *Influence of screw pile installation parameters on the overall pile behavior*, Workshop “Piled Foundations: full scale investigations, analysis and design”, Naples, 1994.
- [6] Hanifah A.A., Lee Sieng K., *Application of global strain extensometer (Glostrest) method for instrumented bored piles in Malaysia*, Piling and Deep Foundations: 10th International Conference, Amsterdam, 31.05 – 02.06.2006.
- [7] Krasiński A., Sieńko R., *Pomiar pionowego rozkładu siły w palu podczas testów statycznych*, Mat. 56 Konf. Nauk. KILiW PAN oraz KN PZiTb, Kielce–Krynica, 19–24.09.2010, 161–168.
- [8] Krasiński A., Sieńko R., *Wykorzystanie pomiaru pionowego rozkładu siły w palu do interpretacji testów statycznych*, Magazyn Autostrady, 11/2010, 24–28.
- [9] Bednarski Ł., Sieńko R., *Pomiary odkształceń konstrukcji czujnikami strunowymi*, „Inżynieria i Budownictwo”, 11/2013, 615–619.
- [10] Bednarski Ł., Sieńko R., Howiacki T., *Wybrane zagadnienia monitorowania konstrukcji*, XXX Jubileuszowe Ogólnopolskie Warsztatach Pracy Projektanta Konstrukcji, Szczyrk, 25-28.03.2015.
- [11] Świniański J., Marchwicki M., *Wzmacnianie gruntu sztywnymi kolumnami – podstawy projektowania według ASIRI i Eurokodu 7*, „Inżynieria i Budownictwo”, 6/2014, 320–337.
- [12] ASIRI National Project, *Recommendations for the design, execution and control of rigid inclusion ground improvements*, IREX I Press de Ponts, Paryż 2013.



Tadeusz Majcherczyk

Zbigniew Niedbalski (niedzbig@agh.edu.pl)

Faculty of Mining and Geoengineering, AGH University of Science and Technology

THE INFLUENCE OF UNDERGROUND COAL MINING ON AN OVERHEAD HIGH-VOLTAGE POWER LINE

WPLYW PODZIEMNEJ EKSPLOATACJI POKŁADÓW WĘGLA NA LINIĘ ELEKTROENERGETYCZNĄ WYSOKIEGO NAPIĘCIA

Abstract

The primary aim of this study is the analysis of the influence of multi-seam coal mining on a specific 110 kV overhead high-voltage power line. The paper presents the results of geodesic measurements of surface deformation in the area of the analysed location. The study also analyses mining-induced changes in the construction and the inclination of the transmission pylons. Some proposals for the reinforcement of the pylons are suggested. Additionally, pressing issues are identified indicating the necessity for the replacement of the existing pylon system of the overhead high-voltage power line.

Keywords: mining, surface deformations, power line protection

Streszczenie:

W artykule poddano analizie wpływ prowadzenia wielopokładowej eksploatacji węgla kamiennego na wybrany odcinek linii wysokiego napięcia 110 kV. W artykule zamieszczono geodezyjne wyniki deformacji powierzchni terenu w rejonie analizowanego obiektu. W dalszej części dokonano analizy zmian zachodzących w konstrukcji słupów oraz ich wychyleń w zależności od stopnia zaawansowania eksploatacji dokonanej i planowanej. Podano także przykłady wzmocnienia istniejących słupów oraz warunki, w których powinna nastąpić wymiana słupów linii wysokiego napięcia.

Słowa kluczowe: górnictwo, deformacje powierzchni, ochrona linii energetycznej

1. Introduction

Underground mining, particularly when executed without the backfilling of post-exploitation voids, usually causes surface deformation. In the case of multi-seam coal mining, such deformations are pronounced; hence, it is necessary to evaluate the impact of underground exploitation on the existing surface structures [6–8, 14]. Due to a high level of public safety risk, large structures – in particular, public buildings and blocks of flats or large industrial plants – are the focus for monitoring attention in these situations. Additionally, various types of transmission lines constitute an important element of surface infrastructure. In the case of overhead power lines, mining-induced uneven distribution of load on the supporting posts may occur – this is particularly dangerous. The significant height of high-voltage power line transmission pylons makes them especially vulnerable to surface inclination and horizontal surface displacement – these factors can cause changes in pylon span and power line cable tension. Such an increase in the construction-related internal forces may cause damage to an individual transmission pylon or even to the entire power line [1, 2, 4, 5].

For this reason, overhead high-voltage power lines designed and newly constructed in mining areas are fulfilled far stricter standards and restrictions than those built elsewhere [11, 12, 13]. Such requirements may also include the need to increase the distance of the power lines from ground level and possible colliding elements by 1–2m, and to decrease tensioning of the electric lines to 0.8–0.9 permissible normal stress (for the line type AFL 6-240, permissible normal stress is 119.91 MPa), to protect the transmission pylon foundations against ground movement in locations designated as fourth-category mining areas and to refrain from the construction of any power lines in fifth-category mining areas or in areas with discontinuous deformation.

In areas subject to mining subsidence, it is hardly possible to build a power line which is completely protected against all negative consequences of mining activity. Therefore, in mining areas, the power transmission lines are monitored regularly and more frequently than elsewhere, this is stipulated in the related regulations. Currently, according to construction law in Poland, the span of time between two consecutive checks must not exceed five years [15]. The examinations are made by the institutions operating particular power lines and their main objective is to undertake adequate repairs and maintenance in order to avoid the occurrence of any critical circumstances.

This paper sets out to analyse the impact of multi-layer coal mining on a selected section of overhead high-voltage power transmission line. The results of geodesic measurements of surface deformation are presented as well as the analyses of changes in the construction and inclination of transmission pylons depending upon the degree of mining progression. Some examples of reinforcement of the currently existing pylons are also discussed and the critical boundary conditions in which the transmission pylons of the overhead high-voltage power line (110 kV) should be definitely replaced are determined.

2. Subject of research and observational study results

The analysed overhead power line (110 kV) runs through the area above an underground coal mine and is mostly fixed on the O24-series suspension lattice pylons supported on four independent foundations. Over the last three decades, the transmission pylons have been subject to the influence of mining activity; hence, geodesic measurements are routinely carried out in observation lines no. XIII–XIII and no. XV–XV as part of a regular monitoring scheme to evaluate the impact of exploitation. Line XIII–XIII consists of a total of 61 points and the measurements have been taken since 1997. In the case of line XV–XV, the measurements have been regularly carried out since 2011. Some points along line XIII–XIII, situated at spacings of 20–200 m from the transmission pylons, were used in this study (Fig. 1).

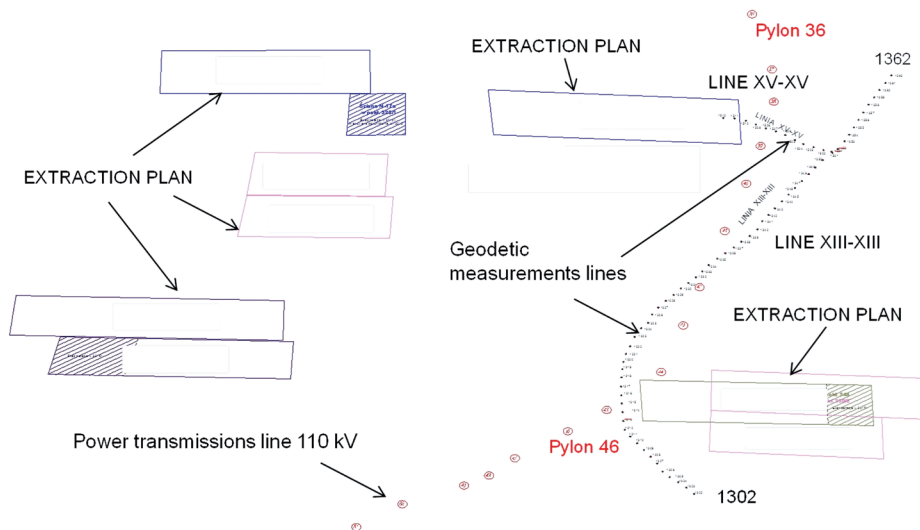


Fig. 1. Location of the power transmission line, measurements geodesic lines and the extraction plan to the year 2018

The measurement results indicate that there is a mining-induced surface subsidence in the range 3.0–6.0 m (Fig. 2, 3), depending upon which point was taken as the point of reference. A detailed analysis of the land survey point of reference proves that some transmission pylons subsided by as much as 4.0–5.0 m – this was a change which was not uniform over time and caused uneven subsidence of the pylons, i.e. their inclination from the vertical plane.

The observation study shows that the ground movements and varied direction of the strains (compressive and tensile) caused ground weakness i.e. discontinuous deformations. Mining induced changes occurring in the surface resulted in: changes of distances between the transmission pylon footings; the occurrence of cracks in spread footings; damage to reinforcement in transmission pylon footings; increase or decrease of the sag of overhead electrical conductors.

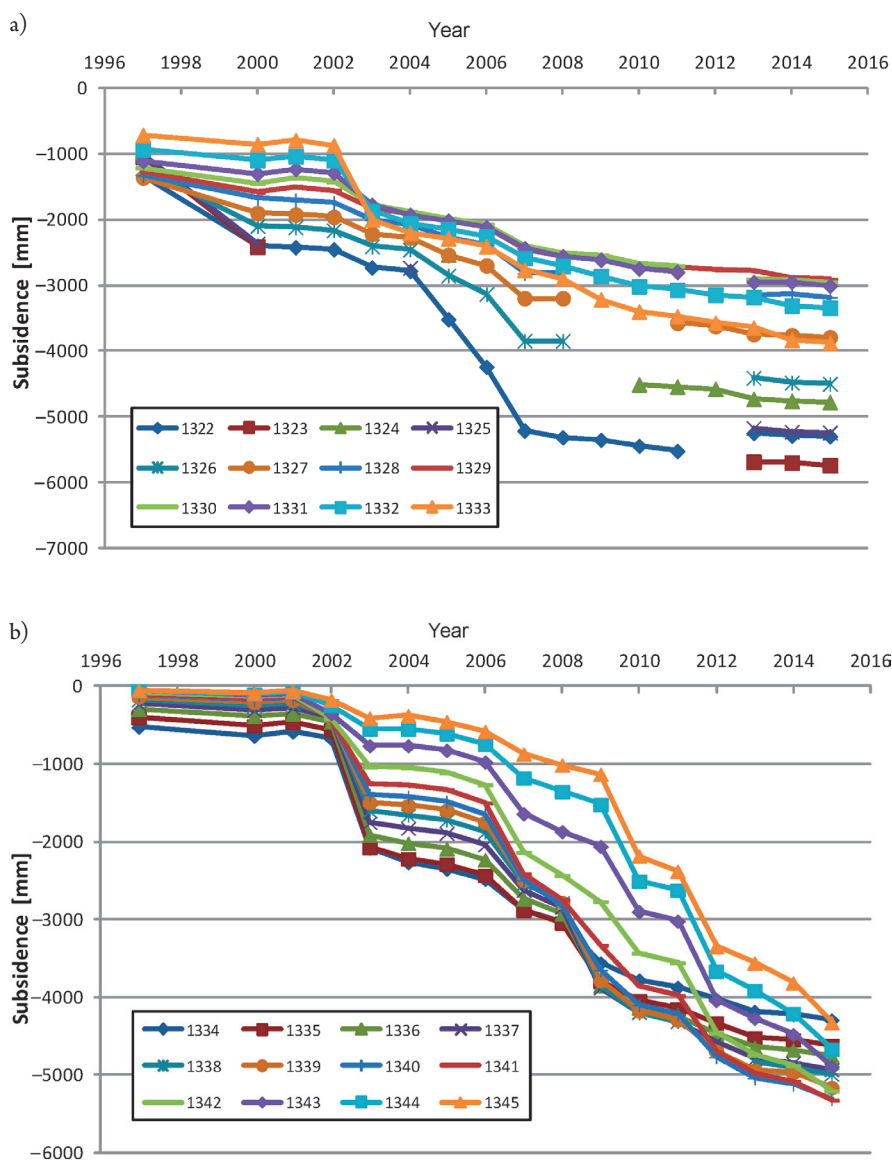


Fig. 2. Subsidence of selected points in measurement line XIII – XIII: a) for points 1322–1338; b) for points 1334–1345

As part of the observation study of the power line, measurements of transmission pylon inclinations were also carried out. According to the standards PN-84/B-03205 [9], horizontal deflection of the transmission pylon peak is $H/50$ where H is the height of the pylon ($\text{tg}\alpha = 0.02$). The latest standards [10] individually determined the permissible inclinations of pylons in the mining area. For these conditions the inclination $\text{tg}\alpha = 0.015$ for pylons was treated by electric power transmission's company owner power line as secure.

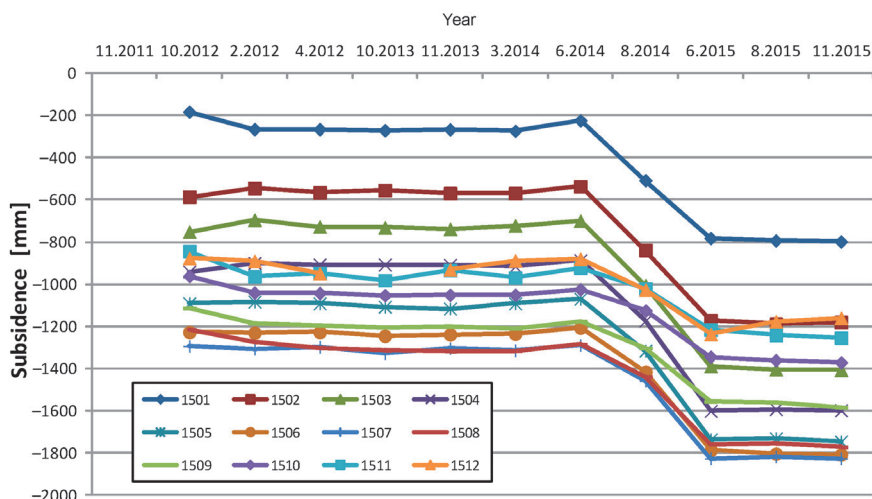


Fig. 3. Subsidence of points in measurement line XV–XV

Due to the varied height of each of the transmission pylons, a different value of displacement the top of pylons from the vertical axis was assumed for each of them. The results of measurements displacements of the tops of the pylons is shown in Table 1. In the year 2015, only transmission pylon no. 38 had exceeded the permissible value of inclination. It was subject to corrective action.

Analysis of measurements from the last 10 years indicates that over time, there are both increases and decreases in the inclination of the transmission pylons – this is related to the intensiveness of the exploitation of the mining areas (Fig. 4). Large decreases in pylon inclination are related to works to restore them to the vertical (e.g. transmission pylon no. 45), and in the case of transmission pylon no. 39, this was due to its total replacement.

Table 1. The results of the inclination measurements in 2015

No.	Pylon number	Height of the pylon [m]	Displacement of the top of the pylon [mm]	Inclination $\text{tg}\alpha$
1	37	23.40	178	0.0076
2	38	19.10	371	0.0194
3	39	40.53	126	0.0031
4	40	26.60	220	0.0083
5	41	25.10	370	0.0147
6	42	26.30	321	0.0122
7	43	23.60	66	0.0028
8	44	22.15	52	0.0024
9	45	26.20	54	0.0021
10	46	21.25	300	0.0141

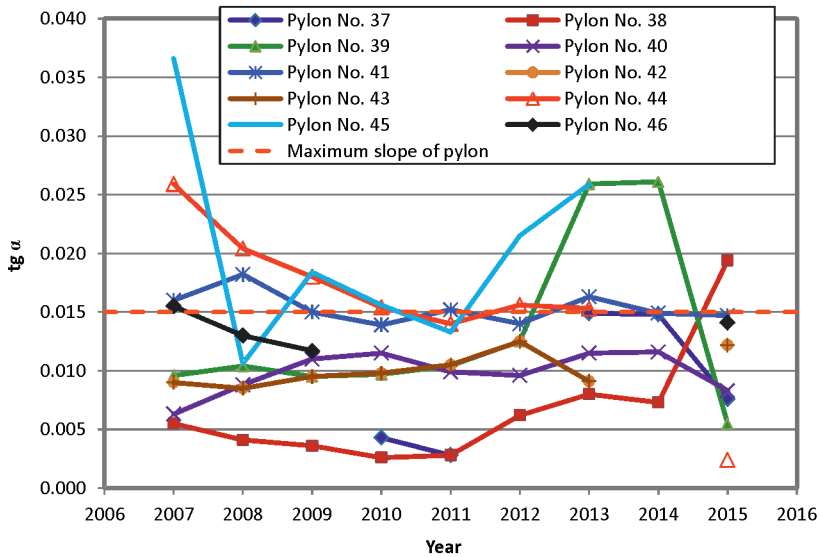


Fig. 4. Change of transmission pylon inclination over time

3. Prediction of the influence of the planned exploitation on the power line

In relation to the planned exploitation in the years 2015–2018, prognostic calculations of surface deformation in the area of the analysed power line were carried out. The day of the last measurements of pylon inclination was assumed as the beginning of the calculation period. The calculations of deformation indices were based on Budryk-Knothe theory [6].

A clockwise coordinate system to describe mining subsidence was adopted (Fig. 5):

- ▶ coordinate system $\xi\eta$ for the extracting area;
- ▶ coordinate system xy for the surface point $P(x, y)$.

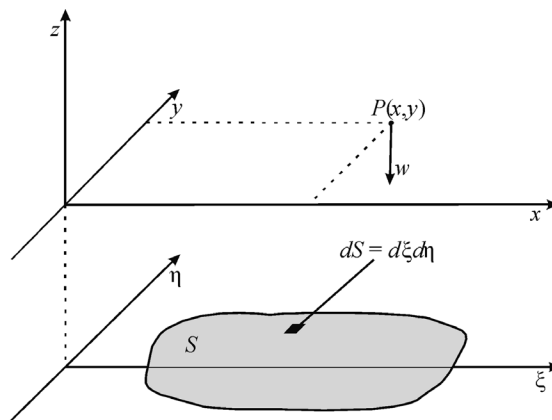


Fig. 5. Coordinate systems used to describe mining subsidence

Maths formulas for subsidence and surface tilt are follows:

► surface subsidence:

$$w(x, y) = \frac{w_{\max}}{r^2} \iint_S \exp \left[-\frac{\pi}{r^2} [(\xi - x)^2 + (\eta - y)^2] \right] dS \quad (1)$$

► surface tilt:

$$T_x = \frac{\partial w(x, y)}{\partial x} \quad T_y = \frac{\partial w(x, y)}{\partial y} \quad (2)$$

$$T_\alpha = T_x \cos \alpha + T_y \sin \alpha \quad T_\alpha = T_x \cos \alpha + T_y \sin \alpha \quad (3)$$

where:

- $w(x, y)$ – surface subsidence in the point P , m;
- w_{\max} – maximum surface subsidence, $w_{\max} = a \cdot g$, m;
- a – subsidence factor depending from backfilling system, $a = 0.2 \div 0.9$,
- g – seam thickness, m;
- r – the radius of the zone of mining influence on surface, $r = H \cdot \text{ctg} \beta$, m;
- H – seam depth, m;
- β – angle of draw, °;
- S – extracting area, m²;
- ξ, λ – coordinates for the extracting area dS , m;
- x, y – coordinates for the points in the surface, m;
- T_x, T_y – surface tilt in directions x and y , mm/m;
- T_α – surface tilt in directions α , mm/m;
- α – angle between x direction and object line (eg. power line), °.

The parameters of the model assumed for the calculations and specified below refer to the history of the coal mine: tangent of the angle of influence range in Knothe theory – $\text{tg} \beta = 2.0$; subsidence factor dependent from backfilling system $a = 0.75$; the coefficient of proportionality between the vertical and horizontal deformation indices – $B = 0.40$.

Prognostic calculations indicate that the increase of deformation indices for the target situation will assume the highest value in the area of transmission pylons marked as 38, 39 and 44. In the immediate vicinity of pylon no. 44, the subsidence will reach approx. 0.7 m (Fig. 6), whereas in the area of the pylons nos. 38–40, 43 and 45, the surface subsidence will range between 0.2 and 0.5 m. Additionally, at a distance of approx. 500 m east from transmission pylon no. 44, the predicted subsidence slightly exceeds a value of 3.0 m.

All of the above should be reviewed with two flights to take account of wind load. The highest level of accuracy currently available is about 1.5 cm – this is sufficient for this purpose.

Surface tilt seems to be a crucial parameter from the perspective of transmission pylon safety. The prognostic calculations clearly indicate that the tilt will reach around 3.0–3.5 mm/m in the area of pylon no. 44, whereas in the case of the remaining pylons, the tilt should not exceed 2.5 mm/m (Fig. 7). The maximum value of this parameter is much higher and slightly exceeds the value of 10 mm/m.

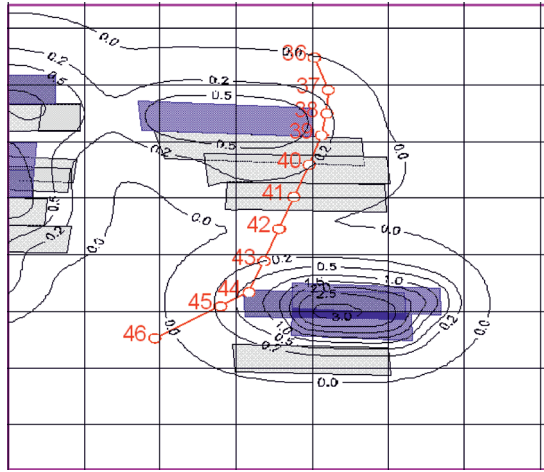


Fig. 6. Target increase of surface subsidence for the mining exploitation planned for the years 2015–2018

The prognostic calculations also indicate that the mining-induced increase of surface deformation in the period 2015–2018 will result in the increase of deformation indices in the area of the 110 kV high-voltage power line, especially in the vicinity of transmission pylons nos. 43–45 and, to a far lower degree, in the vicinity of pylons nos. 38–40. Hence, the mining exploitation will negatively affect their technical status as it will cause changes in the tension of the overhead transmission lines and, thus, increases in the inclinations of the transmission pylons.

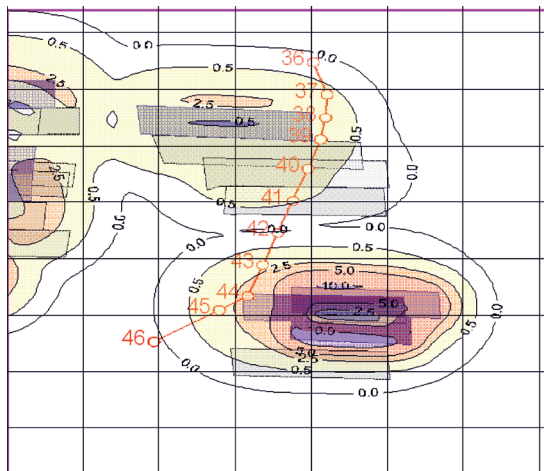


Fig. 7. Target increase of surface tilt for the mining exploitation planned for the years 2015–2018

In order to precisely predict the potential changes likely to occur around the transmission pylons of the analysed electric power line, prognostic calculations of surface deformation indices were carried out for the coordinates of the pylons' centres. This enabled the obtaining

of information on the influence of the predicted direction of tilt on the inclination of particular transmission pylons. Depending on the location of the planned exploitation, it may cause either an increase or decrease of the hitherto recorded inclination.

With reference to the measurement results of the inclination of particular transmission pylons of the analysed 110 kV high-voltage power line, as well as on the basis of the calculations of the predicted increase of surface tilt, deformation and subsidence, it can be argued that as a result of the planned mining exploitation in the years 2015-2018, particular pylons are very likely to be affected by the changes specified in Table 2.

Table 2. Predicted changes of inclination of transmission pylons for the mining exploitation planned for the years 2015–2018

No.	Pylon number	Current pylon inclination ¹⁾ tga	Predicted pylon inclination ¹⁾ tga
1	37	0.0076	0.0085
2	38	0.0194	0.0201
3	39	0.0031	0.0047
4	40	0.0083	0.0091
5	41	0.0147	0.0146
6	42	0.0122	0.0122
7	43	0.0028	0.0019
8	44	0.0024	0.0052
9	45	0.0021	0.0037
10	46	0.0141	0.0141

¹⁾ boundary inclination of transmission pylons $tga > 0.015$

In summary, the highest increase of inclination, also assuming their direction, are predicted for transmission lines nos. 38–40 and 43–45. Locally, a decrease of pylon inclination is expected relative to the existing inclination (pylon nos. 41 & 43). However, it is worth noting the fact that during the last measurement in September 2015, measurements that seriously exceeded the acceptable value of inclination were recorded for pylon no. 38; there were also values close to the critical point of inclination for pylons nos. 41 and 46. In those cases, it was absolutely necessary to employ some safety measures.

4. Preventive measures and repairs to electric power line

The prognostic calculations indicated that mining with roof caving planned in the area of the power line will cause the occurrence of further impacts on the terrain surface, such as the increase of surface subsidence and the appearance of additional increased horizontal deformation and surface tilt. Therefore, the powerline operator may expect that there will be a necessity to undertake additional repairs and servicing work. Such activities may embrace the need to reinforce the transmission pylon foundations, as well as the correction of the overhead cable tensioning.



Although the norm PN-E-05100-1:1998 [10] specifies instructions and recommendations for designing power lines in mining damage areas, in the case of large-scale deformations, engineers should, however, take into account the potential risk of exceeding the acceptable cable tensioning in power line conductors or increasing their sag to an extent that causes potentially dangerous proximity of electric conductors to ground level or other structures.

According to current regulations, the values of acceptable transmission pylon inclination are as follows:

- ▶ deviation from the vertical of the transmission pylon peak, standing without conductors, is $H/300$ (H – height of construction according to the standard BN-90/9056-01 [3]),
- ▶ exploitation-induced horizontal deflection of the transmission pylon peak is $H/70$ ($\text{tg}\alpha = 0.0143$ – according to the norm PN-84/B-03205 [9]).

Horizontal displacement and surface tilt in the locations of transmission pylon foundations are the factors causing marked changes in span length in calculations of tension. In the case of power lines with long spans running through a flat area, span length change caused by the pylon's subsidence may be ignored due to the relatively insignificant values of subsidence in relation to the powerline length. In addition, a dip, where particular transmission pylon foundations are erected, also usually causes subsidence of other objects in the immediate vicinity, hence the fact that there is a relatively low risk of a material proximity issue for power line conductors with respect to the ground or to other objects; furthermore, the potential increase of the sag of conductors seems unlikely to exceed the predicted buffer associated with the vertical distances. Free-hanging electric power conductors form the so-called catenary described by the hyperbolic function. Mining exploitation design takes into consideration the impact of mining-induced surface deformation on the functioning of electric power lines. The calculations suggest that for power lines running through areas of mining damage, one may expect levels of acceptable tensioning of powerline conductors to be exceeded or the excess of acceptable limits with regard to the inclination of transmission pylons. In the analysed case, the predicted horizontal displacement in the area of the observed transmission pylons did not exceed 0.3 m. Such factors as the elastic strain of pylons or their elements and the inclination of isolators may help mitigate the influence of span length changes on the tension of the power line conductors; however, analytical (quantitative) determination of the influence is difficult. The measurements of the sag of conductors and the inclination of transmission pylons should be periodically verified with *in situ* measurements in order to define proper preventive measures against power line damage.

Table 3 presents measurement results obtained before the planned mining exploitation in the years 2015–2018. The analysis proves that the measured sag of electric conductors is usually larger than the theoretical sag; only between the transmission pylons nos. 37–38 and 38–39, is it smaller. The above indicates irregular tension stringing in electric conductors, as well as the irregular load of steel structure pylons especially in the case of pylons nos. 39 and 38.

Table 3. Results of calculations and measurements of the sag of conductors between the transmission pylons of the high-voltage power line (110 kV)

No.	Pylon number	Pylon span length [m]	Theoretical tension of working conductors [MPa]	Sag of conductors (theoretical) [m]	Sag of conductors (measured) [m]	Distance of working conductor from ground surface [m]
1	37–38	216.1	73.6	4.1	3.4	10.7
2	38–39	180.0	73.6	2.8	1.1	13.6
3	39–40	310.6	73.6	8.4	10.1	10.6
4	40–41	298.9	73.6	7.8	8.5	8.9
5	41–42	299.1	73.6	7.8	8.6	9.8
6	42–43	303.2	73.6	8.0	8.8	9.3
7	43–44	290.7	73.6	7.3	8.2	8.9
8	44–45	223.9	73.6	4.4	6.1	10.4

The above-mentioned changes of the terrain surface, as well as their impact on the foundations and construction of transmission pylons and the sag of electric conductors made it necessary to carry out the following repair works:

- ▶ application of additional leg bracing of transmission pylons (Fig. 8a);
- ▶ application of bracing with the possibility of restoring the pylon to the vertical (Fig. 8b);
- ▶ replacement of old transmission pylons (Fig. 8c);
- ▶ regulation of tension stringing of powerline conductors (Fig. 8d).

Protecting the pylons against mining-induced deformation is achieved in the following way:

- ▶ a horizontal system of conductors suspended on transmission pylons is recommended in areas subject to mining influences;
- ▶ in the third or higher category areas, constructions with tall pylons adjusted to take account of the appropriate monolithic foundation technology, are recommended;
- ▶ in the first and second category areas, transmission pylons with narrow constructions, adjusted to cooperate with a monolithic foundation, are recommended. It is also possible to use pylons with broad bodies adjusted to cooperate with the working elements. In second category areas, it is recommended to protect the transmission pylon members against deformation by using frame bracing;
- ▶ for considerable horizontal surface displacement, it is necessary to apply a bracing system made of steel sections at the level of the transmission pylon legs; the connection between the frame and the foundation is made with the use of foundation steel braces; the diagonals between the foundations are additionally reinforced to avoid changes in the position of particular fundamental elements; the foundations can also be strengthened with reinforced concrete structures;
- ▶ it is recommended to design the connection of the transmission pylon body with the bolts in such a way that it allows for the restoration of the pylon to the vertical in situation where its inclination exceeds the allowed displacement assumed in the project.



Fig. 8. Examples of repairs of electric power line: a) bracing of the pylon leg, b) bracing of the leg with the possibility of restoring the pylon to the vertical; c) total replacement of the transmission pylon and its foundations; d) regulation of tension stringing of electric conductors

In the case of the inclination of pylons beyond acceptable levels as a result of mining exploitation, the following repair methods are applied depending on the type of transmission pylons and the extent of inclination:

- ▶ restoring the transmission pylon to the vertical (allowing for a safe usage of the construction) and fixing the bracing frame (if it was not used earlier);
- ▶ restoring the pylon to the vertical by means of steel spacer plates inserted between the curbs of the pylon head and the foundation bolt; the thickness of spacers depends upon the degree and direction of the transmission pylon's inclination from the vertical and the spacing of the bolts;
- ▶ restoring the transmission pylon to the vertical and replacement of all deformed elements of the construction;
- ▶ cutting out the ground under the foundation (only in exceptional situations);
- ▶ rebuilding the whole transmission pylon if its repair proves impossible.

5. Conclusions

The study indicates that such line object as electric power lines, especially high-voltage power lines, may be subject to negative impact of underground exploitation, hence such objects should be regularly monitored (with drone flights) in order to precisely identify all changes affecting their structure. In the case of planned exploitation, it seems absolutely necessary to carry out prognostic calculations of surface deformation and the evaluation of its impact on a particular transmission pylon. Such activities will allow for planning possible repair works in advance, and in extreme cases, they will help to avoid serious failures. The following detailed conclusions can be made on the basis of the analysed case:

- ▶ mining activities affecting the analysed fragment of electric power line, classified as third category, are of resistance to mining impact, were carried out in more than a dozen seams over a period of 30 years; the values of surface subsidence measured in the analysed area during the last 20 years ranged between approx. 5.0 and 6.0 m;
- ▶ the last measurements of the inclination of transmission pylons nos. 37–46 indicate that the excessive values of inclination (i.e. $\text{tg}\alpha$ above 0.015) occur in pylon no. 38 and amount to 0.0194; in pylons nos. 41, 42 and 46, the values assume the acceptable values ($\text{tg}\alpha = 0.0122\text{--}0.0147$);
- ▶ prognostic calculations of surface deformation indices in place of the erection of the transmission pylons indicate that the subsidence may as a maximum reach 0.7 m in the area of pylon no. 44, whereas the surface tilt in this place may increase by 2–3 mm/m; slightly lower values of deformation indices will occur in the area of pylons nos. 38–40, 43 and 45;
- ▶ the inventory showed that the condition of transmission pylons and their foundations was relatively good. There are some symptoms of corrosion of both the steel and reinforced concrete elements. In addition, the damage to bracing was observed at the level the leg of pylon no. 38. Additionally, irregular cable tensioning between particular pylons is noticeable;
- ▶ in order to continue with the safe exploitation of the electric power line in the analysed area, it seems necessary to carry out continuous regular observations focusing on the inclination of transmission pylons; in the case of several pylons, it is necessary to restore them to the vertical or to regulate their cable tensioning.

References

- [1] Ajdukiewicz A., Bról J., Górski M., Krzywoń R., Szojda L., *Stany awaryjne elektroenergetycznych linii przesyłowych na terenach górniczych*, XIX Konferencja Naukowo-Techniczna, Szczecin–Międzyzdroje, 19–22 maja 1999. *Referaty. T. 1*, Politechnika Szczecińska, 1999, 31–38.
- [2] Ajdukiewicz A., Szojda L., *Zagrożenia i zabezpieczenia słupów elektroenergetycznych linii przesyłowych w warunkach deformacji podłoża*, XXIV Konferencja Naukowo-Techniczna „Awary budowlane” Szczecin–Międzyzdroje 2009, 17–28.

- [3] BN-90/9056-01 Elektroenergetyczne stalowe konstrukcje wsporcze. Wymagania i badania.
- [4] Gawor P., *Prognozowanie naprężeń w przewodach linii elektroenergetycznych napowietrznych na terenach objętych uszkodzami górnictwymi*, Mechanizacja i Automatykacja Górnictwa, nr 7, 2010, 94–99.
- [5] Guanglin Y., Qianjin S., Yunfei Z., Liu T., Guoan X., *Model experiment on anti-deformation performance of a self-supporting transmission tower in a subsidence area*, International Journal of Mining Science and Technology, Vol. 22, Issue 1, 2012, 57–61.
- [6] Knothe S., *Prognozowanie wpływów eksploatacji górnictwowej*, Wydawnictwo Śląsk, 1984.
- [7] Kratzsch H., *Mining subsidence engineering*, Springer-Verlag, Berlin 1983.
- [8] Kwiatek J., *Obiekty budowlane na terenach górnictwowych*, Główny Instytut Górnictwa, 2007.
- [9] PN-84/B-03205 Elektroenergetyczne linie napowietrzne. Stalowe konstrukcje wsporcze. Obliczenia statyczne i projektowe.
- [10] PN-E-05100-1:1998 Elektroenergetyczne linie napowietrzne – Projektowanie i budowa – Linie prądu przemiennego z przewodami roboczymi gołymi.
- [11] PN-EN 50341-1:2005/A1:2009 Elektroenergetyczne linie napowietrzne prądu przemiennego powyżej 45 kV. Część 1: Wymagania ogólne. Specyfikacje wspólne.
- [12] PN-EN 50341-3:2005/AC:2009 Elektroenergetyczne linie napowietrzne prądu przemiennego powyżej 45 kV. Część 3: Zbiór normatywnych warunków krajowych.
- [13] PN-EN 50341-3-22:2010P Elektroenergetyczne linie napowietrzne prądu przemiennego powyżej 45 kV. Część 3: Zbiór normatywnych warunków krajowych.
- [14] Popiołek E., *Ochrona terenów górnictwowych*, Wydawnictwa AGH, 2009.
- [15] Strzałka J., *Czasookresy badań eksploatacyjnych instalacji i urządzeń elektrycznych*, Biuletyn Techniczny nr 19, Stowarzyszenie Elektryków Polskich – Oddział Krakowski, 2003, 9–12.



Grzegorz Świt

Anna Adamczak (aadamczak@tu.kielce.pl)

Department of Strength of Materials and Concrete and Bridge Structures,
Faculty of Civil Engineering and Architecture, Kielce University of Technology

STRESS CORROSION OF EPOXY-GLASS COMPOSITES MONITORED USING ACOUSTIC EMISSION

KOROZJA NAPRĘŻENIOWA W KOMPOZYTACH EPOKSYDOWO-SZKLANYCH MONITOROWANA Z ZASTOSOWANIEM EMISJI AKUSTYCZNEJ

Abstract

In the building industry, polymeric matrix composites filled with glass, carbon, graphite, polypropylene, or Kevlar filaments are commonly used. However, it is notable that the wider use of composites is limited by a lack of sound knowledge regarding their properties their responses to exposure to various environments. In this respect, the alkaline and acid environments may have a significant influence on the response of epoxy-glass composites which are most commonly in use. They may undergo stress corrosion and the resulting cracks reduce the strength of the composite. Within this work, a method based on acoustic emission measurement is devised which allows the determination of the beginning of cracking and of the intensity of the corrosive cracking of filaments in a loaded composite. This is substantial in terms of the diagnosing of the functioning structures.

Keywords: monitoring, acoustic emission, stress corrosion, epoxy-glass composites, destructive processes

Streszczenie

W budownictwie najczęściej używane są kompozyty z matrycą polimerową wypełnioną włóknami szklanymi, węglowymi, grafitowymi, polipropylenowymi oraz kevlarowymi. Szersze zastosowanie tych materiałów jest jednak ograniczone ze względu na brak dokładnej wiedzy o ich właściwościach i zachowaniu w różnych warunkach ekspozycji i pod różnym typem obciążenia. W literaturze powszechnie istnieje opinia, że kompozyty włókniste na bazie żywic polimerowych są odporne na działanie środowiska zasadowego i kwasowego, co w przypadku uwzględnienia obciążenia tych kompozytów nie jest prawdą. Kompozyty te w wyniku obciążenia mogą ulegać korozji naprężeniowej lub erozji, co powoduje zmniejszenie ich wytrzymałości, a w konsekwencji pękanie. Stosując metodę emisji akustycznej, istnieje możliwość wykrywania i śledzenia procesów korozyjnych w kompozytach na bazie żywic epoksydowych i włókien szklanych, co jest niezwykle ważne dla bezpieczeństwa użytkowanych konstrukcji.

Słowa kluczowe: monitoring, emisja akustyczna, korozja naprężeniowa, kompozyty polimerowo-szklane, procesy niszczące

1. Introduction

Composites reinforced with continuous fibres have been used for many years in aviation, the armaments industry and sports equipment manufacturing. Over the last decade, the use of composite materials has grown considerably in the building industry, both as strengthening materials and as self-contained structural elements. This trend has now intensely developed in many countries all over the world [1–6].

In the building industry, composites using a polymeric matrix (epoxy resin, polyester resin, phenol resin) are most commonly filled with glass, carbon, graphite, polypropylene, or Kevlar filaments [7–11]. However, it is noted that the wider use of composites is limited by a lack of sound knowledge regarding their properties and their responses to exposure to various environments [9, 11–13].

In general, the selection of an adequate set of characteristics of a composite depends on the prevailing operating conditions and strength requirements. Consequently, it is considered to be of major practical importance to obtain knowledge on the long term performance of composites under a continuous mechanical load exposed to an aggressive environment [5–9].

In the above context, alkaline and acid environments may have a significant influence on the response of epoxy-glass composites which are most commonly in use. They may undergo stress corrosion and the resulting cracks would reduce the strength of the composite [13–17]. Insufficient information about the stress corrosion of such fibres in various chemically active environments is an obstacle to the widespread use of glass fibre composites in the building industry [17–20].

Because of the use of composites in construction, mechanical properties which predominantly depend upon the type and quantities of fibres, the manner of reinforcement, the type and properties of the matrix, the methods of formation and the conditions of hardening are the most important [21–25]. The Young's modules of organic composites with glass fibres is not very high due to the low rigidity of both fibres and resins. In each type of reinforcement, the strength can change depending upon the relative volumetric quantity of fibres.

Because of the following uses of composite materials, it is quite important to know whether or not their volume is substantially changed as a result of stress corrosion. [2–6, 12, 17]:

- ▶ as new structural elements;
- ▶ in the repairing of elements damaged during use;
- ▶ in reinforced elements of building structures the load capacity of which should be increased due to larger loads at exploitation.

This knowledge is especially important because in the materials commercially available, there is always a fibre content threshold, above which the strength drops because of an excessive amount of pores, the bond between the fibres and the matrix being too weak, the non-wetting of some fibres, and other technological defects. The degree of defectiveness of a product is most dependent upon the methods of formation; therefore, for each type of reinforcement, different strengths of products may be obtained.

In composites reinforced one-directionally, their tensile strength mostly depends on the fibres, while bending strength, crushing strength, shear strength and crack resistance of composites of various types of reinforcement predominantly depends upon properties of the resins [2, 4–6].

2. The impact of tensile corrosion on the change of the susceptibility of epoxy-glass composites

Results of microscopic observation (performed by the authors) of the corrosive cracking of a polymeric composite reinforced with parallel laid glass fibres under uniaxial tension in a solution of calcium hydroxide $\text{Ca}(\text{OH})_2$ with pH ranging from 8 to 12 and in regular hydrochloric acid HCl are presented in Figs. 1–5.

A high load causes cracking of the matrix (perpendicular to the direction of the reinforcement), which consequently eases penetration of the corrosive solution into the composite (Fig. 1), or the crushing of the resin and the exposing of the surface of the fibres. Both phenomena cause a loss of protection of the fibres provided by the matrix. As part of this research, a method was worked out allowing for the determination of the beginning of cracking and the intensity of corrosive cracking of filaments in a loaded composite [17]. This is substantial in terms of the diagnosis of the functioning structures.

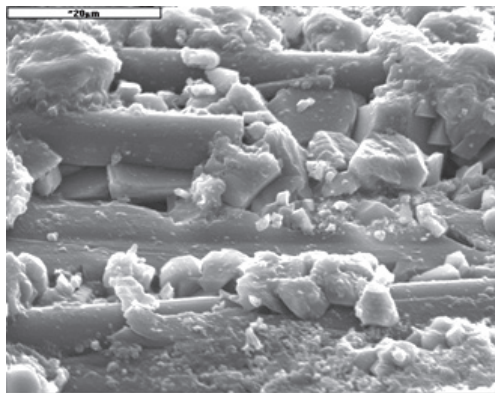


Fig. 1. Cracks of the resin due to high load

As more and more fibres get exposed due to the breaking of the matrix, a process of the penetration of a corrosive environment into the material begins – this leads to the expansion of cracking perpendicular to the reinforcement (Fig. 2), thus breaking its continuity.

As a result of the penetration of an alkali into the cross-section of a composite, the fibres which form reinforcement undergo a gradual degradation and ultimately break due to stress corrosion [16]. Fig. 3 presents the surface of a crack of a composite resulting from load and the concentration of $\text{Ca}(\text{OH})_2$ at about pH12 in the composite (glass fibres – epoxy resin).

Sedimentation which appears on the surface of broken fibres, as mentioned before, is probably the product of the reaction of the alkali with the silicon contained in the fibres.

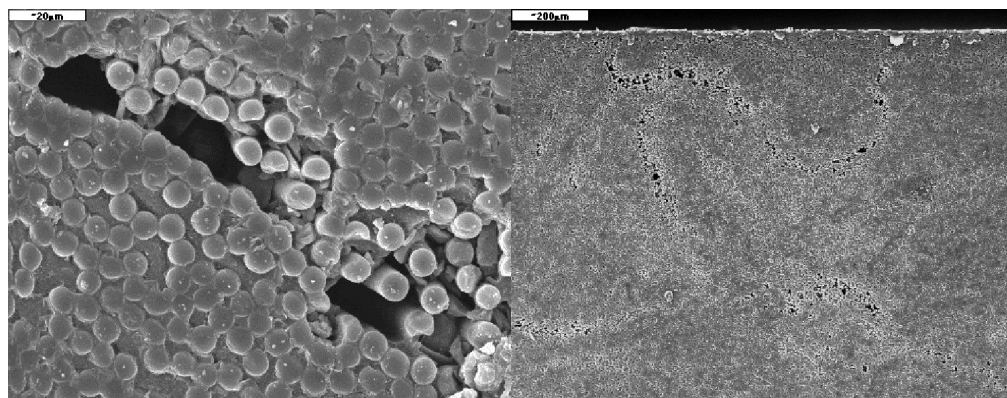


Fig. 2. The depth cracks resulting from further penetration of the solution into a composite

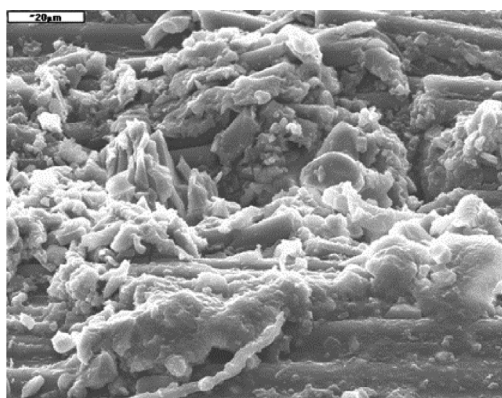


Fig. 3. Surface of composite cracks

The magnified element with oblique cracks shows that there are pits which appeared as a result of the corrosion of fibres and of the breaking of the resin. These pits form extensive and deep cavities on the surface of the reinforcement, corresponding with the manner of destruction of individual fibres as discussed above.

The degree of concentration of the solution and the load level can either speed up or slow down the process of corrosive cracking.

The image across the surface of the tested composite (Fig. 4) shows that the hydrochloric acid (HCl) caused the occurrence of a large number of corrosion pits on the surface of the fibres; furthermore, separation between the fibres and the matrix is visible – this enables penetration of the solution into the composite. The superficial corrosion of fibres occurs most commonly where the matrix and the fibres are joined. In the place where the resin is cracked, hydrochloric acid HCl causes the occurrence of substantial cavities on the surface of the fibres.

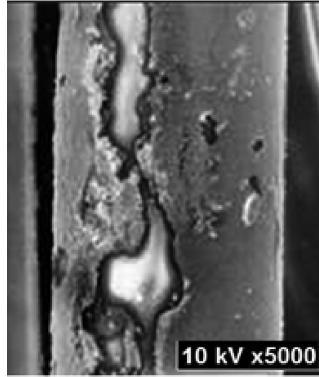


Fig. 4. Magnified section of fibres with corrosion damage

As has been observed, three damage mechanisms can occur during the corrosion:

- ▶ cracking of the resin;
- ▶ degradation of fibres;
- ▶ breaking of fibres.

Although the damage process can be observed microscopically, this can only be achieved in a laboratory environment; therefore, for the in situ testing of real structural elements, it is necessary to use other methods that are non-destructive in order to detect such processes.

In this paper, the acoustic emission (AE) method was applied to detect for the presence of corrosion stress.

3. Identification of AE signals generating during the corrosive cracking of an epoxy-glass composite

3.1. Preliminary tests results

The static test was carried out using the tensile testing machine presented in Fig. 5.

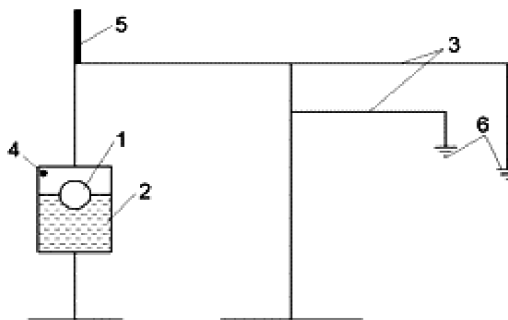


Fig. 5. Scheme of a tensile testing machine

It consists of a set of levers (3) of leverage x10 and x30, and a sample type NOL [26, 27] (1) immersed in a vessel containing solution $\text{Ca}(\text{OH})_2$ (2). On the surface of the sample a, broad-band sensor of acoustic emission (4) was secured, and a 'Peltron' sensor (5) was placed at the beginning of the lever arm to measure the elongation. The whole system was loaded with a set of weights (6).

Samples was ring-shaped with an internal diameter of 42.25 mm and a wall thickness of 5.5 mm with the share of fibres by volume $V_1 = 0.50$. The mean force destroying the composite was identified as $P_n = 10$ kN.

The Young's modulus for the sample was found to be $E_1 = 37$ GPa.

Preliminary acoustic tests were carried out for two levels of load equal to 0.5 and 0.7 of P_n for two concentrations of solution $\text{Ca}(\text{OH})_2$ – pH8 and pH12 – the results of these tests are presented in Figs. 6 & 7, where 'Δl' marks the displacement line and 'EA' marks the line showing the sum of acoustic events.

A sudden increase in the sum of events during the process of loading, accompanying the growth of displacement, is connected with the breaking of individual fibres of the composite and the growth of tensions in the tested sample. The diagrams show that the change of susceptibility is in this case, a discrete process and it occurs jerkily; this is characteristic of brittle materials.

If a change of elongation occurs in a steady manner, then the signal AE does not increase rapidly. It is observed that increases in both emission and displacement are connected.

It is seen that at 0.5 P_n , in the first stage of work of the composite, bearing the initial load, the growths of both signals and of displacement are continuous and linear. During the immersion in the solution, the process begins to progress in a jerky manner, although this is not particularly intense.

At a load level of 0.7 P_n , it appears that the process of growth of both displacement and AE is non-linear and non-continuous, and changes of recorded parameters are clearly visible.

It can be observed that by analysing the signal of acoustic emission, it is possible to assess the intensity of development of defects in composites as a result of the simultaneous influence of tension and a corrosive environment. Hence, the establishment of a special experimental program.

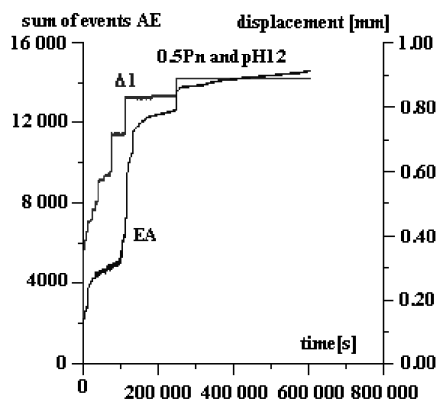


Fig. 6. The results of initial acoustic tests for load of 0.5 P_n and solution of $\text{Ca}(\text{OH})_2$ at pH 12

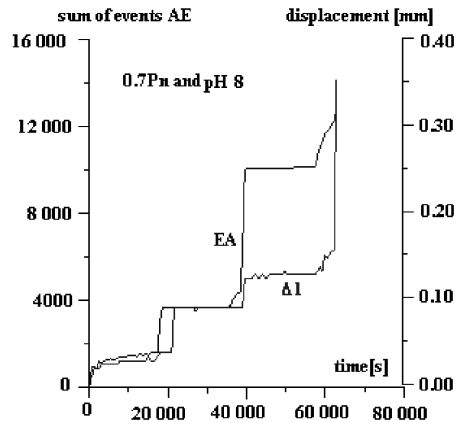


Fig. 7. The results of initial acoustic tests for load of $0.7 P_n$ and solution of $\text{Ca}(\text{OH})_2$ at pH 8

3.2. Experimental results

Experiments were performed on an epoxy-glass composite subjected to three-point bending in an alkaline environment. The test was carried out for constant displacement.

Polymeric composite bars reinforced with parallel running glass fibre in a solution of $\text{Ca}(\text{OH})_2$ and 3% NaCl of varying concentrations ranging from pH8 to pH12 – for reference purposes, testing was also carried out in normal hydrochloric acid (HCl). The composite bars had a matrix of epoxy resin and fibres of type ER-3005, the share of the fibre by volume was $V_f = 0.72$. The fibres were made of glass E (boro-alumino-silicate) containing under 1% of alkalis, with a tex value of 1200 g/km and nominal diameter of the elementary filament $\varnothing = 10 \mu\text{m}$, it was manufactured by Krosno Glassworks. The choice of both of the environment and the concentration of them results from the assumed conditions of operation of the strengthening concrete elements. The concentration of pH12 corresponds to the surface of non-corroded concrete, while pH8 to the surface of corroded concrete.

The tapes with dimensions $200 \times 6 \times 3.2 \text{ mm}$ were tested under simultaneous influence of corrosive environment and force as it is shown in Fig. 8.

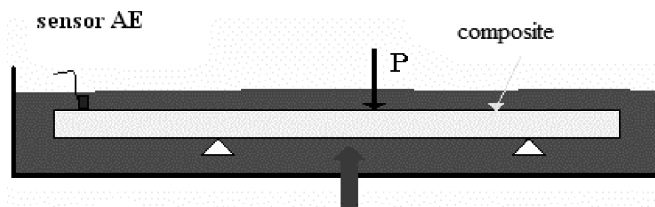


Fig. 8. Scheme of tests of composite bars

The process of corrosive cracking was recorded by a 'MISTRAS 2001' acoustic emission processor; acoustic emission signals were measured using broadband sensors of frequencies

from 100 to 1000 kHz and a resonance sensor of 55 kHz frequency. The measurements were carried out with the use of an amplitude filter in the range of 40 to 100 dB. The obtained signals were subjected to a Fourier transformation. At the same time, in order to assess the change of susceptibility of the tested samples, it was measured their elongation in the function of time under constant load. The measurement was made by 'PELTRON' sensors with a measurement range of 0 to 1 mm. The whole test was recorded in a computer using an analog-digital card.

During the test, such AE parameters as the sum of events, amplitude, duration and rise time in the function of time were recorded. Additionally, the AE waveform and wave spectrum were analysed.

Three types of waves occurring in sequence in the process of corrosive cracking in an alkaline environment $\text{Ca}(\text{OH})_2$ can be distinguished (Fig. 9–11).

Signals of type 'a' are the most common and include around 90% of all recorded acoustic signals; they are characterised by their short rise time and short duration. The spectrum of the signal does not exceed 1 MHz, and the amplitude is in the region of 45 dB. The signal reaches its highest value in the range of 200 to 250 kHz. It is assumed that such a signal is due to the breaking of the epoxy matrix of the composite.

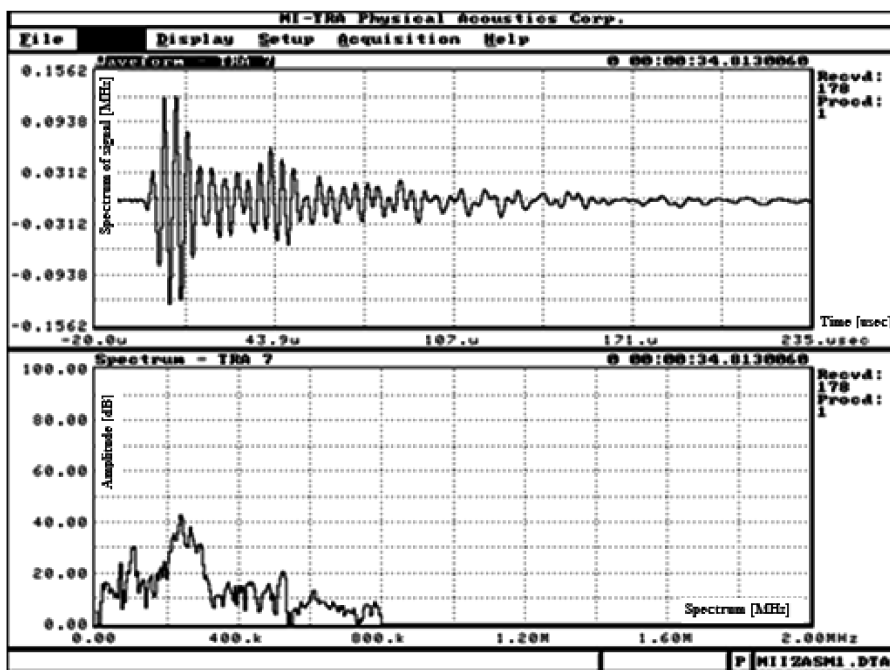


Fig. 9. The emission signal of type 'a'

A second type, signal 'b', is characterised by a higher amplitude reaching a level of 60dB and the spectrum of up to 1.2 MHz; it has a longer rise time and duration than type 'a' – this is probably due to the breaking of the fibres of the composite reinforcement as a result of corrosion– its spectrum does not drop linearly but has local peaks. Corrosion in an alkaline

environment does not occur rapidly, this is probably why the amplitude of the signal is so low. This type of signal accounts for around 5% of the registered signals.

The last 5% belong to the acoustic signal of type 'c' – this substantially differs from the two previous types of signal; it is characterised by a short rise time and long duration. The spectrum shows that the amplitude of the signals exceeds 60 dB and that they fill the entire spectrum. It can also be noticed that the signal reaches its maximum value in the range of 250–300 kHz. It is assumed that this type of signal occurs due to the breaking of fibres. This means that in the case of an alkaline environment, three damage mechanisms due to load corrosion observed microscopically can also be identified using the analysis of the acoustic emission signal. This means that in the case of an alkaline environment, three damage mechanisms due to load corrosion observed microscopically can also be identified using the analysis of the acoustic emission signal.

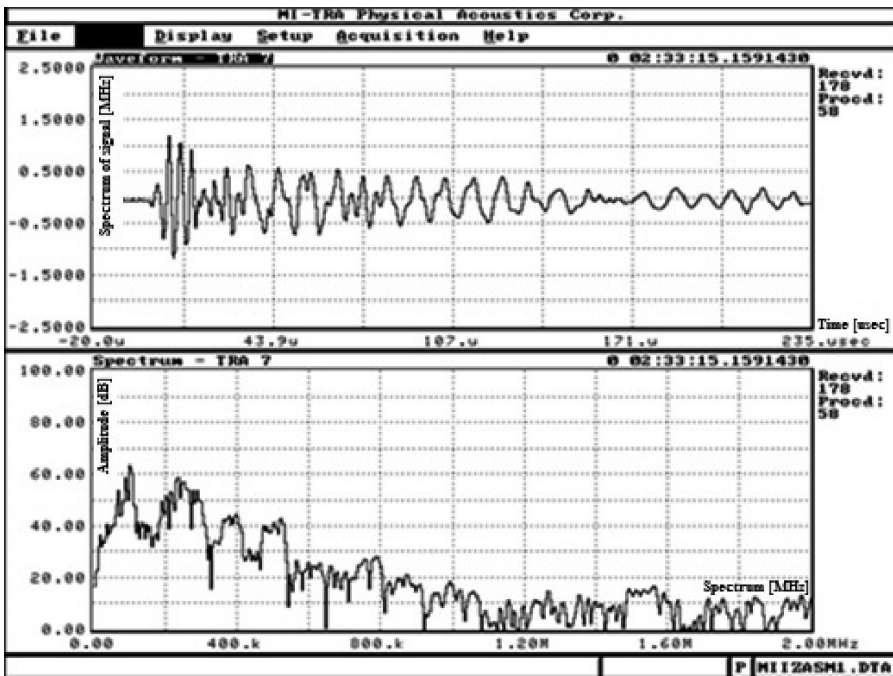


Fig. 10. The emission signal of type 'b'

The situation is not the same if the epoxy-glass composite is immersed in normal hydrochloric acid HCl. As a result of measurements of signals of acoustic emission in the process of the loading of a composite in acid, two types of signal were identified which appeared in the course of the experiment (Fig. 12, 13).

Signals of type 'd' are characterised by their low energy and short rise time, its spectrum is confined within the range of 100 kHz to 1 MHz, and the amplitude does not exceed a value of 45 dB. In the measurement file, signals of this type account for around 95%. It is similar to signal 'a' and is assumed to be due to the breaking of the epoxy matrix of the composite.

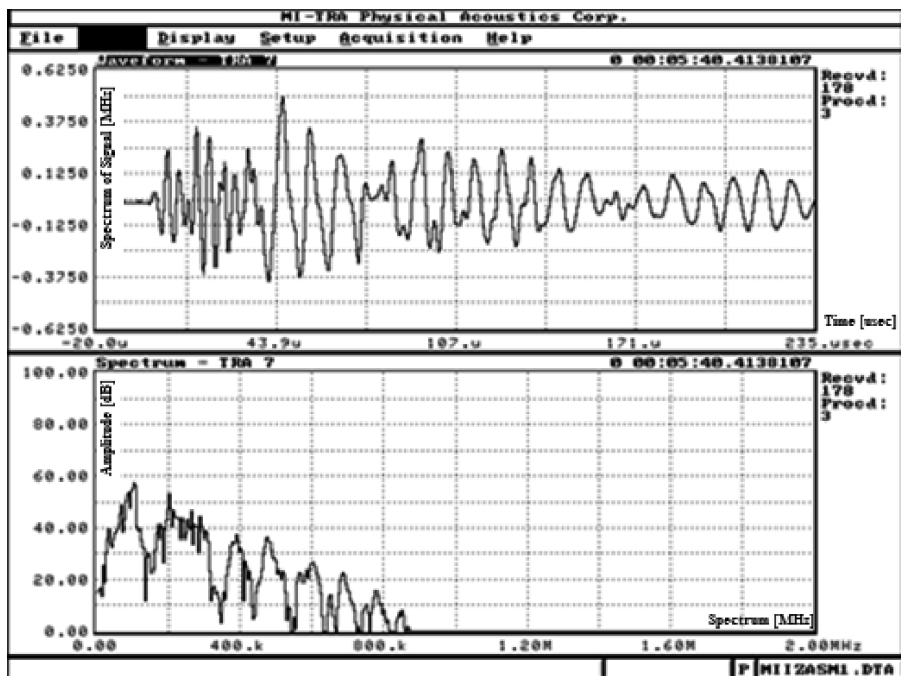


Fig. 11. The emission signal of type 'c'

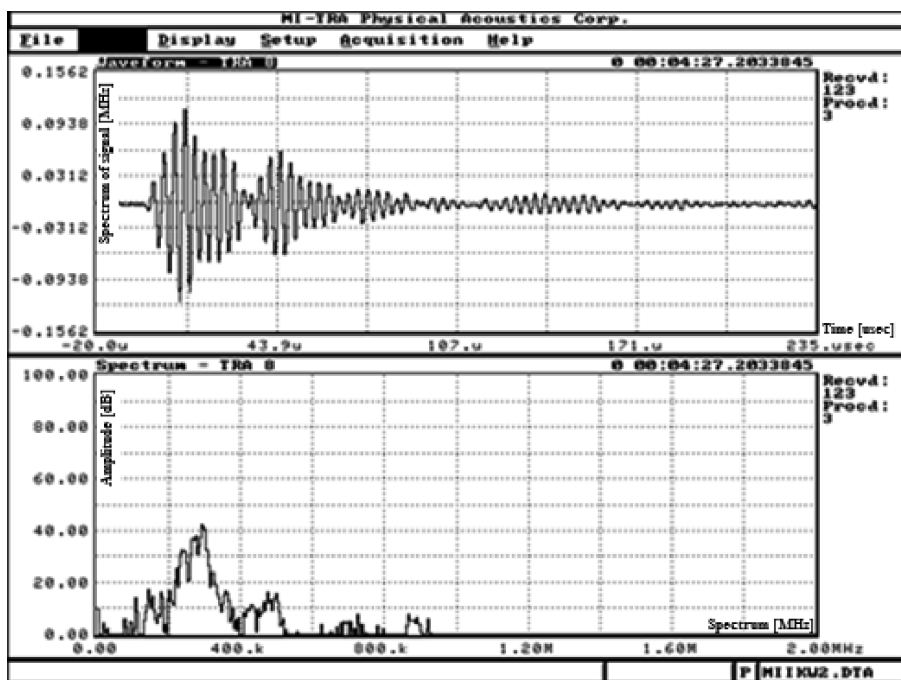


Fig. 12. The emission signal of type 'd'

Signals of type ‘e’ make only around 5%. They have very high energy, a short rise time and a short duration. They include the full spectrum in the range of 100 kHz to 2 MHz. Under such a load, stress corrosion ran quickly and rapidly [16]. It is assumed that the obtained type of signal is due to two mechanisms: fibre degradation and breaking of fibres resulting from the influence of the acid and the high load. Its peak, as with the case of breaking due to corrosion, occurred in the range of 250–300 kHz.

In the case of the acid environment, damage mechanisms occurring as a result of load corrosion observed microscopically can be identified using the analysis of the acoustic emission signal.

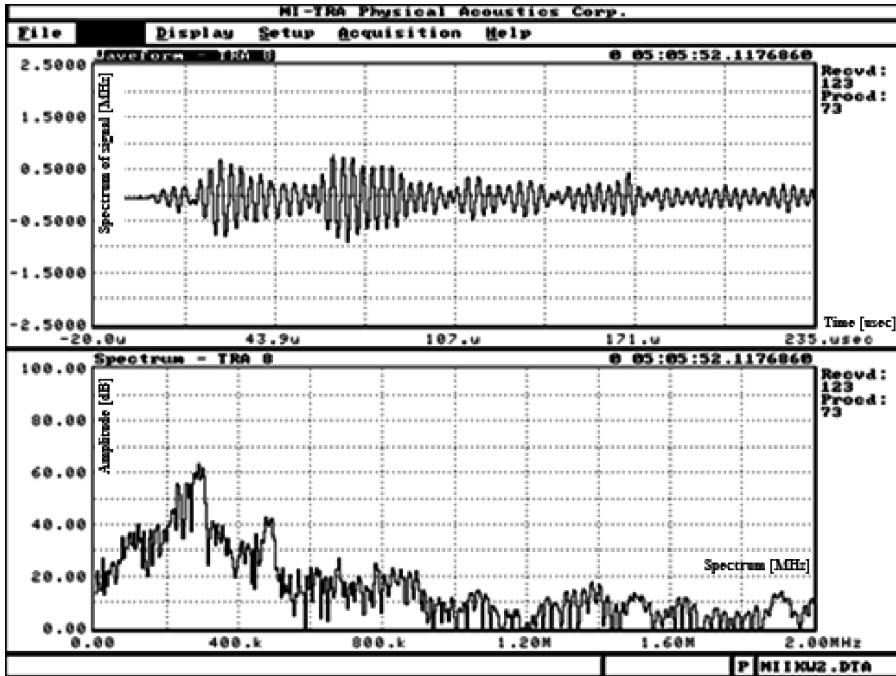


Fig. 13. The emission signal of type ‘e’

4. Conclusions and final remarks

On the basis of the obtained results and an analysis thereof, the following conclusions can be formulated:

- ▶ cracking of the reinforcement of a composite due to corrosion is influenced both by acidic and alkaline environments;
- ▶ specific types of acoustic signals can be assigned to different mechanisms of cracking;
- ▶ using the acoustic emission method, different cracking mechanisms can be identified;
- ▶ it is possible to detect the intensity of the cracking process;
- ▶ full usefulness of the method of acoustic emission to determine the beginning of cracking due to corrosion has been proven, as has its usefulness in following the development of cracks which cause destruction of the reinforcement of a composite,

- ▶ the process of destruction due to corrosion occurs fastest in an alkaline environment of concentration pH8 – pits occur which go deeply into the structure of the fibre, these probably cause the leaching out of ions Ca^{2+} , Mg^{2+} and Na^+ ,
- ▶ no corrosion was noticed in a non-loaded bunch of fibres exposed to a long-lasting influence of an alkaline environment $\text{Ca}(\text{OH})_2$ – this reflects a strong influence of load on stress corrosion.

Cracking caused by corrosion is very dangerous in terms of the use of constructions strengthened with a composite because the process is not perceptible without special tests. Corrosion has an important influence on the strengthening elements in two ways:

- ▶ the cracking composite increases its susceptibility, thus reducing the strengthening effect;
- ▶ as a result of corrosive cracking, the entire composite undergoes destruction.

Therefore, in the case of damage of this nature, the use of acoustic emission is a very helpful technique in determining the degree of degradation of the strengthening element.

An analysis of the obtained results led to the identification of types of signals which characterise the destructive mechanisms which occur during stress corrosion in the entire volume of the test element. Moreover, it was confirmed that acoustic emission is useful for identifying the beginning of cracking as well as for following the process of corrosion of a composite.

References

- [1] Karbhari V., *Correlation of laboratory and field studies of aging degradation of composite systems in civil infrastructure*, DURACOSYS'02, ed. A.A. BALKEMA PUBLISHERS, TOKYO, 2002, 11–18.
- [2] Safaris Gorj M., *Analysis of FRP Strengthened Reinforced Concrete Beams Using Energy Variation Method*, World Applied Sciences Journal, 6 (1), 2009, 105–111.
- [3] Leung Ch.K.Y., NgM.Y.M., Luk H.C.Y., *Empirical Approach for Determining Ultimate FRP Strain in FRP-Strengthened Concrete Beams*, Journal of Composite Constructions, 10, 2006, 125.
- [4] Benmokrane B., *Durability of FRP Composites for Civil Infrastructure Applications*, Durability of Materials and Structures in Building and Civil Engineering, Dunbeath, Caithness: Whittles Publishing, 2006, 300–343.
- [5] fib. *FRP reinforcement in RC structures*, Fédération Internationale du Béton, fib Task Group 9.3, fib Bulletin 40, Lausanne, Switzerland, September 2007, 147.
- [6] Rafi M.M., Nadjai A., Ali F., Talamona D., *Aspects of behaviour of CFRP reinforced concrete beams in bending*, Construction and Building Materials, 2008, 277–285.
- [7] Debaiky A.S., Green M. F., and Hope B. B., *Long-Term Monitoring of Carbon Fiber-Reinforced Polymer-Wrapped Reinforced Concrete Columns Under Severe Environment*, ACI Structural Journal, 2006, 865–873.

- [8] Debaiky A. S., Nkurunziza G., Benmokrane B., Cousin P., *Residual Tensile Properties of GFRP Reinforcing Bars after Loading in Severe Environments*, Journal of Composites for Construction, 2006, 370–380.
- [9] Kawada H., Kobiki A., Koyanagi J., Hosoi A., *Long-Term Durability of Polymer Matrix Composites Under Hostile Environments*, Materials Science and Engineering, 412(1–2), 2005159–164.
- [10] Mufti A., Onofrei M., Benmokrane B., Banthia N., Boulfiza M., Newhook J., Bakht B., Tadros G., Brett P., *Durability of GFRP Reinforced Concrete in Field Structures*, 7th International Symposium on Fiber Reinforced Polymer Reinforcement for Reinforced Concrete Structures (FRPRCS-7), New Orleans, Louisiana, USA, 2005.
- [11] Ray B.C., *Effects of Changing Environment and Loading Speed on Mechanical Behavior of FRP Composites*, Reinforced Plastics and Composites, 25(12), 2006, 1227–1240.
- [12] Micelli F., Nanni A., *Durability of FRP rods for concrete structures*, Construction and Building Materials, 18, 2004, 491–503.
- [13] Pauchard V., Grosjean F., Campion-Boulharts H., Chateauminois A., *Application of a stress-corrosion-cracking model to an analysis of the durability of glass/epoxy composites in wet environments*, Composites Science and Technology, 62, 2002, 493–498.
- [14] Swit G., *Durability of composite GRP under stress corrosion by acoustic emission*, Duracosys'02, ed. A.A. Balkema Publishers, Tokyo 2002, 11–18.
- [15] Swit G., *Evaluation of compliance change in concrete beams reinforced by GRP using AE*, Journal of Materials in Civil Engineering, American Society of Civil Engineering, Vol. 16, No. 5, USA 2004, 414–419.
- [16] Świt G., *Durability of stressed E glass fibre in alkaline medium*, Recent Development in Durability Analysis of Composite Systems, Proceedings 4th International Conference Duracosys'99, ed. A.A. Balkema Publishers, Rotterdam 2000, 473–476.
- [17] Myers T.J., Kytömaa H.K., Smit T.R., *Environmental stress-corrosion cracking of fiberglass: Lessons learned from failures in the chemical industry*, Journal of Hazardous Materials, Vol. 142, Issue 3, 11 April 2007, 695–704.
- [18] Kumosa L., Kumosa M. and Armentrout D., *Resistance to stress corrosion cracking of unidirectional ECR-glass/polymer composites for high voltage composite insulator applications*, Composites Part A: Applied Science and Manufacturing, Vol. 34, Issue 1, 2003, 1–15.
- [19] Khennane A., Melchers R.E., *A Meso-scale finite element model for environmental stress corrosion of GFRP*, Proceedings of The Fourth Australasian Congress on Applied Mechanics, 2005, 573–578.
- [20] Khennane A., Melchers R.E., *Durability of glass polymer composites subject to stress corrosion*, ASCE Journal of Composite for Construction, 2003, 07, 10–117.
- [21] Mortensen A., *Concise encycloped of COMPOSITE MATERIALS*, Second edition, 2007.
- [22] Sekine H., Beaumont P.W.R., *Stress-Corrosion Cracking in Unidirectional GFRP Composites*, Key Engineering Materials, Vol. 430, 2010, 101–113.
- [23] Imielińska K., *Environmental stress cracking in e-glass and aramid/glass epoxy composites*, Kompozyty, Vol. 6, 2006, 19–23.



- [24] Almusallam T.H., Al-Salloum Y.A., *Durability of GFRP Rebars in Concrete Beams under Sustained Loads at Severe Environments*, Journal of Composite Materials, 40(7), 2006, 623–637.
- [25] Chen Y., Davalos J.F., Ray I., *Durability Prediction for GFRP Reinforcing Bars Using Short-Term Data of Accelerated Aging Tests*, Journal of Composites for Construction, 10(4), 2006, 279–286.
- [26] ISO 6259: 1997, Thermoplastic pipes – determination of tensile properties – Part 1: General test method.
- [27] ASTM D 2290, Apparent tensile strength of parallel reinforced plastics by split disk method.

Andrzej Więckowski (awiecko@agh.edu.pl)

Department of Geomechanics, Civil Engineering and Geotechnics, Faculty of Mining and Geoengineering, AGH University of Science and Technology

INFLUENCE, OF TIME RANDOMNESS EXECUTION OF WORK, ON LENGHT OF THE CONSTRUCTION CYCLE

WPLYW LOSOWOŚCI CZASÓW WYKONYWANIA ROBÓT NA DŁUGOŚĆ CYKLU BUDOWY

Abstract

The objective of this paper is to analyse the time reserves in scheduling periods for conducting processes that ensure construction deadlines can be met. By using the probability account and numerical analyses methods, including 'Monte Carlo', execution cycles have been analysed, as well as summary stoppage times for executing teams and working areas. On the basis of calculations made using data from studies made during the construction office building in Krakow it was stated that in order to keep to the planned deadline, must be smaller periods of performance of works by individual brigades, an average of 0,103 times of rhythm.

Keywords: time reserves, random processes, construction cycle

Streszczenie

Celem jest analiza buforów czasu gwarantujących dotrzymanie planowanego terminu realizacji zadania. Z wykorzystaniem rachunku prawdopodobieństwa i metod analiz numerycznych, w tym „Monte Carlo”, zbadano okresy cykli realizacji zadań oraz sumaryczne czasy przestojów brygad wykonawczych i działek roboczych (frontów pracy). Na podstawie obliczeń danych z budowy biurowca w Krakowie stwierdzono, że dla zachowania planowanego terminu realizacji zadania, konieczne były mniejsze okresy wykonywania robót przez poszczególne brygady, średnio o 0,103 czasu trwania rytmu.

Słowa kluczowe: bufor czasowe, procesy losowe, cykl zadania

1. Introduction

The execution of particularly large construction projects requires the simultaneous employment of a significant number of staff, often several dozen, and sometimes, several hundred or more. In such cases, the organisation of work for specialist teams is a complex task [1, 2, 6–9, 11, 12]. With the assumption of a constant duration of particular processes, a work execution cycle can be easily determined by using the formulas developed by A. Dyżewski [3, 5, 7, 10]. However, the actual execution of work at the construction site is characterised by random variability in the duration of particular processes. In line with the studies that follow, such random deviations cause many distortions in execution and elongation of the work execution cycles.

The analysed office building in Krakow, with a total area of 57,000 m², features one underground car-parking level under the building and from the east, under the car park and greens on the ground level, and under a one-storey administration building. The height difference between the floors is 320 cm, except for the south-western part of the building, where the ground floor is double the height of the standard storey at 675 cm, and the 12th storey, the height is 375 cm.

The building has been designed as a pole-and-slab system made of vertical and horizontal joists and poles, set on a slab of reinforced concrete with a 1.0m thickness, at a depth of 5.05m below ground level, with recesses up to 6.60 m below the lift shafts. The building features: two cores of reinforced concrete, each comprising lift shafts, four for the transport of people, and one freight lift; stiffening shafts and a staircase. The building is constructed as a monolithic of reinforced concrete in Peri formwork: the walls have a thickness of 20 cm, formed with flat multidimensional disks, rectangular poles with dimensions 60 cm × 60 cm. And floors of 26 cm thickness made on supports with stabilising tripods and on wooden beams covered with formwork plywood of 22 mm, while untypical shapes are individually formed, also using Peri systemic elements.

Concrete class C30/37. Concrete mix with S4 and S5 consistencies, with cement setting start after 3 hours.

2. Balanced workload method

Professor Aleksander Dyżewski from Warsaw University of Technology, author of *Doktryna pracy równomiernej w realizacji budowlanej* [*Doctrine of balanced workload in construction works*] [3], and later other authors [7, 10], pointed to the balanced workload method (*PR*) as the most favourable approach for the organisation of work at the construction site.

In order to apply the *PR* method, the works differentiate n – work areas. Each work area should be a construction area which:

- ▶ comprises the entire facility, in the case of several small facilities forming the works, or a part of a large facility resulting from its division into fragments requiring similar labour R , materials M , and equipment operation S ;



- ▶ is necessary to create a workstation and assure work area;
- ▶ is usually entrusted to one team to execute a consecutive work forming a separate whole.

Work areas analysed below have been labelled as $i, i = 1, 2, \dots, n$ and described with a set $i \in I$.

In other works, in the case of the *PR* method, the building facility is divided into n – work areas with similar *RMS* outlays, or in the case of n – repeatable smaller facilities, each one is treated as a work area. Usually, one work area is entrusted to one team who carry out a particular process during the ‘rhythm’ – r , or its multiplicity. A team carries out the same work process while moving consecutively along all work areas, from the first to the last one. After completing a particular process, each area is taken over by the next team who, after completing their work, hand it over to a team executing the next process (according to the construction technology). In such a way, each area, in the technological order, undergoes all processes $j, j = 1, 2, \dots, m$ described with the set $i \in I$, consecutively from the first $j = 1$, to the last $j = m$.

In the deterministic approach, with the assumption of constant times for executing each process at work area during rhythm r , execution of a set of all m – processes at one, e.g. the first area, lasts for the time $t = mr$. Processes at each consecutive area commence at rhythmic intervals, hence their completion occurs, respectively, a rhythm r later. Therefore, completion of the execution of a process at area n – the last area occurs later than at the first area by $r(n - 1)$.

The period t^{PR} – of work execution cycle using the *PR* method thus totals:

$$t^{PR} = t + r(n - 1), \quad (1)$$

or

$$t^{PR} = r(m + n - 1), \quad (1a)$$

$$r = \text{const.}$$

In the case of the balanced workload method, and when we can perfectly predict the above times for the execution of each process in the work area during rhythm r , it is very favourable to have t_{pc}^{PR} – continuous working time of any team on the task, which is n times greater than the period of rhythm r (as it is repeated on execution of a particular process at all areas) totalling:

$$t_{pc}^{PR} = nr, r = \text{const.} \quad (2)$$

In actual conditions at the construction site, particular execution times t_{ij} at work areas i , of processes j are undetermined, but are characterised with random values, with significant dispersion against the central tendency. Using the example below, the impact of the random process duration on the execution cycle of the entire task is analysed.



3. Example

On each storey of the building, four work areas are defined, with the width of facility projection, in the other direction (along the building) limited with axes 1÷4, 4÷7 with core I, 7÷9 with core II, and 9÷11. Due to the building structure, the first and second work areas are larger than work areas 3 and 4.

According to actual execution works, $m = 8$ processes have been differentiated:

- 1) formwork, pole reinforcement;
- 2) concrete pouring of poles;
- 3) formwork, reinforcement of core of the buildings and elevators;
- 4) concrete laying for core of the buildings and elevators;
- 5) formwork of joists, beams, lintels and floors;
- 6) reinforcement of joists, beams, lintels and floors;
- 7) concrete laying of joists, beams, lintels and floors;
- 8) formwork, reinforcement and concrete laying of stairs.

Formwork and reinforcement of poles, and the other processes of concrete laying of poles, were executed in the same work areas.

Formwork and reinforcement of walls in core I of the building and elevator shafts, and the other processes of concrete laying of walls in core I of the building and elevator shafts, were carried out in parallel with pole execution on work areas $1k$ and $2k$ (k – refers to storey of the building). Analogically, execution of core II and the elevator shafts was performed in parallel with pole execution on work areas $3k$ and $4k$.

Formwork of joists, beams, lintels and floors, was executed in advance of one work area against reinforcement of joists, beams, lintels and floors, and one work area against concrete laying for such elements. The last process involved formwork, reinforcement and concrete laying for stairs.

3.1. Task execution cycles and stoppages of teams and work areas

Following the analysis of process execution times at the construction in question, it was determined that average time totalled $t_m = 3.125$ work shifts with a standard deviation of particular measurement results $\sigma = 1.287$. Therefore, the relative standard deviation is very high, totalling as much as $\delta\sigma = 41.18\%$. Distribution of process execution times ranged from $t_{\min} = 2.5$ shift to $t_{\max} = 6.5$ work shift.

In further analysis, the average time $t_m = 3.125$ work shift has been identified with one time unit: 1 t.u. = 3.125 shift.

For the adopted values of rhythm time $r = 1$ t.u., $m = 8$ processes and $n = 4 \cdot 12 = 48$ work areas (4 work areas on each of the 12 storeys) task execution time using the balanced workload method totals $t^{PR} = 55$ t.u.

Based on numerical calculations using a network model with a deterministic *see above note* structure and meeting the conditions of the technological order of execution of works and as above with random process duration characteristics, after carrying out 10,000 simulations, obtained average values, namely values occurring with the probability of 50%, have been presented in Table 1 and Fig. 1.

Table 1. Task execution periods and summary waiting times of teams at work areas

Process execution period t_m	Task execution cycle t^{PR}	Task execution time t_{los}	Absolute cycle elongation Δ_c	Relative cycle elongation δ_c	Work area waiting time τ_d	Team waiting time τ_b
[t.u.]	[t.u.]	[t.u.]	[t.u.]	[%]	[t.u.]	[t.u.]
1.0	55.000	61.146	6.146	11.17	156.32	24.141
0.897	49.335	55.000	5.665	11.48	142.043	18.771

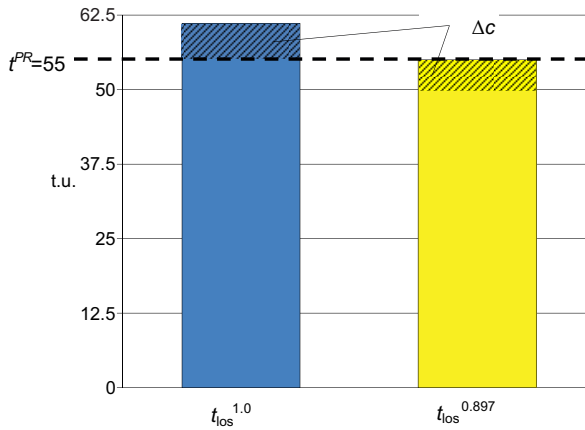


Fig. 1. Task execution times $t_{los}^{1.0}$, $t_{los}^{0.897}$ considering random process duration, respectively for $t_m = 1.0$ t.u. and $t_m = 0.897$ t.u. and Δ_c – execution of task execution time against the cycle t^{PR}

Following the results of numerical calculations, while considering random duration of particular processes, task execution time is elongated, in absolute terms by $\Delta_c = 6.15$ t.u., while in relative terms by $\delta_c = 11.17\%$ as compared to the cycle $t^{PR} = 55$ t.u. calculated according to the balanced workload method.

In turn, in order to ensure that task execution time is equal to the calculated $t^{PR} = 55$ t.u., it is necessary to ensure a smaller value of rhythm duration by $0.103r$, specifically, the process duration to be applied should be $t_m = 0.897$ t.u.

This problem is very frequent in construction works. Despite process execution times with average values equal to the rhythm r , actual random values of such times cause significant prolongation of the task execution period. For example, at the analysed construction site, relative elongation of the execution time amounted to, as above, over 11%. Therefore, in order to preserve the cycle t^{PR} , the planned rhythm duration in the analysed case (with the determined empirical characteristics of processes completed) should be reduced by approximately 10.3%.

As a consequence of the impact of the random duration of particular processes, there are both periodic stoppages in work areas whilst waiting for the start and execution of the next process, and periodic stoppages of teams occurring as a result of failure in making work areas

available by the teams still completing previous processes, Fig. 2. Waiting time in work areas totalled $\tau_d^{1.0} = 156.32$ t.u. Prolongation of the task execution time amounted to $\Delta_c = 6.146$ t.u.; this prolongation of the task execution is over twenty-five times less than the total waiting time of all work area results from the fact that waiting time refers to forty-eight work areas, at each of which may have been down time for several times (in the special case: 8 times – corresponding to the number of processes executed), or there may have been no stoppages at all.

In turn, summary waiting time of the teams, totalling $\tau_b^{1.0} = 24.141$ t.u. is about 3.9 times greater than the elongation of task execution time Δ_c .

Similar proportions of stoppages for work areas and teams were observed while applying, in the calculations, of expected process execution time $t_m = 0.897$ t.u.

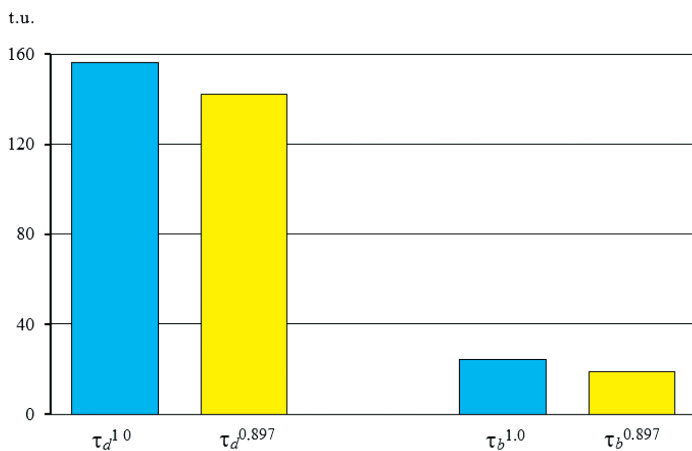


Fig. 2. Waiting times at work areas $\tau_d^{1.0}, \tau_d^{0.897}$ and of teams $\tau_b^{1.0}, \tau_b^{0.897}$ considering the impact of random process duration, respectively for $t_m = 1.0$ t.u. and $t_m = 0.897$ t.u.

3.2. Variability of task execution time and stoppages of teams and work areas

Task execution times t_{los} and summary waiting time of work areas τ_d and of the teams τ_b depending on the number of work areas n where the eight processes are repeated, are presented in Table 2 and Fig. 3.

Table 2. Variability of task execution periods t_{los} and total waiting times of work areas τ_d and teams τ_b , depending on work area number n

n	1	2	4	8	16	32	64	128	256	512	1024	2048
t_{los}	8.3629	9.6551	12.146	16.78	25.727	43.111	77.183	144	276.05	537.75	1057.7	2093.7
t_{los}/n	8.3629	4.8275	3.0365	2.0975	1.6079	1.3472	1.2059	1.125	1.0783	1.0502	1.0329	1.0223
τ_d	0.2834	0.8884	3.0506	9.142	27.672	81.09	242.02	722.48	2101.9	6094.7	17705	50767
τ_d/n	0.2833	0.4442	0.7626	1.1427	1.7295	2.5341	3.7815	5.6443	8.2104	11.903	17.289	24.788
τ_b	1.5874	3.0974	5.1067	8.528	12.849	19.369	29.046	42.291	61.482	89.38	127.99	183.12
τ_b/n	1.5873	1.5487	1.2766	1.066	0.8031	0.6053	0.4538	0.3304	0.2402	0.1745	0.1249	0.0894

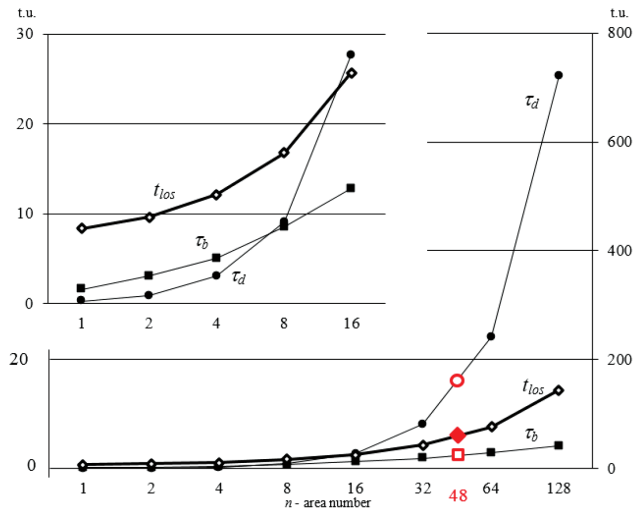


Fig. 3. Task execution times t_{los} and summary waiting times of work areas τ_d and teams τ_b , by work area number n

In the case of increasing the work area number n , for example, as a result of multiplying the number of storeys or extension of the planned facility, the time for process execution t_{los} is extended. According to the results of calculations (Fig. 1, Table 2), for the analysed values $n = 1, 2, 4, \dots, 2048$ ($n \in I$), task execution times are greater than the corresponding τ_b – than summary waiting times of the teams:

$$t_{los} > \tau_b, n \in I. \quad (3)$$

In the analysed case, for a smaller number of work areas n , from about 15, namely for $n < \sim 15$, summary waiting times of work areas τ_d , similarly as team stoppages, are smaller than task execution times t_{los} . In turn, for a greater number of work areas n , from about 15, namely for $n > \sim 15$, summary waiting times of work areas τ_d are greater than task execution times t_{los} , with the intensively growing discrepancy together with further growth of the value n .

Therefore:

$$t_{los} > \tau_d, n < \sim 15, \quad (4)$$

$$t_{los} < \tau_d, n > \sim 15. \quad (5)$$

In cases where the work area number is smaller than 8, namely for $n < m$ (where m means the number of teams, here $m = 8$) the total waiting times of work areas is smaller than the summary team stoppages, while in cases with a greater number of work areas – work area stoppages are greater than team stoppages, with the intensively growing discrepancy with the further increasing number of work areas:

$$\tau_d < \tau_b, n < m, \quad (6)$$

$$\tau_d > \tau_b, n > m. \quad (7)$$

Fig. 4 and Table 2 present the variability of task execution periods t_{los} and total waiting times of work areas τ_d and teams τ_p depending on work area number n where the processes are repeated.

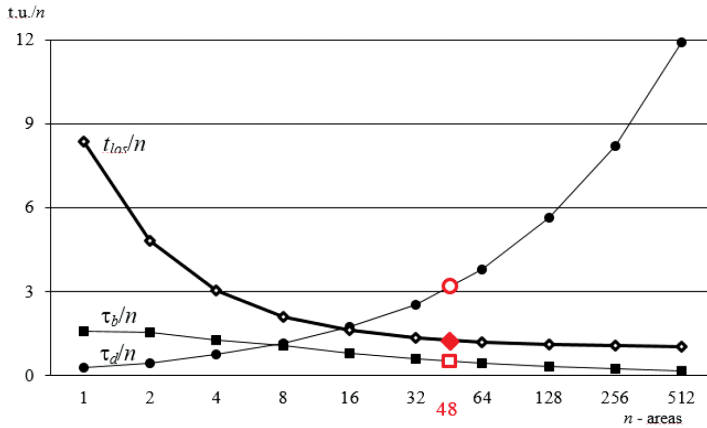


Fig. 4. Variability of the proportions between task execution periods t_{los} and summary waiting times of work areas τ_d and teams τ_p depending on work area number n

The proportion of task execution time t_{los} to the number of work areas n where processes are repeated, with n growing from 1 to 2048, suggest that with further increasing of the value $n \rightarrow \infty$, there is a correlation of proportion value to 1. In turn, the proportions of summary team stoppage times τ_p to the number of work areas n , also in the case of n growing from 1 to 2048, suggest that in the case of increasing the value n as above, there is a correlation of proportion results to 0. In the case of work area number also growing from 1 to 2048, the proportions of summary waiting times of work areas τ_d to their number n indicate that for $n \rightarrow \infty$ there is a discrepancy of proportion results to the infinity.

4. Conclusion

The analysed actual process execution times while executing the building shell were characterised with average duration $t_m = 3.1$ shift, a high standard deviation of $\sigma = 1.3$, a large distribution of process execution times, with minimum time $t_{\text{min}} = 2.5$ shift, and $t_{\text{max}} = 6.5$ shift.

On the basis of numerical calculations, with the application of model distributions compatible with the actual characteristics at the site, it is determined that random times of particular process duration has caused, among other factors, long waiting times of particular teams for their work areas. Team stoppages totalled approximately 39%, against the task cycle time. In turn, the total work area waiting time (at 48 work areas) lasted over 2.5 times longer than the average task execution cycle $t^{\text{los}} = 191$ shifts.

As compared to the task execution period calculated using the deterministic method as the total of average process duration, the actual task execution cycle, accounting for random

conditions at the site, is longer by over 11%, and keeping the deadline with 50% certainty requires the application of over 10% shorter times of particular process execution.

The performed analyses allow for pointing to the interdependence where if the n – work area is smaller than m – number of teams (processes), summary waiting times of work areas τ_d are smaller than summary team stoppage times τ_b . Therefore, $\tau_d < \tau_b$ for $n < m$, and the contrary correlation $\tau_d > \tau_b$ at $n > m$.

The characteristic large distributions of particular process execution times that were actually observed at the site, are a significant cause for stoppages of teams and work areas, and cause significant prolongation of the task execution cycle, hence the need to account for their impact.

References

- [1] Cho C., Shin Y., Park J., Lee. Y., Cho M., *Lifting load calculation method of computing simulation for super-tall building construction*, The 29th International Symposium of Automation and Robotics in Construction, Eindhoven, Netherlands 2012.
- [2] Belniak S. et al., *Zastosowanie metod matematycznych w wybranych problemach zarządzania w budownictwie*, Wydawnictwo Politechniki Krakowskiej, Kraków 2015.
- [3] Dyżewski A., *Doktryna pracy równomiernej w realizacji budowlanej*, PWG, Warszawa 1949.
- [4] International Standard ISO 10005: 2005. Quality management systems – Guidelines for quality plans.
- [5] Jaworski K., *Metodologia projektowania realizacji budowy*, Państwowe Wydawnictwo Naukowe PWN, Warszawa 2009.
- [6] Kenzo K., Nobuyuki N., *Efficient Monte Carlo simulation method of GERT-type network for project management*, Elsevier, Computers & Industrial Engineering, V. 42, I. 2–4, P. 521–531, New York 2002.
- [7] Mrozowicz J., *Metody potokowe organizacji procesów budowlanych o charakterze deterministycznym*, Prace Naukowe Instytutu Budownictwa PWr, nr 32, Monografie, nr 14, Wydawnictwo PWr, Wrocław 1982.
- [8] Pritchard C., *Risk Management: Concepts and Guidance*, Fourth Edition, ESI, 2010.
- [9] Shtub A., Bard J., Shlomo G., *Project Management. Engineering, Technology, and Implementation*, Prentice Hall, Englewood Cliffs, New Jersey 1994.
- [10] Wątorski J., *Organizacja i mechanizacja budowy*, Cz. III, PWN, Kraków–Warszawa–Łódź 1965.
- [11] Więckowski A., *Principles of the NNM method applied in the analysis of process realisation*, Automation in Construction, Elsevier Science BV, Amsterdam–London–New York–Paris–Shannon–Tokyo 2002, vol. 11/4, 409–420.
- [12] A. Więckowski, *Time reserves in the realizations of building*, Creative Construction Conference, Krakow 2015, Poland, 482–492.
- [13] <http://opolskabusinesspark.pl/>



Paweł Falaciński (pawel_falacinski@is.pw.edu.pl)
Faculty of Building Services, Hydro and Environmental Engineering,
Warsaw University of Technology

INFLUENCE OF FLY ASH FROM THE THERMAL TREATMENT OF MUNICIPAL SEWAGE SLUDGE ON CHOSEN PROPERTIES OF HARDENING SLURRIES

WPLYW POPIOŁU Z TERMICZNEGO PRZEKSZTAŁCANIA KOMUNALNYCH OSADÓW ŚCIEKOWYCH NA WYBRANE WŁAŚCIWOŚCI ZAWIESIN TWARDNIEJĄCYCH

Abstract

Over recent years in Poland, there has been a rapid accumulation of sewage sludge – a by-product of the treatment of urban wastewater. This has come about as a result of infrastructure renewal, specifically, the construction of modern sewage treatment plants. As a consequence, the amount of fly ash resulting from the thermal treatment of municipal sewage sludge has grown significantly. The aim of this experiment was to evaluate the possibility of using the fly ash that results from municipal sewage sludge thermal treatment (SST) as an additive to hardening slurries. The article presents the technological and functional parameters of hardening slurries with the addition of fly ash obtained by SST. Moreover, the usefulness of these slurries is analysed on the basis of their basic properties. The mandated requirements for slurries employed in the construction of cut-off walls in flood embankments are listed as a criterion of usefulness. On the basis of this experiment, the usefulness of fly ash obtained through SST as an addition to hardening slurries was identified.

Keywords: hardening slurry, cut-off walls, fly ash from thermal treatment of municipal sewage sludge, hydraulic conductivity

Streszczenie

W ostatnich latach odnotowano dość szybki wzrost ubocznych produktów w procesie oczyszczania ścieków komunalnych – osadów ściekowych. Jest to pochodna rozwoju cywilizacyjnego Polski i budowy nowoczesnych oczyszczalni ścieków. W wyniku takich działań ilość powstałych lotnych popiołów po spaleniu komunalnych osadów ściekowych znacząco rośnie. Celem przeprowadzonego eksperymentu była ocena możliwości zastosowania lotnego popiołu z termicznego przekształcania komunalnych osadów ściekowych (TPKOŚ) jako dodatku do zawiesin twardniejących. W artykule zaprezentowano wyniki badań parametrów technologicznych i użytkowych zawiesin twardniejących z dodatkiem lotnego popiołu z TPKOŚ. Na podstawie oznaczonych wartości podstawowych właściwości (w stanie płynnym oraz po stwardnieniu) analizowano przydatność projektowanych zawiesin twardniejących. Jako kryterium porównawcze zastosowano wymagania w stosunku do zawiesin twardniejących stosowanych podczas realizacji przesłon przeciwfiltracyjnych w walach przeciwpowodziowych. Na podstawie przeprowadzonego eksperymentu stwierdzono przydatność popiołu z TPKOŚ jako dodatku do zawiesin twardniejących.

Słowa kluczowe: zawiesina twardniejąca, lotny popiół z termicznego przekształcania komunalnych osadów ściekowych, przesłony przeciwfiltracyjne

1. Introduction

After the Polish accession to the European Union (EU), the criteria and procedures concerning the management of water and sewage, as well as waste, have been significantly tightened. The National Programme for Urban Wastewater Treatment involves the construction of modern sewage treatment plants. From 2004 to 2014, a more than 14% increase in the number of municipal sewage treatment plants was recorded – from 2875 in 2004 to 3288 in 2014 [3]. However, the rise in the number of highly efficient specialist facilities has resulted in a relatively fast increase in the amount of the major by-product of the sewage treatment process, namely municipal sewage sludge. According to the data from the Central Statistical Office of Poland [3], the amount of municipal sewage sludge produced in 2014 alone reached 556.0×10^6 kg d.m. Thus, the steady annual increase in the amount of municipal sewage sludge at around 2.0–2.5%, poses enormous problems with regard to its safe management. This data clearly indicates a decrease in the amount of sludge stored in landfills (from around 16% in 2008, to around 5% in 2014) and an increase in the amount of sludge processed thermally (from about 1% in 2008, to around 15% in 2014). The above trends also meet the goals set by the municipal sewage sludge management directives [22]. These are:

- ▶ reducing (or abandoning) sewage sludge storage;
- ▶ increasing the amount of municipal sewage sludge processed before re-introduction to the environment, as well as the amount of sludge recycled by thermal methods;
- ▶ maximising the use of biogenic substances contained in the sludge, while meeting all the requirements related to health and chemical safety.

Experts in the field of waste agree on the current absence of a clear strategy for municipal sewage sludge management in Poland, as well as on the need for development and investment in modern thermal treatment methods [13].

The sewage sludge thermal treatment technique (SSTT) makes it possible to change the chemical and biological composition of sludge, to reduce the heavy metal content, to neutralise pathogens and to significantly decrease the weight and volume of sludge. The thermal methods of dealing with municipal sewage sludge (MSS) include incineration, co-incineration and other processes such as wet oxidation, pyrolysis, gasification and vitrification [13]. Over recent years, the use of these methods has increased in Poland, and therefore, the amount of coal combustion products (CCP), such as ash, has also increased. Unfortunately, the sewage sludge incineration process does not eliminate the high content of phosphorous and heavy metals in sewage sludge. Therefore, research continues to develop effective, environmentally safe methods of managing/using ash from the thermal treatment of sewage sludge. A popular solution for the processing of fly ash from SSTT is their use in the ceramics industry or in construction, for example, in the solidification of concrete blocks or their sintering into a granulated form [10, 14, 20]. The main purpose of these methods is the safe and economical immobilisation of hazardous compounds within the obtained material structure.

This paper presents research on the possibility of using fly ash resulting from SSTT as a constituent of hardening slurries used for fabricating cut-off walls (anti-filtration barriers) in hydraulic structures and in environmental protection structures. It should be noted that research on hardening slurries containing other types of coal combustion products (e.g. conventional ash



resulting from fluidised bed combustion) showed an improvement in the hydraulic conductivity of hardening slurries under both capillary and diffusive conditions [6].

2. Types and Properties of Hardening Slurries

In hydraulic structures, cut-off walls are normally constructed by way of narrow (trench) spatial excavations. The excavations are first loosened by the addition of bentonite and water slurries, and are then filled with cohesive soil, modified local soils, concrete and loam-concrete or so-called hardening slurries.

A hardening slurry is defined as a slurry which hardens over time and contains cement or another binder and additional materials, such as loam (bentonite), granulated blast furnace slag or fly ash, fillers and admixtures [19].

If chemical admixtures are excluded from the slurry compositions, the remaining components are of a mineral character; some of these are by-products of certain waste technology processes.

The slurries used or tested in Poland can be classified in terms of their components [8], these are:

- ▶ cement-bentonite-water;
- ▶ cement-bentonite-water with chemical admixtures;
- ▶ cement-bentonite-water with additives, such as sand, hard or lignite coal ash, hard or lignite coal fluidised bed combustion ash, blast furnace slag;
- ▶ bentonite-water with additives, such as lignite coal ash, hard coal ash, lime;
- ▶ cement-bentonite-water with additives, the so-called 'company mixes'.

Information on the properties of the above-mentioned slurries can be found in [2] and [8]. Information on the of ready mixes can be found in the approved technical specifications issued for these products [21].

The values of the selected properties of hardening slurries presented in Table 1 characterised by requirements for various methods of cut-off wall construction in flood embankments. In

Table 1. Selected properties of hardening slurries used in the fabrication of cut-off walls in flood embankments [2, 9]

No.	Properties	Unit	Value	Marked by
1	2	3	4	5
properties of hardening slurries in the liquid state (technological)				
1	density	[g/cm ³]	1.30–1.50	BN-90/1785-01 1990
2	deep soil mixing method (DSM)			
3	vibro injected thin-wall method (WIPS)			
4	narrow spatial excavation method			
5	conventional viscosity (the time of flow from Marsh funnel)	[s]	max. 50	BN-90/1785-01 1990
6	24h water setting	[%]	max. 4.0	PN-85/G-02320 1985



Tab. 1 cont.

1	2	3	4	5
7	structural strength after 10 min	[Pa]	1.4–10.0	BN-90/1785-01 1990
8				
properties of hardening slurries after hardening (functional)				
9	uniaxial compressive strength after 28 days of curing	[MPa]	0.5–2.0	PN-EN 12390-3 2011
10	hydraulic conductivity after 28 days of curing	[m/s]	≤ 10 ⁻⁸	the same laboratory methods as for cohesive soil

relation to sealings (cut-off walls) used in other specialised hydraulic structures (bunds in sewage treatment plants or in landfills), the requirements for this type of construction are specified individually, depending on the design requirements.

3. Characteristics of Ash from The Thermal Treatment of Sewage Sludge Used in the Experiment

Sewage sludge ash is produced by the incineration of sewage sludge at a high temperature (around 600–920°C), most often in the fluidised bed process. This process ensures a considerable reduction in the volume of material, while the yield of thermal energy results in ash with specific characteristics, not found among the by-products of coal combustion. The ash produced in the process has unique characteristics that are not found in other coal combustion products. Owing to the high content of organic substances in sewage sludge, ash from the thermal treatment of sewage sludge may contain 0.3–1.5% of phosphorus [11], which negatively affects the cement hydration process in concrete based on this additive by delaying it [12]. The relatively high content of heavy metals is also problematic, so it is necessary to immobilise them (e.g. in hardening slurries).

The ash examined here came from a large municipal sewage treatment plant equipped with a sewage sludge thermal utilization (SSTU) station. Sewage sludge mixed with screenings and fats is pumped onto a fluidised bed of sand, where it is incinerated. The by-products of this process are slag, ash and the products of dry flue gas cleaning.

The test results presented in literature [4, 7, 10, 14, 20] indicate a very limited suitability of SSTT ash for the construction industry, and particularly for modern concrete technology. Moreover, the high water demand and low pozzolanic activity of this ash preclude its use as an additive in concrete. However, these properties open up the possibility of using it in hardening slurries, in which the ratio of w/s (water/dry ingredients) and the resulting strength are subject to other assessment criteria.

4. Formulae of Hardening Slurries

The hardening slurries used in this study were prepared from tap water, sodium bentonite, Portland cement CEM I 32.5R and SSTT fly ash.

Table 2 shows the composition of these slurries (the content of component kg/m³ of the slurry), for each formulae (from R1 to R4), the water/cement ratio (w/c) and water/dry ingredients ratio (w/s) are listed.

Table 2. Formulae of hardening slurries (the content of component kg/m³ of the slurry)

No.	Formula	Water	Bentonite	Ash	Cement	w to c	w to s
1	2	3	4	5	6	7	8
1	R1	806	32	363	145	5.56	1.49
2	R2	771	31	455	154	5.00	1.20
3	R3	746	22	373	336	2.22	1.02
4	R4	740	15	370	370	2.00	0.98

5. Scope of testing

5.1. Tests of Technological Properties

Tests were performed to determine the density (ρ) of the liquid slurries, their conventional viscosity ratio (L), 2h and 24h water settings (O_d) and structural strength (t).

The volumetric density (ρ) of the slurries was tested by Barroid's balance [1], and their conventional viscosity (L) was measured with a viscometer (*Marsh's funnel*) [1]. The 2h and 24h water setting (O_d) test determines the percentage share of the volume of spontaneously separating water in 1.0 dm³ of liquid slurry after the slurry had remained in a measuring cylinder for two hours and one day [15]. Finally, the structural strength (τ) of the slurries was tested by Szirometer apparatus [1]. The readings of structural strength (in [Pa]) were carried out at one and ten minute intervals.

5.2. Preparation of Samples for Testing after Hardening

Hardening slurry test cylinders were prepared in PVC and steel cylindrical moulds with a diameter of 8.0 cm and a height of 8.0 cm. Before the slurry set, the samples were kept under a foil covering in the laboratory. After 2–3 days, the samples were submerged in water at a temperature of $+18 \pm 2^\circ\text{C}$. They were left under water until being measured.



5.3. Tests of Functional Properties

5.3.1. Density of hardened slurry

The volumetric density of the hardened slurry was determined for cylindrical samples made in steel moulds [18]. These tests were performed after 28 days of slurry maturation. After a sample was removed from the water-filled container, it was left to dry for several minutes. It was then weighed, and its diameter and height were measured. After the volume of the sample had been calculated, the following formula was used to determine its density (Eq. 1):

$$\rho_o = \frac{m}{V} \text{ [kg/m}^3\text{]} \quad (1)$$

where:

- ρ_o – volumetric density of the sample, [kg/m³];
- m – mass of the sample, [kg];
- V – volume of the sample, [m³].

5.3.2. Hydraulic Conductivity Tests

The hydraulic conductivity of hardening slurries is very low (similar to that of cohesive soils); therefore, the time needed to obtain the balance of supply and outflow of water from the sample in tests with a constant hydraulic gradient is quite low. In such cases, conductivity tests are performed with a variable hydraulic gradient. This method consists of determining, at specific times (t_1, t_2 , etc.) the values of water pressure (h_1, h_2 , etc.) in the supply tube of cross-sectional area a during the flow of the liquid through the sample of length (height) L and cross-sectional area A . In this case, hydraulic conductivity is calculated using the following formula (Eq. 2):

$$k_T = \frac{a \cdot L_p}{A \cdot \Delta t} \ln \frac{h_1}{h_2} \text{ [m/s]} \quad (2)$$

where:

- k_T – hydraulic conductivity at temperature T , [m/s];
- a – cross-sectional area of the supply tube, [m²];
- L – length (height) of the sample, [m];
- A – cross-sectional area of the sample, [m²];
- Δt – time between pressure measurements h_1 and h_2 , $\Delta t = t_2 - t_1$, [s];
- $h_{1,2}$ – values of water pressure at times t_1 and t_2 , [m].

The main advantage of this testing method is the possibility it offers for measuring minute water flow, as well as the forcing of high water pressures. The hydraulic conductivity tests with tap water were conducted using apparatus specially built from chemical-resistant plastic (plexiform and polyvinyl chloride) [5]. The action of the infiltrating medium (tap water) on the tested sample was of a gravitational nature, and the measurements were performed with a decreasing initial hydraulic gradient. All tests were performed after 28 days of slurry

maturation. The hydraulic conductivity calculated by Eq. 2 does not take into account the influence of the temperature of the infiltrating liquids. The k_T values obtained during the tests (at temperature T) were recalculated into k_{10} values corresponding to a temperature of +10°C. The following formula (Eq. 3) was used:

$$k_{10} = \frac{k_T}{0.7 + 0.03T} \quad [\text{m/s}] \quad (3)$$

where:

- k_{10} – hydraulic conductivity at temperature +10°C, [m/s];
- k_T – hydraulic conductivity at temperature T , [m/s];
- T – temperature of the infiltrating liquids, [°C].

5.3.3. Compressive strength tests

Compressive strength values f_c were determined for cylindrical samples made in steel moulds [16]. The tests were performed after 28 days of slurry maturation. The samples were matured under laboratory conditions in tap water. After a sample had been taken out of the water-filled container, it was left to dry for several minutes. Its upper surface (and the lower if it was uneven) was then smoothed to fit the surface of the sample precisely to the heads of the testing machine. Compressive strength measurements were performed with a ZD 20 testing machine. Each sample was compressed with a stress gain of 0.04–0.06 MPa/s until destruction. Three samples were compressed in each series. The following formula was used to calculate the compressive strength (Eq. 4):

$$f_c = \frac{P}{A} \quad [\text{MPa}] \quad (4)$$

where:

- f_c – compressive strength, [MPa];
- P – stress force destroying the sample, [N];
- A – cross-sectional area of the cylindrical sample, [mm²].

5.3.4. Tensile splitting strength tests

Tensile splitting strength values f_{ct} were determined for cylindrical samples made in steel moulds [17]. The samples were matured under laboratory conditions in tap water. After a sample was taken out of the water-filled container, it was left to dry for several minutes. The tests were performed after 28 days of slurry maturation. The tensile splitting strength measurements were performed with a ZD 20 testing machine. Each sample was placed on the cylinder surface (side surface) on a disc machine and then exposed to load-induced tension with a stress gain of 0.04–0.06 MPa/s until destruction. Three samples of the slurry were tested in each series. The following formula was used to calculate the tensile splitting strength (Eq. 5):

$$f_{ct} = \frac{2P}{\Pi d^2} \quad [\text{MPa}] \quad (5)$$



where:

- f_{ct} – tensile splitting strength, [MPa];
- P – stress force destroying the sample, [N];
- d – diameter of the cylindrical sample, [mm²].

6. Tests results for Technological Properties of Liquid Slurries

Tests results for the aforementioned technological properties of liquid slurries are shown in Table 3.

Table 3. Technological parameters of liquid slurries

No.	Parameter		R1	R2	R3	R4
1	2		3	4	5	6
1	density	[g/cm ³]	1.36	1.41	1.48	1.50
2	conventional viscosity	[s]	46	50	48	46
3	water setting (2h)	[%]	5.0	3.0	3.5	4.0
4	water setting (24h)	[%]	10.0	6.0	5.0	4.0
5	structural strength after 1 minute	[Pa]	2.00	1.60	1.70	2.70
6	structural strength after 10 minutes	[Pa]	2.00	1.90	3.30	4.10

7. Test Results for Functional Properties of Hardened Slurries

The averaged values of the functional properties after hardening are shown in Table 4. In brackets are shown as scatter of results from the average as a coefficient of variation (n in percentages). In addition, table 4 shows the values of brittleness.

Table 4. Functional parameters of hardening slurries after hardening

No.	Parameter		R1	R2	R3	R4
1	2		3	4	5	6
1	volumetric density ρ_o	[kg/m ³]	1390 (2.5)	1430 (2.0)	1500 (1.0)	1520 (3.0)
2	hydraulic conductivity k_{10}	[m/s]	6.50×10^{-7} (10.0)	2.20×10^{-7} (13.5)	3.90×10^{-8} (11.0)	1.50×10^{-8} (12.0)
3	compressive strength f_c	[MPa]	0.29 (15.1)	0.35 (16.2)	1.12 (20.1)	1.30 (20.5)
4	tensile splitting strength f_{ct}	[MPa]	0.09 (10.2)	0.13 (8.0)	0.22 (9.0)	0.32 (9.0)
5	brittleness f_{ct}/f_c	[-]	0.31	0.37	0.20	0.25

8. Analysis of Test Results

The obtained values of the parameters were compared with the requirements for hardening slurries used in the fabrication of cut-off walls in flood embankments presented in Table 1. It should be noted that the density of all hardening slurries tested in this study (shown in Table 3) is sufficient to ensure drilling excavation stability. These slurries show a density increase in accordance with the theoretical assumptions of [8], as well as a decrease in the w/c and w/s ratios (Fig. 1).

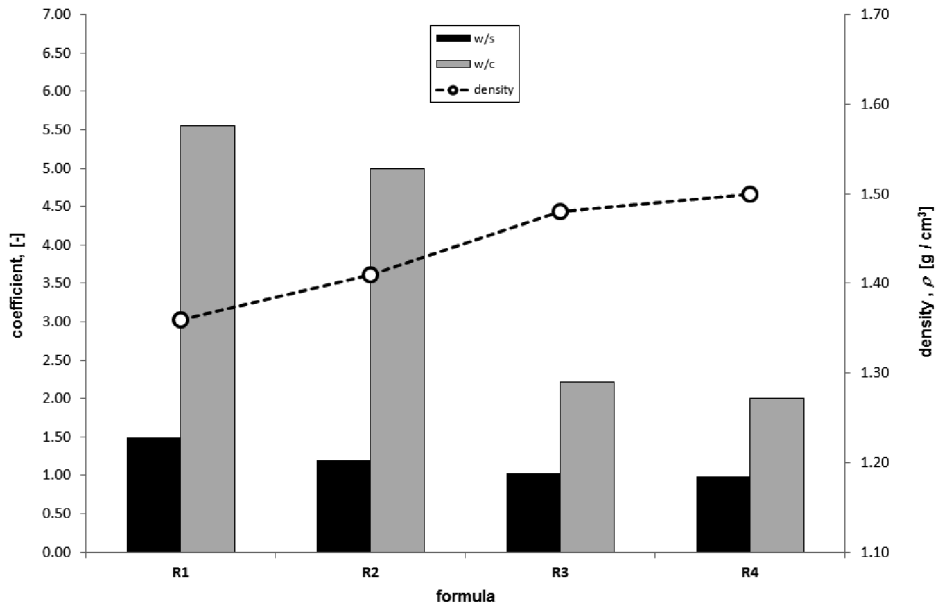


Fig. 1. Relationship between density and the w/s and w/c ratios

All tested formulas meet the limit values for conventional viscosity (estimated to be a maximum of 50 sec) because of the hydraulic transport of the slurry at the construction site, as well as its movement in the drilled excavation. Furthermore, there is no clear trend in the variability of the conventional viscosity values in relation to the w/c and w/s ratios (Fig. 2).

The values of water setting after two hours meet the assumed criteria (maximum 4.0%) for all the formulas except R1 (Fig. 3). However, in the case of water setting determined after 24 hours, the limit value was met only by the R4 formula (Fig. 3). It should be noted that a higher value of this parameter can result in the lack of uniformity of any wall made of such a slurry. The decrease in the value of water setting after 24 hours is proportional to the decrease in the w/s and w/c ratios.

The structural strength, also defined as the gel strength, describes the thixotropic properties of the slurry [8]. The appropriate structural strength value is conducive to the stability of excavation walls, as it protects them from soil particle run-in and ensures the required stability

of slurries contaminated by excavated soil; therefore, soil particles remain suspended in the slurry weight and do not settle out. The values determined during the experiment (Fig. 4) meet the acceptable criteria (above 1.4 Pa as stated by [9]).

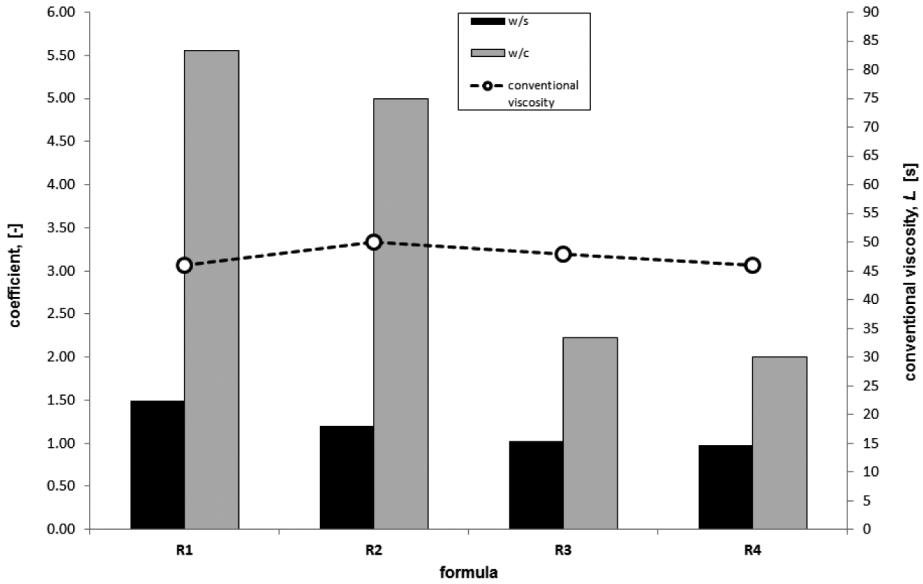


Fig. 2. Relationship between conventional viscosity and the w/s and w/c ratios

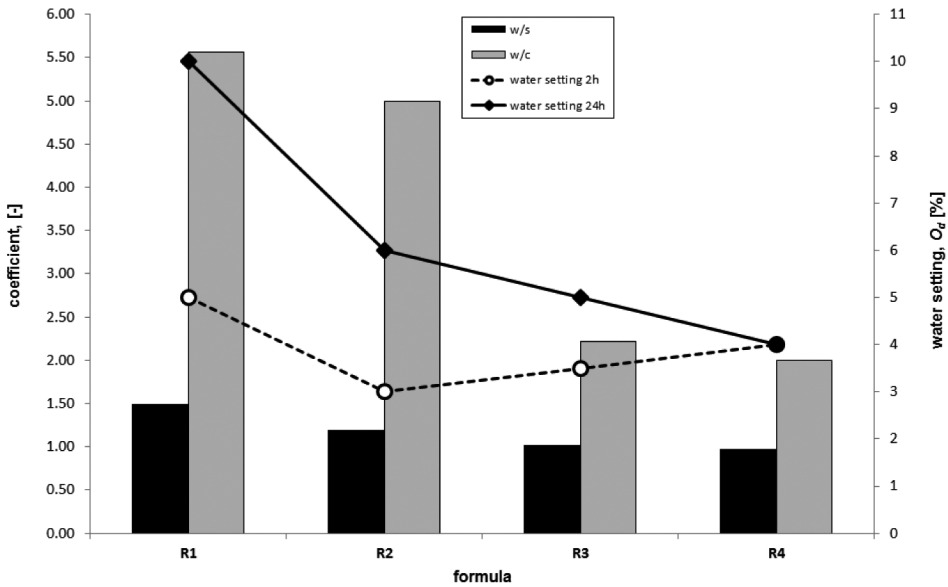


Fig. 3. Relationship between water setting and the w/s and w/c ratios

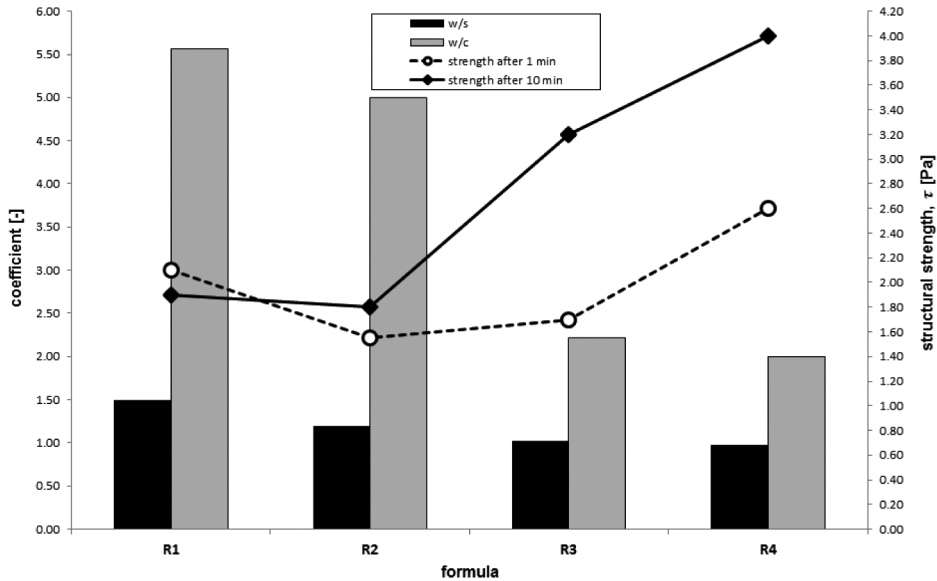


Fig. 4. Relationship between structural strength and the w/s and w/c ratios

The volumetric density values presented in Table 4 show that the volumetric density after hardening is at an acceptable level for all the formulas, and the increase in this parameter is (generally) inversely proportional to the increase in the w/s and w/c ratios.

The hydraulic conductivity of the slurries as a function of the w/s and w/c ratios is presented in Figure 5. The hydraulic conductivity limit value for hardening slurries used for fabricating cut-off walls in flood embankments is $k_{10} \leq 1.0 \times 10^{-8}$ (Table 1), which ensures an appropriate tightness of the flood embankment. For all hardening slurry formulas tested in this study, k_{10} values above the limit value were obtained. In the case of the R4 formula, the k_{10} value (1.50×10^{-8}) was only slightly above the limit value.

In the analysed hardening formulas, a clear correlation can be observed between the hydraulic conductivity values and the quantity of the binder (cement) and dry ingredients (Fig. 5).

With regard to hardening slurries used for fabricating cut-off walls in flood embankments, the compressive strength values are designed to be at a level of 0.5 to 2.0 MPa. It is worth noting that, because of the lacking hydraulic and pozzolanic properties of the ash used in this study, the binder (cement) affects the strength parameters. The compressive strength values of the slurries as a function of the quantity of the binder (cement) are therefore presented in Figure 6. The f_c values obtained during the tests confirm the usefulness of the R3 and R4 formulas.

Because of the need to maintain the continuity of any structure made of hardening slurries, it is necessary to know the appropriate f_{ct} tensile splitting strength. For the slurries investigated here, this value was about 30% of the compressive strength value [8]. The quotient of the tensile splitting strength (f_{ct}) and the compressive strength (f_c) are measures of the material's

fragility. For the slurry formulas tested here, this parameter ranged from 0.20 to 0.37, which is over twice as high as the fragility of a mortar and cement concrete (below 0.125). This is due to the presence of bentonite as well as the high porosity and moisture of slurries, and consequently, it ensures the good cooperation of structures made from hardening slurries with their subsoil.

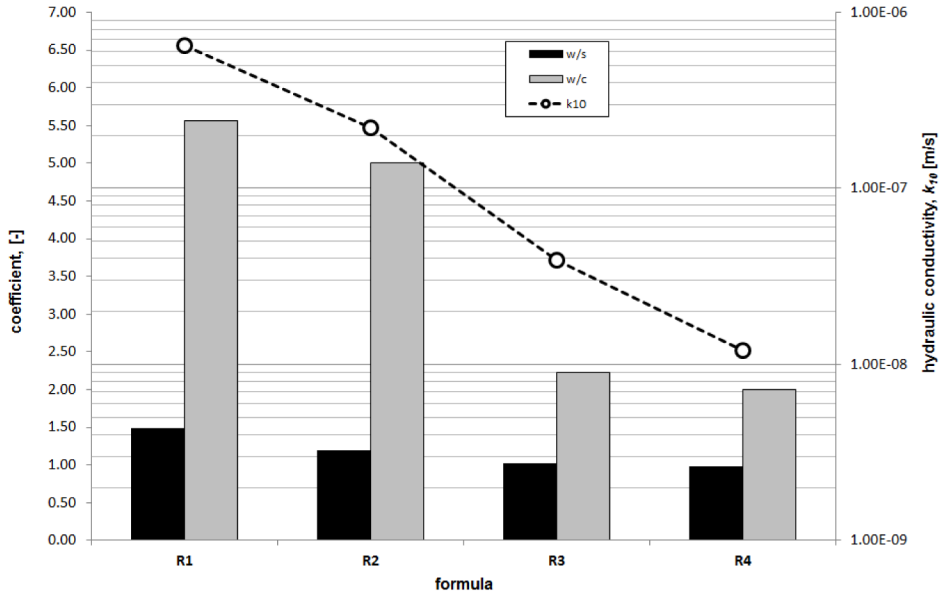


Fig. 5. Relationship between hydraulic conductivity and the w/s and w/c ratios

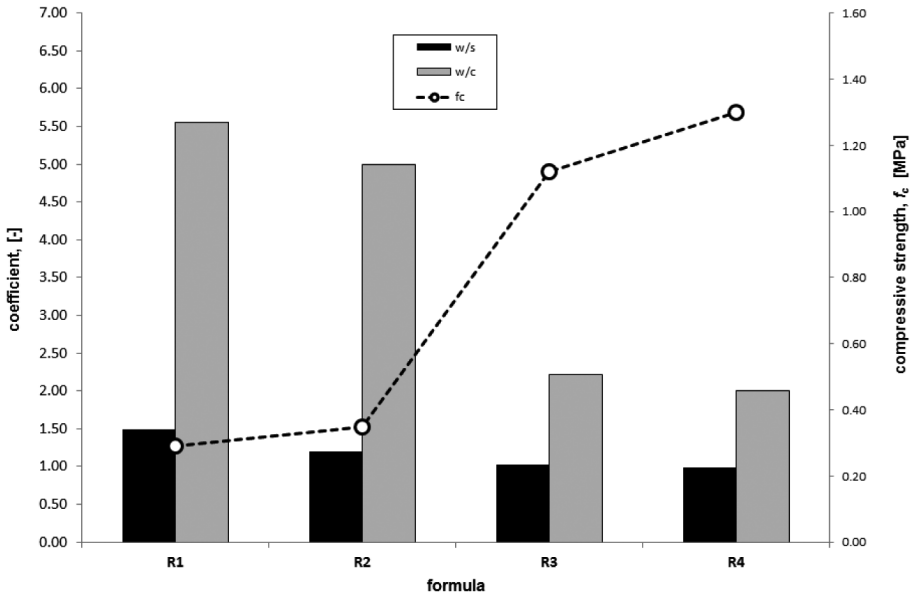


Fig. 6. Relationship between hydraulic conductivity and the w/s and w/c ratios

9. Conclusion

Considering all the technological and performance parameters analysed above, it should be noted that the R4 formula met most of the criteria which qualify hardening slurries as a material for cut-off walls in flood embankments. Only a slight excess of the acceptable hydraulic conductivity value was recorded ($k_{10} = 1.50 \times 10^{-8}$). It must be pointed out that, owing to the lack of hydraulic and pozzolanic properties in the ash utilised in this study, the proportion of the binder has to be increased to improve the slurry matrix tightness. This binder can be cement (as in this experiment) or another type of binder, e.g. ground blast furnace slag or fly ash resulting from the combustion of hard or lignite coal (additional coal combustion products).

The obtained results show the potential of the fly ash resulting from thermal treatment of municipal sewage sludge when used as an additive to hardening slurries. Such a utilisation of fly ash can constitute a new direction in the management of this type of industrial waste. The values of slurry properties recorded in this study confirm the safe bounding of ash in the slurry matrix. Tests for the leaching of heavy metals and other substances from the slurry matrix are the next stage in research on the safe use fly ash.

The proposed experiment in the direction of the use of fly ash from thermal treatment of municipal sewage sludge is part of a broader policy of sustainable development.

The test results presented in this paper form the basis of further studies on the potential use of ash from the thermal treatment of sewage sludge as a component of hardening slurries used in fabricating cut-off walls in environmental protection structures or in other civil structures, for example, for mining damage recovery and site restoration.

References

- [1] BN-90/1785-01 Drilling Fluids. The field test methods (in Polish).
- [2] Borys M., *Execution instructions of vertical cut-off walls from hardening slurries in corps and substratum of river embankments*, Materiały instruktażowe. Procedury 125/9, Wydawnictwo IMUZ Falenty, 2008 (in Polish).
- [3] Central Statistical Office of Poland. Environmental Protection (2004–2014) (in Polish).
- [4] Chang F.C., Lin J.D., Tsai C.C., Wang K.S., *Study on cement mortar and concrete made with sewage sludge ash*, Water Science and Technology, Vol. 62, Issue 7, 2010, 1689–1693.
- [5] Falaciński P., *Leak Tightness of hardening slurries with fluidal fly ashes in chemically aggressive environments*, Archives of Environmental Protection, Polish Academy of Sciences, 37 (1), 2011, 115–134.
- [6] Falaciński P., *Possible applications of hardening slurries with fluidal fly ashes in environment protection structures*, Archives of Environmental Protection, Polish Academy of Sciences, 38 (3), 2012, 91–104.
- [7] Hudziak G., Gorazda K., Wzorek Z., *Main directions in application of ash after thermal treatment of sewage sludge*, Technical Transactions, Issue 16, 2012, 41–50 (in Polish).

- [8] Kledynski Z., Rafalski L., *Hardening slurries*, KILiW PAN, IPPT PAN, Warszawa 2009 (in Polish).
- [9] Kłosinski B., *Technical conditions for execution diaphragm walls*, Wydawnictwo Instytut Badawczy Dróg i Mostów, Seria I, Informacje, instrukcje, z. 35, Warszawa 2003 (in Polish).
- [10] Kosior-Kazberuk M., *Application of SSA as partial replacement of aggregate in concrete*, Polish Journal of Environmental Studies, Vol. 20, Issue 2, 2011, 365–370.
- [11] Łukawska M., *Speciation analysis of phosphorus in sewage sludge after thermal utilization of sludge*, Inżynieria i Ochrona Środowiska, 17 (3), 2014, 433–439 (in Polish).
- [12] Małolepszy J., Tkaczewska E., *The influence of fly ash from co-firing of coal and biomass on hydration process and properties of cement*, Materiały konferencji Dni betonu, Wisła 2006, 591–601 (in Polish).
- [13] Pająk T., *Thermal treatment of sewage sludge and the challenges of year 2016*, Inżynieria i Ochrona Środowiska, 17 (3), 363–376, 2014 (in Polish).
- [14] Pérez-Carrióna M., Baeza-Brotons F., Payáb J., Savala J.M., Zornoza E., Borrachero M.V., Garcésa P., *Potential use of sewage sludge ash (SSA) as a cement replacement in precast concrete blocks*, Materiales de Construcción, Vol. 64, Issue 313, 2014, e0002.
- [15] PN-85/G-02320. Drilling. Cements and cement pastes for cementing of boreholes (in Polish).
- [16] PN-EN 12390-3, 2011. Testing hardened concrete – Part 3: Compressive strength of test specimens (in Polish).
- [17] PN-EN 12390-6, 2011. Testing hardened concrete – Part 6: Tensile splitting strength of test specimens (in Polish).
- [18] PN-EN 12390-7, 2011. Testing hardened concrete – Part 7: Density of hardened concrete (in Polish).
- [19] PN-EN 1538+A1, 2015-08. Execution of special geotechnical works – Diaphragm walls (in Polish).
- [20] Rutkowska G., Iwaszko M., *Effect of fly ash from the incineration of sewage sludge on the strength and frost resistance of fine-grained concrete*, Inżynieria Ekologiczna, Ecological Engineering, 45, 2015, 59–67. DOI: 10.12912/23920629/60595 (in Polish).
- [21] Technical approval ITP AT/18-2011-0052-00, Instytut Technologiczno-Przyrodniczy, 2011, Falenty (in Polish).
- [22] Updating the National Waste Management Plan 2014 (2015) Warszawa (in Polish).



Paweł Popielski (pawel.popielski@is.pw.edu.pl)

Apoloniusz Kodura

Błażej Smoliński

Department of Hydraulic Engineering and Hydraulics, Faculty of Environmental Engineering, Warsaw University of Technology

ANALYSIS OF THE TECHNICAL CONDITION OF THE SEWAGE COLLECTOR WITH THE USE OF NUMERICAL SIMULATION

ANALIZA STANU TECHNICZNEGO KOLEKTORA ŚCIEKOWEGO Z WYKORZYSTANIEM MODELOWANIA NUMERYCZNEGO

Abstract

This article presents a comprehensive analysis of the technical condition of the sewage collector located under Krakowska Avenue in Warsaw. The cross section of the collector is an extended ovoid with the dimensions of 1400×800 mm. Current operational problems as well as the reasons for specific faults and failures were discussed. The numerical models generated according to the collected data and the technical documentation were presented. Boundary and initial conditions taken into account in the analysis process and the assumed calculation scenarios were also described. The results obtained as well as the considered modernization projects, along with selected optimal technical solutions, were discussed.

Keywords: numerical simulation, sewage collectors, geotechnics

Streszczenie

W artykule przedstawiono kompleksową analizę stanu technicznego kolektora ściekowego o przekroju jajowym podwyższonym i wymiarach 1400×800 mm, znajdującego się pod Aleją Krakowską w Warszawie. Omówiono obecne problemy eksploatacyjne, wraz z podaniem przyczyn występowania konkretnych usterek i awarii. Zaprezentowano wygenerowane na podstawie zgromadzonych danych oraz dokumentacji technicznej modele numeryczne obiektu. Przedstawiono uwzględnione podczas analiz warunki brzegowo-początkowe oraz przyjęte scenariusze obliczeń. Omówiono uzyskane wyniki oraz możliwe metody modernizacji kolektora, wraz z doborem optymalnej technologii.

Słowa kluczowe: modelowanie numeryczne, kolektory ściekowe, geotechnika

1. Introduction

All building materials undergo changes and wear. Their parameters are variable in time. The intensity of changes depends on many factors, including project assumptions, appropriate selection, working conditions and detrimental factors that they are exposed to.

The considered collector was raised in the '60s and '70s of the 20th century. It was constructed according to the assumptions of the trenchless tunneling method. The cladding was constructed of reinforced concrete. The construction is elaborated and characterized by the combination of co-working diverse building materials. It should be taken into consideration that the production quality was usually not splendid at the time. Building processes were carried out quickly and efficiently, but obligatory standards were often omitted. What is more, during the forty years of the collector's operation, the construction was constantly exposed to varied detrimental factors.

Factors that are harmful to the collector can be divided into the following three types:

- ▶ mechanical factors
- ▶ physical factors
- ▶ chemical factors

In addition, corrosion processes should be taken into consideration. This process can pose a considerable danger for the cooperation of concrete and steel. In practice, particular factors causing corrosion often occur at the same time. This situation is additionally complicated by the fact that particular parts of the construction are exposed to detrimental factors to varying degrees.

In short, the assessment of technical condition of the construction is a complex assignment, which requires analyzing various processes and phenomena.

2. The object of research

The object of conducted researches and analysis is the bricksewage collector constructed at the end of the 1960s and the beginning of the 1970s, located in Warsaw between Malownicza Street and 1 Sierpnia Street (Fig. 1).

Technical data of the object were obtained from the technical documentation, which had been made available by Warsaw Municipal Water Supply and Sewerage Company (MPWiK). Documentation studying was problematic due to the age of the object and the then methods of technical documentation elaborating and archiving. The difficulties were caused by a diversified level of detail in the documentation, including picture data, which were sometimes significantly inconsistent and different from each other. The situation was additionally complicated by the numerous changes and reconstructions of the collector over the years of operation. For the purposes of this analysis, the most probable technical data of the collector, confirmed in field researches, were assumed.

The considered collector with an extended ovoid cross-section and the dimensions of 1400 × 800 mm was constructed with the use of the trenchless tunneling method. The

cladding was constructed of A-type facing, made of prefabricated reinforce concrete boards with the dimensions of $125 \times 11 \times 6$ cm, 6 cm thick wooden wedges and T-beam shaped steel frames with the dimensions of $11,5 \times 13$ cm. The steel frames were supported on the base constructed of wooden beams with the dimensions of $135 \times 20 \times 24$ cm. The walls of the collector were built of two layers of “150” class sewer brick and “80” mark mortar. According to the project assumptions, the space between the brick layer and the reinforced concrete cladding was filled with concrete of $R_w = 140$ at. Corresponding construction schemes of the collector were presented in Fig. 2.

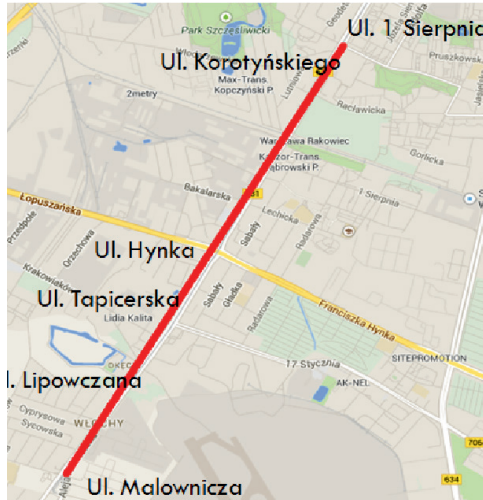


Fig. 1. Construction scheme of the collector (source: own elaboration)

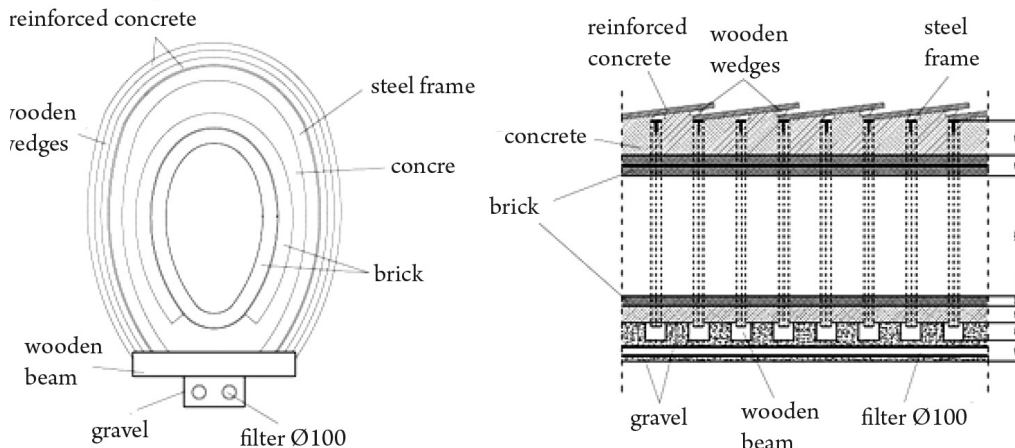


Fig. 2. Construction scheme of the collector (source: own elaboration)

Geological conditions in the subsoil are created mainly by quaternary structures. Occurrence of sandy clay, loamy sand and silt layer was observed. Gravel layers of a small



thickness were formed deeper in the subsoil. The ground water level was localized at the depth of 26.65 m above the level of the Vistula River (Fig. 3). The ground water shows qualities of sulphate and carbonate aggression towards the concrete.

The construction of the very collector as well as the tunnel cladding must carry not only the load resulting from the soil layer above them, but also load of car and tram traffic on the surface.

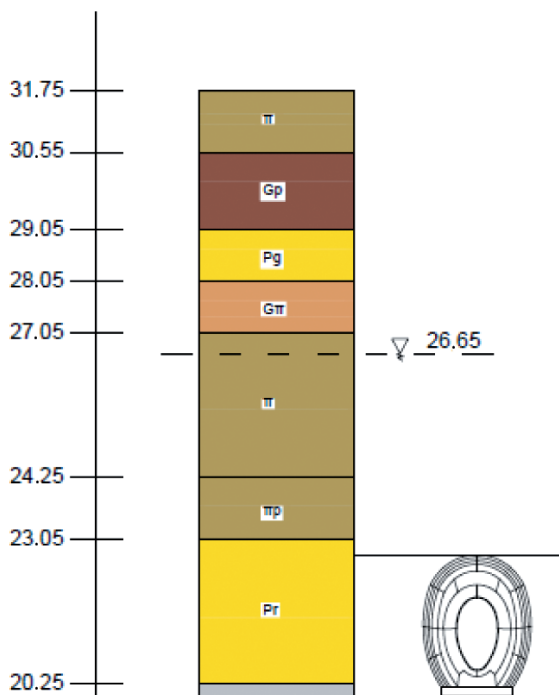


Fig. 3. Geological profile (source: [13])

3. Operational problems

The considered sewage collector causes many operational problems. Its present technical condition can be defined as unsatisfactory. While conducting field research, numerous damages of collector walls, including 3–15 mm wide cracks, were noticed. In addition, a significant loss of bricks and mortar was observed in some places (Fig. 4).

Significant problems with the collector's tightness were observed. Numerous accretions indicate that water strongly infiltrates inside the object (Fig. 5). A large number of accretions and a tight structure (Fig. 6) limit the possible sewage flow and cause problems with the capacity of the collector.

Accretion forming is caused by mortar and concrete leaching from the construction, which is a result of chemical aggression. Occurrence of empty spaces within the collector cladding, which cause change in static scheme of the cladding work, should be assumed. Significant

cracks and scratches result in the necessity of constant carrying of groundwater flow load by the already weakened construction. Attempts of impact removal of the accretions resulted in strong outflow of highly pressurized water.



Fig. 4. The wall of the collector. No 1, 2, 3 are places of mortar loss (source: [13])



Fig. 5. Leakage into the collector (source: [13])

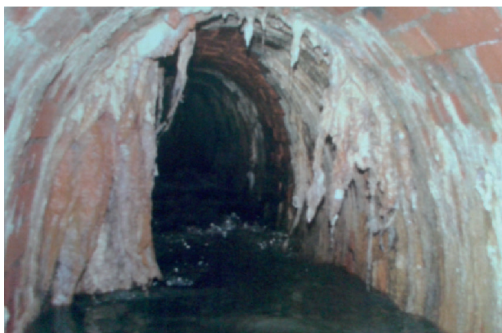


Fig. 6. Strongly developed accretions on the collector wall (source: [13])



Disturbances in the flow speed in the collector as well as disturbances in longitudinal slopes result in problems with the accumulation of sediments, which cause frequently observed high concentration of hydrogen sulphide. This hampers or periodically precludes conducting works and inspections within the collector.

As a result of occurring leakiness and soil material (brought by infiltrating water) lying on the bottom, there is a significant risk of suffosion processes, which can lead to loosening of the soil structure near the considered object. Processes that can result in soil parameter deterioration can also be caused by sewage, which leaks out of the collector through cracks in its cladding. Taking into account chemical aggression of the sewage and ground water, it must be stated that the probability of damaging the reinforced concrete cladding is high.

The natural consequence of the aforementioned processes and phenomena is soil subsidence. It can lead to damages of the ground surface infrastructure, e.g. tram trackway as well as building disaster and complete destruction of the collector.

In May of 2012, it came to the collapse of the collector near Tapicerska Street [13]. Cave in of the roadway on Krakowska Av. in March of 2010 paralyzed that part of Warsaw for a few hours. Currently, determining the main reasons of the damages and forecasting of the likely course of now occurring processes in the future seems to be the most essential assignment for elaborating optimal renovation plan and modernization of the object.

4. Research of the collector brick lining

For the purpose of determining specific material properties, samples of the bricks and mortar for laboratory researches were taken during the field researches. On the basis of conducted axial compression test, the compressive strength of the sample was determined to be 18 MPa. This results in the range of values required for sewer brick, the strength of which should be at least 15 MPa.

The material obtained from the brick lining of the collector was also subjected to chemical analysis. Samples of water infiltrating into the collector as well as material taken from collector walls, which are samples of accretions, were analyzed [elaboration].

Aggressive carbon dioxide was not detected in the samples in conducted chemical research. The reason is that the carbonate balance is establishing. However, in case of reaction (pH) or temperature change, the possibility of the occurrence of this substance in the water should be assumed. An increase of the alkalinity is probably caused by leaching of concrete hydration products by the flowing water. Solid sample investigation showed a significant amount of calcium compounds, which confirmed the assumption taken before. On the basis of conducted research and analysis, the strength of collector lining bricks was assessed as satisfactory. However, local damages and decreases of material parameters associated to them must be also taken into consideration.

Results of the chemical research indicated problems connected with mortar and concrete. Their strength parameters must be assessed as unsatisfactory. The results obtained were used in further analysis and constructing of numerical model of the object.

5. Numerical simulation

In order to simulate the course of the processes and phenomena occurring within the considered sewage collector, a numerical model of the object was constructed. The simulation was carried out with use of ZSoil 2013v.13.09 [Z_SOIL PC 2013 v.13.09; Zace Services; Lausanne 2014] computer program. Individual sections of the collector were drawn in the AutoCAD software. Then, their geometry was implemented into the Z-Soil program. The calculations were carried out on the assumption of an already raised object, plane strain state and steady filtration. The construction of the collector was reflected in individual parts of the model as accurately as possible.

In the initial stage, the situation was simulated in the 2D model, in regard to different sections of the collector. The following step was 3D simulation in regard to 10 m long section of the collector. The material parameters in the various areas of the model were diversified, while carrying out calculations in order to reflect processes and phenomena occurring within the construction. On this basis, determining the most likely causes of occurring damage and forecast of their further development in time was possible.

5.1. The 2D model

2D simulating was carried out as preliminary calculations in the preparation process of a three-dimensional model of the collector. In the following stages, fields showing individual material areas were created and their parameters were defined (Fig. 7). Material properties of the subsoil were determined on the basis of conducted geological research. In the analysis, typical geotechnical boundary conditions were implemented: horizontal displacements on the outer vertical edges and displacements in both horizontal and vertical direction on the bottom edge of the model were blocked. In addition, the position of the groundwater table was taken into account. In the point of contact of the collector lining and the ground, contact elements of interface type were used (Fig. 7). One elastic-plastic model with Coulomb-Mohr yield criterion was comprehensively used in the calculations.

The specification of material property values used in calculations and presented in the legend of the pictures is shown in Table 1. Due to the lack of the reliable data, the dilatation angle values were omitted.

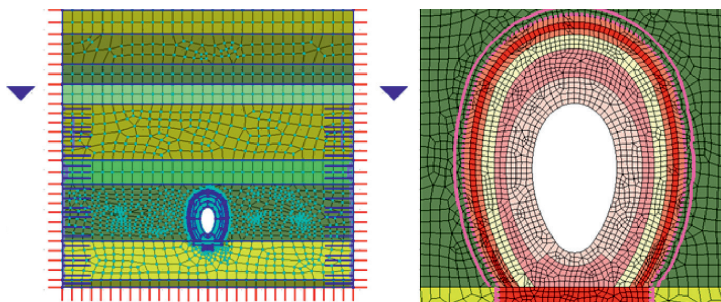


Fig. 7. 2D model generated by Z-Soil (source: own elaboration)

Table 1. The material parameters used in the numerical calculations

No.	Material	E [MPa]	ν [-]	γ [kN/m ³]	k [m/d]	ϕ [°]	c [kPa]
1	Sewer brick	30000	0.20	20	0.00011	45	2360
2	Concrete	23100	0.20	23	0.05	45	3350
3	Reinforced concrete cladding	32000	0.30	25	1	45	5000
4	Wood	200	0.25	5	1	45	2000
5	Steel	205000	0.25	25	0	45	5000
6	Gravel	200	0.20	21.0	100	40	0
7	Silt	50	0.30	21.0	0.5	20	20
8	Sandy clay	150	0.30	22.5	0.5	20	20
9	Loamy sand	50	0.30	22.0	1	20	5
10	Silty clay	50	0.30	21.0	0.5	20	20
11	Sandy loam	100	0.30	21.0	0.5	20	20
12	Coarse sand	150	0.25	20.0	25	35	0

Typical symbols were used in the Table:

E – Young's modulus,

ν – Poisson's ratio,

γ_d – soil/soil skeleton volume density,

c – cohesion,

ϕ – angle of internal friction,

k – coefficient of permeability (Darcy's coefficient).

The calculations were carried out for several different scenarios. In the first one, the process of steady filtration on the assumption of tight collector cladding was analyzed. Afterwards, the influence of local leakages on the course and intensity of the filtration phenomena was simulated. For this purpose, the material parameter values were locally reduced by increasing the value of the hydraulic conductivity coefficient. An elastic-plastic analysis of the construction was carried out in order to determine stress distribution and tensile stresses. To show damages and failures, appropriate material parameters were successively modified with reference to particular areas (E , ϕ , c). Tensile stresses are particularly dangerous to the collector cladding for they can lead to scratches and leakage in the construction. The results of filtration calculations are presented in Fig. 8 as velocity vectors within the analyzed model. The vectors indicate directions of water flow. Lengths of individual vectors are proportional to flow velocity. On the basis of the calculations, it can be noticed that the largest flow concentration occurs directly under the structure (gravel and drains) and in the soil layer above the collector. These are the places of potential suffusion processes, which can result in local deterioration of the material properties of the subsoil.

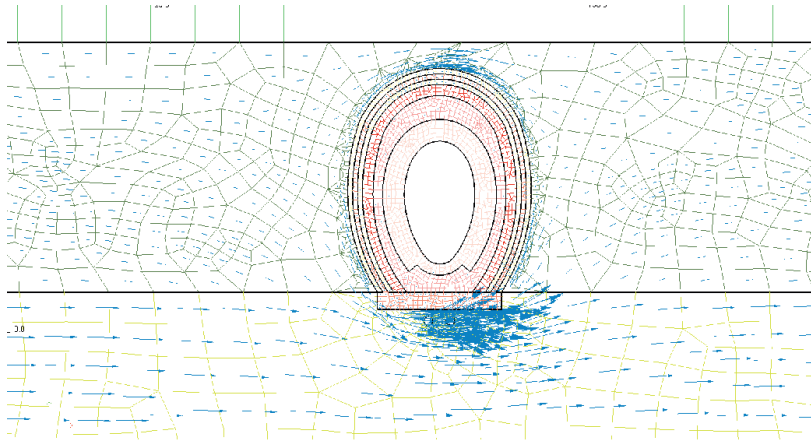


Fig. 8. Vectors of water flow velocity (source: own elaboration)

Stress distribution of the collector lining is presented in Fig. 9. Tensile stresses were marked in red. Occurrence of the tensile stresses in that area may cause chink forming in the mortar or its flaking off the bricks. Both these factors are conducive to forming of preferential leak paths. During field researches, leakages in the upper part of the collector were frequently observed.

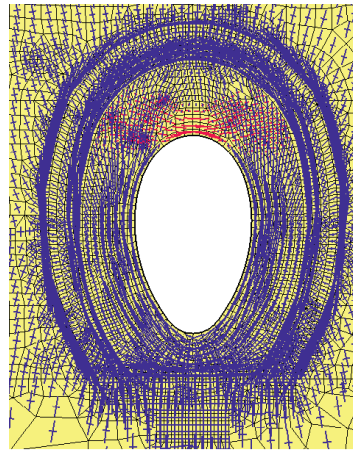


Fig. 9. Tensile stresses in the collector vault (source: own elaboration)

While carrying out further calculations, the material parameter values were being diversified in the individual areas of the model. The course of processes and phenomena within the structure was reflected as accurately as possible. This way, determining the most likely causes of damages was possible. In addition, prognosis of their further development in time and influence on the soil nearby the structure was made. Two variants in which material parameter values were reduced in the upper and lower part of the collector cladding were simulated.

In the first stage, calculations reflecting the potential influence of the tensile stresses in the vault were performed. Then, the possibility of damage in lower parts of the collector cladding was analyzed. This type of damage could have been caused by e.g. incorrect connection of the sewer connectors or subsidences induced by decaying (biological corrosion) of the wooden base made of steel frames. The conducted analysis of the results unambiguously showed the possibility of soil transferring into the collector, which would pose the explanation for locally increased sediment accumulation. Concentration of the flow in the soil occurs directly on the external walls of the collector. The discussed processes were observed and described in the documentation system of WMWSSC (MPWIK) works while repairing the failure near Tapicerska and Instalatorów Streets in Warsaw.

The following step of the calculations was displacement and deformation analysis nearby the structure. For this purpose, the calculations were carried out once more, having taken into account the aforementioned material parameters. The boundary conditions used in this stage were identical as in filtration analysis. Moreover, the load generated by traffic on the ground surface was taken into account. The second stage of the displacement analysis was implementing local decrease of material parameter values of the soil in the immediate vicinity of the collector and above it. Their values are in the range of suffosion danger. The values of deformation module, cohesion and angle of internal friction were modified, mainly in regard to cohesive soil (silts) above the collector. The obtained results confirmed the possibility of ground surface subsidences, which is consistent with field research observations.

5.2. 3D model

The three-dimensional model of the considered collector was generated according to the geometry used before in 2D simulation. It was used to analyze the ground relaxations, which occur locally on the analyzed collector length and to illustrate subsidence of the surface ground in a better way. In that stage, the model of a 10 m long section of the collector, consisting of two 3 m long parts and four 1 m sections between them, was generated. The geometry of points and lines was elaborated using the AutoCAD software. Then, it was imported into the Z-Soil program. Using the program, appropriate three-dimensional solids reflecting the construction of the collector and soil layers nearby were created. The virtual mesh was created by adding new nodes to the already generated elements. It allowed to cover the whole model with mesh coherently.

In the calculations, identical material parameter values as in 2D simulation were implemented. The same type of boundary conditions was used, which is blocking of horizontal displacements on the external vertical edges of the model and blocking of displacements in vertical and horizontal direction on the bottom edge of the model. The elastic-plastic model with Coulomb-Mohr yield criterion was used in the calculations for all material areas, which were taken into account.

The boundary conditions in the calculations were used in the form of variable ground water levels and traffic loads (tram trackway is located directly above the collector). In the zone between the collector and the ground adjacent to it, the elements of interface type were used once more (Fig. 10). Soil loosening was also assumed in the calculations. For this



purpose, geotechnical parameters (E , φ , c) of the sandy loam, silt and silty clay layer were reduced. This way, potentially occurring suffosion processes associated with detrimental filtration phenomena were simulated.

In the area of soil loosening, increased subsidences of the ground surface were noticed (Fig. 10). This confirms previous observations, taken near Tapicerska Street. This situation puts ground infrastructure safety at risk. What is more, it can also generate additional tensile stresses in the construction of the collector. Directly in the area of soil loosening, displacements of the upper surface of the model were noticed. These processes can be additionally intensified by both progressive suffosion and effects of dynamic factors. Consequently, there is a risk of ground surface collapse, which can result in building disaster.

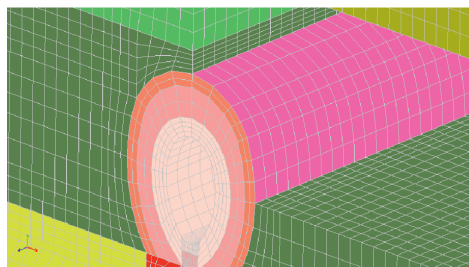


Fig. 10. The contact zone between the collector and the ground (source: own elaboration)

6. Conclusion

The conducted field researches and compression test allowed to determine the condition of the lining bricks as satisfactory. Both infiltrating water and solid samples showed a high content of calcium compounds. This indicates that the collector lining concrete undergoes degradation and leaching out of the hydration products. The mortar is prone to the same processes. Increase of the permeability coefficient (Darcy's coefficient) is followed by strong water flow into the collector. Migration of the soil particles into the object is confirmed by local accumulations of sediments.

Because of detrimental groundwater conditions and flow concentration near the collector cladding, the occurrence of suffosion processes in the subsoil was assumed. These phenomena are recognized by local loosening of the soil, which results in local subsidences.

In each of the analyzed cases, tensile stresses occurred in the upper parts of the collector. The usual indications of their formation are numerous cracks and scratches. These are the places of a particularly intensive groundwater leakage into the object. Results of analysis carried out with the use of the 3D model explain the reasons for ground collapse near Tapicerska Street, which was caused by suffosion processes in silty soils above the collector.

Wooden beams used as a support for steel frames of the reinforced concrete cladding have a negative effect on the current work of the collector. After years of work, they have undergone serious damages due to wood decay process. The idea of using these construction elements proved to be a project mistake.

Currently, the main purpose of the collector modernization should be reducing the inflow of infiltrating water as well as tightening of the collector along with sealing its lining.

Examples of solutions that are possible to implement include:

- ▶ constructing of a new collector,
- ▶ use of GRP modules,
- ▶ use of sleeve,
- ▶ compaction grouting technology and chemical technologies.

Construction of a new collector is not possible due to legal reasons (obtaining a construction permit is a long-lasting process) as well as technical causes: a new object would have to be connected to sewer connector pipes.

The whole situation is additionally complicated because of the social costs of potential maintenance works, which would result from the fact that the collector is located under one of the most important roads of Warsaw.

The use of GRP modules seems to be a problematic solution, as they must be input inside the collector. The implementation of this method would require building shafts and chambers. Intensively conducted works on the ground surface could lead to a significant increase of the investment costs. The elaborate shape of the cross section of the collector (extended ovoid) constitutes an obstacle to use the so-called sleeve. In addition, providing constant contact of the lining with the wall of the collector, particularly in the upper part of its cross section, poses some difficulty. This solution cannot be implemented due to risk of potentially creating preferential leakage paths. In addition, it must be noticed that the latter two solutions would result in the reduction of the cross sectional area of the collector and its capacity.

In these conditions, the optimal solution is using local compaction grouting technology in sites, which are most endangered by groundwater infiltration, along with applying thermosetting lining on the walls of the collector. Instead of thermosetting lining, mortar rich with highly penetrating compounds may be used. The introduction of this solution would provide construction tightness as well as an increase of the strength parameter values of the whole lining and soil surrounding of the collector.

Using this technology, renovation costs are proportional to the quantity of used material (injection substance). Determining the quantity and effectiveness of the method is not possible at this stage of research. Another essential issue is the number of necessary holes. The method of performing injections should also be considered. It can be realized vertically, from the inside of the collector or horizontally from sewer manholes.

In this case, construction of modernization test sections is indispensable. Conducting an accurate assessment is also necessary.

7. Findings

- ▶ While performing technical condition assessment of a collector, taking into account soil conditions of its foundation place is indispensable.

- ▶ Carrying out a geotechnical research, including investigation of groundwater conditions in the place of foundation, especially in the surroundings of changes inside the collector, is indispensable in order to perform the technical condition assessment.
- ▶ Changes of groundwater conditions have a significant influence on the condition of the collector as well as infrastructure nearby.
- ▶ Inappropriate choice of construction materials (wooden beams) combined with adverse groundwater conditions is the main reason for failures and operational problems in case of the considered object.
- ▶ Periodical technical condition assessments of collectors' built with use of similar technology are essential for further operation of these objects.
- ▶ The suffosion process can result in severe damages of hydrotechnical constructions. It should be taken into account while analyzing technical condition assessments of underground structures.
- ▶ Numerical modelling provides broad opportunities for technical condition assessing of constructions. However, the accuracy of calculations depends on the assumed material parameter values and calculation variants.
- ▶ Technologies of modernization depend on execution and economic factors.

References

- [1] Bolt A., Burszta-Adamiak E., Gudelis-Taraszkiewicz K., Suligowski Z., Tuszyńska A., *Kanalizacja. Projektowanie, wykonanie, eksploatacja*, Seidel-Przywecki Ltd. Publishing, 2012.
- [2] Cała M., Tajduś A., Tajduś K., *Geomechanika w budownictwie podziemnym. Projektowanie i budowa tuneli*, AGH University of Science and Technology Publishing, Cracow 2012.
- [3] Glinicki S., *Budowle podziemne*, University of Technology Publishing, Białystok 1994.
- [4] Kobiak J., Stachurski W., *Konstrukcje żelbetowe*, Vol. I, III, Arkady, Warsaw 1984.
- [5] Kodura A. et al., *Analiza stanu kolektora III klasy w Al. Krakowskiejna odcinku od Stacji Pomp Kanałowych OCHOTA do ul. Rękodzielniczej*, Warsaw 2014.
- [6] Madryas C., Kolonko A., Wysocki L., *Konstrukcje przewodów kanalizacyjnych*, University of Technology Printing House, Wrocław 2002.
- [7] Madryas C., Wysocki L., *Badania stanu technicznego XIX-wiecznych ceglano-kamiennych kolektorów kanalizacyjnych – studium przypadków*, Technical Transactions 2-B/2009, Cracow 2009.
- [8] Neville A.M., *Właściwościbetonu*, The Association of Concrete Producers, Cracow 2012.
- [9] Lambe William T., Whitman R.V., *Mechanika Gruntów*, Vol. I, II, Arkady.
- [10] ZSOIL.PC-*Getting started*.(2013). Elmeppress International, Zace services Ltd.
- [11] Polish Standard PN-B-03002-1999 *Konstrukcje murowe niezbrojone. Projektowanie i obliczanie*.
- [12] Polish Standard PN-81-B-03020 *Grunty budowlane. Posadowienie bezpośrednie budowli. Obliczenia statyczne i projektowanie*.
- [13] The project documentation shared by WMWSSC (MPWiK).



Małgorzata Kryłów (gosiak@wis.pk.edu.pl)

Piotr Rezka

Institute of Water Supply and Environmental Protection, Faculty of Environmental Engineering, Cracow University of Technology

POLYBROMINATED FLAME RETARDANTS IN SEWAGE SLUDGE AND SEDIMENTS (REVIEW)

POLIBROMOWANE ŚRODKI OBNIŻAJĄCE PALNOŚĆ W OSADACH ŚCIEKOWYCH I DENNYCH (PRZEGLĄD)

Abstract

This paper is a wide review of literature concerning the presence of flame retardants in sediments, treated wastewater, sewage sludge and the possibilities of their biodegradation. These compounds are widely applied in, for example, the textile and electronics industries. Flame retardants (FRs) are hydrophobic with very low solubility in water; however, they are released slowly during the washing of clothing, and as a result of the discarding of waste electronic products, etc. FRs show low mobility in the environment and can accumulate in wastewater, sewage sludge, in sediments in the beds of rivers and lakes, and in soil. Total concentrations of polybrominated diphenyl ethers (PBDEs) ranged from 0.59 to 48.000 ng/g d.w and decaBDE (BDE 209) concentrations from 0.4 to 47,400 ng/g d.w. BDE 209 dominated the congener profile.

Keywords: PBDE, FRs, wastewater treatment plant, WWTP, sewage sludge, sediments

Streszczenie

W artykule przedstawiono przegląd literatury dotyczący występowania związków obniżających palność w osadach dennych, ściekach i osadach ściekowych oraz możliwości ich biodegradacji. Związki te są szeroko stosowane, np. w przemyśle tekstylnym i elektronicznym. Środki niepalniące są substancjami hydrofobowymi o bardzo niskiej rozpuszczalności w wodzie, jednakże są powoli uwalniane podczas prania odzieży lub wmywane ze składowisk odpadów. Wykazują dość niską mobilność w środowisku i mogą kumulować się w osadach ściekowych, osadach dennych rzek i jezior oraz w glebie. Stężenia opisywanych polibromowanych eterów difenyłowych (PBDEs) wynosiły od 0,59 do 48,000 ng/g suchej masy, a stężenia decaBDE (BDE 209) wynosiły 0,4–47,400 ng/g s.m. BDE 209 zdominował profil kongenerów.

Słowa kluczowe: PBDE, środki obniżające palność, oczyszczalnia ścieków, osady ściekowe, osady denne

1. Introduction

In recent decades, most of the attention related to persistent organic pollutant (POP) monitoring has focused on the release of these chemicals resulting from production, use and their environmental occurrence. Contemporary studies have shown that wastewater treatment plants (WWTPs), which treat waste primarily from domestic and industrial origins, are sources of POPs and require further investigation with regards to their overall contribution to the contaminant burden on the environment [9, 44]. Widely available consumer products containing these compounds can end up becoming a source of these contaminants. This is the case for flame retardants (FRs) which are chemicals added to an extensive variety of manufactured items in order to inhibit or delay combustion processes [63]. To date, at least seventy-five different brominated flame retardants (BFRs) [2] have been commercially produced. So far, studies have been primarily focused on three groups: polybrominated diphenyl ethers and biphenyls (PBDEs and PBBs); hexabromocyclododecanes (HBCDs); tetrabromobisphenol A (TBBP-A) [9]. The structures of selected organic pollutants are presented in Fig. 1.

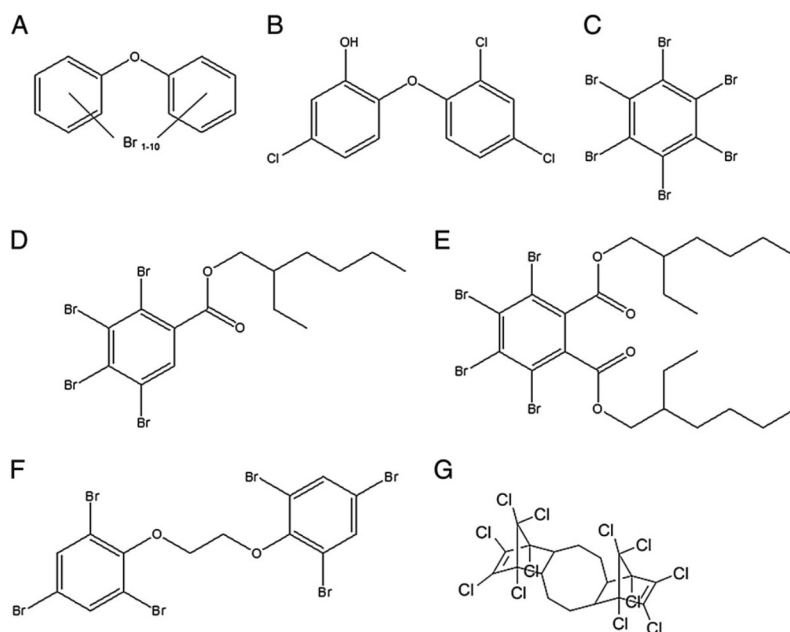


Fig. 1. Structures of (A) PBDEs, (B) triclosan, (C) HBB, (D) TBB, (E) TBPH, (F) BTBPE, and (G) DP [12]

Hexabromocyclododecane (HBCD) is used as a flame retardant mainly in building insulation composed of extruded or expanded polystyrene foam (over 85% of total volume) and some minor uses as backings of upholstery textiles [12]. Since HBCD is used as a flame retardant in several applications, it has the potential for release into the environment from production processes and from the disposal of products containing fire retardants. These

compounds are very hydrophobic and have been reported to be persistent in the environment [3]. With increased regulatory attention directed towards elimination or reduction of discharges, and emissions and losses of organic compounds, it is important that we have a good understanding of the environmental fate and lifetime of HBCD. Moreover, HBCD is listed as a priority substance under the EU Existing Substance Regulations (793/93/EEC) and is currently undergoing a risk assessment in the EU [14]. In the early 1990s, decabromodiphenyl ethane (deBDEthane) was introduced as an alternative to its polybrominated diphenyl ether (PBDE) analogue, decabromodiphenyl ether (DecaBDE). Over the past twenty years, PBDEs have been shown to be ubiquitously present and persistent in the environment.

2. Biodegradation

Reductive debromination of TBBPA was shown to occur under anaerobic conditions in sediments. In the year 2000, Ronen & Abeliovich observed the degradation of more than 90% of the initially present TBBPA within fifteen days [57]. Voordeckers et al. [65] reported rapid degradation of TBBPA after a duration of sixty days under methanogenic conditions. In both experiments, TBBPA was fully debrominated into bisphenol A (BPA), a well-known estrogenic compound. Depending on the conditions, TBBPA can be biotransformed into BPA (reductive debromination in anaerobic conditions) or TBBPA DME (dimethyl ether) and TBBPA monomethyl ether (O-methylation in aerobic conditions) [41]; however, recent studies have demonstrated a low mineralisation potential for TBBPA in anaerobic digester sludge, soils and freshwater sediments [40]. Mono-, di-, and tri-brominated bisphenol A were identified as intermediate products in an anaerobic batch reactor [4]. The rapid anaerobic degradation of a technical HBCD mixture has also been reported [13, 28]. Products of degradation were not identified and enantioselective degradation of HBCD stereoisomers was not addressed in these studies. No significant degradation of DecaBDE was observed by Schaefer and Flaggs [21] in an anaerobic sediment within thirty-two weeks. Additionally, studies in China have indicated limited bioaccessibility of PBDEs in sewage sludge based on their low desorption rate [43]. In contrast to these findings, Gerecke found that, in fact, DecaBDE slowly degrades under anaerobic condition in sewage sludge [21]. He observed a decrease of the DecaBDE concentration with a corresponding pseudo-first order degradation rate constant of $1 \times 10^{-3} \text{ d}^{-1}$. Reductive dehalogenation was indicated by the formation of octa- and nona-bromodiphenyl ether congeners. Gerecke et al. [20] suggested that pseudo-first-order degradation rate constants decreased according to the following sequence: $\text{TBBPA} \cong (\pm)\text{-}\gamma\text{-HBCD} \cong (\pm)\text{-}\beta\text{-HBCD} > (\pm)\text{-}\alpha\text{-HBCD} \gg \text{DecaBDE}$. DecaBDE ($\log K_{ow} \sim 10$), this is certainly more hydrophobic than the other compounds investigated (HBCD $\log K_{ow} \sim 6$, TBBPA $\log K_{ow} \sim 6$). Therefore, free concentrations of DecaBDE in aqueous environments will be lower than those of TBBPA and HBCD, and this very low free concentration of DecaBDE might be a rate-limiting factor for the biologically mediated transformation of DecaBDE.

Reductive debromination of BDE-209 in the environment could constitute a significant source of lesser-brominated PBDEs to biota. A more recent study [62] showed that BDE-



209 debrominates in sewage sludge and another demonstrated that some halo-respiring bacteria will debrominate BDE-209. To determine whether the reductive debromination of BDE-209 occurs in sediments, parallel experiments were conducted using anaerobic sediment microcosms. In the biological system, reductive debromination occurred at rates corresponding to bromine substitution levels with a BDE-209 half-life of only eighteen seconds in comparison with a half-life of almost sixty days for 2,2',4,4'-tetrabromodiphenyl ether. In sediment, the measured debromination half-life of BDE-209 was well over a decade – this strongly agreed with the predicted value obtained from the biological experiment. Product congeners were predominantly double para-substitute. BDE-209 debrominated in sediment with a corresponding increase in nona-, octa-, hepta-, and hexa-PBDEs. Nine new PBDE congeners appeared in sediment from reductive debromination; furthermore, there is evidence for the debromination of PBDEs that occur in aquatic biota [35].

Less brominated congeners, such as penta- and tetra-BDEs, are more toxic and have higher bioavailability than more highly brominated congeners, such as octa-BDEs [46, 47]. It is therefore important to understand the dominant debromination pathways in order to predict the likely congeners produced from the transformation of environmentally prevalent PBDEs [54]. According to Rodenburg et al. [55], the location of degradation is also very important. If microbial debromination occurs in sediments, then, in the long run, PBDEs will be less persistent and will have a lower tendency to accumulate in sediments. If debromination occurs in sewers, then products of debromination could accumulate more easily in sediments and be problematic in the future – this is consistent with studies conducted by La Guardia et al. [36], who stated that PBDE 47 has a greater biota-sediment accumulation factor than PBDE 209 and could result in greater bioaccumulation of PBDEs in some organisms. Stiborova et al. [60] investigated the potential of autochthonous microflora for the removal of PBDEs and HBCDs in sludge under anaerobic conditions for fifteen months (Table 1). HBCDs were degraded to below detection limits after three months of incubation. The higher brominated congeners were removed faster than those which were lower brominated; however, there was a significant increase in tetra-brominated BDE-49. This implies that degradation of predominant BDE-209 could result in increased concentrations of more toxic lower brominated PBDEs. The initial concentrations of PBDE's and HBCD's are provided in Table 1 [60].

Table 1. The initial concentration of individual PBDE congeners and HBCD and their percentage residues after fifteen months of degradation [60]

Congener	Hradec Kralove		Brno	
	Initial concentration [ng/g d.w.]	PBDEs residue [%]	Initial concentration [ng/g d.w.]	PBDEs residue [%]
Tri-BDE-28	7.9 ± 0.1	Not detected	2.2 ± 0.1	Not detected
Tetra-BDE-47	216.6 ± 1.7	57.9 ± 8.8	54.2 ± 1.6	80.7 ± 14.8
Tetra-BDE-49	18.2 ± 0.5	240.3 ± 35.9	9.6 ± 0.4	249.7 ± 18.2

Tetra-BDE-66	11.2 ± 0.1	62.1 ± 6.6	4.8 ± 0.9	58.6 ± 2.0
Penta-BDE-85	17.5 ± 0.2	107.3 ± 23.7	7.5 ± 0.1	138.3 ± 60.2
Penta-BDE-99	208.8 ± 2.1	57.3 ± 4.7	57.0 ± 1.5	60.9 ± 15.9
Penta-BDE-100	55.3 ± 1.0	81.5 ± 6.9	17.2 ± 1.1	47.6 ± 1.9
Hexa-BDE-153	23.3 ± 0.5	54.5 ± 2.1	12.9 ± 0.1	0.9 ± 1.3
Hexa-BDE-154	22.2 ± 0.1	51.6 ± 4.2	12.8 ± 0.1	23.2 ± 2.2
Hepta-BDE-183	24.3 ± 0.7	17.8 ± 2.2	27.1 ± 0.5	17.7 ± 1.2
Deca-BDE-209	685.3 ± 25.7	42.5 ± 8.5	1402.6 ± 44.6	26.5 ± 1.2
Tetra-BDEs	246.0 ± 1.3	73.9 ± 10.7	68.6 ± 0.1	102.8 ± 12.5
Penta-BDEs	281.6 ± 1.9	65.2 ± 7.3	81.7 ± 1.9	65.2 ± 3.1
Hexa+hepta-BDEs	69.8 ± 0.1	40.8 ± 1.6	52.8 ± 0.3	14.9 ± 0.3
Σ10 BDEs	605.3 ± 5.6	64.1 ± 7.4	205.3 ± 2.6	64.1 ± 3.2
Σ11 PBDEs	1290.6 ± 20.1	52.6 ± 8.0	1607.9 ± 47.1	31.3 ± 1.3
HBCD	23.9 ± 0.9	Not detected	19.6 ± 1.2	Not detected

3. Flame retardants in sewage sludge and sediments

While the use of FRs may spare lives and reduce material damage costs incurred during fires, these compounds are able to leach out of products and find their way into the environment, in particular, via WWTPs. Being largely lipophilic, organic FRs are predisposed to binding to lipid-rich sewage sludge once in the WWTP stream. Mass balance calculations of the widely-used flame retardant, polybrominated diphenyl ethers (PBDEs), concluded that 96% are sorbed to sewage sludge [63]. In 2007, Knoth analysed sewage sludge from eleven municipal wastewater treatment plants in Germany. Samples were collected from WWTP of the Rhine-Main in Germany from March 2002 to June 2003. Knoth observed no significant change to the congeners' profile (% of total BDE 28,47,99,153,154 without 209) in sludge sample from different stages of the wastewater treatment process (primary sludge, secondary excess sludge and digested sludge) indicating a degradation of DeBDE for these congeners [33]. The data from this experiment is presented in Table 2.

The highest levels of decaBDE were found in the USA and the United Kingdom, these levels were up to 19,000 and 12,000 ng/g d.w., respectively. Findings in the USA are unsurprising considering that they had the world's highest market demand for decaBDE in 2001 [37]. The per capita market demand for decaBDE in the United Kingdom was suggested to be in line with that of North America due to the UK's history of restrictive fire regulations [25]. It was in samples from the UK that Harrad et al. [25] found the highest ever recorded decaBDE levels in domestic or office dust, these levels were 520,000 and 100,000 ng/g on a dry weight basis. Relatively high decaBDE levels were also found in one sample from New



Zealand and in one sample from China (9500 and 3300 ng/g d.w., respectively). Wang et al. [67] reported decaBDE levels between <LOD and 1108 ng/g d.w. in sludge from thirty-one WWTPs in China. A lot of the Asian production of decaBDE takes place in eastern China [66], this is where both of the Chinese samples in the presented data set originate. In Table 3, the concentrations of FRs in sediments are given.

Table 2. Concentrations of significant PBDE in sewage sludge from different stages of the wastewater treatment process [33]

WWTP/population equivalent	Sludge	Concentration [ng/g d.w.]	
		DeBDE 209	ΣCongeners 28–209
45,000 (3)	Primary sludge	169–225	242–281
	Digested sludge	193–354	269–450
	Dewatered digested sludge	135–450	221–558
48,000 (1)	Primary sludge	256	494
	Secondary excess sludge	341	569
	Digested sludge	690	960
	Dewatered digested sludge	556	781
50,000 (1)	Primary sludge	1895	2104
	Secondary excess sludge	2217	2491
	Digested sludge	1339	1627
63,500 (1)	Primary sludge	239	328
	Secondary excess sludge	234	321
	Digested sludge	605	699
	Dewatered digested sludge	417	523
75,000 (2)	Primary sludge	169–217	182–266
	Secondary excess sludge	182	294
	Digested sludge	411–1141	520–1261
	Dewatered digested sludge	204–340	280–452
240,000 (1)	Primary sludge	199	234
	Secondary excess sludge	334–486	466–640
	Digested sludge	393	537
350,000 (1)	Primary sludge	97.1	142
	Secondary excess sludge	206–220	352–437
	Digested sludge	217	266
1,820,000 (1)	Primary sludge	209	305
	Secondary excess sludge	182	264
	Dewatered digested sludge	133	186

Table 3. Concentrations in ng/g of dry weight (min–max or max) of flame retardants in sediments

Compound	Concentration in ng/g d.w.		References	
	Sewage sludge	Sediments	Sewage sludge	Sediments
BDE-17	0.89–42.2	–	[12, 38, 64]	–
BDE-28	0.2–73	–	[12, 34, 38, 49, 64]	–
BDE-47	0.81–1133	0.031–62.3	[5, 12, 15, 34, 38–39, 49, 56, 64]	[5, 10, 11, 29, 50]
BDE-49	0.6–62	0.020–0.053	[34, 64]	[29]
BDE-66	0.2–26.1	–	[12, 34, 38, 64]	–
BDE-85	0.12–57	0.016–0.151	[12, 34, 38, 64]	[29]
BDE-99	1.17–1510	0.022–59	[5, 12, 15, 34, 38–39, 49, 56, 64]	[5, 10, 11, 29, 50]
BDE-100	0.8–311	0.014–0.241	[5, 12, 15, 34, 38, 39, 49, 64]	[5, 29]
BDE-153	0.06–145	0.01–2.18	[5, 12, 15, 34, 38–39, 49, 64]	[5, 29]
BDE-154	0.08–128	0.016–4.29	[5, 12, 15, 34, 38–39, 49, 64]	[5, 29]
BDE-183	0.3–32.6	0.01–9.14	[12, 34, 38, 39, 56, 64]	[5, 29]
BDE-196	0.2–18.1	0.212–0.549	[38–39]	[29]
BDE-197	0.4–19.9	0.132–0.259	[38–39]	[29]
BDE-203	0.2–59.2	0.153–0.577	[38–39]	[29]
BDE-206	12–1420	0.440–7.93	[12, 38, 64]	[29]
BDE-207	6.43–1430	0.060–1.64	[12, 38, 64]	[29]
BDE-208	7–965	–	[12, 64]	–
BDE-209	0.54–47400	0.03–970	[5, 12, 15, 17, 22, 24, 30, [33–34, 38, 39, 56, 64]	[5, 10–11, 29, 30, 50, 71, 72]
Σ PBDEs	0.59–48000	0.36–910	[12, 17, 22, 24, 30, [33, 38, 63]	[5, 7, 11, 30, 32, 50, 72]
TBBPA	0.016–76	0.06–127	[15, 39]	[29, 61]
BPA	262–3590	4.5–100	[23]	[23]
Σ HBCD	0.008–9120	0.005–9.4	[15, 30, 45, 51, 68, 69]	[18, 30, 32, 50, 72]
α-HBCD	0.003–358	0.04–3.9	[30, 39]	[29–30, 32]
γ-HBCD	0.009–26	0.04–1.95	[30, 39]	[29–30, 32]
γ-HBCD	0.005–9.3	0.005–38.4	[30, 39]	[29–30, 32]



Ricklund et al. [52] also detected DBDPE in sewage sludge from all forty-two WWTPs studied in twelve countries worldwide, suggesting that DBDPE is a widespread contaminant, in Europe at least. The highest concentration observed (216 ng/g d.w.) was in a sample from the Ruhr area of Germany. BTBPE, DBDPE and TBBPA-DBPE were determined in sewage sludge samples from southern China [59]. Maximum concentrations of these compounds were 1.7 ng/g, 2000 ng/g and 8950 ng/g d.w., respectively. The high concentrations of DBDPE and TBBPA-DBPE are consistent with their use in the electronics industry in the Pearls' River Delta (PRD) region of China. Primary sludge samples from South Africa contained HBCD (10.69–133.16 ng/g d.w.), TBBPA (19.24 ng/g d.w.) and polybrominated biphenyls – PBB-18, PBB-49 and PBB-101 (14.717, 3.94–15.32 and 14.01–87.96 ng/g d.w., respectively) [8]. Sewage sludge samples collected from the city of Guangzhou in southern China in 2007 had BTBPE concentrations ranging from 0.31 to 1.66 ng/g d.w. with a mean of 0.88 ng/g d.w. [59]. The concentrations of PBDEs in sludge in this study are generally lower than those reported in studies around the world (see Table 3). Hale et al. for example, reported concentrations ranging from 1100 and 2290 µg/kg for samples collected from 11 wastewater treatment plants from four regions in the United States [24]. In another study, North reported similar concentrations with values ranging from 1918 to 2086 µg/kg [48] for sludge samples collected from wastewater treatment plants in Palo Alto, California. In European countries, the levels of PBDEs in sludge from municipal sources are much lower than those in North America by almost one order of magnitude. Sellstrom et al. [58] reported PBDEs in sludge from three sewage treatment plants from Sweden ranging from 140 to 350 µg/kg whereas that reported by Hellstrom [26] were between 8.5 and 275 µg/kg for fourteen wastewater treatment plants also from Sweden. Slightly higher values were reported by Fabrellas et al. [17] in samples collected from six wastewater treatment plants in Spain ranging from 844 to 5939 µg/kg. One of the plants receiving wastewater from an industrial area manufacturing textiles had PBDE sludge concentrations as high as 18146 µg/kg [17].

4. Level of deBDethane

The level of deBDethane found in Germany is at 220 ng/g d.w., the highest so far reported in literature. This is higher than the mean levels for the European samples (81 ng/g d.w.) and the North American samples (31 ng/g d.w.) by factors of 2.7 and 7.0, respectively. The WWTP is located in a highly industrial area (the Ruhr Region) of Germany. According to the sampling protocol, the WWTP receives water from the automobile industry – the automobile industry is a known user of BFRs [19]. There were 3 other samples from the Ruhr Area containing deBDethane levels of 121, 74 and 70 ng/g d.w. Two of these were also among the ten highest in this study. The other eight came from Switzerland, the Czech Republic, China, Singapore, and the USA. There was no information in the sampling protocols suggesting particular industrial sources. However, Germany was reported to account for a majority of the total import of deBDethane into Europe in 2001 [31, 52]. The high levels in sludge from Germany as well as Switzerland and the Czech Republic, which both have close economic



ties to Germany, are consistent with high imports of goods containing FRs'. Unfortunately, more information on the import of deBDethane to the countries studied was not found [52].

Two other studies have reported the presence of deBDethane in sewage sludge. In sludge from eight Spanish WWTPs, deBDethane levels ranged between 0.2 and 15 ng/g d.w. [16], while in ten Canadian sludges, these levels were between 6 and 30 ng/g d.w. [42]. The levels in the Spanish sludge were more than five times lower than the European mean in this study, while the levels from Canada presented by McCrindle et al. [42] were in the same range as the Canadian mean for this study [9].

5. Conclusions

Sewage treatment methods have been evaluated and the results indicate that using the biological N and P elimination treatment method can contribute to the decrease of flame retardant concentrations in sludge. BFR (PBDEs and DP) concentrations correlate with levels of industrial contributions to the wastewater stream. This implies that the release of these compounds is related to industrial activity, likely stemming from the use of the technical product during the manufacture of consumer goods. However, use and disposal of products containing PBDEs could not be dismissed. There is a potential for the bioaccumulation of this class of chemicals from sludge treated soils in food chains, thereby contributing to wildlife and human exposure to these chemicals. Therefore, new methods of bioremediation, such as the usage of spent mushroom compost which shows high TBBPA removal efficiency [70], should be considered.

References

- [1] Abramowicz D.A., *Aerobic and anaerobic biodegradation of PCBs: A review*, Critical Reviews in Biotechnology, Vol. 10, 1990, 241–251.
- [2] Alae M., Arias P., Sjodin A., Bergman A., *An overview of commercially used brominated flame retardants, their applications, their use patterns in different countries/regions and possible modes of release*, Environment International, Vol. 29, 2003, 683–689.
- [3] Alae M., Wenning R.J., *The significance of brominated flame retardants in the environment: current understanding, issues and challenges*, Chemosphere, Vol. 46, 2002, 579–582.
- [4] Arbeli A., Ronen Z., *Enrichment of a microbial culture capable of reductive debromination of the flame retardant tetrabromobisphenol-A, and identification of the intermediate metabolites produced in the process*, Biodegradation, Vol. 14, 2003, 385–395.
- [5] Baron E., Santin G., Eljarrat E., Barcelo D., *Occurrence of classic and emerging halogenated flame retardants in sediment and sludge from Ebro and Llobregat river basins (Spain)*, Journal of Hazardous Materials, Vol. 265, 2014, 288–295.
- [6] Bezares-Cruz J., Jafvert C.T., Hua I., *Solar photodecomposition of decabromodiphenyl ether: products and quantum yield*, Environmental Science & Technology, Vol. 38, 2004, 4149–4156.



- [7] Chen S.J., Feng A.H., He M.J., Chen M.Y., Luo X.J., Mai B.X., *Current levels and composition profiles of PBDEs and alternative flame retardants in surface sediments from the Pearls see note in text p. 7 River Delta, southern China: comparison with historical data*, *Science of the Total Environment*, Vol. 444, 2013, 205–211.
- [8] Chokwe T.B., Okonkwo J.O., Sibali L.L., Ncube E.J., *An integrated method for the simultaneous determination of alkylphenol ethoxylates and brominated flame retardants in sewage sludge samples by ultrasonic-assisted extraction, solid phase clean-up, and GC-MS analysis*, *Microchemical Journal*, Vol. 123, 2015, 230–236.
- [9] Covaci A., Harrad S., Abdallah M.A.-E., Ali N., Law R.J., Herzke D., de Wit C.A., *Novel brominated flame retardants: A review of their analysis, environmental fate and behavior*, *Environment International*, Vol. 37, 2011, 532–556.
- [10] Cristale J., Lacorte, S., *Development and validation of a multiresidue method for the analysis of polybrominated diphenyl ethers, new brominated and organophosphorus flame retardants in sediment, sludge and dust*, *Journal of Chromatography A*, Vol. 1305, 2013, 267–275.
- [11] Cristale J., Vazquez A.G., Barata C., Lacorte S., *Priority and emerging flame retardants in rivers: Occurrence in water and sediment, Daphnia magna toxicity and risk assessment*, *Environment International*, Vol. 59, 2013, 232–243.
- [12] Davis E.F., Klosterhaus S.L., Stapleton H.M., *Measurement of flame retardants and triclosan in municipal sewage sludge and biosolids*, *Environment International*, Vol. 40, 2012, 1–7.
- [13] Davis J.W., Gonsior S.J., Markham D.A., Friederich U., Hunziker R.W., Ariano J.M., *Biodegradation and Product Identification of [14C]Hexabromocyclododecane in Wastewater Sludge and Freshwater Aquatic Sediment*, *Environmental Science & Technology*, Vol. 40, 2006, 5395–5401.
- [14] Davis J.W., Gonsior S.J., Marty G., Ariano J., *The transformation of hexabromocyclododecane in aerobic and anaerobic soils and aquatic sediments*, *Water Research*, Vol. 39, 2005, 1075–1084.
- [15] Eljarrat E., Barcelo D., *Sample handling and analysis of brominated flame retardants in soil and sludge samples*, *Trends in Analytical Chemistry*, Vol. 23, 2004, 727–736.
- [16] Eljarrat E., Labandeira A., Martinez A., Fabrellas B., Barcelo B., *Occurrence of the “new” brominated flame retardant, decabromodiphenyl ethane, in sewage sludge from Spain*, *Organohalogen Compounds*, Vol. 67, 2005, 459–461.
- [17] Fabrellas B., Larrazabal D., Martinez M.A., Eljarrat E., Barcelo D., *Presence of brominated diphenyl ethers in Spanish sewage sludges: Important contribution of deca-BDE*, *Organohalogen Compounds*, Vol. 66, 2004, 3755–3760.
- [18] Feng A.H., Chen S.J., Chen M.Y., He M.J., Luo X.J., Mai B.X., *Hexabromocyclododecane (HBCD) and tetrabromobisphenol A (TBBPA) in riverine and estuarine sediments of the Pearl River Delta in southern China, with emphasis on spatial variability in diastereoisomer- and enantiomer-specific distribution of HBCD*, *Marine Pollution Bulletin*, Vol. 64, 2012, 919–925.
- [19] Gearhart J., Posselt H., Dempsey D., Costner P., Griffith C., Juska C., *Toxic at any speed. Chemicals in cars and the need for safe alternatives*, Ecology center report, 2006, <http://pureti.com/content/documents/Ecology-Center-ReportToxic-At-Any-Speed.pdf> (access: 22.06.2016).

- [20] Gerecke A.C., Giger W., Hartmann P.C., Heeb N.V., Kohler H.-P.E., Schmid P., Zennegg M., Kohler M., *Anaerobic degradation of brominated flame retardants in sewage sludge*, *Chemosphere*, Vol. 64, 2006, 311–317.
- [21] Gerecke A.C., Hartmann P. C., Heeb N.V., Kohler H.P.E., Giger W., Schmid P., Zennegg M., Kohler M. *Anaerobic degradation of decabromodiphenyl ether*, *Environmental Science & Technology*, Vol. 39, 2005, 1078–1083.
- [22] Gevao B., Muzaini S., Helaleh M., *Occurrence and concentrations of polybrominated diphenyl ethers in sewage sludge from three wastewater treatment plants in Kuwait*, *Chemosphere* vol. 71, 2008, 242–247.
- [23] Gorga M., Insa S., Petrovic M., Barcelo D., *Analysis of endocrine disrupters and related compounds in sediments and sewage sludge using on-line turbulent flow chromatography-liquid chromatography-tandem mass spectrometry*, *Journal of Chromatography A*, Vol. 1352, 2014, 29–37.
- [24] Hale R.C., Alae M., Manchester-Neesvig J.B., Stapleton H.M., Ikononou M.G., *Polybrominated diphenyl ether flame retardants in the North American environment*, *Environment International*, Vol. 29, 2003, 771–779.
- [25] Harrad S., Ibarra C., Diamond M., Melymuk L., Robson M., Douwes J., Roosens L., Dirtu A.C., Covaci A., *Polybrominated diphenyl ethers in domestic indoor dust from Canada, New Zealand, United Kingdom and United States*, *Environment International*, Vol. 34, 2008, 232–238.
- [26] Hellstrom T., *Brominated flame retardants (PBDE and PBB) in sludge – a problem?*, The Swedish Water and Wastewater Association, Report No M 113 (eng), April 2000.
- [27] Hites R.A., *Polybrominated diphenyl ethers in the environment and in people: A meta-analysis of concentrations*, *Environmental Science & Technology*, Vol. 38, 2004, 945–956.
- [28] Hunziker R.W., Gonsior S.J., MacGregor J.A., Desjardins D., Ariano J., Friederich U., *Fate and effect of hexabromocyclododecane in the environment*, *Organohalogen Compounds*, Vol. 66, 2004, 2275–2280.
- [29] Hlouskova V., Lankova D., Kalachova K., Hradkova P., Poustka J., Hajslova J., Pulkrabova J., *Brominated flame retardants and perfluoroalkyl substances in sediments from the Czech aquatic ecosystem*, *Science of the Total Environment*, Vol. 470–471, 2014, 407–416.
- [30] Ilyas M., Sudaryanto A., Setiawan I.E., Riyadi A.S., Isobe T., Tanabe S., *Characterization of polychlorinated biphenyls and brominated flame retardants in sludge, sediment and fish from municipal dumpsite at Surabaya, Indonesia*, *Chemosphere*, Vol. 93, 2013, 1500–1510.
- [31] Kierkegaard A., *PBDEs in the Environment: time trends, bioaccumulation and the identification of their successor, decabromodiphenyl ethane*, Ph.D. thesis, Department of Applied Environmental Science, Stockholm University, 2007.
- [32] Klosterhaus S.L., Stapleton H.M., La Guardia M.J., Greig D.J., *Brominated and chlorinated flame retardants in San Francisco Bay sediments and wildlife*, *Environment International*, Vol. 47, 2012, 56–65.
- [33] Knoth W., Mann W., Meyer R., Nebhuth J., *Polybrominated diphenyl ether in sewage sludge in Germany*, *Chemosphere*, Vol. 67, 2007, 1831–1837.



- [34] Kupper T., de Alencastro L.F., Gatsigazi R., Furrer R., Grandjean D., Taradellas J., *Concentrations and specific loads of brominated flame retardants in sewage sludge*, Chemosphere, Vol. 71, 2008, 1173–1180.
- [35] La Guardia M.J., Hale R.C., Harvey E., *Evidence of Debromination of Decabromodiphenyl Ether (BDE-209) in Biota from a Wastewater Receiving Stream*, Environmental Science & Technology, Vol. 41, 2007, 6664–6670.
- [36] La Guardia M.J., Hale R.C., Harvey E., Mainor T.M., Ciparis, S., *In situ accumulation of HBCD, PBDEs, and several alternative flame-retardants in the bivalve (Corbicula fluminea) and gastropod (Elimia proxima)*, Environmental Science & Technology, Vol. 46, 2012, 5798–5805.
- [37] Law R.J., Allchin C.R., de Boer J., Covaci A., Herzke D., Lepom P., Morris S., Tronczynski J., de Wit C.A., *Levels and trends of brominated flame retardants in the European environment*, Chemosphere, Vol. 64, 2006, 187–208.
- [38] Lee S., Song G.-J., Kannan K., Moon H.-B., *Occurrence of PBDEs and other alternative brominated flame retardants in sludge from wastewater treatment plants in Korea*, Science of the Total Environment, Vol. 470–471, 2014, 1422–1429.
- [39] Mascolo G., Locaputo V., Mininni G., *New perspective on the determination of flame retardants in sewage sludge by using ultrahigh pressure liquid chromatography-tandem mass spectrometry with different ion sources*, Journal of Chromatography A. Vol. 1217, 2010, 4601–4611.
- [40] McAvoy D.C., Pittinger C.A., Willis A.M., *Biotransformation of tetrabromobisphenol A (TBBPA) in anaerobic digester sludge, soils and freshwater sediments*, Ecotoxicology and Environmental Safety, Vol. 131, 2016, 143–150.
- [41] McCormick J.M., Paiva M.S., Haggblom M.M., Cooper K.R., White L.A., *Embryonic exposure to tetrabromobisphenol A and its metabolites, bisphenol A and tetrabromobisphenol A dimethyl ether disrupts normal zebrafish (Danio rerio) development and matrix metalloproteinase expression*, Aquatic Toxicology, Vol. 100 (3), 2010, 255–262.
- [42] McCrindle R., Chittim B., Konstantinov A., Kolic T., McAlees A., MacPherson K., Reiner E., Potter D., Tashiro C., Yeo B., *Native and mass labeled [13C14]-decabromodiphenylethane: characterization and use in determination of DBDPE in sewage sludge*, Organohalogen Compounds, Vol. 66, 2004, 3744–3750.
- [43] Meng X.Z., Xiang N., Yu L., Zhang J., Chen L., Dai X., *Exploring the bioaccessibility of polybrominated diphenyl ethers (PBDEs) in sewage sludge*, Environmental Pollution, Vol. 207, 2015, 1–5.
- [44] Moon H.B., Yoon S.P., Jung R.H., Choi M., *Wastewater treatment plants (WWTPs) as a source of sediment contamination by toxic organic pollutants and fecal sterols in a semi-enclosed bay in Korea*, Chemosphere, Vol. 73, 2008, 880–889.
- [45] Morris S., Allchin C.R., Zegers B.N., Haftka J.J.H., Boon J.P., Belpaire C., Leonards P.E.G., Van Leeuwen S.P.J., De Boer J., *Distribution and fate of HBCD and TBBPA brominated flame retardants in North Sea estuaries and aquatic food webs*, Environmental Science & Technology, Vol. 38, 2004, 5497–5504.
- [46] Morris P.J., Quensen J.F., Tiedje J.M., Boyd S.A., *Reductive debromination of the commercial polybrominated biphenyl mixture Firemaster BP6 by anaerobic microorganisms from sediments*, Applied and Environmental Microbiology, Vol. 58, 1992, 3249–3256.

- [47] Morris P.J., Quensen J.F., Tiedje J.M., Boyd S.A., *An assessment of the reductive debromination of polybrominated biphenyls in the Pine River Reservoir*, Environmental Science & Technology, Vol. 27, 1993, 1580–1586.
- [48] North K.D., *Tracking polybrominated diphenyl ether releases in wastewater treatment plant effluent, Palo Alto, California*, Environmental Science & Technology, Vol. 38, 2004, 4484–4488.
- [49] Novak P., Zuliani T., Milacic R., Scancar J., *Development of an analytical method for the determination of polybrominated diphenyl ethers in sewage sludge by the use of gas chromatography coupled to inductively coupled plasma mass spectrometry*, Analytica Chimica Acta, Vol. 915, 2016, 27–35.
- [50] Peverly A.A., O’Sullivan C., Liu L.-Y., Venier M., Martinez A., Hornbuckle K.C., Hites R.A., *Chicago’s Sanitary and Ship Canal sediment: Polycyclic aromatic hydrocarbons, polychlorinated biphenyls, brominated flame retardants and organophosphate esters*, Chemosphere, Vol. 134, 2015, 380–386.
- [51] Pulkrabova J., Hajslova J., Poustk J., Hradkova P., *Brominated flame retardants in river sediments and sewage sludges collected in the Czech Republic*, Proceedings of the 4th International Workshop on Brominated Flame Retardants, Amsterdam, Netherlands.
- [52] Ricklund N., Kierkegaard A., McLachlan M.S., *An international survey of decabromodiphenyl ethane (deBDethane) and decabromodiphenyl ether (deca-BDE) in sewage sludge samples*, Chemosphere, Vol. 73, 2008, 1799–1804.
- [53] Ricklund N., Kierkegaard A., McLachlan M.S., Wahlberg C., *Mass balance of decabromodiphenyl ethane (deBDethane) and decabromodiphenyl ether (deca BDE) in a WWTP*, Chemosphere, Vol. 74, 2008, 389–394.
- [54] Robock K.R., Korytar P., Alvarez-Cohen L., *Pathways for the Anaerobic Microbial Debromination of Polybrominated Diphenyl Ethers*, Environmental Science & Technology, Vol. 42, 2008, 2845–2852.
- [55] Rodenburg L.A., Meng Q., Yee D., Greenfield B.K., *Evidence for photochemical and microbial debromination of polybrominated diphenyl ether flame retardants in San Francisco Bay sediment*, Chemosphere, Vol. 106, 2014, 36–43.
- [56] Rodriguez-Rodriguez C.E., Baron E., Gago-Ferrero P., Jelic A., Llorca M., Farre M., Diaz-Cruz M.S., Eljarrat E., Petrovic M., Caminal G., Barcelo D., Vicent T., *Removal of pharmaceuticals, polybrominated flame retardants and UV-filters from sludge by the fungus Trametes versicolor in bioslurry reactor*, Journal of Hazardous Materials, Vol. 233–234, 2012, 235–243.
- [57] Ronen Z., Abeliovich, A., *Anaerobic–aerobic process for microbial degradation of tetrabromobisphenol A*, Applied and Environmental Microbiology, Vol. 66(6), 2000, 2372–2377.
- [58] Sellstrom U., Kierkegaard A., de Wit C., Jansson B., *Polybrominated diphenyl ethers and hexabromocyclododecane in sediment and fish from a Swedish river*, Environmental Toxicology and Chemistry, Vol. 17, 1998, 1065–1072.
- [59] Shi T., Chen S.J., Luo X.J., Zhang X.L., Tang C.M., Luo Y., Ma Y.J., Wu J.P., Peng X.Z., Mai B.X., *Occurrence of brominated flame retardants other than polybrominated diphenyl*



ethers in environmental and biota samples from southern China, Chemosphere, Vol. 74, 2009, 910–916.

- [60] Stiborova H., Vrkoslavova J., Pulkrabova J., Poustka J., Hajslova J., Demnerova K., *Dynamics of brominated flame retardants removal in contaminated wastewater sewage sludge under anaerobic conditions*, Science of the Total Environment, Vol. 553, 2015, 439–445.
- [61] Tan X.X., Luo X.J., Zheng X.B., Li Z.R., Sun R.X., Mai B.X., *Distribution of organophosphorus flame retardants in sediments from the Pearl River Delta in South China*, Science of the Total Environment, Vol. 544, 2016, 77–84.
- [62] Tokarz J.A.3rd, Ahn Mi-Y., Leng J., Filley T.R., Nies, L., *Reductive Debromination of Polybrominated Diphenyl Ethers in Anaerobic Sediment and a Biomimetic System*, Environmental Science & Technology, Vol. 42, 2008, 1157–1164.
- [63] de la Torre A., Sverko E., Alae M., Martinez M.A., *Concentrations and sources of Dechlorane Plus in sewage sludge*, Chemosphere, Vol. 82, 2011, 692–697.
- [64] Venkatesan A.K., Halden R.U., *Brominated flame retardants in U.S. biosolids from the EPA national sewage sludge survey and chemical persistence in outdoor soil mesocosms*, Water Research, Vol. 55, 2014, 133–142.
- [65] Voordeckers J.W., Fennell D.E., Jones K., Haggblom M.M., *Anaerobic biotransformation of tetrabromobisphenol A, tetrachlorobisphenol A, and bisphenol A in estuarine sediments*, Environmental Science & Technology, Vol. 36, 2002, 696–701.
- [66] Wang Y., Jiang G., Lam P.K.S., Li A., *Polybrominated diphenyl ether in the East Asian environment: a critical review*, Environment International, Vol. 33, 2007, 963–973.
- [67] Wang Y., Zhang Q., Lv J., Li A., Liu H., Li G., Jiang G., *Polybrominated diphenyl ethers and organochlorine pesticides in sewage sludge of wastewater treatment plants in China*, Chemosphere, Vol. 68, 2007, 1683–1691.
- [68] de Wit C.A., Nylund K., Eriksson U., Haglund M., Kierkegaard A., Asplund L., *Brominated flame retardants in sludge from 50 Swedish sewage treatment plants: evidence of anaerobic degradation of HBCD and TBBPA*, Proceedings of the 4th International Workshop on Brominated Flame Retardants, Amsterdam, Netherlands.
- [69] Xiang N., Chen L., Meng X.-Z., Dai X., *Occurrence of hexabromocyclododecane (HBCD) in sewage sludge from Shanghai: Implications for source and environmental burden*, Chemosphere, Vol. 118, 2015, 207–212.
- [70] Yang C.W., Chen W.Z., Chang B.V., *Biodegradation of tetrabromobisphenol-A in sludge amended soil*, Ecological Engineering, Vol. 91, 2016, 143–147.
- [71] Zhen X., Tang J., Xie Z., Wang R., Huang G., Zheng Q., Zhang K., Sun Y., Tian C., Pan X., Li J., Zhang G., *Polybrominated diphenyl ethers (PBDEs) and alternative brominated flame retardants (aBFRs) in sediments from four bays of the Yellow Sea, North China*, Environmental Pollution, Vol. 213, 2016, 386–394.
- [72] Zhu B., Lam J.C.W., Yang S., Lam P.K.S., *Conventional and emerging halogenated flame retardants (HFRs) in sediment of Yangtze River Delta (YRD) region, East China*, Chemosphere, Vol. 93, 2013, 555–560.

Sebastian Kujawiak (sebastian.kujawiak@gmail.com)

Małgorzata Makowska

Radosław Matz

Anna Gawrońska

Department of Hydraulic and Sanitary Engineering, Faculty of Environmental Engineering and Landscape Planning, Poznań University of Life Sciences

THE EFFICIENCY OF THE AERATION PROCESS IN AIRLIFT REACTORS WITH MOVING BEDS

EFEKTYWNOŚĆ PROCESU NAPOWIETRZANIA W REAKTORACH BARBOTAŻOWYCH ZE ZŁOŻEM RUCHOMYM

Abstract

The current work consisted of performing tests on the prototype airlift reactor, examining the efficiency of oxygenation in an airlift reactor equipped with an airlift pump and an additional nozzle to aerate and mix water in the tank. In particular, the objective was to find the optimal submergence of the nozzle which would allow achieving the best possible oxygenation of water with adequate lift efficiency. The testing was performed in two series: with a tank fully filled with water; with a tank filled with 80% water and 20% moving bed. The use of a moving bed with a high specific surface area significantly improved aeration conditions and decreased mixture flow velocity thus causing an increase of gas and liquid contact time. The research has shown the effect of nozzle position on the aeration and circulation conditions in the reactor.

Keywords: airlift reactor, aeration, moving bed

Streszczenie

Praca polegała na wykonaniu serii doświadczeń na modelu fizycznym prototypowego reaktora barbotażowego. Badano skuteczność natleniania wody w reaktorze barbotażowym wyposażonym w podnośnik powietrzny, zaopatrzony w dodatkowy króciec napowietrzający i powodujący cyrkulację cieczy w zbiorniku. Celem było znalezienie optymalnego zagłębienia króćca, które pozwoliłoby na osiągnięcie jak najlepszego natlenienia cieczy przy odpowiedniej wydajności podnośnika. Badania wykonano w dwóch seriach: dla zbiornika napelnionego wyłącznie wodą i dla zbiornika wypełnionego w 20% objętości złożem ruchomym. Zastosowanie złoża o dużej powierzchni właściwej znacznie poprawiło warunki napowietrzania, zmniejszyło prędkość cyrkulacji mieszaniny, co pozwoliło zwiększyć czas kontaktu cieczy i gazu. Badania wykazały wpływ położenia króćca na warunki tlenowe i cyrkulację mieszaniny w reaktorze.

Słowa kluczowe: reaktor barbotażowy, napowietrzanie, złożo ruchome

1. Introduction

Bubbling processes in the form of gas flows of bubbles can be found in many installations such as airlift reactors and airlift pumps [3, 5]. The latter are considered to be the simplest in terms of pump construction – these operate by transporting liquid through the creation of a significant difference between the densities of the liquid and gas-liquid mixture. The first commercial use of airlift reactors dates back to 1958 when Lamont [5] modified a gold ore flotation tank. Airlift reactors have found widespread use in chemical engineering and industrial biotechnology due to their unique construction and oxygenation of the reaction environment [5].

2. Airlift reactor constructions

Due to modification of bubble column of reactor there are two main types of air lift reactor constructions [5, 7]: a) with internal circulation of medium; b) with external circulation of medium. Four main hydrodynamic zones of airlift reactor can be distinguished [5]: I – riser zone, wherein gas-liquid mixture rises; II – downcomer zone, wherein a completely or partially degassed gas-liquid mixture falls; III – degas zone, wherein gas-liquid mixture degasses either completely or partially; IV – bottom zone.

3. Aeration of liquid-basics

Currently, the use of airlift reactors in biotechnology is very popular – it is, for example, successfully used in wastewater aeration. Methods can be found in various papers in the literature [3, 15]. Appropriate selection of technology, equipment and efficiency affects operating costs and process parameters [1, 2, 14, 15]. Oxygen capacity is a parameter that characterises the process of aeration – this is described by Borowski [2]. The main factors affecting oxygen capacity are temperature, salinity, and pressure [2]. To obtain an effective aeration process requires adjusting the amount of dosed air to comply with reactor parameters; appropriate bubble size; identification of the number of carriers which fill the reactor [2, 14]. Materials used for the production of carriers are mainly plastics with fibres that have a solid texture firm consistency. The selection of appropriate carriers influences the effectiveness of the aeration and treatment processes in bioreactors [6, 8, 9, 10]. Moving beds can occupy 20–70% of the reactor volume [11]. Many studies confirm the beneficial impact on aeration by using a moving bed in reactors [13]; due to the bed circulation effect and resistance to motion, it is assumed that a 60–70% fill is the maximum value [9, 10, 12].

4. Subject matter and methodology of laboratory tests

Laboratory tests were performed on a physical model located in the water laboratory of the Department of Hydraulic Engineering. The subject matter of the research was a physical model of a prototype airlift reactor. The efficacy of water oxygenation in an airlift reactor that was equipped with an airlift pump with a diameter of 50 mm was studied – this included use of an additional nozzle that aerates and circulates water in the tank. The purpose of the study was to find the optimal degree of submergence of the nozzle which would allow achieving the best possible oxygenation of water with adequate lift efficiency. The test was performed in two series: tank fully filled with water; tank filled with 20% moving bed and 80% water, by volume. Before the measurements were taken, water was deoxygenated using sodium sulfate. Additionally, measurements of dissolved oxygen concentration, for various levels of water in the tank (H_s from 40 to 50 cm) and for the various position of the nozzle ($H = 34$ cm and $H = 84$ cm), were performed using a Hach Lange LDO optical oxygen sensor with HQ40D multimeter. The measurements were taken at 10-minute intervals [4]. The scheme of the installation is shown in Fig. 1.

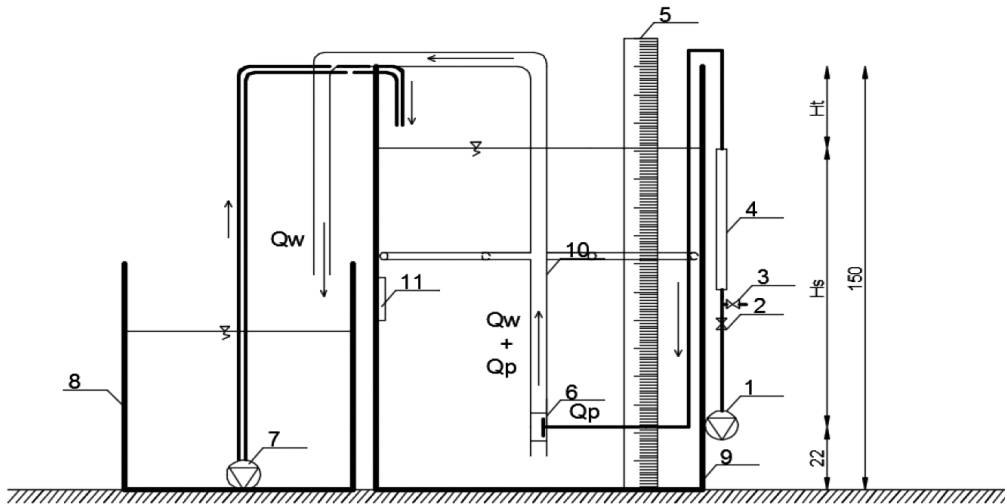


Fig. 1. Schematic of the installation: 1 – air blower; 2 – control valve; 3 – blow-off valve; 4 – rotameter; 5 – scale; 6 – diffuser; 7 – rotodynamic pump; 8 – recirculation tank; 9 – main tank; 10 – air lift pump with nozzle; 11 – hydrostatic liquid level sensor

5. The results of laboratory tests

The results of laboratory tests are presented in graph form in Figs. 2 & 3 for various levels of water in the reactor and for both positions of the nozzle. The most favorable oxygen condition was obtained for settings with nozzle position $H = 84$ cm and 20% fill of the moving bed (Fig. 2).

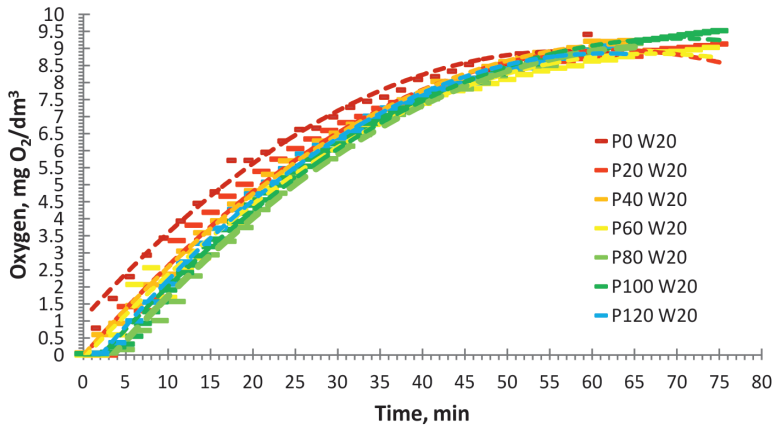


Fig. 2. Graph of the dissolved oxygen concentration in the reactor. Nozzle position $H = 84$ cm, 20% fill of moving bed

From the raw data, average values of dissolved oxygen concentration were calculated for the four variations of reactor construction ($H = 34$ cm, 0% fill; $H = 34$ cm, 20% fill; $H = 84$ cm, 0% fill; $H = 84$ cm, 20% fill) with measurements obtained at 10-minute intervals. A graph of average values of dissolved oxygen concentration is shown in Fig. 3.

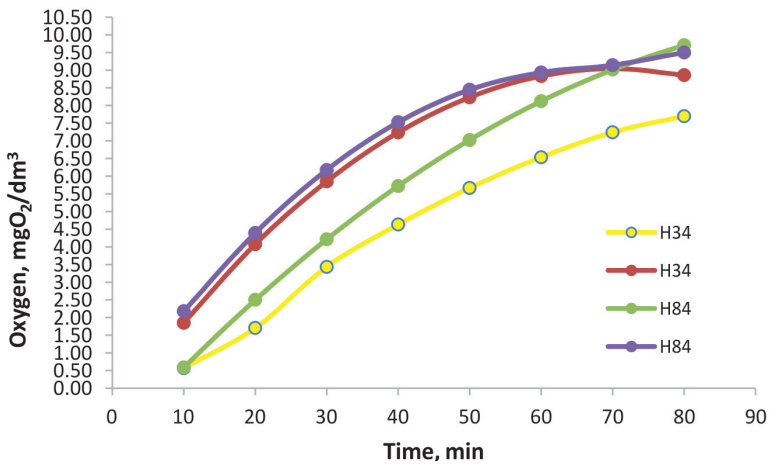


Fig. 3. The average value of dissolved oxygen concentration in the reactor. Nozzle position $H = 34$ cm, 20% fill of moving bed

6. Conclusions

The purpose of the study was to determine the effectiveness of an airlift reactor equipped with an airlift pump and an additional nozzle that aerates and circulates water in the tank. The results of this research indicate that:

- ▶ the use of a moving bed improves oxygen conditions in both reactor constructions – this is caused by the extended contact time of liquid and gas, and the high specific surface area of the bed;
- ▶ based on analysis of the impact of the nozzle position on aeration and circulation in the reactor, oxygen conditions in the construction with the nozzle located at a height of 84 cm are more favourable than in the construction with the nozzle at height of 34 cm – this was possibly caused by locating the nozzle in the middle of the tank with regard to height;
- ▶ for both constructions ($H = 34$ cm and $H = 84$ cm) and both filling levels (0% and 20%), there are three hydrodynamic zones (upper, central, bottom); the size of the first two zones is dependent on the position of the nozzle;
- ▶ the use of moving bed, which accounted for 20% of the volume of the reactor, caused a significant non-linear resistance – this reduced the output of the airlift pump for both of the constructions by an average of 20%.

References

- [1] Banaszek P., *Klimzowiec według algorytmu*, Kierunek Wod-Kan, nr 3, 2014, 26–29.
- [2] Borowski J., *Monitoring natleniania przy cyklicznym napowietrzaniu w reaktorach o małej skali typu MBBR*, Inżynieria Ekologiczna nr 14, Warszawa 2006.
- [3] Dziubiński M., Prymer J., *Mechanika płynów dwufazowych*, Wydawnictwo Naukowo-Techniczne, Warszawa 2009.
- [4] Gawrońska A., *Skuteczność natleniania cieczy przez podnośnik powietrzny zanurzony w złożu ruchomym*, Uniwersytet Przyrodniczy w Poznaniu, Praca magisterska, 2005.
- [5] Grzywacz R., *Właściwości stacjonarne bioreaktorów barbotażowych typu airlift*, Monografia 410, Politechnika Krakowska, Kraków 2012, 7–22.
- [6] Hosseiny S.H., Borghei S.M., *Modelling of organic removal in a moving bed biofilm reactor (MBBR)*, Scientia Iranica, 9 (1), 2002, 53–58.
- [7] Merchuk J.C., Gluz M., *Bioreactors, Air-lift Reactors*, Encyclopedia of Bioprocess Technology, Ben-Gurion University of the Negev, Beer-Sheva, Israel 2002.
- [8] Ødegaard, H., *The moving bed biofilm reactor*, Water Environmental Engineering and Reuse of Water, Hokkaido Press, 1999, 250–305.
- [9] Ødegaard, H., *Innovations in wastewater treatment: The moving bed biofilm process*, Water Science and Technology, 53 (9), 2006, 17–33.
- [10] Oliveira, i in., *Evaluation of a MBBR (moving bed biofilm reactor) pilot plant for treatment of pulp and paper mill wastewater*, International Journal of Environmental Monitoring and Analysis, 2(4), 2014, 220–225.
- [11] Orantes J.C., González-Martínez S., *A new low-cost biofilm carrier for the treatment of municipal wastewater in a moving bed reactor*, Water Sci Technol, 48 (11–12), 2003, 243–50.
- [12] Rees A.J., Rodman D.J., Zabel T.F., *Evaluation of Dissolved-Air Flotation Saturator Performance*, TR 143, Water Research Centre, Medmenham, U.K 1980.



- [13] Suschka J., Zieliński J., Grajcar Z., *Urządzenia do natleniania ścieków*, Wydawnictwo Arkady, Warszawa 1979.
- [14] Woźniak-Vecchié R., *Biologiczne oczyszczanie ścieków. Sztuka napowietrzania*, Magazyn Instalatora 3 (187), 2014.
- [15] www.akwatech.pl

Krzysztof Kędzia (krzysztof.kedzia@pwr.edu.pl)

Department of Operation and Maintenance of Logistics, Transportation and Hydraulic Systems, Mechanical Faculty, Wrocław University of Science and Technology

AN ALGORITHM FOR THE DETERMINATION OF THE CONTROL
PARAMETERS OF A MULTISOURCE DRIVE SYSTEM

ALGORYTM WYZNACZANIA PARAMETRÓW STEROWANIA
DLA WIELOŹRÓDŁOWEGO UKŁADU NAPĘDOWEGO

Abstract

This article presents an application of the kinetostatic method. The kinetostatic method is a universal method for determining optimum control of unit components in a multisource drive system with regard to selected energetic or ecological criteria. The method's algorithm and mathematical models for components with descriptions are presented. Example results of this method when applied to a hydrostatic multisource drive system composed of hydrostatic transmission, gas-loaded accumulator and IC engine as the primary source of energy, are presented.

Keywords: multisource drive systems, kinetostatic method algorithm, hydrostatic drives, energy optimization, ecology

Streszczenie

W artykule przedstawiono zastosowanie metody kinetostatycznej. Metoda kinetostatyczna jest uniwersalną metodą wyznaczania optymalnego sterowania komponentami wieloźródłowego układu napędowego ze względu na wybrane kryteria: energetyczne lub ekologiczne. Przedstawiono algorytm metody oraz modele opisujące komponenty układu. Artykuł zawiera przykładowe wyniki działania metody wyznaczone dla hydrostatycznego wieloźródłowego układu napędowego zbudowanego z: przekładni hydrostatycznej, akumulatora gazowo-hydraulicznego oraz silnika spalinowego jako pierwotnego źródła energii.

Słowa kluczowe: wieloźródłowy układ napędowy, metoda kinetostatyczna, napęd hydrostatyczny, optymalizacja energetyczna, ekologia

1. Introduction

The kinetostatic method is a universal method applied for the purpose of determining the following parameters for a multisource drive system (Fig. 1). The system is created from components of known characteristics for a known load presented in the form of a machine operating cycle and has the criteria [1–3]:

- ▶ optimum work point for the primary source of energy;
- ▶ initial parameters for the secondary source of energy;
- ▶ control parameters for other components in the drive system.

The method assumes the following:

- ▶ for the full duration of machine operation, the primary source of energy will operate at one point;
- ▶ the energy level of the secondary source, at the beginning and at the end of the operating cycle, shall remain the same.

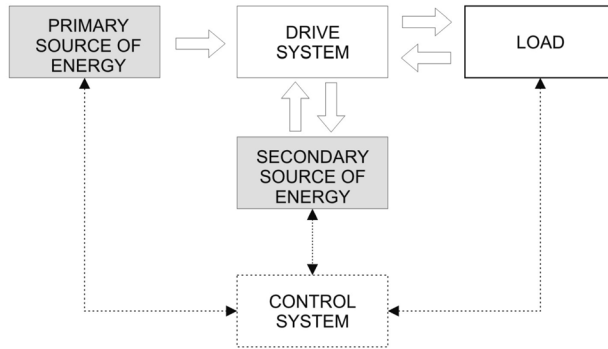


Fig. 1. Multisource drive system scheme

The result of using this method is a set of parameters for controlling the multisource drive system. The results obtained through the application of the kinetostatic method will be presented for the multisource hydrostatic drive system under investigation (Fig. 2) [1, 4].

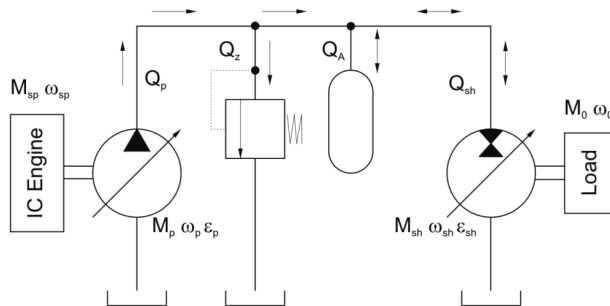


Fig. 2. Schematic of the structure of the multisource hydrostatic drive system

The multisource hydrostatic drive system covers:

- ▶ IC engine work point (M_{sp}, ω_{sp}) for the selected optimisation criteria, e.g. minimum fuel consumption in cycle G_e (Fig. 3d), minimum emission of nitrogen oxides NO_x in exhaust gases, DYM – smoke level, etc.;
- ▶ diagram of $\varepsilon_p(t)$ and $\varepsilon_{sh}(t)$ hydrostatic unit control in the operation cycle (Fig. 3c);
- ▶ initial pressure p_{a0} in the accumulator (in this case, 30.2 MPa);
- ▶ accumulator initial charge pressure, p_{gwst} (gas pressure in the accumulator is not connected to the hydraulic system – 25 MPa).

The figure below (Fig. 3) presents the control parameters of selected components of the multisource drive system [5].

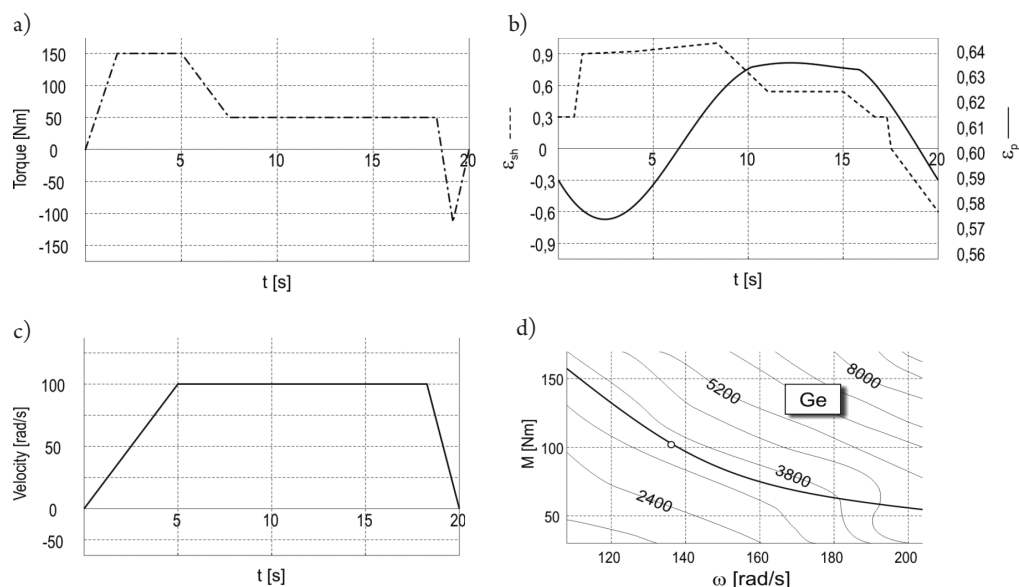


Fig. 3. An example of results obtained with the use of the kinetostatic method for Load I: a) M_o – load torque; b) ω_o – load angular velocity; c) hydrostatic units control; d) specified combustion engine work point

2. Algorithm for the determination of the control parameters of the multisource drive system (kinetostatic method)

The method for selecting the parameters of operation for the multisource drive system was based on the kinetostatic method [1, 2, 6]. Block diagrams (Figs. 4, 5) present the algorithm of performance while calculating the settings for the hydrostatic units, pump – ε_p , engine – ε_{sh} , M_{sp} IC engine work point, and ω_{sp} and p_{gwst} parameters of the initial accumulator load.

The following assumptions were made:

- ▶ real characteristics of the hydrostatic units were taken into account by means of applying regression equations;

- ▶ the engine work point (M_{sp}, ω_{sp}) is constant during the whole working cycle;
- ▶ M_{sp} torque and ω_{sp} angular velocity of the IC engine will reduce to M_p torque and ω_p angular velocity on the hydrostatic pump shaft;
- ▶ torque (M_o) and angular velocity (ω_o) of the load in GROSS form will reduce to torque (M_{sh}) and angular velocity (ω_{sh}) on the hydrostatic engine shaft;
- ▶ the universal characteristics of the combustion engine were presented in the form of discrete points with criteria values assigned;
- ▶ the gas and hydraulic accumulator were presented in the form of BWR model;
- ▶ self-locking phenomena of the hydrostatic unit operating as a hydrostatic engine takes place within the range of swash plate angle $0 < \varepsilon_{sh} < 0.3$;
- ▶ the impact of temperature on the operation of the hydrostatic unit was neglected;
- ▶ the impact of fluid compressibility was neglected;
- ▶ there were no leaks in the hydraulic system.

Step 1. The allowable possible working area is determined depending on the characteristic features of the engine. Based on the above, the set of analysed engine work points $M_{sp}, \omega_{sp}, G_{sp}, CO, NO_x, DYM$ (smokiness) are specified.

Step 2. The machine load characteristics in the working cycle within duration time T are presented in the form of a table or in analytical form – it involves the dependencies of load torque (power) $M_o(t_j)$ and angular velocity (linear) $\omega_o(t_j)$. In this step, it is also necessary to assume the values of time increments Δt . The parameters of the accumulator are selected: capacity and initial determination of the accumulator charge status $E_a(t_i = 0)$ (equations from 1–4).

Table 1. Dependencies describing the energy either supplied to or taken from the accumulator for different movement phases [1]

Movement phase	Energy flowing via the wheels' points of contact with the pavement	Energy supplied to or taken from the accumulator	Equation number
1. Acceleration	$ E_{1k} = \sum_i \int_0^{S_{1i}} N_{1i}(t) dt$	$E_{1a} = \sum_i \int_0^{S_{1i}} \left(\frac{-N_{1i}(t)}{\eta_{a1i}(t) \cdot \eta_{s1i}(t) \cdot \eta_{M1i}(t) \cdot \eta_{p1i}(t)} + \bar{N}_z \right) \cdot \eta_{a1i}(t) \cdot \eta_{s1i}(t) \cdot dt$	(1)
2. Steady flow	$ E_{2k} = \sum_i N_{2i} s_{2i}$	$E_{2a} = \sum_i \left(\frac{-N_{2i} s_{2i}}{\eta_{a2i} \cdot \eta_{st2i} \cdot \eta_{M2i} \cdot \eta_{p2i}} + \bar{N}_z s_{2i} \right) \cdot \bar{\eta}_{st2i} \cdot \bar{\eta}_{a2i}$	(2)
3. Locking (braking)	$ E_{3k} = \sum_i \int_0^{S_{3i}} N_{3i}(t) dt$	$E_{3a} = \sum_i \int_0^{S_{3i}} \left(-N_{3i}(t) \eta_{p3i}(t) \eta_{M3i}(t) + \bar{N}_z \right) \eta_{st3i}(t) \eta_{a3i}(t) dt$	(3)
4. Active stoppage	$ E_{4k} = 0$	$E_{4a} = \bar{N}_z \bar{\eta}_{st4} \bar{\eta}_{a4} \sum_i s_{4i}$	(4)

Step 3. In accordance with the load cycle, the values of combustion engine power $N_{spj} = f(M_{spj}, \omega_{spj})$ are compared, with reference to the assumed area allowable j^{th} work point, to the power demand of $N_{oi}(M_{oi}, \omega_{oi})$ in t_i time.

As:

- ▶ the power of the primary source and load power are expressed by applicable values of their M_{spj} and M_{oi} effort variables and ω_{spj} , ω_{oi} flow variables;
- ▶ values of engine power N_{spj} and load N_{oi} are generally diverse, then the function of the hydrostatic power transfer unit is:
- ▶ accurate transformation of the forms of M_{sp} effort variable and ω_{sp} flow variable of the combustion engine to the form required by M_o effort variable and ω_o flow variable of the load;
- ▶ balancing the power supplied by the primary source of energy with the load power demand by means of taking the excess of the energy to the accumulator or supplementing its insufficiency with it.

The power of the primary source, in the form of the M_{sp} and ω_{sp} signals, is transmitted to the shaft of the positive-displacement pump of changeable efficiency. The initial values of M_p and ω_p are transformed for the given p pressure – by means of solving the equations which describe the real power characteristic features of the M_p and Q_p pump – into the deflection signals for the element which controls the efficiency ε_p .

While the momentary value of load power, in the form of M_o and ω_o signals, is transmitted to the shaft of the hydrostatic engine of changeable absorption capacity. The values of M_o and ω_o are transformed for the given p pressure by means of solving the equations which describe the real power characteristic features of M_s and Q_{sh} (hydrostatic unit) into the signals which control ε_{sh} . Power losses related to Q_p and Q_{sh} that flows in the hydraulic system referred to the summing junction, where p pressure is present, were projected in other diagrams. In the summing junction, by the given value of p pressure, power is balanced due to the flow continuity equation $Q_p + Q_{sh} + Q_a = 0$ being met. If the power from the primary source is in excess in relation to the load, the accumulator collects the fluid stream with the power of $p \cdot (Q_p - Q_{sh})$, while in the case of insufficiency, it gives back the power of $p \cdot (Q_{sh} - Q_p)$.

Pressure p in the summing junction is related to the accumulator power condition. It is not, however, a simple and unambiguous dependency in general. It depends on the type of accumulator applied and how it is controlled. In the system, a hydraulic accumulator was applied which was directly connected with the hydraulic system.

The kinetostatic method was specified as a consequence of own research. A modified algorithm of the step is presented in Fig. 5.

In **block A**, p pressure for the given (k -th) iteration in the summing junction is calculated. The pressure value depends on the accumulator load condition. For the given M_o values of load and M_{spj} combustion engine torque, the values of ε_p and ε_{sh} parameters for units control (**diagram B**) are calculated. The values in relation to their previous values in $t_i - \Delta t$ time have to meet the condition for the border clipping velocity.

In the event that the conditions are not observed (**diagram C**), it goes back to diagram A. If the maximum clipping velocities of the pump and hydrostatic engine are real, then we

need to check whether the swash plate angle of the hydrostatic engine is greater than the self-locking range. If this condition is observed, we move to **diagram D**. The engine will be found within the specified zone, so in order to minimise the volumetric losses, we need to decrease the swash plate angle to zero and attempt to do this as quickly as possible. In **diagram D**, we calculate the power loss. To start, we determine the real pump capacity Q_p and engine absorption capacity Q_{sh} . We then determine the power loss within time $t_i - t_{i-1} = \Delta t$:

- ▶ in the positive-displacement pump $\Delta E_p(\omega_p, p_p, \Delta p_p)$;
- ▶ in the hydrostatic engine $\Delta E_{sh}(\omega_{sh}, p_{sh}, \Delta p_{sh})$;
- ▶ in the hydraulic unit $\Delta E_t(Q_{sh}, Q_p)$;
- ▶ in the energy accumulation unit $\Delta E_a(E_a, N_a)$ (with use of the BWR model).

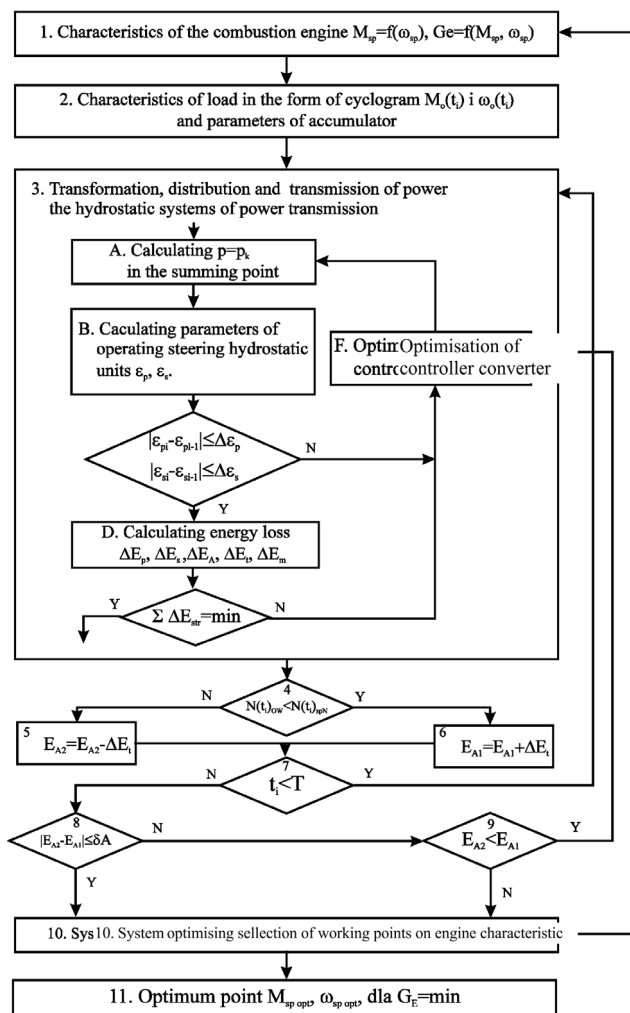


Fig. 4. The procedure of the method applied for the purposes of determining the control parameters for the set load of the hybrid system – kinetostatic method

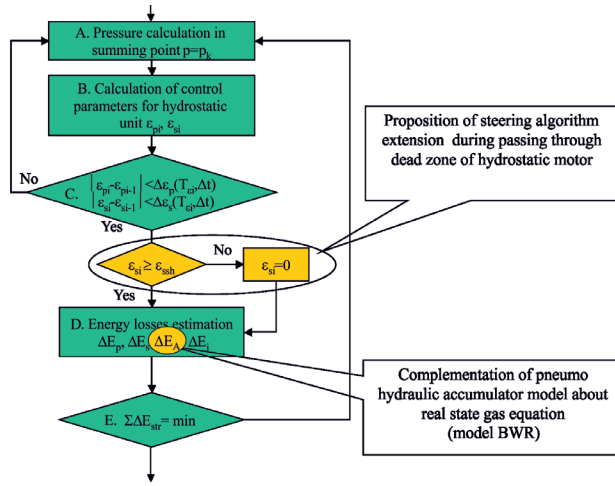


Fig. 5. Unit 3 of power transformation and transmission in the power transfer hydrostatic unit

Power losses in the accumulation unit depend on: the E_a accumulator charge condition; charging and discharging velocity $\frac{dE_a}{dt}$ (power that is supplied or taken back); power storage time in the accumulator; accumulator structural parameters (wall thickness, wall thermal conductivity co-efficient, ambient temperature, etc.)

In **diagram E**, the decision is made about moving on to subsequent 4 step of the algorithm or subsequent iteration $k + 1$ and moving on to searching for another possible transducer control. The general problem then involves the selection of the power transducer controlling signal E_a so that for:

- ▶ combustion engine work point M_{spj}, ω_{spj} ,
- ▶ the point from the load characteristics for the moment $t_p, M_o(t_i), O_o(t_i)$,

the sum of power losses $\Sigma\Delta E_{str}$ is minimum.

Step 4. In the algorithm, the values of momentary power reduced to the summing junction are compared, in other words transformation and energy transfer losses are taken into account.

Step 5. In the block, the values of power taken from the accumulator E_{a2} are calculated.

Step 6. In the block, the energy supplied to the accumulator in time $\Delta t = t_i - t_{i-1}$, and reduced to the summing junction are calculated. The operation of diagram 5 or 6 depends on the inequality sign $N(t_i)_{ow} < N(t_i)_{spw}$.

Step 7. This is where the calculations for the given moment of t_i cycle are completed. Providing that inequality $t_i < T$ is true, the algorithm loop for $t_i = t_i + \Delta t$ is repeated. After all the calculations in the working cycle are made (for $t_i = T$), we move to another diagram.

Step 8. This is where the condition $|E_{a2} - E_{a1}| < \sigma_a$ is examined. Depending on the result load obtained for the given cycle, the algorithm anticipates the following procedures:

- ▶ if the condition presented in **diagram 8** is observed, then the new work point of the combustion engine M_{spj}, ω_{spj} is selected;

- ▶ if the condition is not observed, two possibilities should be considered – these are shown in Step 9.

Step 9.

1. When the power supplied to the accumulator is less for the given cycle than less than the collected one, it means a negative cycle power balance exists, while the insufficiency exceeds σ_a . This is an unacceptable option, therefore, it is necessary to move on to step 10 and select the new work point of the combustion engine M_{spj}, ω_{spj} .

2. When the power supplied to the accumulator is, for the given cycle, greater than the collected one and the excess exceeds σ_a , it is necessary to go back to diagram 3 (determination of the signal which controls the power transducer) and recalculate the load cycle under consideration for the given work point of the combustion engine M_{spj}, ω_{spj} .

Step 10. The power analysis presented in the algorithm is run by the optimisation unit (**diagram 10**) until quality criteria for the moment the characteristics of the engine point $M_{spopt}, \omega_{spopt}$ for the given load cycle are accepted: G_c fuel consumption reaches the minimum value within the set area.

3. Summary

The presented kinetostatic method allows for the multisource drive system, determination of the control parameters for all components of the system, using any criterion of control e.g.: G_c – fuel consumption in the cycle, CO – carbon monoxide content in exhaust gases, NO_x – nitrogen oxides content in exhaust gases, as well as DYM – range of smokiness. It enables free choice of criteria, depending on the location of the machine, for example, on highways it can be controlled due to the minimum cost of fuel (min G_c). In mines and urban areas, the cost of fuel is a secondary consideration; ecology, and ensuring the health and safety of workers through minimising the emission of harmful substances becomes the most important criterion.

References

- [1] Kędzia K., *Metoda optymalizacji energetycznej i ekologicznej hydrostatycznego wieloźródłowego układu napędowego*, praca doktorska, Wrocław 2004.
- [2] Kędzia K., *Development of kinetostatic method algorithm of control system of multisources driving system*, *Hidraulica*, nr 3/4, 2009, 39–45.
- [3] Kędzia K., *What to do with a hybrid drive system?* “HIDRAULICA” (No. 2/2013) ISSN, Magazine of Hydraulics, Pneumatics, Tribology, Ecology, Sensorics, Mechatronics, Romania 2013.
- [4] Kędzia K., *Wyznacznik zmienności cyklu obciążenia wieloźródłowego hydrostatycznego układu napędowego*, Oficyna Wydawnicza Politechniki Wrocławskiej, Wrocław 2014.
- [5] Kučík P., Strážovec I., Kriššák P., *Hydraulický prenos energie. Mobilné stroje*, EDIS, vydavateľstvo ŽU, 2000, 384.

- [6] Kędzia K., Chrostowski H., *Self-locking phenomenon in hydrostatic motor working as reversible unit in multisources hydrostatic driving system*, *Hydraulika a Pneumatika (Žilina)*, Roc. 8, cis. 3/4, 2006.
- [7] Kędzia K., Chrostowski H., *Electrohydraulic controller as a hydrotronic element of driving system*, 4th FPNI – PhD Symposium, Proceedings, Sarasota, Florida, USA, June 13–17, 2006. Vol. 2, Ed. M. Ivantysynova, [B.m.]: FPNI Fluid Power Net Publ., cop. 2006, 523–532.
- [8] Conrad F., Pobedza J., Sobczyk A., *IT-Tools Concept for Simulation and Design of Water Hydraulic Mechatronic Test Facilities for Motion Control and Operation in Environmentally Sensitive Application Areas – Proceedings of ASME Intl Mechanical Engineering Congress IMECE '04*, Fluid Power Systems and Technology, 1–9, The American Society of Mechanical Engineering – ASME, USA, New York 2004.
- [9] Imre M., Rahmfeld R., Zavadinka P., Kriššák P., *Simulation model of priority flow control valve compared with a flow compensation tests results*, *Hydraulika a Pneumatika*, 1-2/2010, 25–28.
- [10] Janicka A., Kolanek C., Walkowiak W., *Podstawy procesów termodynamicznych w silnikach spalinyowych*, Oficyna Wydawnicza Politechniki Wrocławskiej, 2013.
- [11] Kędzia K., Chrostowski H., *The analysis of pneumo-hydraulic accumulator efficiency, applied as element of hybrid driving system*, Scientific Papers of the University of Pardubice, Series B, the Jan Perner Transport Faculty, 2004 nr 10, 93–99.
- [12] Kędzia K., Kulczyk J., *Benefits of hydrostatic multisources power systems using in mobile machines in term of selected criteria*, *Innovacii v nauke i obrazovanii – 2008*, VI Jubilejnaja mezdunarodnaja naucnaja konferencija: trudy, [Kaliningrad], 21–23 oktjabrja 2008. C/2, red. V.E. Ivanov, Kaliningradskij gosudarstvennyj techniceskij universitet, Kaliningrad 2008, 154–157.
- [13] Kollek W., Osiński P., Stosiak M., Wilczyński A., Cichoń P., *Problems relating to high-pressure gear micropumps*, *Archives of Civil and Mechanical Engineering*, 2013.
- [14] Osiński P., W. Kollek, *Assessment of energetistic measuring techniques and their application to diagnosis of acoustic condition of hydraulic machinery and equipment*, *Archives of Civil and Mechanical Engineering*, Vol. 13, Issue 3, 2013.
- [15] Stosiak M., *The modelling of hydraulic distributor slide-sleeve interaction*, *Archives of Civil and Mechanical Engineering*, vol. 12, nr 2, 2012, 192–197.
- [16] Stryczek J., Antoniak P., Banaś M., *An idea of the electronic control system for the multifunctional hydraulic machine*, *Journal of Vibroengineering*, vol. 12, nr 3, 2010, 329–332.
- [17] Zavadinka P., Kriššák P., *Simulation of vehicle working conditions with hydrostatic pump and motor control algorithm*, *JAMRIS*, 3/2012, 40–46.
- [18] Zawisłak M., *Numerical modelling of vehicle interior in aspect of human exposure on volatile organic compounds*, *Polish Journal of Environmental Studies*, 2012.
- [19] Guzowski A., Sobczyk A., *Reconstruction of hydrostatic drive and control system dedicated for small mobile platform*, Proceedings of the 8th Fluid Power Net International PhD Symposium. – [S.l.], ASME (American Society of Mechanical Engineers), 2014.
- [20] Sobczyk A., *Improvement of hydraulic system efficiency by means of energy recuperation*, Politechnika Krakowska, Kraków 2011.

- [21] Sobczyk A., *Badania układu odzysku energii w hydraulicznym układzie napędu i sterowania ruchem wysięgnika koparki Logistyka* (dokument elektroniczny), 2014.
- [22] [wwwhttp://mathworks.com/products](http://mathworks.com/products), Matlab optimization Toolbox 2.1 documentation, 2013.

Anna Korzeń (korzen@mech.pk.edu.pl)

Institute of Thermal Power Engineering, Faculty of Mechanical Engineering, Cracow University of Technology

Dawid Taler

Institute of Heat Engineering and Air Protection, Faculty of Environmental Engineering, Cracow University of Technology

MATHEMATICAL MODELLING OF THE UNSTEADY OPERATION OF A PLATE AND FIN HEAT EXCHANGER FOR THE TIME-VARYING MASS FLOW RATE OF LIQUID AND AIR VELOCITY

MODELOWANIE MATEMATYCZNE PRACY WYMIENNIKA CIEPŁA Z RUR OŻEBROWANYCH DLA ZMIENNYCH W CZASIE STRUMIENIA MASY PŁYNU I PRĘDKOŚCI POWIETRZA

Abstract

The mathematical simulation of a plate fin and tube heat exchanger is presented in this paper. The simulation of the transient operation of the heat exchanger was carried out using a general numerical model that was previously developed by the authors. The Reynolds number of the water flowing inside the tubes varied in the range from 4000 to 12000. A detailed analysis of the transient response of a heat exchanger to sudden increase in water mass flow rate and the simultaneous reduction in air flow velocity was modelled. Heat transfer correlations for air and water were determined based on the experimental data. Unknown parameters appearing in the relationships for the Nusselt numbers on the air- and water-sides were estimated using the least squares method. A set of partial differential equations for the temperature of water, air, tube wall, and fins was solved using the finite volume method. The results of the numerical simulations of a heat exchanger using experimentally determined air and water-side heat transfer formulas for the calculation of heat transfer coefficients were compared with the experimental data. Excellent agreement between computation results (air and water temperatures at the outlet of the heat exchanger) and experimental results was obtained.

Keywords: plate-fin and tube heat exchanger; experimental determination of heat transfer correlations; numerical modelling; transient response; transition tube flow

Streszczenie

Przedstawiona została symulacja matematyczna wymiennika ciepła z rur ożebrowanych. Symulacja niestabilnej pracy wymiennika przeprowadzona została za pomocą modelu matematycznego opracowanego wcześniej przez autorów. Liczba Reynoldsa po stronie wody zmieniała się w zakresie od 4000 do 12 000. Szczegółowa analiza zmian temperatury została przeprowadzona dla przypadku nagłego wzrostu strumienia masowego płynu z jednoczesnym obniżeniem prędkości powietrza. Korelacje na współczynniki wnikania ciepła dla powietrza i wody określono na podstawie danych doświadczalnych. Nieznane parametry, które pojawiają się w równaniach na liczbę Nusselta dla powietrza i wody wyznaczono za pomocą metody najmniejszych kwadratów. Układ równań różniczkowych cząstkowych umożliwiający wyznaczenie temperatury wody, powietrza, ścianki rury i żeber zostały rozwiązane z użyciem metody objętości skończonej. Wyniki numerycznej symulacji pracy wymiennika z użyciem współczynników wnikania ciepła wyznaczonych z korelacji na liczby Nusselta od strony powietrza i wody porównano z danymi eksperymentalnymi. Uzyskano bardzo dobrą zgodność wyników obliczeń i pomiarów.

Słowa kluczowe: instalacje energetyczne, badania termowizyjne, termogram, emisyjność, temperatura odbicia

Nomenclature

A	– surface area, m^2
A_{oval}	– area of the oval opening in the fin, m^2
a, b	– minor and major semi-axis of the inner tube surface, m
c_p	– specific heat at constant pressure, $J/(kg \cdot K)$
c_1, c_2, c_3	– constants
d_h	– air-side hydraulic diameter, m
d_r	– water-side hydraulic diameter of the tube, m
f_1, f_2	– mean air temperature at the inlet and outlet of the heat exchanger, $^{\circ}C$ or K
h	– heat transfer coefficient, $W/(m^2 \cdot K)$
h_o	– weighted heat transfer coefficient of the fin at the surface, $W/(m^2 \cdot K)$
k	– thermal conductivity, $W/(m \cdot K)$
L_{ch}	– tube length in the radiator, m
m	– mass, kg
\dot{m}	– mass flow rate, kg/s
n_r	– number of tubes
N	– number of heat transfer units
Nu_1	– liquid-side Nusselt number, $Nu_1 = h_1/d_r/k_1$
Nu_2	– air-side Nusselt number, $Nu_2 = h_2/d_h/k_2$
p_1, p_2	– transversal and longitudinal tube pitch, m
Re_1	– liquid-side Reynolds number, $Re_1 = w_1 \rho_1 d_r / \mu_1$
Re_2	– air-side Reynolds number, $Re_2 = w_2 \rho_2 d_h / \mu_2$
s	– fin pitch, m
t	– time, s
T	– temperature, $^{\circ}C$ or K
U	– tube perimeter, m
w	– velocity, m/s
x, y	– Cartesian coordinates, m
x^+	– non-dimensional coordinate, $x^+ = x/L_{ch}$
y^+	– non-dimensional coordinate, $y^+ = y/p_2$

Greek symbols

δ	– thickness, m
Δx	– control volume length, m
η	– fin efficiency
μ	– dynamic viscosity, $kg/(m \cdot s)$
ρ	– density, kg/m^3
τ	– the time constant, s

Subscripts

- 1 – fluid (water) flowing in the tube
- 2 – fluid *I don't think that air can be described as a fluid* (air) flowing perpendicularly to the tube axis
- bbf – surface of a bare tube between fins
- bo – outer surface of a bare tube
- f – fin
- in – inner surface of a tube
- l – laminar
- m – mean
- T – uniform tube wall temperature
- w – tube wall

1. Introduction

Publications on the dynamics of plate fin and tube heat exchangers (PFTHE) are limited in number. Mathematical models of heat exchangers that simulate non-steady state operation are needed to analyze the start-up and shutdown of heat exchangers. Dynamical models of heat exchangers are also used in PID control systems as well as in model-based control systems. However, a steady state of heat exchangers is analyzed in most of the works [1].

The transient response of the PFTHE was modelled in [2–6]. Usually, fins are modelled as elements with lumped thermal capacity while the equivalent heat transfer coefficient on the air side is calculated assuming the steady-state [2–6]. The steady-state temperature distribution in fins is used to determine the equivalent heat transfer – this simplification can lead to some errors, especially for higher fins.

The system of governing differential equations is solved by the Laplace transform or the finite difference method. The Laplace transform method has been widely used by Roetzel and Xuan [2] to model the transient operation of various heat exchangers. Taler [4] modelled the transient response of the PFTHE for a stepwise increase in liquid or gas temperature using the Laplace transform method. The transient temperature of the fluids was compared with temperature obtained by the finite volume method.

Korzeń and Taler [6] developed a new mathematical model of the PFTHE to simulate its transient operation. In contrast to the existing methods for the modelling of the transient response of heat exchangers with extended surfaces in which the weighted steady-state heat transfer coefficient on the finned tube side is used, the transient temperature distribution is calculated in each fin. This allows for a more exact computation of the heat flow rate from the fins to the flowing gas.

Usually, modelling PFTHEs assumes that the fluid flow inside the tubes is turbulent. However, many low-duty heat exchangers operate in the transitional region when the Reynolds number varies in the range of 2,300 to around 12,000.

In this paper, the numerical modelling of the transient work of a PFTHE for a low Reynolds numbers on the liquid side is carried out.

2. Mathematical formulation of the problem

The system of partial differential equations describing the space and time changes of liquid T_1 , tube wall T_w , and air T_2 temperatures in one-row plate-fin and tube heat exchangers are [6]:

► liquid

$$\frac{1}{N_1} \frac{\partial T_1}{\partial x^+} + \tau_1 \frac{\partial T_1}{\partial t} = -(T_1 - T_w) \quad (1)$$

► tube wall

$$U_m \delta_w \rho_w c_w \frac{\partial T_w}{\partial t} + \frac{m_f c_f}{s} \frac{\partial \bar{T}_f}{\partial t} = \frac{k_w U_m \delta_w}{L_{ch}^2} \frac{\partial^2 T_w}{\partial (x^+)^2} + h_w U_{in} (T_1 - T_w) + h_o U_{bo} (\bar{T}_2 - T_w) \quad (2)$$

► air

$$\frac{1}{N_2} \frac{\partial T_2}{\partial y^+} + \tau_2 \frac{\partial T_2}{\partial t} = T_w - T_2 \quad (3)$$

where \bar{T}_2 denotes the mean air temperature over the row thickness, defined as:

$$\bar{T}_2(x^+, t) = \int_0^1 T_2(x^+, y^+, t) dy^+ \quad (4)$$

The symbols $x^+ = x/L_{ch}$ and $y^+ = y/p_2$ in equations (1)–(3) represent dimensionless coordinates. The numbers of heat transfer units N_1 and N_2 are given by:

$$N_1 = \frac{h_1 A_{in}}{\dot{m}_1 c_{p1}}, \quad N_2 = \frac{h_2 A_{bo}}{\dot{m}_2 c_{p2}} \quad (5)$$

where:

$$\begin{aligned} s &= L_{ch}/n_p \\ A_{in} &= n_r \bar{U}_{in} L_{ch} \\ A_{bo} &= n_r \bar{U}_{bo} L_{ch} \end{aligned}$$

The time constants τ_1 and τ_2 are:

$$\tau_1 = \frac{m_1 c_{p1}}{h_1 A_{in}}, \quad \tau_2 = \frac{m_2 c_{p2}}{h_2 A_{bo}} \quad (6)$$

The symbols in equations (1)–(6) denote:

$$m_1 = n_r A_{in} L_{ch} \rho_1, \quad m_2 = n_r (p_1 p_2 - A_{oval}) (s - \delta_f) n_f \rho_2, \quad m_w = n_r U_m \delta_w L_{ch} \rho_w$$

$$m_f = (p_1 p_2 - A_{oval}) \delta_f \rho_w, \quad A_{in} = \pi ab, \quad A_{oval} = \pi (a + \delta_w) (b + \delta_w), \quad U_m = (U_{in} + U_{bo}) / 2.$$

The subscript w refers to the wall, f refers to the fin, and m refers to the mean value. The weighted heat transfer coefficient h_o is defined by:

$$h_o(t) = h_2(t) \left[\frac{A_{bbf}}{A_{bo}} + \frac{A_f}{A_{bo}} \cdot \eta_f(h_2, t) \right] \quad (7)$$

The initial temperatures of both fluids are equal and amount to T_0 . The initial conditions are:

$$T_1(x^+, t) \Big|_{t=0} = T_{1,0}(x^+) \quad (8)$$

$$T_w(x^+, t) \Big|_{t=0} = T_{w,0}(x^+) \quad (9)$$

$$T_2(x^+, y^+, t) \Big|_{t=0} = T_{2,0}(x^+, y^+) \quad (10)$$

The boundary conditions have the following form:

$$T_1(x^+, t) \Big|_{x^+=0} = f_1(t) \quad (11)$$

$$T_2(x^+, y^+, t) \Big|_{y^+=0} = f_2(t) \quad (12)$$

$$\frac{\partial T_w}{\partial x} \Big|_{x=0} = 0 \quad (13)$$

$$\frac{\partial T_w}{\partial x} \Big|_{x=L_{ch}} = 0 \quad (14)$$

where:

$f_1(t), f_2(t)$ – functions of time describing the variation of the liquid and air temperatures at the inlets to the exchanger.

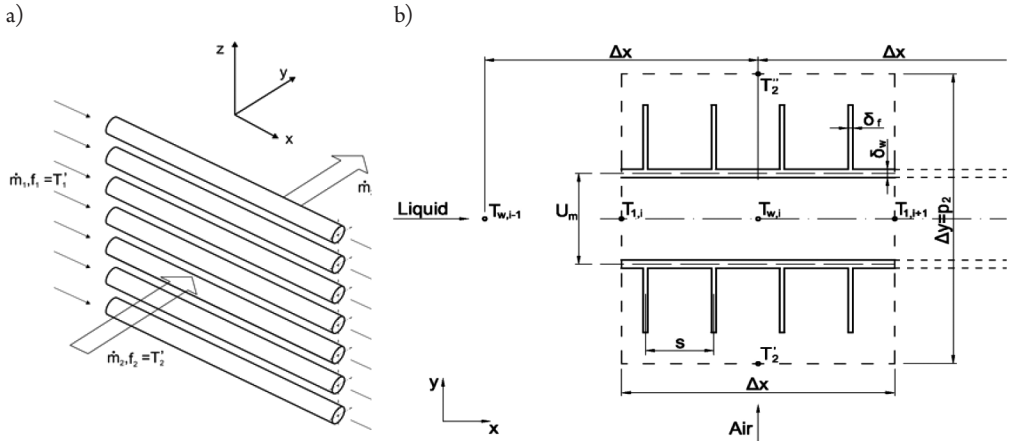


Fig. 1. Scheme of the one-row heat exchanger (a) and control volume (b)

The fin efficiency appearing in a relationship (7) was calculated using the finite volume method based on the finite element method. The division of the fin into finite volumes with specified numbers of nodes is shown in Fig. 2.

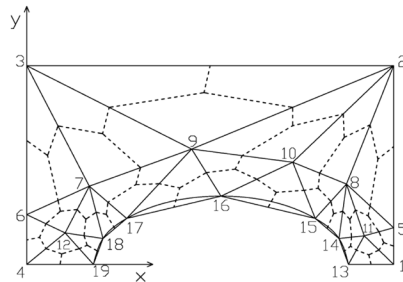


Fig. 2. Division of the fin model into finite volumes with node numbers

The initial-boundary value problem defined by equations (1–14) applies to heat exchangers made of bare or finned tubes. For bare tubes, m_f is equal to zero because there are no fins.

The transient temperatures of the fluids and tube wall in the one-row heat exchanger (Fig. 1) were determined by the explicit finite difference method. To calculate the time-dependent efficiency η_f of the rectangular fin attached to an oval tube, the finite volume – finite element method (FVM-FEM) was used. A mathematical model of the whole heat

exchanger with a complex flow system was built based on the mathematical model of the one-row heat exchanger.

The automotive radiator for a spark-ignition combustion engine with a capacity of 1.580 cm³ is a double-row, two-pass plate-finned heat exchanger. The radiator consists of aluminium tubes with an oval cross section. The cooling liquid flows in parallel through both tube rows.

3. Experimental correlations for water- and air-side Nusselt numbers

In the developed mathematical model of the exchanger, the heat transfer coefficients on the air and water side are calculated from experimental correlations. The correlations for the heat transfer coefficients are derived assuming a fully developed turbulent flow in straight tubes. One of the most common correlations is the Dittus-Boelter formula [7–9]:

$$\text{Nu}_w = 0.023 \text{Re}_w^{0.8} \text{Pr}_w^n \left[1 + \left(\frac{d_r}{L_{ch}} \right)^{2/3} \right] \quad (15)$$

where $n = 0.4$ when the fluid is heated and $n = 0.3$ when it is cooled.

Over recent years, the Gnielinski correlation has been becoming more and more popular [10–11].

$$\text{Nu}_w = \frac{(\xi/8)(\text{Re}_w - 1000)\text{Pr}_w}{(1 + 12.7\sqrt{(\xi/8)}(\text{Pr}_w^{2/3} - 1))} \left[1 + \left(\frac{d_r}{L_{ch}} \right)^{2/3} \right] \quad (16)$$

where the friction loss coefficient ξ is defined as:

$$\xi = \frac{1}{(1.82 \log \text{Re}_w - 1.64)^2} = \frac{1}{(0.79 \ln \text{Re}_w - 1.64)^2} \quad (17)$$

In Formula (16), symbols d_r and L_{ch} denote the tube hydraulic diameter and length, respectively. The reason for the growing popularity of the Gnielinski formula (16) is its greater accuracy in the transition area of $2300 < \text{Re}_w < 10000$. Despite the fact that the Gnielinski proposal gives smaller values of the heat transfer coefficient in the transition area compared to the Dittus-Boelter formula, these values are still inflated [12–13]. If $\text{Re}_w < 2300$, the flow is laminar; the Nusselt number is $\text{Nu}_w = 4.364$ and does not depend on the Reynolds number [8–9]. It can be easily checked that both the Dittus-Boelter and the Gnielinski formulae give values of Nu_w much higher than 4.364. For this reason, the correlations for the Nusselt numbers on the water and air side were determined based on experimental testing.

The following form of the correlation for the Nusselt number at the air side was taken:

$$\text{Nu}_a = \alpha_1 \text{Re}_a^{\alpha_2} \text{Pr}_a^{1/3} \quad (18)$$

Considering that the range of changes in the Reynolds number at the air side is not too wide, it is possible to approximate experimental data effectively using the exponential equation written above (18).

The correlation for the Nusselt number at the water side was taken in a form similar to the formulae developed by Petukhov & Kirillov [14] and Gnielinski [10].

$$\text{Nu}_w = \frac{(\xi/8)(\text{Re}_w - x_3)\text{Pr}_w}{(1 + x_4 \sqrt{(\xi/8)(\text{Pr}_w^{2/3} - 1)})} \left[1 + \left(\frac{d_r}{L_{ch}} \right)^{2/3} \right] \quad (19)$$

The values of coefficients x_1, x_2, \dots, x_m will be selected so that the sum of the squares of differences in temperature:

$$S = \sum_{i=1}^n [f''_{w,i} - T''_{w,i}(x_1, \dots, x_m)]^2 = \min \quad (20)$$

$$f''_{w,i} = T'_{w,i} - \Delta T_{w,i} \quad (21)$$

should reach the minimum.

The real values of the determined parameters $\tilde{x}_1, \dots, \tilde{x}_m$ are included with the probability $P = (1 - \alpha) \cdot 100$ [%] in the following intervals [15–16]:

$$x_i - t_{n-m}^{\alpha/2} \cdot s_t \sqrt{c_{ii}} \leq \tilde{x}_i \leq x_i + t_{n-m}^{\alpha/2} \cdot s_t \sqrt{c_{ii}} \quad (22)$$

where:

- x_i – parameter value determined using the least squares method,
- $t_{n-m}^{\alpha/2}$ – t -Student distribution quantile for the confidence level $1 - \alpha$ and $n - m$ degrees of freedom.

Quantity s_t^2 is the variance estimate calculated from:

$$s_t^2 = \frac{\sum_{i=1}^n [T''_{w,i}(x_1, \dots, x_m) - f''_{w,i}]^2}{n - m} = \frac{S(\tilde{x}_1, \dots, \tilde{x}_m)}{n - m} \quad (23)$$

where:

- n – number of measuring points,
- m – number of sought parameters.

Quantities c_{ii} are diagonal elements c_{ii} of the covariance matrix.

In this case, the number of measuring points is $n = 47$, and the number of unknown parameters is $m = 4$.

3.1. Measurement results

The thermal and flow measurements of the exchanger were performed for different air and water flow velocities. The measurement results are listed in Table 1.

Table 1. Radiator measurement results

Test run number	$w_{0,i}$ [m/s]	$\dot{V}'_{w,i}$ [l/h]	$T'_{am,i}$ [°C]	$T'_{w,i}$ [°C]	$\Delta T_{w,i}$ [°C]
1	0.40	947.40	12.65	62.21	3.89
2	0.66	945.60	10.96	62.24	5.74
3	0.92	945.00	9.91	62.14	7.41
4	1.18	944.40	9.28	62.04	8.85
5	1.44	946.20	8.95	61.95	10.09
6	1.70	945.60	8.83	61.70	11.02
7	1.96	945.00	8.77	61.35	11.79
8	2.22	945.60	8.94	61.14	12.40
9	2.22	1150.80	8.64	60.81	10.87
10	1.96	1151.40	8.65	60.51	10.17
11	1.70	1153.20	8.83	60.24	9.28
12	1.44	1152.60	9.23	60.13	8.48
13	1.18	1150.20	8.96	60.03	7.48
14	0.92	1151.40	9.22	60.04	6.37
15	0.66	1150.80	9.42	60.00	5.13
16	0.40	1509.00	11.56	61.08	2.68
17	0.66	1509.60	10.73	61.10	3.79
18	0.92	1510.20	10.23	61.08	4.85
19	1.18	1511.40	9.87	61.07	5.88
20	1.44	1509.60	9.44	60.94	6.75
21	1.70	1508.40	9.00	60.73	7.57
22	1.96	1509.60	8.98	60.51	8.21
23	2.22	1507.80	9.01	60.30	8.74
24	2.22	1842.60	8.88	59.97	7.42
25	1.96	1842.60	8.90	59.75	6.86
26	1.70	1843.20	8.91	59.47	6.24
27	1.44	1840.20	9.06	59.24	5.54
28	1.18	1840.80	9.13	59.19	4.84
29	0.92	1842.60	9.10	59.17	4.11
30	0.66	1840.20	9.37	59.16	3.25
31	0.40	1842.60	9.88	59.30	2.30
32	0.40	2146.20	11.71	60.02	1.69
33	0.66	2146.20	10.84	60.17	2.54
34	0.92	2145.60	10.09	60.18	3.39
35	1.18	2143.20	9.52	60.18	4.22
36	1.44	2142.60	9.27	60.07	4.84
37	1.70	2142.60	8.99	59.75	5.46
38	1.96	2139.60	8.96	59.44	5.92
39	2.22	2135.40	9.41	59.22	6.35
40	2.22	2412.00	9.08	58.76	5.70
41	1.96	2413.20	9.12	58.68	5.21
42	1.70	2410.80	9.22	58.40	4.75
43	1.44	2410.80	9.38	58.17	4.23
44	1.18	2410.80	9.10	58.14	3.73
45	0.92	2409.60	9.36	58.23	3.05
46	0.66	2409.60	9.77	58.16	2.46
47	0.40	2410.20	10.05	58.33	1.76



The Reynolds number values at the air side is $Re_a = w_{\max} d_h / \nu_a$ and at the water side, it is $Re_w = w_{wg} d_r / \nu_w$. The physical properties of the air were calculated at the average air temperature. Similarly, the thermophysical properties of water were calculated at the average temperature. The average temperature is understood as the arithmetic mean of the average temperature at the exchanger inlet and outlet. The water velocity in the upper pass w_{wg} is smaller than the water velocity in the lower pass w_{wd} because in the upper pass, water flows in parallel through 20 tubes whereas in the lower one, through 18.

3.2. Experimental correlations

Based on the data presented in Table 1, the following values of individual coefficients were obtained:

$$x_1 = 0.0713 \pm 0.0053; x_2 = 0.7055 \pm 0.0136; x_3 = 0.4624 \pm 0.3194; x_4 = 22.2273 \pm 0.3163$$

The coefficients are present in Formulae (18) and (19).

The value of the sum of squares is $S = 1.07041 K^2$.

The correlations for the Nusselt numbers on the water and air side have the following forms:

$$Nu_a = 0.0713 Re_a^{0.7055} Pr_a^{1/3}, 60 \leq Re_a \leq 351 \quad (24)$$

$$Nu_w = \frac{(\xi/8)(Re_w - 0.4624)Pr_w}{(1 + 22.2273\sqrt{(\xi/8)(Pr_w^{2/3} - 1)})} \left[1 + \left(\frac{d_r}{L_{ch}} \right)^{2/3} \right], 3850 \leq Re_w \leq 11317 \quad (25)$$

In the mathematical model of the radiator operation under unsteady-state conditions, relationships (24) and (25) were used.

3.3. The sudden increase in water mass flow rate and the simultaneous reduction in air flow velocity

The comparison of the results obtained from measurements and calculations is presented in Fig. 3.

The water volume flow \dot{V}'_w was increased from about 950 l/h to about 2,400 l/h. Additionally, the air velocity before the exchanger w_0 was reduced from about 2.2 m/s to about 1.2 m/s. Both of these changes contribute to a rise in the water and air temperatures after the exchanger. The smaller velocity of air involves a drop in the heat transfer coefficient on the outer surface of tubes and fins, which in turn decreases the heat flux transferred from water to the flowing air. The air temperature rises after the heat exchanger due to the air mass flow being smaller.

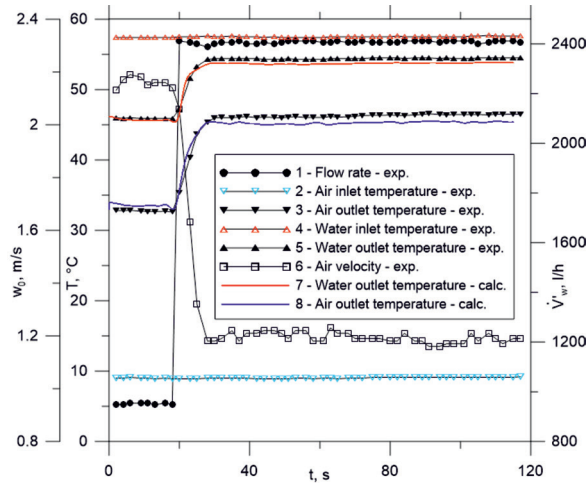


Fig. 3. The exchanger unsteady-state operation caused by a sudden reduction in the water volume flow

- 1 - \dot{V}'_w – measured water volume flow at the heat exchanger inlet, l/s
- 2 - T'_{am} – measured mean air temperature at the heat exchanger inlet, °C
- 3 - T''_{am} – measured mean air temperature after the exchanger, °C
- 4 - T'_w – measured water temperature at the heat exchanger inlet, °C
- 5 - T''_w – measured water temperature at the heat exchanger outlet, °C
- 6 - w'_0 – measured air velocity at the heat exchanger inlet, m/s
- 7 - T''_w – calculated water temperature at the heat exchanger outlet, °C
- 8 - T''_{am} – calculated average air temperature at the heat exchanger outlet, °C.

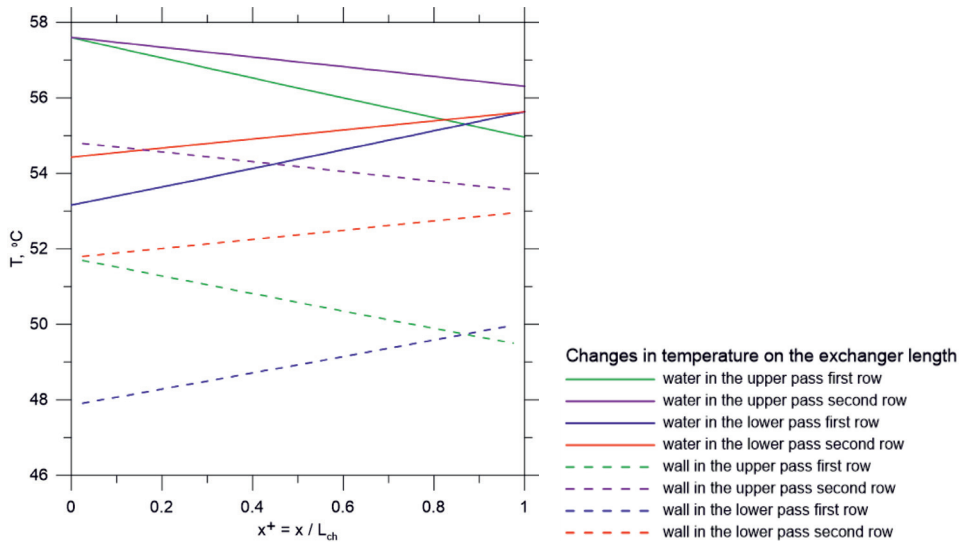


Fig. 4. Distribution of the water and the tube wall temperatures on exchanger length for time $t = 117s$ in the steady state

Fig. 4 presents changes in the water and the tube wall temperatures on the exchanger length for $t = 117$ s.

In analyzing the results presented in Fig. 4, it can be seen that water in the first row of tubes cools down more than in the tubes placed in the second row. This concerns both the upper and lower pass. It can be observed that the tube wall temperature is lower than the water temperature because cold air absorbs heat.

The curves illustrating time-dependent changes in the temperatures of selected fins are presented in Fig. 5a-d. An analysis of the results indicates that the highest temperature is at the fin base, and the lowest in node 3 (Fig. 2), which is the most distant from the tube axis. It can be seen that the temperatures of the fins in the first tube row (Fig. 5a and 5c) are lower than in the second row (Fig. 5b and 5d). The cold inflowing air cools the fins and tubes located in the first row more effectively. The air temperature after the first tube row is much higher compared to the inlet air temperature. Due to a reduction in the difference between the temperatures of the flowing air and the tubes located in the second row, the temperature of the water and fins in the second tube row is higher than in the first row.

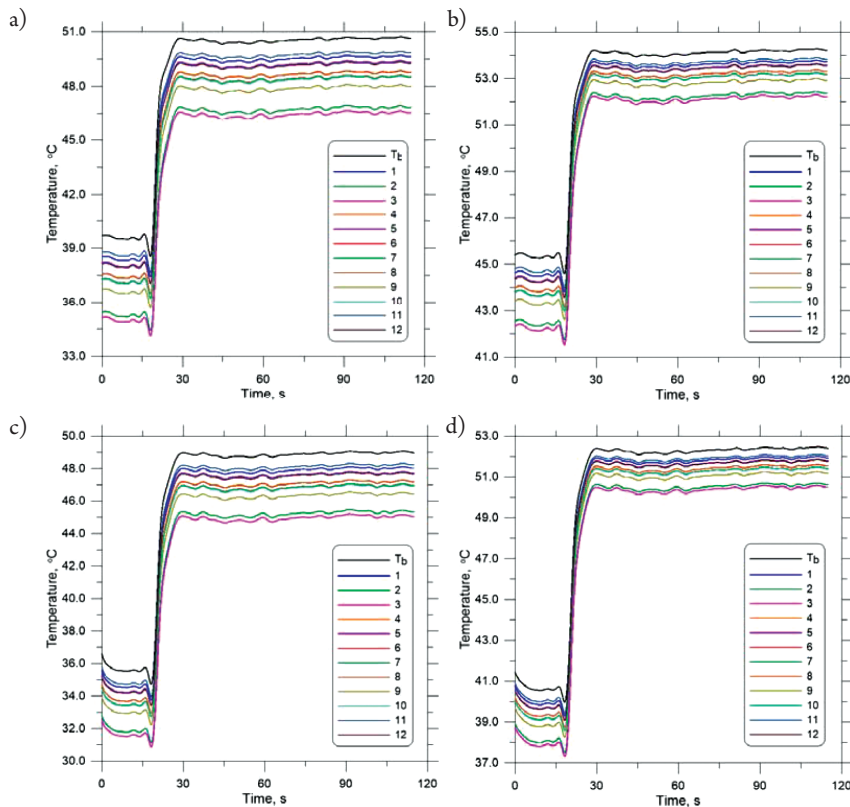


Fig. 5. Changes in the fin base temperature T_b and the fin temperature in 12 nodes that are marked in Fig. 2, at a distance of 247 mm (9.5 cell lengths) from each pass inlet: (a) – first tube row in the first (upper) pass; (b) – second tube row in the first (upper) pass; (c) – first tube row in the second (lower) pass; (d) – second tube row in the second (lower) pass

4. Conclusions

The calculations and measurements carried out in the paper confirm that the developed numerical model of the plate fin and tube heat exchanger has a high level of accuracy. This model is particularly useful to simulate the exchanger, where the temperature of the fins can be very high. Thanks to the experimental determination of heat transfer correlations on the air and water sides, a very strong agreement of calculations and measurements was reached. The developed model can be used to simulate the heating and cooling heat exchanger and in automatic control systems.

References

- [1] Taler D., *Mathematical modeling and control of plate fin and tube heat*, Energy Conversion and Management, 96, 2015, 452–462.
- [2] Roetzel W., Xuan Y., *Dynamic behaviour of heat exchangers*, Computational Mechanics Publications, Vol. 3, WIT Press, Southampton 1998.
- [3] Ataer Ö.E., *An approximate method for transient behavior of finned-tube cross-flow heat exchangers*, Int. J. Refrig., 27, 2004, 529–539.
- [4] Taler D., *Direct and inverse heat transfer problems in dynamics of plate fin and tube heat exchangers*, in: Belmiloudi A. (ed.) *Heat transfer, mathematical modelling, numerical methods and information technology*, InTech, Rijeka 2011, 77–100, free online edition: www.intechopen.com.
- [5] Vaisi A., Talebi S., Esmailpour M., *Transient behavior simulation of fin-and-tube heat exchangers for the variation of the inlet temperatures of both fluids*, International Communications in Heat and Mass Transfer, 38, 2011, 951–957.
- [6] Korzeń A., Taler D., *Modeling of transient response of a plate fin and tube heat exchanger*, Int. J. Therm. Sci., 92, 2015, 188–198.
- [7] Arpaci V.S., Kao S.H., Selamet A., *Introduction to Heat Transfer*, Prentice Hall, Upper Saddle River, NJ, USA 1999.
- [8] Bejan A., Kraus A.D., Ed., *Heat Transfer Handbook*, John Wiley & Sons, Inc., Hoboken, New Jersey 2003.
- [9] Wiśniewski S, Wiśniewski T.S., *Wymiana ciepła (Heat exchange)*, Wydanie 6, WNT, Warszawa 2009.
- [10] Gnielinski V., *Neue Gleichungen für den Wärme- und den Stoffübergang in turbulent durchströmten Rohren und Kanälen*, Forschung im Ingenieurwesen, 41/1975 Nr 1, 8–16.
- [11] Webb R. L., *Principles of enhanced heat transfer*, John Wiley & Sons, Inc., Hoboken, New Jersey 1994.
- [12] Mirth D.R., Ramadhyani S., Hittle D.C., *Thermal performance of chilled-water cooling coils operating at low water velocities*, ASHRAE Transactions, 99, 1993, Part 1, 43–53.
- [13] Mirth D. R., Ramadhyani S., *Correlations for predicting the air side Nusselt numbers and friction factors in chilled-water cooling coils*, Experimental Heat Transfer, 7, 1994, 143–162.



- [14] Petukhov B.S., Genin A.G., Kovalev S.A., *Heat transfer in nuclear power plants*, Atomizdat, Moscow 1974 (in Russian).
- [15] Brandt S., *Data Analysis. Statistical and computational methods for scientists and engineers*, 3rd edn. Springer, Berlin 1999.
- [16] Coleman H.W., Steele W.G., *Experimentation, validation, and uncertainty analysis for engineers*, 3rd edn. Wiley, Hoboken 2009.

Paweł Ziółkowski (pawel.ziolkowski@imp.gda.pl)

Janusz Badur

Energy Conversion Department, Institute of Fluid Flow Machinery, Polish Academy of Sciences, Gdańsk, Poland

A THERMODYNAMIC AND TECHNICAL ANALYSIS OF A ZERO-EMISSION
POWER PLANT IN POMERANIA

ANALIZA TERMODYNAMICZNA I TECHNICZNA ZEROEMISYJNEJ
ELEKTROWNI DLA POMORZA

Abstract

This paper presents the results of a thermodynamic analysis and a method of selecting individual devices and their components to design a zero-emission power plant project in Pomerania. Another aim of the paper is to present the technological abilities of the application of gas-steam turbines with a particular emphasis on enhanced energy conversion in the construction of a wet combustion chamber using cooling water transpiration and a gas-steam expander.

Keywords: enhanced energy conversion, thermal transpiration, nanoscale effect

Streszczenie

W artykule przedstawiono wyniki analizy termodynamicznej oraz dobór poszczególnych urządzeń i ich części istotnych przy projekcie zeroemisyjnej elektrowni dla Pomorza. Kolejnym celem pracy jest przedstawienie technologicznych możliwości wdrożenia turbiny gazowo-parowej, ze szczególnym uwzględnieniem zagadnień wzmożonej konwersji energii przy konstrukcji mokrej komory spalania wykorzystującej chłodzenie transpiracyjne wodą i ekspandera gazowo-parowego.

Słowa kluczowe: wzmożona konwersja energii, termiczna transpiracja, efekty nanoskali

1. Introduction

Due to the fact that Pomerania and its surrounding area does not have enough electrical energy and devices stabilising the RES (renewable energy sources), the legitimacy of building a power plant in this area is a particularly important question. However, the problem is that renewable sources often cause the dispersion of energy – both in terms of its quality and quantity. To ensure the conversion of the highest quality and quantity that satisfy the needs of the PSE (Polish energetic system), we should also take into account energy from fossil fuel such as natural gases. Flammable gases (including hydrogen, methane, shale gas or other unconventional gases interacting with RES) are developing the world economy. This not only makes conducting start-ups and shut-downs of gas turbines much easier, it also increases the diversification of energy sources. This paper presents a zero-emission power plant developing in works [1–4]. We assume that enhanced energy conversion is possible in two devices which are new for gas turbines: 1) wet combustion chamber using oxy-combustion and water cooling by thermal transpiration; 2) a spray-ejector condenser. These devices are all important in modelling thermodynamic cycles [5]. This system is based on the use of shale gas at the location from where it is extracted in a compact, zero-emission, gas-steam power plant. The compactness of the cycle is achieved by using two new devices [1–3]: 1) a wet combustion chamber (in a porous walls of combustion chamber there is no place for typical bulk phenomena, since the whole flow is dominated by surface processes for example Navier slip and Reynolds transpiration); 2) a spray-ejector condenser (condensation of steam from gas-steam medium occurs due to the contact with surface injected water). The main aim of this paper is to present the thermodynamic and technological benefits of the application of a gas-steam turbine, with a particular emphasis on a wet combustion chamber using cooling transpiration, regenerative heat exchangers and gas-steam expanders. Hence, the aim of this study is to present concepts and examples of solutions for a zero-emission power plant for Pomerania.

To adopt these constructions for the enhanced conversion of energy (when fluid acts close to the wall surface it enables the enhancement of the normal Navier slip), we use surface phenomena to improve the exchange of mass, momentum and energy. One example of a method to improve the flow in porous structures is thermal transpiration that uses the mobility force. Besides the classical ‘bulk’ behaviour, wall stress also appears to introduce new quantities such as surface friction force, surface mobility force, etc. So mobility forces is the ability of a fluid (gas or liquid) to flow along the wall without the assistance of, or even in opposition to, bulk (volume) forces. In this paper has been postulated that generally surface “*vis impressa*” can be additively split into friction and mobility forces. A summary of the phenomenon is presented in [4, 6–8].

1.1. Literature survey

The technologies, which are based on high-efficiency power plant blocks using oxy-combustion and the capture of the carbon dioxide, may stabilise and support the electroenergetical system with regard to the reduction of gas emissions in accordance with



UE policies. Such a system can be based on: 1) oxy-fuel combustion in a circulating fluidised bed [9–11]; 2) pulverised coal-fed boiler with oxy-combustion and the recirculation of flue gas [12, 13]; 3) gas turbine using an oxy-combustion cycle with flue gas recirculation [14–18]; 4) gas-steam turbine using oxy-combustion and the injection of water/steam to the combustion chamber [1–3, 17, 19–23]. A double Brayton cycle with oxy-combustion in a wet combustor chamber with water condensation combined with carbon dioxide capture is analysed in paper [3]. As in this cycle, working fluid is a mixture of steam and gas, it is an example of a gas-steam turbine cycle which combines the advantages of both, gas and steam systems.

It should be added, that Clean Energy Systems and the Siemens Corporation cooperate together to invent a large-scale, oxy-combustion power plant, which combines both gas and steam turbine operation [21]. In the literature, this cycle with oxy combustion and water injection is referred to as a water cycle [3, 19–21] because of the fact that steam makes up 90% of the content of mixture; the remaining 10% is carbon dioxide from methane combustion. A more sophisticated cycle which works on steam and enables reaching a higher level of efficiency is the GRAZ cycle [19].

In paper [21], research results relating to the gas-steam turbine are presented; gas-steam is the working fluid of these turbines. The gas-steam generator, into which the fuel, pure oxygen and water are injected, is a very important element of the cycle. In the presence of oxygen without nitrogen, the fuel burns at a much higher temperature than in traditional burning chambers; however, the temperature is decreased as the result of the evaporation of water [21]. There have already been modifications made to the GE J79 combustion chamber into gas-steam mixture generator, it works at a pressure of 11.6 bar and at 760°C. In the second-generation power plant cycle, with use of the SGT900 both gas-steam mixture generator and turbine, due to the temperature is expected to rise up to 1080–1260°C before the first stage turbine. In the third generation gas-steam turbine, the work flux is expected to reach approximately 1650–1760°C and 40 bar [21].

In principle, the oxy-combustion and capture of CO₂ can be accomplished more easily and cheaply than the post-combustion removal of CO₂ from the exhaust gases emitted by a conventional coal plant. The promise of more efficient carbon capture is one of the main reasons that has led to the development of clean gas technology (CGT). This concept is based on the introduction of compact nanotechnology devices leading to the removal of large-scale devices such as heat recovery steam generators (HRSGs).

2. Thermodynamic analysis

This section briefly discusses the specifics of the cycle (Fig. 1) and presents the main results. The dual Brayton cycle (Fig. 1a) consists of a traditional Brayton cycle – BC (points 1–4) and a second inverted Brayton cycle – IBC (points 1ⁱⁿ–4ⁱⁿ). The term ‘inverted cycle’ refers to a change of order of the compressor and turbine; therefore, firstly, expansion of the medium occurs in the expander GTⁱⁿ (points 1ⁱⁿ–2ⁱⁿ), then regeneration occurs in the heat

exchanger HE^{in} (points $2^{in}-2^{in,a}$), heat rejection then occurs in the condenser CON^{in} (points $2^{in,a}-3^{in}$), and finally, compression occurs in the compressor C^{in} (points $3^{in}-4^{in}$) [3]. With hot working fluid at atmospheric pressure flowing out of the GT from the Brayton cycle, we could get additional turbine GT^{in} power by expanding the exhaust fumes below ambient pressure [3]. Thus, this expansion of gas-steam mixture is similar to low pressure expansion taking place in the steam turbine. The main disadvantage of the whole system is the necessity for an air-separation unit (ASU), to supply the combustion chamber with pure oxygen. Moreover, the problem of the NO_x emission is almost entirely eliminated by the 95% oxy combustion. Additionally, the nitrogen turbine (GT_{N_2}) might be used and would be fuelled from the oxygen and nitrogen separation station (ASU).

Technical realisation of the IBC may cause such problems as the increase of the power unit size by extension the low-pressure gas-steam turbine cylinder (points $1^{in}-2^{in}$), the heat exchanger (points $2^{in}-2^{in,a}$), and the steam condenser (points $2^{in,a}-3^{in}$). The extension of the “cold end” of the turbine can be undesirable from economic and technical standpoints. So, in other words, the low specific volume of the turbine outlet gas-steam mixture in IBC (inverted Brayton cycle) leads to an increase in the demand for materials. The increase of the diameter is caused by the necessity to reduce the axial velocity of gases flowing through the blading system; furthermore, the nature of the work performed by the exchanger requires more complex geometry to reduce the loss of movement.

The calculations of the heat cycle have been performed for the constant mass flow rate of: oxygen $\dot{m}_o \approx 51.8$ kg/s; water $\dot{m}_{11} = 117.7$ kg/s; fuel $\dot{m}_f = 12.83$ kg/s on the combustion chamber inlet. Total exhaust mass flow rate is approximately $\dot{m}_{ex} = 182.3$ kg/s. The combustion chamber pressure was also fixed to 4 MPa. Moreover, the temperature difference in the heat exchanger HE was also assumed to be $\Delta T = 30$ K. Additionally, the condensation temperature was assumed to be $t_{s^{in}} = 30^\circ C$.

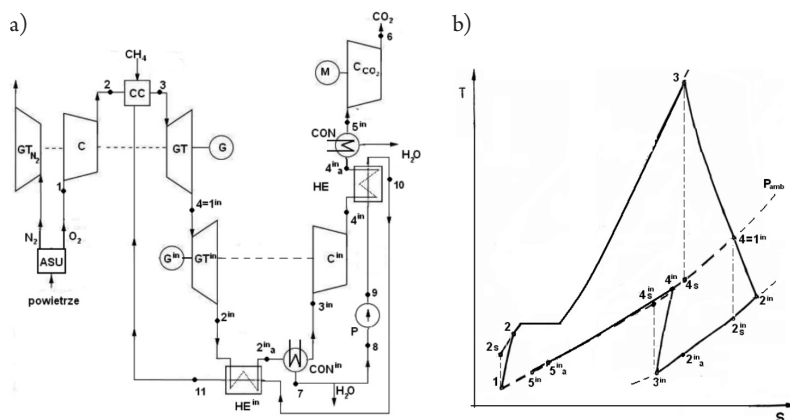


Fig. 1. a) Scheme of dual Brayton cycle using oxy-combustion in the wet combustion chamber, the condensation of the water vapour and the capture of CO_2 , where: ASU – station of oxygen separation; CC – combustion chamber; C – compressor; GT – gas turbine; HE – heat exchanger; G – generator; M – motor; CON – condenser; P – pump; GT_{N_2} – additional turbine for N_2 ; C_{CO_2} – CO_2 compressor, b) graph of entropy temperature [3]

Gas-steam mixture (exhaust gases) leaving GT^{in} is of a high temperature; therefore, it requires cooling in a special heat exchanger HE^{in} (exhaust gases – water), in which water is warming up and is then injected into the combustion chamber (CC). After being cooled, the exhaust emissions go to the condenser (CON^{in}) in which the steam component of steam-gas is condensed – the amount of condensed water depends on the final expansion pressure. Because the gas pressure is lower than the atmospheric pressure, the pressure is raised through use of compressor C^{in} and it dries the exhaust ($HE+CON$) in subsequent devices [3]. Changes in the dual Brayton cycle are shown on the temperature-entropy graph (Fig. 1b).

A graph of efficiency versus condensing pressure is shown in Fig. 2. The analysis shows that despite an initial decrease in traditional Brayton cycle efficiency η_{el-BC} , the total block efficiency η_{el-DBC} increased (Fig. 2) due to the decrease in condensation pressure. The efficiency of the Brayton cycle η_{el-BC} decreased because the temperature behind the gas turbine dropped and thereby the degree of heat recovery reduced in the regenerative heat exchanger (HE). In turn, the efficiency of the inverted Brayton cycle η_{el-IBC} increased to a value of $\eta_{el-IBC} = 15.3\%$ at a condensing pressure of around $p = 7$ kPa. As a result of these phenomena, the optimal efficiency value $\eta_{el-netto}$ for the entire block was identified as being at a pressure of $p = 7.7$ kPa in the condenser. This value may rise due to increased flow in the wet combustion chamber – this is further described in the next section. Additionally, the whole system efficiency falls by around 8.66% due to the production of oxygen (6.38%) and the capture of CO_2 (2.28%).

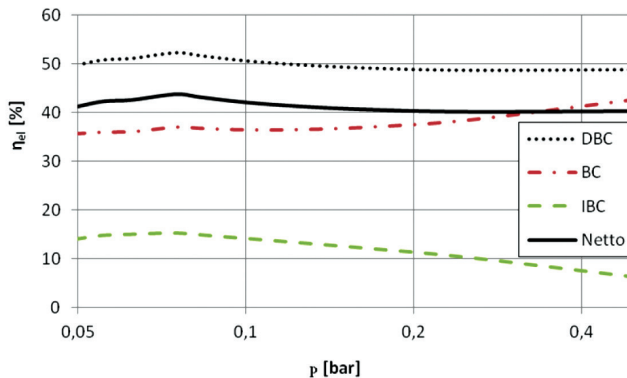


Fig. 2. The dependence of the efficiency of the entire system with capture carbon $\eta_{el-netto}$, efficiency of the Brayton cycle η_{el-BC} , dual Brayton cycle η_{el-DBC} and inverted Brayton cycle η_{el-IBC} upon condensing pressure p [3]

3. Flow reinforcement in the wet combustion chamber

The joint action of the both Reynolds thermal mobility force and surface Navier slip should be predicted by measuring the fluid (gas or liquid) mass flow rate in porous materials. If pores become larger than 2–5 times the free length of rarefied gas, then an additional bulk contribution of viscous flow (Poiseuille's type) will be visible and the mass flow rate will be the summary effect of two surface and one bulk contributions. The enhancement of flow in the area of porous walls of the combustion chamber, through which cooling water

flows, can occur by two mechanisms: reduction of the frictional forces between the surface and a medium (fluid in this case); the emergence of mobility forces associated with thermal transpiration. A detailed description of the phenomenon of thermal transpiration as well as other phenomena relating to mobility can be found in [4, 6, 7] and can be expressed as follows:

$$\mathbf{f}_m = -c_{m\varpi} \text{grad}_s(\varpi) - c_{m\theta} \text{grad}_s(\theta) - c_{mN} \text{grad}_s(N) - \dots \quad (1)$$

in which there are factors affecting the mobility of the relevant coefficients specific to interfacial interactions, namely: $c_{m\varpi}$ – transpiration coefficient of Graham pressure; $c_{m\theta}$ – the coefficient of Reynolds thermal transpiration; c_{mN} – the coefficient of Graham component transpiration [7, 8]. These values depend on surface variation, there are also important changes occurring on the surface in a perpendicular direction, such as: velocity slip (momentum); the temperature jump (energy); the concentration jump of component of the mixture (mass). In case of the flow of a fluid mixture an effect of concentration jump (drop) may occur, particularly when the reacting mixture is considered, and channel walls have catalytic properties. Thus the discontinuity of concentration may take place in the direction normal to the wall. If we are talking about flow rate, an essential component is the velocity drop (slip) that affects both linear and parabolic friction forces. In the case of surface friction force, we can obtain the following equation by adding the adhesive link [4]:

$$\mathbf{f}_r = \nu_0(p - \varpi)\mathbf{e}_f + \nu(\mathbf{v} - \mathbf{v}_{wall}) + \nu_2(\mathbf{v} - \mathbf{v}_{wall})^2 \mathbf{e}_f \quad (2)$$

where the directional versor is $\mathbf{e}_f = (\mathbf{v} - \mathbf{v}_{wall}) / |\mathbf{v} - \mathbf{v}_{wall}|$ with three coefficients ν_0 ; ν ; ν_2 . (Duhem, Navier, du Buat, respectively). In turn, the velocity difference between the liquid and the wall $\mathbf{v} - \mathbf{v}_{wall}$ is usually equal to the drop (slip) velocity \mathbf{v}_s . Besides boundary effects and surface forces, the fluid volume behaves normally. The dimensionless enhancement of mass flow rate should be consider with respect to the Poiseuille pressure driven flow. In considering laminar flow through a conventional tube with a round cross section, we should consider the equation of mass flow rate:

$$\dot{m}_{no-slip} = \dot{m}_{Poiseuille} = \frac{\pi \rho d^4}{128 \mu L} (p_{in} - p_{out}) \sim \Delta p \quad (3)$$

where:

- ρ – density.
- d – diameter,
- L – length,
- μ – dynamic viscosity;
- $p_{in} - p_{out}$ – pressure difference.

Then, considering the flow through the nano-diameter whilst only taking into account the effect of the linear Navier link, we obtain [7]:

$$\dot{m} = \dot{m}_{Navier} = \frac{\pi a^2 \rho}{\nu} \frac{\Delta p}{L} \frac{a}{2} \left(1 + \frac{\nu a}{\mu 2}\right)^{-1} = \frac{\pi a^3 \rho l_s}{2\mu} \frac{\Delta p}{L} \left(1 + \frac{1}{2} \frac{a}{l_s}\right)^{-1} \quad (4)$$

The new constants: l_s slip length and ν surface viscosity are related to each other directly by dynamic viscosity $l_s = \mu/\nu$. We can also determine the dimensionless length of slip as a Navier number $Na = l_s/a$. Depending on the channel material and the medium flowing in this channel, the value l_s slip length and the slip (drop) velocity ν_s are varied. Taking Navier's and Poiseuille's solution into consideration for the round capillary pipe flow, we can easily find the flow enhancement due to the presence of a drop (slip) [7]:

$$\eta_{enh} = \frac{\dot{m}_{Navier}}{\dot{m}_{Poiseuille}} = \left(1 + \frac{8l_s}{a}\right) \left(1 + \frac{a}{2l_s}\right)^{-1} = (1 + 8Na)(1 + Na^{-1}/2)^{-1} \quad (5)$$

However, Helmholtz & von Piotrowski obtained quite similar formulae on the ratio of the mass flow rate in slipping flow and no-slip flow (Poiseuille flow) in a straight circular pipe with the inner radius a as [7]:

$$\eta_{enh} = \frac{\dot{m}_{slip}}{\dot{m}_{Poiseuille}} = \left(1 + 4 \frac{l_s}{a}\right) = 1 + 4Na \quad (6)$$

The joint action of the both Reynolds thermal mobility force and surface Navier slip (drop) should occur in porous wall of wet combustion chamber. However, the solution for a flow of a fluid in a capillary tube having inner radius a , which occurs under two deriving constant forces: the first one is the Navier pressure driven flow due to difference of pressure on the ends of the tube, and second one is the thermal transpiration due to difference of temperatures on the same ends of the tube. Since the fluid (gas, liquid or even changing phase mixture) is flowing from the higher pressure to lower pressure and, simultaneously, from the colder to the hotter ends, then these effects can be summarized. In this case, the following equation is obtained:

$$\dot{m} = \rho(\pi a^2) v_z^{avera} = -\rho(\pi a^2) \left[\frac{1}{8\mu} (a^2 + 4l_s a) \frac{dp}{dz} + \frac{c_{m\theta}}{\nu} \frac{d\theta}{dz} \right] \quad (7)$$

where dp/dz and $d\theta/dz$ defined the changes along the channel length. Therefore, the enhanced mass flow rate can be defined by equation:

$$\eta_{enh} = \frac{\dot{m}_{Maxwell}}{\dot{m}_{Poiseuille}} = \left(1 + 4 \frac{l_s}{a}\right) + \frac{8}{\pi} \frac{c_{m\theta}}{\nu} \frac{\mu}{\rho a^4} \frac{d\theta}{dz} \left(\frac{dp}{dz}\right)^{-1} \quad (8)$$

It should be added that the numerical implementation of Navier flow and Reynolds model of thermal transpiration and its usefulness for describing experiments is found in papers [7, 23, 24]. Additionally, the concept of a porous structure or microchannel cooling for gas turbine blades is the natural application of thermodynamics and heat transfer to accomplish two goals: firstly, to spread out the cooling network in a series of smaller and highly distributed channels in order to provide a much stronger uniformity of cooling and thermal gradients; secondly, to bring the cooling fluid closer to the blade surface (or combustion chamber) and to create more efficient heat transfer [25, 26].

4. Enhancement heat transfer

To design a compact power plant, it is necessary to firstly take into account not only the reduction in the size of the upper heat source but also a system of regenerative heat exchangers. In systems with enhanced heat transport, there are discontinuities in temperature, commonly known as temperature drops or jumps [27]. This extremely difficult problem in thermal-FSI (Fluid Solid Interaction) means that the temperature jumps can occur on the both side of a surface layer, hence the Smoluchowski thermal layer jump appears simultaneously in solid and fluid as was presented in Fig. 3. Mathematical model of this phenomenon should be self-equilibrated and self-consistent. Taking these requirements into account, a discontinuities temperature profile in a solid-fluid contact layer (Fig. 3) is discussed in work [4] and implemented in paper [27]. Some theoretical issues have been developed and presented in this section.

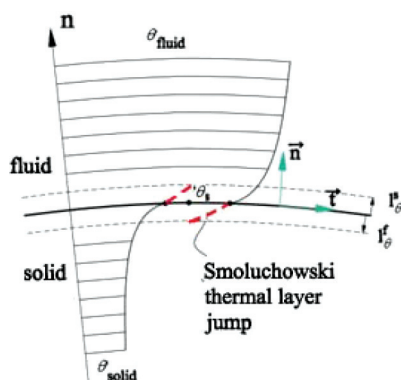


Fig. 3. Discontinuity of temperature θ in Smoluchowski thermal layer jump (the expected path of temperature changes is indicated by the red dotted line without taking into account the jump in temperature in solid l_0^s and fluid l_0^f) [27]

It should also be noted that the effect of the temperature jump is not identified with the effect of thermal transpiration phenomenon. Reynolds thermal transpiration can be presented as the macroscopic movement occurring at a fluid-solid phase interface induced in a fluid by a wall temperature gradient along its surface. While the second phenomenon (thermal

transpiration) is due to the increase in the flow direction of transport, the first phenomenon (temperature jump) is associated with a discontinuity or ambiguity of the wall temperature and fluid in its vicinity, in a direction normal to the wall surface, as shown in Fig. 3 [27]. This difficult issue, like others related to heat exchange [28–33], is still developing.

Proposed by Smoluchowski in 1896, the model assumes that it is possible to enter special parameter l_0 which is the length of the temperature jump and is related to the Stokes heat model in the following way [4]:

$$h(\theta - \theta_{wall}) + \mathbf{q} \cdot \mathbf{n} = 0 \quad (9)$$

where:

- h – heat transfer coefficient,
- θ_{wall} – wall temperature,
- θ – fluid temperature in volume,
- \mathbf{n} – the unit normal vector on the boundary surface,
- \mathbf{q} – Fourier heat flux. The heat flux \mathbf{q} is defined by Fourier law:

$$\mathbf{q} = \lambda \text{ grad } \theta \quad (10)$$

where:

- λ – coefficient of Lambert thermal conductivity in volume.

In discussing the two-way interaction between solid and fluid, the authors have in mind the problem of interphase surface mechanical motion. It should be added that extended boundary condition between CFD approach (Computational Fluid Dynamic) and CSD approach (Computational Solid Dynamic) are required to take into account phenomenon occurs at the interphase surface layer. This interphase surface layer is connection of mechanical motion between fluid–solid interaction. Usually, these mechanical conditions leads to the motion of discretisation lattices (finite volumes or finite elements), since both CFD and CSD obey the discretisation of the whole domain divided into solid and fluid parts. It is known that motion of the fluid domain discretisation lattices follows a large displacement of solid boundaries, and vice-versa – the motion of solid discretisation lattices follows an action such as mass sedimentation, swelling, etc.

From the point of view of thermal motion, the problem of a thermal interphase motion is also important and should be taken into account in the formulation of a general mathematical model for the thermal-FSI. Therefore, we should consider thermal contact layer with thermal energy interaction between solid and fluid. As shown in Fig. 3, thermal layer between hot fluid continua and cold solid continua can be described by a thin but finite contact interphase. The length of temperature jump was defined by von Smoluchowski to be [4, 27]:

$$l_0 = l_0^s + l_0^f = \frac{\lambda}{h} \quad (11)$$

where:

- l_0^s, l_0^f – the length of thermal jump, respectively for solid and fluid side (see Fig. 3).

It should be added that l_θ is the closure which depends on physical properties of thermal layer. The length of temperature jump l_θ is direct analogy to Navier slip length l_s . Generalised formulation of the condition of energy balance in the Smoluchowski layer, proposed in the IMP PAN, has the following form:

$$\partial_t(c_{p,s}\theta_s) + \text{div}_s(c_{p,s}\theta_s \mathbf{v}_{s||}) - \theta_s I_d \mathbf{v}_s \mathbf{n} + \text{div}_s(\lambda_s \text{grad}_s \theta_s) + h(\theta - \theta_{\text{wall}}) + \mathbf{q} \cdot \mathbf{n} = 0 \quad (12)$$

where:

- θ_s – temperature of the Smoluchowski layer;
- λ_s – thermal conductivity of the layer;
- $c_{p,s}$ – specific heat on the layer;
- $\mathbf{v}_{s||} = \mathbf{v}_s \mathbf{I}_s$ – tangent to surface component of the slip velocity;

$I_d = \text{tr}(\mathbf{d})$ – trace of rate of deformation and $\mathbf{d} = 1/2(\text{grad} \mathbf{v} + \text{grad}^T \mathbf{v})$ the rate of deformation.

The surface contribution to equation (12) is especially important in micro- and nano-scales where the mechanism of the von Smoluchowski thermal jump becomes most valid. Also in nano-scales, the energetic contribution from the mechanical slip – for instance the Navier slip – is considerable.

5. The last stages of the turbine

The last aim of this study is to analyse the free-standing blade of the last stages of the gas-steam turbine, which was used as a commercial element of the steam turbine. It is well known that the most exploited stages of turbines (especially steam turbine) are the first and last [34–36]. The high pressure stages of steam turbine are designed for majority new types of turbines, because the possibility to manufacture the cylindrical profile of blade is relatively simple. On the other hand, the low pressure stages of steam turbine are usually selected from profile of blade already done. However, last stages of the turbine are checked additionally to ensure the proper functionality. The complexity of the configuration such as non-uniform cross-section, twist, thickness, and curvature makes the research of blades of the last stage difficult [36]. On the other hand, it is quite significant for the design, safety and lifetime of machinery to determine their dynamic characteristics accurately because they are working at high speed – this prompts researchers and producers to devote greater efforts to the problem [34–36].

In particular, it is important to investigate the stress state of turbine and steam boilers [28, 34, 37, 38]. Some elements of above facilities are manufactured with high-strength steels or, in general, ultra-fine grained alloys and nano-metals. So state stress of some turbine elements can depend on so-called strength differential effect, i.e. asymmetry of elastic range. Therefore, the original Burzyński's formulation of yield condition [39] remains actual and acquires increasing significance. However, the yield criterion proposed by Huber [40] for isotropic solids characterized by equal magnitude of yield stress in tension and compression,

was well established and confirmed experimentally. The Huber–Mises effort definition is also used during thermal-FSI analysis of power turbine [37, 38].

The geometry of the analysed blade is shown in Fig. 4. It is a free-standing rotor blade that is twisted and used in the final stages of the steam turbine. The above 3-D shapes are known as ‘blade lean’ and ‘blade sweep’. For a fixed hub configuration, a tangential ‘lean’ is defined as the shifting of the stacking line tangentially to the pressure side. A ‘blade sweep’ makes an appearance when the stacking line is modified toward the inflow as the blade radius increases, so the upper part of the blade (tip) is bevelled in such way that fit its shape to the diffuser, as shown in Fig. 4. The average height is about 770 mm and made of a titanium alloy with: a density of 4507 kg/m³; Young modulus of 100 GPa; Poisson ratio of 0.34; yield strength of 650 MPa. During turbine operation, the blade elastically untwists due to centrifugal forces. The CSD approach was used in order to perform the analysis.

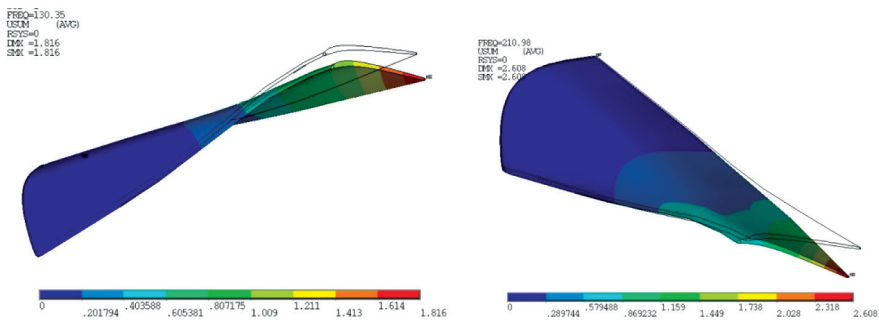


Fig. 4. Two of the first modes of vibrations (left side, first mode; right side, second mode)

A first mode dominated by flexural (bending) vibration of a nodal line coinciding with the base of the blade is shown on the left side of Fig. 4. On the right side, we can see a second mode of combining flexural and torsion vibration with two nodal lines – one at the base of the blade and a second along the leading edge. Additionally, results of numerical analysis are shown in Fig. 5 which contains modes and frequencies of vibrations depending on rotation speed. Hence, the Campbell diagram (Fig. 5) is presented as a final result of modal analysis and resonating force.

Analysis of the mode and frequency of vibration is necessary in order to find out if the design will not work in the area of resonance. Dangerous areas are marked on the Campbell chart (Fig. 5). Furthermore, it is important to: 1) identify the distribution and the places of the highest reduced stresses in the profile of the blades; 2) show the change in the blade untwist; 3) show the state of stresses, both total (mainly the Huber–Mises stresses) and stretching; 4) show the state of displacement.

Based on the graphs of resonance, we can say that the frequency of the second form for vibration values of 3000 [r/min] is in the dangerous range H_4 . It could lead to the destruction of the blade because the frequency of natural vibrations is close to the frequency of the vibration of the exciting force which causes mechanical resonance. Also, for the third form – the torsion form of vibration, the frequency is close to the dangerous range, the blade should be redesigned. Analyses of the state of stresses and displacements came out positively.

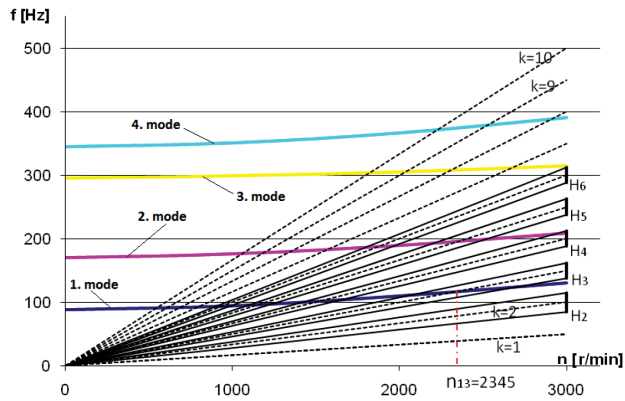


Fig. 5. Campbell graph of resonance

6. Conclusions

The results of the thermodynamic analysis indicates the legitimacy of building cycles based on enhancement energy conversion. However, many questions arise in the selection of individual devices and their components that are important for the zero-emission power plant project for Pomerania. The discussed system, based on the use of shale gas in the location from which it is extracted in a compact, zero-emission gas-steam turbine should contain small-sized devices, for example: 1) a wet combustion chamber (with oxy-combustion and using cooling water transpiration); 2) a spray-ejector condenser (using a bulk condensation on the surface of steam-gas water droplets); 3) compact heat exchanger. Due to the specific working conditions, there is also a need to combine design issues in the field of steam turbines, gas and reinforced energy conversion. The paper presents the problems of modelling the enhancement mass flow rate in a wet combustion chamber using transpiring cooling and the issues of heat transfer exchangers with a temperature jump. It also presents an example of the calculations for the free-standing rotor blade – this is a mainly dynamic and kinetostatic analysis. The Huber-Mises-Hencky stress, deformation and untwist angle of the profile blade have been presented following kinetostatic analysis.

References

- [1] Ziółkowski P., Badur J., *Clean Gas Technologies – towards zero-emission repowering of Pomerania*, Trans IFFM, no 124, 2012, 51–80.
- [2] Ziółkowski P., Zakrzewski W., Badur J., *Innowacyjny obieg termodynamiczny oparty na poślizgu, mobilności, transpiracji i innych zjawiskach nano-przepływowych*, [in:] B. Węglowski, P. Duda (Eds.), *Analiza systemów energetycznych*, Wyd. Pol. Krakowskiej, Kraków 2013, 351–360.
- [3] Ziółkowski P., Badur J., *Selection of thermodynamic parameters in order to improve the environmental performance on the gas-steam turbine cycle*, [in:] K. Wójs, T. Tietze

- (Eds.), *Aktualne Zagadnienia Energetyki Tom III*, Oficyna Wydawnicza Politechniki Wrocławskiej, Wrocław 2014, 445–456.
- [4] Badur J., Ziółkowski P., *Modelowanie konwersji energii w nano-skali*, [in:] B. Węglowski, P. Duda (Eds.), *Analiza systemów energetycznych*, Wyd. Pol. Krakowskiej, Kraków 2013, 15–28.
 - [5] Feidt M., *Thermodynamics of energy systems; a review and perspectives*, *Journal of Applied Fluid Mechanics*, vol. 5(2), 2012, 85–98.
 - [6] Badur J., Karcz M., Lemański M., *On the mass and momentum transport in the Navier-Stokes slip layer*, *Microfluid Nanofluid*, vol. 11, 2011, 439–449.
 - [7] Badur J., Karcz M., Lemański M., Nastalek L., *Foundations of the Navier-Stokes boundary conditions in fluid mechanics*, *Trans IFFM*, No. 123, 2011, 3–55.
 - [8] Reese J.M., Zheng Y., Lockerby D.A., *Computing the near-wall region in gas micro- and nanofluidics: critical Knudsen layer phenomena*, *J. Computational and Theoretical Nanoscience*, vol. 4(4), 2007, 807–813.
 - [9] Nowak W., *Fluidalne spalanie węgla w tlenie*, *Energetyka Ciepłna i Zawodowa*, no 2, 2010, 46–48.
 - [10] Krzywański J., Czakiert T., Muskała W., Nowak W., *Modelling of CO₂, CO, SO₂, O₂ and NO_x emissions from the oxy-fuel combustion in a circulating fluidized bed*, *Fuel Processing Technology*, vol. 92, 2011, 590–596.
 - [11] Czakiert T., Sztokler K., Karski S., Markiewicz D., Nowak W., *Oxy-fuel circulating fluidized bed combustion in a small pilot-scale test rig*, *Fuel Processing Technology*, vol. 91, 2010, 1617–1623.
 - [12] Kotowicz J., Brzeczek M., Job M., *Efficiency of supercritical coal power stations with integrated CO₂ capture and compression systems based on oxy-combustion technology*, *Acta Energetica*, no 1/26, 2016, 69–76.
 - [13] Skorek-Osikowska A., Bartela Ł., Kotowicz J., *A comparative thermodynamic, economic and risk analysis concerning implementation of oxy-combustion power plants integrated with cryogenic and hybrid air separation units*, *Energy Conversion and Management*, vol. 92, 2015, 421–430.
 - [14] Kotowicz J., Job M., *Thermodynamic and economic analysis of a gas turbine combined cycle plant with oxy-combustion*, *Archives of thermodynamics*, vol. 34(4), 2013, 215–233.
 - [15] Horlock J., *Advanced gas turbine cycles*, Pergamon, Elsevier Sc. Ltd., Oxford, 2003.
 - [16] Mathieu Ph., Nihart R., *Sensitivity analysis of the MATIANT cycle*, *Energy Conversion and Management*, vol. 40(15), 1999, 1687–1700.
 - [17] Yantovsky E., Górski J., Shokotov M., *Zero emissions power cycles*, Taylor&Francis Group, Boca Raton, 2009.
 - [18] Yang H.J., Kang D.W., Ahn J.H., Kim T.S., *Evaluation of design performance of the semi-closed oxy-fuel combustion combined cycle*, *Proceedings of ASME Turbo Expo 2012*, GT2012-69141, 1–12.
 - [19] Sanz W., Hustad Carl-W., Jericha H., *First generation Graz cycle power plant for near-term deployment*, *Proceedings of ASME Turbo Expo 2011*, GT2011-45135, 1–11.
 - [20] Kolev N., Schaber K., Kolev D., *A new type of a gas – steam turbine cycle with increased efficiency*, *Applied Thermal Engineering*, vol. 21, 2001, 391–405.



- [21] Anderson R., MacAdam S., Viteri F., Davies D., Downs J., Paliszewski A., *Adapting gas turbines to zero emission oxy-fuel power plants*, ASME Paper No. GT2008-51377, 2008, 1–11.
- [22] Chodkiewicz R., Porochnicki J., Kaczan B., *Steam – gas condensing turbine system for power and heat generation*, ASME Paper No. 2001-GT-0097, 2001, 1–8.
- [23] Ziółkowski P., Badur J., *Navier number and transition to turbulence*, Journal of Physics: Conference Series, vol. 530, 2014, 012035.
- [24] Ziółkowski P., Badur J., *On the unsteady Reynolds thermal transpiration law*, Journal of Physics: Conference Series, vol. 760, 2016, 012041.
- [25] Szwaba R., Ochrymiuk T., *Transpiration effects in perforated plate aerodynamics*, Journal of Physics: Conference Series, vol. 760, 2016, 012032.
- [26] Bunker R., *Gas turbine heat transfer ten remaining hot gas path challenges*, ASME Journal of Turbomachinery, vol. 129(2), 2007, 193–201.
- [27] Badur J., Ziółkowski P., Zakrzewski W., Sławiński D., Kornet S., Kowalczyk T., Hernet J., Piotrowski R., Felicjancik J., Ziółkowski P.J., *An advanced Thermal-FSI approach to flow heating/cooling*, Journal of Physics: Conference Series, vol. 530, 2014, 012039.
- [28] Taler J., *A method of determining local heat flux in boiler furnace*, Int. J. Heat Mass Transfer, vol. 35(6), 1992, 1625–1634.
- [29] Taler D., *A new heat transfer correlation for transition and turbulent fluid flow in tubes*, International Journal of Thermal Sciences, vol. 108, 2016, 108–122.
- [30] Ocloń P., Łopata S., *Modeling of the flow distribution inside the collectors of the high performance heat exchanger*, Technical Transactions, series Mechanics, vol. 7(4), 2011, 391–400.
- [31] Taler D., Tokarczyk J., *Modeling of pipeline heating*, Technical Transactions, series Mechanics, vol. 11(6), 2012, 127–134.
- [32] Bejan A., Kraus A.D., *Heat transfer handbook*, 2003 John Wiley & Sons, Hoboken New Jersey 2003.
- [33] Gyftopoulos E.P., Beretta G.P., *Thermodynamics Foundations and Applications*, Dover Pub. Mineola, New York 2005.
- [34] Banaszkiwicz M., *Multilevel approach to lifetime assessment of steam turbines*, International Journal of Fatigue, vol. 73, 2015, 39–47.
- [35] Hu X.X., Sakiyama T., Matsuda H., Morita C., *Fundamental vibration of rotating cantilever blades with pre-twist*, Journal of Sound and Vibration, vol. 271, 2004, 47–66.
- [36] Szewalski R., *O racjonalne obliczanie długości łopatek w akcyjnych turbinach parowych*, Czasopismo Techniczne, vol. 55, Lwów 1930, 12–21.
- [37] Banaś K., Badur J., *On an approach to the thermo-elastic-plastic failure based on the Burzyński-Pęcherski criterion*, Proc. 11th Int. Cong. On Thermal Stresses, University of Salerno, Italy, 5–9 June 2016, 19–22.
- [38] Badur J., Ziółkowski P., Sławiński D., Kornet S., *An approach for estimation of water wall degradation within pulverized-coal boilers*, Energy, vol. 92, 2015, 142–152.
- [39] Burzyński W.T., *Teoretyczne podstawy hipotez natężenia*, Czasopismo Techniczne, vol. 47, Lwów 1929, 1–41.
- [40] Huber T.M., *Właściwa praca odkształcenia jako miara wytrzymałości materiału*, Czasopismo Techniczne, vol. 22, Lwów 1904.